

DOCTORAL THESIS

Additive Manufacturing of
Mo-Mo_(x)S_(x+1) Functional
Structures: Engineering and
Electrochemical Applications

Navid Alinejadian

TALLINN UNIVERSITY OF TECHNOLOGY
DOCTORAL THESIS
43/2022

**Additive Manufacturing of Mo-Mo_(x)S_(x+1)
Functional Structures: Engineering and
Electrochemical Applications**

NAVID ALINEJADIAN



TALLINN UNIVERSITY OF TECHNOLOGY

School of Engineering

Department of Mechanical and Industrial Engineering

This dissertation was accepted for the defence of the degree 19/07/2022

Supervisor: Prof. Prashanth Konda Gokuldoss, PhD
School of Engineering
Tallinn University of Technology
Tallinn, Estonia

Co-supervisor I: Dr. Lauri Kollo, PhD
School of Engineering
Tallinn University of Technology
Tallinn, Estonia

Co-supervisor II: Prof. Inger Charlotta Odnevall, PhD
School of Engineering Sciences in Chemistry, Biotechnology and Health (CBH)
KTH Royal Institute of Technology
Stockholm, Sweden

Opponents: Dr. Mohammadreza Karamad, PhD
Faculty of Science
University of Calgary
Alberta, Canada

Dr. Saman Hosseinpour, PhD
Faculty of Engineering
Friedrich-Alexander University Erlangen-Nuremberg
Erlangen, Germany

Prof. Eduard Hryha, PhD
Division of Materials and Manufacturing, Industrial and Materials Science
Chalmers University of Technology
Gothenburg, Sweden

Defence of the thesis: 19/08/2022, Tallinn

Declaration:

Hereby I declare that this doctoral thesis, my original investigation and achievement, submitted for the doctoral degree at Tallinn University of Technology has not been submitted for doctoral or equivalent academic degree.

Navid Alinejadian



European Union
European Regional
Development Fund



Investing
in your future

signature

Copyright: Navid Alinejadian, 2022

ISSN 2585-6898 (publication)

ISBN 978-9949-83-875-2 (publication)

ISSN 2585-6901 (PDF)

ISBN 978-9949-83-876-9 (PDF)

Printed by Koopia Niini & Rauam

TALLINNA TEHNIKAÜLIKOO
DOKTORITÖÖ
43/2022

**Lisandustehnoloogia teel valmistatud
Mo-Mo_(x)S_(x+1) funktsionaalsed struktuurid
inseneri- ja elektrokeemilistele rakendustele**

NAVID ALINEJADIAN



Contents

Contents.....	5
List of publications	7
Author's contribution to the publications	8
Introduction	9
Abbreviations and symbols of chemical elements.....	12
1 Literature review.....	14
1.1 Electrochemical energy conversion/storage systems.....	14
1.1.1 Supercapacitors and batteries	14
1.1.2 Pseudocapacitors	15
1.2 2D materials for electrochemical applications.....	17
1.2.1 Transition-metal dichalcogenides	17
1.2.2 MoS ₂	18
1.2.2.1 Properties.....	18
1.2.2.2 MoS ₂ applications.....	19
1.2.2.2.1 Hydrogen evolution reaction (HER) and fuel cells	19
1.2.2.2.2 Battery and supercapacitor.....	20
1.3 Additive manufacturing of energy storage materials	20
1.4 Selective laser melting	21
1.4.1 SLM for electrochemical energy storage applications	22
1.4.2 The advantages of the selective laser melting process.....	23
1.4.3 Parameter optimization by SLM.....	23
1.4.3.1 Scanning strategy	23
1.4.3.2 Variation of exposure time.....	24
1.4.4 Crack mitigation in SLM processes.....	24
1.4.5 Processing of molybdenum by SLM: difficulties and solutions	25
1.4.6 Addition of MoS ₂ to Mo feedstock.....	26
1.4.7 Processing of composites by SLM: difficulties and solutions	26
2 Aim and objectives	28
3 Materials and methods	29
3.1 SLM processing	29
3.1.1 Materials	29
3.1.2 Method	29
3.1.3 SLM parameter optimization for composites	30
3.2 Electrochemical characterization	31
3.2.1 Materials	31
3.2.2 Methods.....	31
3.2.2.1 Electrochemical energy conversion/storage studies	31
3.2.2.2 Electrochemical polarization and corrosion studies	31
3.3 Physical characterization.....	32
3.3.1 Methods.....	32
4 Results and discussion.....	33

4.1 Phase transformation and crystallographic studies	33
4.2 Microstructural studies	35
4.3 Physical characterization of phase transformation	44
4.4 Electrochemical characterization	46
4.4.1 Corrosion studies	46
4.4.2 Study on energy conversion/storage	49
5 Conclusion	53
6 Outlook.....	54
References	55
Acknowledgments.....	68
Abstract	69
Lühikokkuvõte.....	70
Appendix 1	71
Appendix 2	81
Appendix 3	105
Curriculum vitae.....	115
Elulookirjeldus.....	116

List of publications

- I N. Alinejadian, P. Wang, L. Kollo, K.G. Prashanth, Selective Laser Melting of Commercially Pure Molybdenum by Laser Rescanning, 3D Print. Addit. Manuf. 00 (2022) 1–7. <https://doi.org/10.1089/3dp.2021.0265>.
- II N. Alinejadian, L. Kollo, I. Odnevall, Progress in additive manufacturing of MoS₂ - based structures for energy storage applications – A review, Mater. Sci. Semicond. Process. 139C (2022) 106331. <https://doi.org/10.1016/j.mssp.2021.106331>.
- III N. Alinejadian, S.H. Kazemi, I. Odnevall, SLM-processed MoS₂/Mo₂S₃ nanocomposite for energy conversion/storage applications, Sci. Rep. 12, 5030 (2022). <https://doi.org/10.1038/s41598-022-08921-7>.

Author's contribution to the publications

- I Investigation – SLM processing, experiments, and characterizations; Writing – original draft.
- II Conceptualization; Funding acquisition; Investigation; Validation; Writing – the original manuscript, reviewing, and editing.
- III Conceptualization; Funding acquisition; Investigation – SLM-based fabrication of samples, experiments, and characterizations by electrochemical, Raman spectroscopy, XRD, and SEM techniques; Validation of data; Writing – the original manuscript, reviewing, and editing.

Introduction

The global market for advanced energy storage systems was in 2020 valued at US\$ 16.3 billion, and it is predicted to reach US\$ 29.93 billion by the end of 2028 (Advanced Energy Storage Systems Market Size, Share, Trends & Forecast, n.d.). The compound annual growth rate (CAGR) of 8.29% has been ascribed to the global growth in renewable energy investments, the electric vehicles market, and demanding energy efficiency (Advanced Energy Storage Systems Market Size, Share, Trends & Forecast, n.d.). Investigations of next-generation manufacturing methods for processing functional materials, and the fabrication of products with improved performance/functionalities have always been a challenge in terms of energy efficiency, cost-effectiveness, and eco-friendliness. Hence, the advancement of novel electroactive materials, devices, and their processing techniques are globally critical for the energy sector, aerospace industries, and the global economy since they are widely used in transportation systems and energy-based industries.

Furthermore, sustainable energy supply and clean energy utilization have been recently highlighted in a variety of state-of-the-art research due to the reduction of greenhouse gas emissions and the enhancement of industrial power generation. Efficient EECSS have been widely developed in different areas ranging from electric vehicles to smart grids and aerospace applications, toward the reduction of greenhouse gas emissions and enhancement of industrial power generation.

Rechargeable lithium-ion energy storage electrodes with high energy density, long cycling durability, and negligible self-discharge have attracted a wide range of interest and have been extensively extended to portable electronics and even hybrid electric vehicles (F. Li et al., 2018). However, the limited abundance of Li (≈ 20 ppm in the earth's crust) and local natural reserves have during recent decades resulted in the increasing costs of lithium as raw material (F. Li et al., 2018). Interestingly, sodium (Na) is more abundant (≈ 2.75 wt.%) and widely distributed which turns it into an ideal alternative to Li, possessing similar chemical and physical properties. The pseudocapacitive behavior of Na makes it a potential candidate for both rechargeable SIBs and SICs. Hence, the next generation of Na-ion energy storage systems can merge the complementary features of high-power supercapacitors and high-energy batteries (F. Li et al., 2018; Yu et al., 2017).

A wide range of two-dimensional materials, e.g., graphene, TMDCs, etc., have attracted increased attention both from the industrial sector and academia. TMDCs are a class of 2-dimensional atomic layers consisting of metal atoms sandwiched between two layers of chalcogen atoms with a stoichiometry of MX_2 . The transition metal – M and the chalcogen atom – X exhibit the oxidation states of +4 and -2, respectively (Huang et al., 2015). 2D crystals, e.g., MoS_2 , MoTe_2 , MoSe_2 , NbSe_2 , and TaSe_2 , possess large surface area, high mechanical strength, and high electrical and thermal conductivity introducing them as potential candidates to be utilized in versatile functional applications such as catalysis, energy storage, electronics, etc (Coleman et al., 2011; Mukherjee et al., 2018; Yao et al., 2012).

Considering the advantages and potential of TMDCs in the field of energy storage, TMDCs have despite their existing drawbacks been widely processed by conventional methods (Paper II; Brown et al., 2019; Cao et al., 2013; Castellanos-Gomez et al., 2012; Chang et al., 2020; Cohen et al., 2018; Gao et al., 2013; L. Hu et al., 2017; Huang et al., 2015; Kim et al., 2017; Xiaodan Li et al., 2017; H. Lin et al., 2010; Mukherjee et al., 2018; Ning et al., 2015; Pang et al., 2020; Sajedi-Moghaddam et al., 2020; Shao et al., 2020; S. Wang et al., 2010; Yao et al., 2012; H. Zhang et al., 2011; J. Zhou et al., 2016; Xiaoping

Zhou et al., 2014; Z. Zhou et al., 2014). Thanks to the current state-of-the-art technologies, several additive manufacturing (AM) techniques have been extensively employed with the aim to fabricate enhanced 3D electrodes of a wide range of materials with the intended use in e.g. electrochemical applications (Paper II; Brown et al., 2019; Gallardo et al., 2017; Jewel et al., 2020; Jiantong Li, Lemme, et al., 2014; Jiantong Li, Naiini, et al., 2014; Seo et al., 2019; Shao et al., 2020; X. Wang et al., 2017). Nevertheless, these techniques have demonstrated some specific limitations, which hinder the industrial scale-up of additively manufactured products. It has already been shown that laser-based processing can effectively control the thinning of MoS₂. This can enable the fabrication of 3D geometries from 2D nanomaterials (Alexaki et al., 2018; L. Hu et al., 2017) and enhance the capacitance of thinned components (Xiaowen Zhou et al., 2018). Hence, SLM can successfully be applied not only to overcome the disadvantages of conventional processing approaches of 2D nanomaterials (M. Cheng et al., 2020; F. Zhang et al., 2017), but also to advance the rapid prototyping of functional sustainable components via simultaneous thinning of 2D nanomaterials, fabrication of electroactive nanocomposites, and tuning of the chemical, physical, and crystallographic characteristics (Paper II; Zhu et al., 2017). Compared with other AM methods, SLM is a technique applicable to directly utilize raw materials *in-situ* and deliver functionality during the fabrication of intricate parts.

Within the framework of this thesis, green (more eco-friendly than other conventional chemical and electrochemical techniques, in terms of no residual chemicals, wastes, environmental pollutants, etc.) (Babu et al., 2009; Hunt, 1988; Putra et al., 2019; Reis et al., 2019), and novel SLM-processed Mo_(x)S_(x+1)-incorporated electroactive composites have been elaborated. The investigations reveal the unprecedented capability of the SLM technology both in the transformation of MoS₂ from bulk 2H phase to metallic 1T phase through direct laser-assisted thinning and in the *in-situ* formation and distribution of Mo₂S₃ nanoparticles in the structures of the nanocomposite. The outstanding electroactivity (remarkable power density, energy density, and cyclic charge-discharge stability) of Mo/MoS₂/Mo₂S₃ nanocomposite electrodes (SLM-Mo/Mo_(x)S_(x+1)) for Na-ion energy storage applications have been elaborated to demonstrate the ability of the fabrication method and fabricated electrodes, that pave a novel way facilitating the fabrication of the hybrid capacitors and next-generation EECSS.

Aspects of sustainability, improved printability, higher structural quality, and environmental corrosion resistance of SLM-processed Mo_(x)S_(x+1)-incorporated composites were studied by means of physical (SEM, XRD, Raman spectroscopy, etc.) and electrochemical characterization (cyclic potentiodynamic polarization and electrochemical impedance spectroscopy) of Mo/MoS₂/Mo₂S₃ lattice composites in different solutions. The results elucidate why SLM-processed Mo_(x)S_(x+1)-incorporated composites should be used for Na-ion energy storage systems. The achievements of this thesis and the results are believed to advance further research on laser-based AM processing of 2D nanomaterials for a wide range of functional structures with the intended use in, e.g. EECSS, high-temperature solid-state energy conversion/storage systems, and aerospace components.

Concerning the coherency of this novel research line, initiated by this thesis, with the sustainable development goals (SDG) of the UN, the achievements can be utilized and somehow meet a part of the requirements shortlisted under the SDG numbers 7, 11, and 13 (United Nations, 2015). There are different reports indicating the sustainability and wide availability of energy sources throughout the globe. Therefore, the enhanced

SLM-processed electrodes can be used for application in microgrids connected to renewable clean energy sources such as solar cells (SDG 7). The increasing urbanization of the world's population is projected to reach 60% by 2030, which accounts for about 70 percent of global carbon emissions for which sources of road and transport can be considered. Thus, the enhancement of SLM-processed electrodes can be utilized for the energy sector related to electric vehicles (SDG 11) and play a vital role as a new technology framework in the alleviation of global CO₂ emission and global warming (SDG 13).

Abbreviations and symbols of chemical elements

CAGR	compound annual growth rate
EECSS	electrochemical energy conversion/storage systems
0D	zero-dimensional (nanoparticles, quantum dots)
1D	one-dimensional (nanotubes)
2D	two-dimensional (nanosheets, nanoplatelets)
3D	three-dimensional (nanostructured materials)
AC	alternating current
AJP	aerosol jet printing
AM	additive manufacturing
BCC	body-centered cubic
BSE	back-scattered
CA	areal capacitance
CPP	cyclic potentiodynamic polarization
CV	cyclic voltammetry
D	coherent domain size
d50	average particle size
DBTT	ductile-to-brittle transition temperatures
DIW	direct ink writing
E	potential
E_{corr}	corrosion potential
EDL	electrical double layer
EDLC	electrical double-layer capacitors
EIS	electrochemical impedance spectroscopy
E_{pp}	pitting potential
ESR	equivalent series resistance
FDM	fused deposition modeling
FWHM	full width half maximum
GCD	galvanostatic charge-discharge
H_2SO_4	Dihydrogen sulfate (sulfuric acid)
HER	hydrogen evolution reaction
I_{corr}	corrosion current
i_{corr}	corrosion current densities
IJP	ink-jet printing
I_{pp}	pitting current
i_{pp}	pitting current density
K	Potassium
LDS	laser double scanning
Li	lithium
LOF	lack of fusion

L-PBF	Laser-based powder bed fusion
LPSA	laser scattering particle size distribution analyzer
LSS	laser single scanning
MFCs	microfluidic-based micro fuel cells
MMCs	metal-matrix composites
Mo	molybdenum
Mo ₂ S ₃	dimolybdenum trisulfide
MoS ₂	molybdenum disulfide
Na	sodium
Na ₂ SO ₄	Disodium sulfate
NaCl	sodium chloride
OCP	Open-circuit potentials
ORR	oxygen reduction reactions
PBR	Pilling–Bedworth ratio
PEMFCs	proton exchange membrane fuel cells
ppm	part per million
R _{ct}	semi-circle arc
RE	rare-earth compounds
R _p	polarization resistance
SCC	stress corrosion cracking
SDG	sustainable development goals
SE	secondary electron
SEM	scanning electron microscope
SIBs	Sodium-ion batteries
SICs	Sodium-ion supercapacitors
SLA	stereolithography
SLM	Selective laser melting
SLM-Mo/Mo _(x) S _(x+1)	SLM-processed Mo/MoS ₂ /Mo ₂ S ₃ nanocomposite
SLM-Mo	SLM-processed pure Mo structure
SLS	selective laser sintering
T.C.	texture coefficient
TAE	template-assisted electrodeposition
TMDCs	transition-metal dichalcogenides
XPS	X-ray photoelectron spectroscopy
XRD	X-ray diffraction
β _a	anodic Tafel constants
β _c	cathodic Tafel constants
δ	dislocation density
ΔE _(corr-pp)	corrosion-pitting potential deviation
ε	lattice strain

1 Literature review

1.1 Electrochemical energy conversion/storage systems

The combustion of fossil fuels as a resource for energy consumption/production has globally shown to have a severe impact on the economy and ecology. Electrochemical energy conversion/storage systems have been developed for almost two decades as promising, sustainable, eco-friendly, and versatile alternative energy storage sources either connected to other energy conversion sources (such as photovoltaic systems) or substituted instead of fossil-fuelled engines.

1.1.1 Supercapacitors and batteries

Although there exist many differences in the mechanism of storage/depletion and charge/discharge performance, some mutual facets can be considered for all EECSS including ion/electron transportation at the electrode/electrolyte interface. Batteries and supercapacitors consist of conductive anodes (more negative), cathodes (more positive), electrolytes, and separators.

The structure of batteries is constructed by two ion-storage electrodes, an ion-conducting electrolyte, and a separator (Figure 1a). All the components in supercapacitors are similar to batteries, except that capacitor-type materials are used as cathode materials (Figure 1b). As a result, the energy storage mechanism differs from batteries to supercapacitors, depending on the reversible ion exchange mode between the anode and the cathode. Redox reactions at the anode and cathode are the prominent mechanisms of electrochemical energy conversion in batteries, whereas the orientation of anions and cations at the electrical double layer (EDL) is the main mechanism of energy storage in electrical double-layer capacitors (EDLC). In supercapacitors, the ions can shuttle back and forth between a capacitor-type cathode and a battery-type anode (Figure 1) (F. Li et al., 2018).

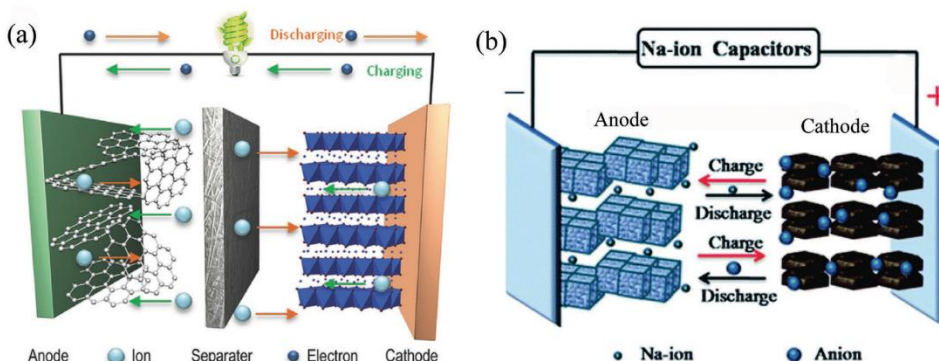


Figure 1. Schematic illustration of SIBs and b) Schematic illustration of SICs [adapted with permission from John Wiley and Sons under the license number 5306680649394 dated May 12, 2022 (F. Li et al., 2018)].

In terms of power density or energy density, a designed system can be evaluated based on Ragone plots (Figure 2). Batteries can provide high energy density, while supercapacitors provide high power density as a function of discharge time. Addressing a tremendous global demand for electrochemical energy storage providing simultaneous

high power and high energy densities, pseudocapacitors can overcome the capacity limitations of electrical double-layer capacitors and the mass transfer limitations of batteries (Fleischmann et al., 2020).

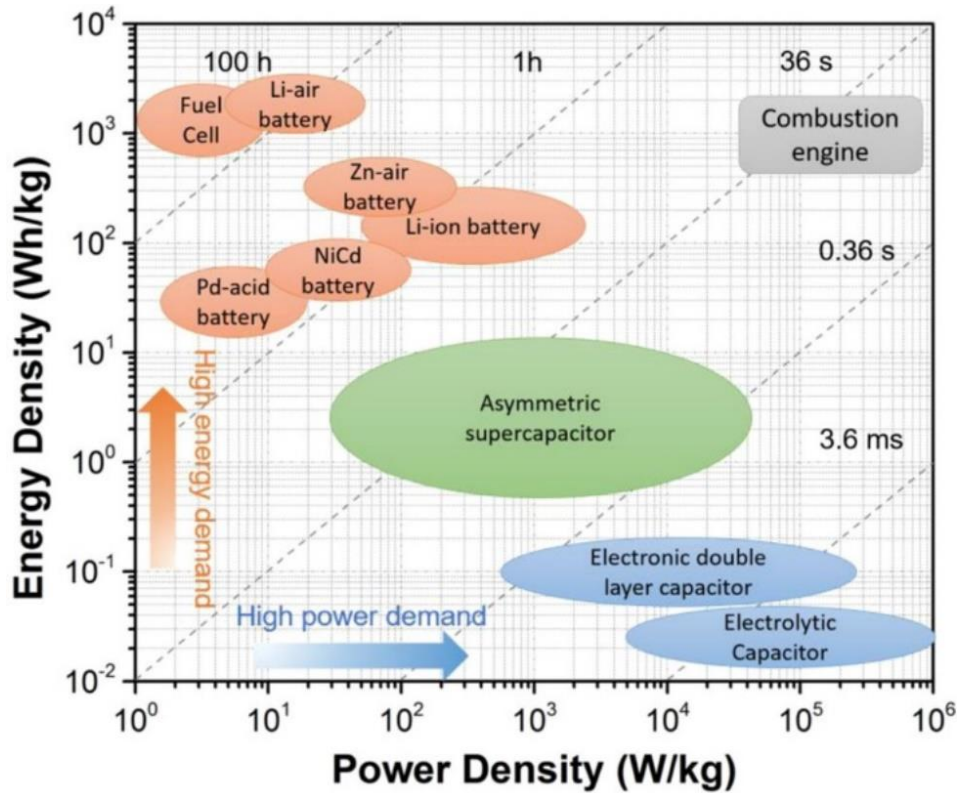


Figure 2. Ragone plot illustrating the specific power vs. specific energy based on discharge time for different electrical energy-storage technologies [adapted with permission from American Chemical Society dated May 12, 2022 (Shao et al., 2018)].

1.1.2 Pseudocapacitors

A pseudocapacitor electrode can generally possess a simple or a combined electrochemical characteristic, categorized in [Figure 3](#). Accordingly, surface redox electrodes ([Figure 3b](#)), intercalation-type electrodes ([Figure 3d](#)), or combined electrochemically reversible redox/intercalation-type electrodes ([Figure 3e](#)) can be suggested (Gogotsi et al., 2018). [Figure 3a](#) and [Figure 3g,h](#) illustrate an ideal rectangular cyclic voltammogram (CV) for supercapacitors (double-layer energy storage on high surface area conductors) and typical Faradaic electron transfer curves for batteries (Li⁺- or Na⁺-ion intercalation charge compensating), respectively. Discharge responses for each category are compared in [Figure 3c,f,i](#). Different linear or non-linear responses can be considered as one of the well-identified characteristics to evaluate the charge/discharge mechanisms, and categorize the designed electrodes/materials as a super-/pseudocapacitor or battery. The potential-independent capacitance of ELDCs can result in a constant current in response to potential scanning ([Figure 3a,b](#)). Widely separated redox peaks are a unique characteristic of batteries ([Figure 3g,h](#)) (Gogotsi et al., 2018; Winter et al., 2004).

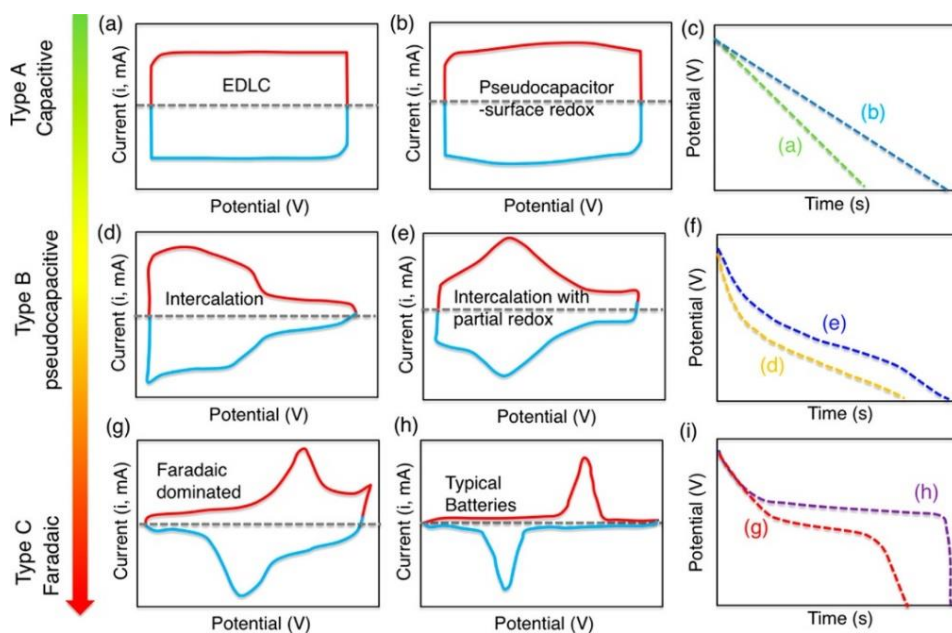


Figure 3. (a, b, d, e, g, h) Schematic cyclic voltammograms, and (c, f, i) corresponding galvanostatic discharge curves for various kinds of energy-storage materials [adapted with permission from American Chemical Society dated May 12, 2022 (Gogotsi et al., 2018)].

The linear potential versus time (E vs. t) plot illustrates the linear discharge of an EDLC (Figure 3c), whereas nonlinear plateaus of nearly constant potential correspond to Faradaic redox interactions (Figure 3i). An intermediate posture of these two forms of plots is associated with pseudocapacitive behavior (Figure 3f) (Gogotsi et al., 2018; Winter et al., 2004). The applications of solid-state and electrolytic capacitors require milli- to microsecond charge and discharge time (Figure 3c). However, pseudo- and supercapacitors can charge/discharge in less than a second to a minute (Figure 3f) (Gogotsi et al., 2018; Winter et al., 2004). The corresponding charge/discharge time scales of batteries are measured in minutes or hours (Figure 3i) (Gogotsi et al., 2018; Winter et al., 2004).

As explained above, specific intermediate mechanisms of pseudocapacitors can simultaneously provide enhanced power density and energy density. Figure 4 illustrates different electrochemical pseudocapacitive materials responses in terms of material thickness, morphology, and topology. Thin-film, or nanostructured pseudocapacitor materials with a thickness less than 20 nm, show a nearly symmetric CV caused by unlimited ion diffusion in thin thicknesses (Figure 4a). For thicker materials, designed pseudocapacitors can show different electrochemical behavior (extrinsic and intrinsic) due to the morphology of the electroactive layer and prevailing diffusion mechanisms. For instance, in a high-density bulk electroactive layer (extrinsic pseudocapacitor), the mechanism turns to diffusion-controlled. This results in a Faradic CV curve (battery-like pseudocapacitor) (Figure 4b), whereas fast ion diffusion in a low-density porous electroactive layer (intrinsic pseudocapacitor) results in an asymmetric rectangular-shaped CV curve (ELDC-like pseudocapacitor) (Figure 4c) (Fleischmann et al., 2020; Shao et al., 2018).

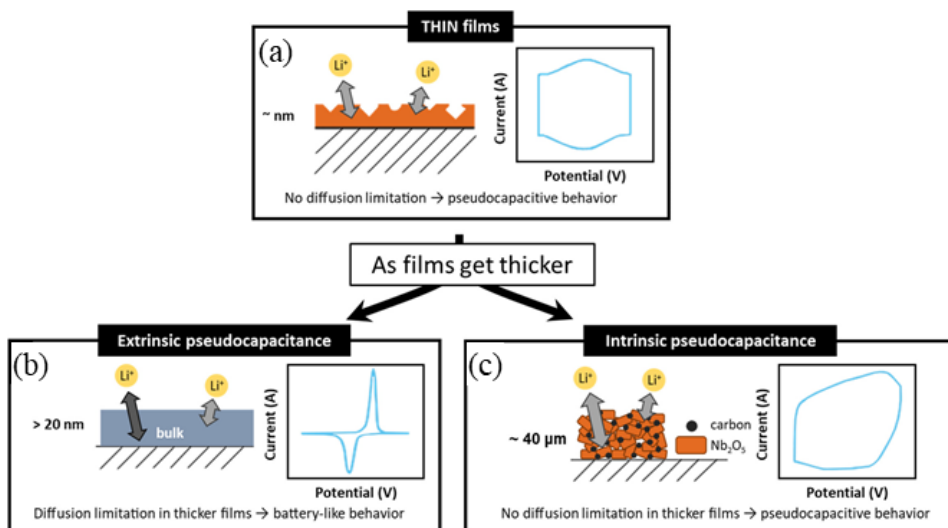


Figure 4. Schematic illustrations of thin-film-, extrinsic-, and intrinsic pseudocapacitive behavior and corresponding cyclic voltammograms [adapted with permission from American Chemical Society dated May 12, 2022 (Fleischmann et al., 2020)].

1.2 2D materials for electrochemical applications

Extensive research is currently focused on the development of cost-effective, efficient, environmentally safe, and reliable EECSS. The use of 2D materials as negative electrodes in ever-emerging non-Li EECSS, such as the Na-ion- or K-ion EECSS, has gained increased attention (Mukherjee et al., 2018).

1.2.1 Transition-metal dichalcogenides

Layered materials, particularly TMDCs such as MoS₂, TiS₂, WS₂, TaS₂, MoSe₂, MoTe₂, WSe₂, and NbSe₂, have the potential to become a diverse source of 2D crystals applicable for a wide range of functional applications such as catalysis, energy storage, and electronics. (Chhowalla et al., 2013; W. Choi et al., 2017; Samadi et al., 2018). TMDCs consist of hexagonal layers of metal atoms (M) sandwiched between two layers of chalcogen atoms (X) with a stoichiometry of MX₂ which exhibit oxidation states of +4 and -2, respectively (Huang et al., 2015). The advantageous properties, such as large surface area, high electrical, and high thermal conductivity, make TMDCs prominent materials for such functional applications (Coleman et al., 2011; Mukherjee et al., 2018; Yao et al., 2012).

The applicability of single-layered TiS₂ and TaS₂ nanosheets and their Pt- and Au-based nanocomposites have already been studied as potential 2D materials for electrocatalytic applications, i.e., hydrogen evolution reaction (HER) (B. Wang et al., 2014). WSe₂ and WS₂, in the forms of pure nanosheets (Guo et al., 2018; Hasani et al., 2018; Y. Zhang et al., 2017; Y. Zhao et al., 2013) and within 2D nanomaterial, have widely been suggested as potential 2D materials for HER due to their high-efficient electrocatalytic performance (Guo et al., 2018; Hasani et al., 2018; Yelgel et al., 2017; Y. Zhang et al., 2017). Aside from the above-mentioned TMDCs, exfoliated NbSe₂ has been investigated and shown to be a promising large-area semiconductor material for high-performance electronic applications

(Z. Lin et al., 2018). MoTe₂, in different pure and composite forms (Elibol et al., 2018; Lee et al., 2018; Lehnert et al., 2019; Mukherjee et al., 2019; Samadi et al., 2018), can be widely processed for different EECSS, ranging from high-performance HER materials (Lee et al., 2018) to Li-ion and Na-ion batteries (Mukherjee et al., 2019) as well as tunable optical and electronic quantum devices (Elibol et al., 2018; Lehnert et al., 2019). High-performance MoSe₂ can, similar to MoS₂, be tuned with different morphologies for various applications from HER (Kong et al., 2013; Tran et al., 2017) to supercapacitors, (Balasingam et al., 2015) and from piezo-catalyst (M. H. Wu et al., 2017) to sensing applications (W. Choi et al., 2017).

1.2.2 MoS₂

MoS₂ is one of the most studied materials among the existing various layered TMDCs. It has attracted huge attention during the last decade because of its excellent energy harvesting-, nanoelectronic-, and optoelectronic properties (Huang et al., 2015; Mukherjee et al., 2018).

1.2.2.1 Properties

Structural and mechanical characterizations reveal that mechanically flexible single-layer MoS₂ consists of different types of honeycomb lattice structures (Figure 5) with a weak interface van der Waals force between atomic layers, a lattice parameter of 3.12 Å, a vertical S-layer distance of 3.11 Å, a thickness of 6.5 Å (Huang et al., 2015; Xiao Li et al., 2015), and Young's modulus of 330±7 GPa. Differences between bulk and monolayer MoS₂ in terms of atomic structure and bandgap demonstrate that MoS₂ in its bulk form acts as a semiconductor with an indirect bandgap of ~1.29 eV, whereas, as a monolayer, it shifts upwards in energy to ~1.8 eV (Huang et al., 2015; Mortazavi et al., 2014). Such differences in surface properties between single-/few-layered forms, compared to their bulk counterparts, can though be optimized to enhance the electrochemical performance (Huang et al., 2015; Xiao Li et al., 2015; Mukherjee et al., 2018).

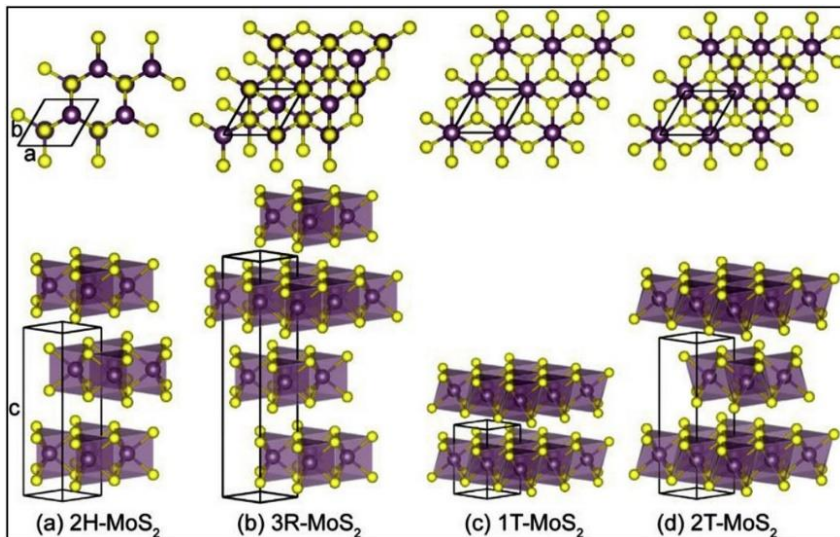


Figure 5. Layered MoS₂ of different structural polytype: (a) 2H, (b) 3R, (c) 1T, and (d) 2T. a, b and c denote the lattice constants of the hcp (hexagonally closed packed structure) unit cell. Yellow and purple spheres represent S and Mo atoms, respectively [adapted with permission from Elsevier under the license number 5306690916746 dated May 12, 2022 (Mortazavi et al., 2014)].

The electrochemical performance as a function of morphology and physical properties needs optimization as this is of large importance for the applicability of TMDCs (e.g., MoS₂ and MoS₂-based composites) in sensors and EECSS. MoS₂ nanosheets aligned vertically exhibit for example a higher capacity and active surface area compared with surface-parallel aligned sheets (Yang et al., 2014). Figure 6 clearly shows an example of the difference between bulk MoS₂ particles and exfoliated MoS₂ nanosheets.

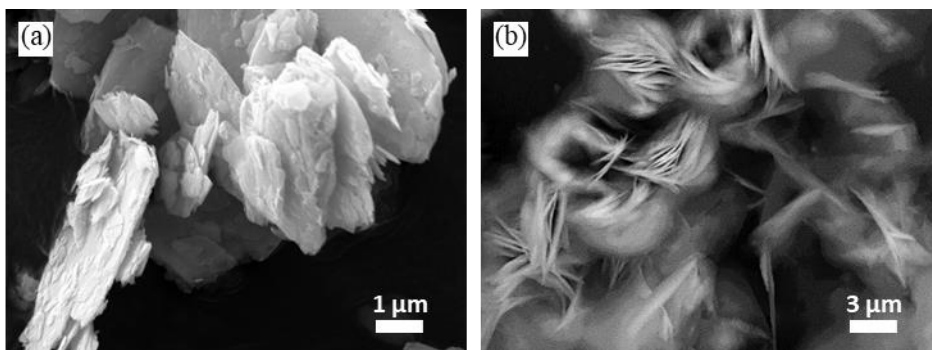


Figure 6. SEM micrographs of (a) bulk 2H-MoS₂ particles and (b) exfoliated 1T-MoS₂ nanosheets aligned vertically.

Efficient intercalation of ions is a prerequisite in layered materials used in EECSS. The rather large interlayer spacing of MoS₂ (0.65 nm) provides a conducive possibility for accommodating large-sized alkali metal ions (e.g., Na⁺, K⁺) (Acerce et al., 2015; Shao et al., 2020). However, the large size of ions such as Na⁺ and K⁺ may though challenge the intercalation process and result in reduced ionic mobility and poor kinetics. A careful configuration of the microstructure and the adaptation of the next-generation electrode design (based on additive technologies) are therefore of outermost importance.

1.2.2.2 MoS₂ applications

MoS₂ is due to its extraordinary properties and electrochemical performance, an outstanding candidate for a wide range of future sensors and EECSS (Acerce et al., 2015; Ambrosi et al., 2016; Bissett et al., 2015b; W. Choi et al., 2017; David et al., 2014; F. Li et al., 2018; L. Lin et al., 2019; Y. Liu et al., 2020; Mukherjee et al., 2018; Pan et al., 2020; Tianyi Wang et al., 2017; Yang et al., 2014; X. Zheng et al., 2018; Xiaoping Zhou et al., 2014). It has been shown that intercalation of Na can lead to phase transformation of MoS₂ from its 2H to 1T phase that retains high capacitance values in Na₂SO₄ even at the scan rates exceeding 200 mV s⁻¹ (Chhowalla et al., 2013; Mortazavi et al., 2014). In the following sub-sections, the electrochemical performance of MoS₂ is discussed for different applications, i.e., for the hydrogen evolution reaction (HER), in fuel cells, batteries, and supercapacitors.

1.2.2.2.1 Hydrogen evolution reaction (HER) and fuel cells

Different techniques have been suggested to increase the electroactive specific surface and proton exchange of MoS₂ films. It has been approved that the edge orientation of nano-porous MoS₂ films can enhance the cation intercalation and reversible redox reactions between different valence states of Mo(IV) ↔ Mo(III), which turns MoS₂ into a potential candidate for HER and supercapacitor applications (Yang et al., 2014). Accordingly, improved intramolecular proton transfer in COOH-functionalized MoS₂ can result in enhancement in HER performance (Lee et al., 2018). Increasing the specific

surface area via the inclusion of MoS₂ in carbon-based nanomaterials is also suggested to enhance the HER performance (Corrales-sánchez et al., 2014) as well as the catalytic performance of PEMFC cathodes (Y. Hu et al., 2016). The incorporation of oxygen can deliberately generate atomic defects in the MoS₂ nanosheet and subsequently enhance both the HER performance and the long-term cyclic stability (up to 20 000 cycles) (J. Zhou et al., 2016). Interestingly, the improved electrocatalytic performance in acidic electrolytes shows MoS₂ as a highly efficient electrocatalyst candidate for oxygen reduction reactions (ORR) in hydrogen fuel cells and proton exchange membrane fuel cells (PEMFCs) (Rowley-Neale et al., 2016). These unique characteristics provide MoS₂ with large possibilities to be utilized in different industrial energy storage applications.

1.2.2.2 Battery and supercapacitor

Similar to other EECSS, the morphology, layer orientation, specific surface area, and crystallographic phase of MoS₂ affect its electrochemical functional performance. For instance, the metallic phase of exfoliated 1T-MoS₂ can, with extraordinary efficiency, electrochemically intercalate cations (H⁺, Li⁺, Na⁺, and K⁺) (Acerce et al., 2015). On the other hand, edge-oriented MoS₂ films show an increased areal capacitance (C_A) of 2.2 to 10.5 mF cm⁻² after 10 000 cycling tests with a quasi-triangular shaped charge/discharge curve. This can also be influenced by almost no charge transfer resistance (Yang et al., 2014).

Compared to FeS₂ or CoS₂, porous flower-like MoS₂ cathodes offer a low weight loss, outstanding thermal stability, excellent electrolyte compatibility, and longer discharge time of improved capacity in thermal battery applications (X. Zheng et al., 2018). The highly reversible capacity and excellent rate capability of MoS₂ have been attributed to its microstructural and electrochemical properties (Yang et al., 2014). The pseudo-capacitance, resulting from ion intercalation and redox reactions, improves both the supercapacitor performance and the electric double-layer capacitance (EDLC) (Yang et al., 2014).

These versatile characteristics suggest MoS₂-based composites to be used as both anodes and cathodes in Li-ion batteries (Stephenson et al., 2014). With capacitance values up to 700 F cm⁻³, MoS₂ can be potentially utilized at high-voltage (3.5 V) operations (Acerce et al., 2015). Regarding the wide range of applications of MoS₂ and Mo_(x)S_(x+1)-incorporated structures, these 2D TMDCs can be considered to be processed by the next generation of cutting-edge manufacturing techniques (Acerce et al., 2015).

1.3 Additive manufacturing of energy storage materials

AM processes have distinct advantages over traditional manufacturing processes in terms of process flexibility, design freedom, and geometry controllability to fabricate 3D structures of 0D (nanoparticles, quantum dots, etc.), 1D (carbon nanotubes, etc.), 2D nanomaterials (graphene, graphene oxide, TMDCs, MoS₂, etc.), and cellular materials (M. Cheng et al., 2020; Gulzar et al., 2020; Pang et al., 2020; Tian et al., 2020) with defined spaces, tuning ion transportation, charge/discharge speed, and storage capacity in EECSS (Ge et al., 2020; Lee et al., 2018; Y. Wang et al., 2019; Y. Wu et al., 2015). In terms of thickness, the layer-by-layer fabrication mechanism follows a possibility to precisely control the electrodes made of thin layers (for flexible/wearable devices) to thick electrodes, which promotes fast ion diffusion and energy density. Such energy-conservative and environment-friendly AM technologies enable one-step fabrication and eliminate

material wastage and are hence considered ideal processes for the fabrication of energy storage devices (Chang et al., 2019; M. Cheng et al., 2020; Gulzar et al., 2020; F. Zhang et al., 2017).

Due to the wide progress in AM techniques to generate complex 3D shapes of superior electrochemical materials (Pang et al., 2020), advanced research is currently ongoing to use MoS₂-containing solid-state electrolytes for batteries in high-demand energy storage devices (Xu et al., 2017). **Table 1** shortlists different characteristics of AM techniques applicable for EECSS fabrication, followed by brief categorized explanations for different AM methods. Some pros and cons of each AM technique are addressed. The main characteristic item, which is evident in different AM techniques (except for SLM), is that the 3D-processed structure inevitably needs a secondary process step to obtain the desired functionality for its intended use, i.e. for electrochemical energy conversion/storage. This thesis elaborates on how SLM can process MO_(x)S_(x+1)-incorporated 3D structures which directly have electrochemical functionality without the need for any secondary process step.

Table 1. Categorized methods for AM of batteries [adapted with permission from John Wiley and Sons under the license number 5306690510271 dated May 12, 2022 (Pang et al., 2020)].

3D-printing method	Available materials	Printing resolution	Advantage	Disadvantage
FDM	Thermoplastics	50-200 μm	User-friendly, low cost, high speed, large size capability, and lack of necessity for chemical post-processing	Limited resolution on the z-axis, weak mechanical properties, high viscosity of the molten materials, low surface quality
DIW	Polymers, metals, ceramics, and food	1 μm	Affordable cost, easy operation, large material diversity, and no mask requirement	Weak mechanical properties, high requirement for inks
TAE	Polymers, metals, oxides, and hydroxides	50 nm to 10 μm	High-ordered macroporous structure, low cost, high efficiency, simplicity, versatility, and controllability	Weak mechanical properties, strong limitation in materials
IJP	metals, conductive polymers, and carbon-based and protein materials	20 μm	Low cost, multi-material printing capability, able to print large areas	Low printing speed, not good for high-volume printing, less durable print head
AJP	Nanoparticles, nanowires, CNTs, 2D materials, dielectric materials	10 μm	High-resolution, high efficiency, compactable with inks of different viscosity	Overspray, printing quality not stable, high-cost of equipment
SLA	Photopolymers	0.25-10 μm	High resolution, high surface finish, high efficiency	Strong limitation in multi-material deposition

1.4 Selective laser melting

The L-PBF is attributed to additive manufacturing technologies that use a laser beam to fuse powder particles in a layer-by-layer fashion and allow the production of complex three-dimensional (3D) structures as dictated by the CAD design (Herzog et al., 2016). L-PBF is commonly known as selective laser melting (SLM) (Prashanth et al., 2014, 2015; Prashanth, Scudino, & Eckert, 2017; Salman et al., 2019; Scudino et al., 2015). The SLM technology completely fuses the loose metal powders and converts them into near-net-shape parts. The density of the parts largely depends on the process parameters and the powder characteristics (Prashanth, Scudino, Maity, et al., 2017). A schematic illustration describing the operating principle of the layer-by-laser SLM process is given in [Figure 7](#).

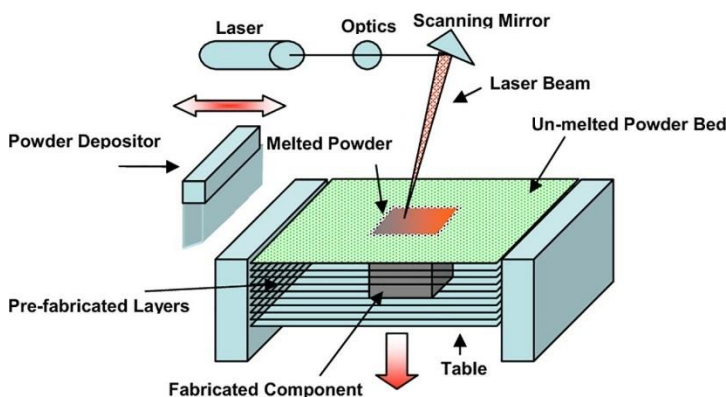


Figure 7. Schematic illustration describing the operating principle of the SLM process [adapted with permission from Elsevier under the license number 5306691274553 dated May 12, 2022 (Gunasekaran et al., 2021)].

The improved mechanistic understanding and integration of the SLM technique with other conventional methods have increased the interest in utilizing 3D printing techniques for various applications. However, upscaling of productivity in each technique for industrial manufacturing is still limited by drawbacks such as formulation of feedstock, complexity, time constraints, expensive pre-processing stages, photo-curing, heat treatment, post-processing stage, lack of mass production, and poor mechanical properties.

1.4.1 SLM for electrochemical energy storage applications

As evident from the literature survey summarized in previous sections, SLM has never been applied for the direct processing of 2D-material-included electrodes with *in-situ* added functionalities for EECSS, batteries, or supercapacitors. Despite the difference in materials and product scale, the SLM can overcome many of the disadvantages of other 3D printing techniques though seldom employed compared to other AM techniques (M. Cheng et al., 2020; F. Zhang et al., 2017). In the following sections, the SLM technique is discussed in more detail.

Even though several electroactive ceramics were successfully fabricated using the AM techniques for electrochemical and energy-based applications (Ambrosi et al., 2016; Pumera, 2019; Tian et al., 2017; F. Zhang et al., 2017), only a countable number of reports are available on these materials processed by SLM for energy-based applications. Recently the potentials of SLM, SLS, SLA, and DIW methods have been studied and the advantages of these AM techniques toward fabrication of EECSS elaborated (Chang et al., 2019; M. Cheng et al., 2020; Zhu et al., 2017).

SLM has recently shown its capability for processing different fuel cell components. For instance, SLM-processed metallic bipolar plates for PEMFCs electrochemically performed and provided a current density of 200 mA cm^{-2} at a potential of 0.5 V, similar to plates manufactured by CNC milling (Dawson et al., 2015). Furthermore, a porous gas diffusion layer of 316L stainless steel was processed by SLM to be used instead of carbon-based substrates in a multilayer tubular high-temperature proton exchange membrane fuel cell (HT-PEMFC) (Bermúdez Agudelo et al., 2020). The fabricated component with a porosity of 16% showed a power density of 330 W m^{-2} at a current density of 125 A m^{-2} after 5 h of operation at $160 \text{ }^\circ\text{C}$ in H_2/air atmosphere at ambient

pressure (Bermúdez Agudelo et al., 2020). SLM has shown its potential in AM of miniaturized microfluidic-based micro fuel cells (MFCs) of stainless steel with enclosed cavities, obtaining a current density of 1.515 A cm^{-2} and a power density of 363 mW cm^{-2} (Scotti et al., 2016). An SLM-processed Ti6Al4V electrode was reported to be applied in a solid-state supercapacitor able to deliver a volumetric capacitance of 2.4 F cm^{-3} , an energy density of 213.5 Wh m^{-3} , and a power density of 15.0 kW m^{-3} at a current density of 37.4 mA cm^{-3} (Chen Zhao et al., 2014). However, the SLM-printed electrode was just used as a current collector part of the 3D-printed supercapacitor (Chen Zhao et al., 2014).

1.4.2 The advantages of the selective laser melting process

Despite the present cost factors involved in the SLM process (raw materials cost, installation cost, running costs, etc.), it can fabricate a wider spectrum of materials. Hence, SLM can be considered for the rapid prototyping of energy storage system materials (Zhu et al., 2017). This near-net-to-shape process can directly deliver the functionality during the fabrication of intricate parts, such as current collectors and electroactive parts for EES devices, directly from metal powders with added functionalities and without any additional additives or binders (M. Cheng et al., 2020). The weight reduction, improved design characteristics, and improved functionality aspects can compensate for the cost factor. Hence, the promising potential of the SLM process can overcome most of the disadvantages mentioned for the conventional EECSS fabrication methods. Moreover, SLM-based processes can eliminate a part of the deficiencies mentioned for other 3D printing methods, such as expensive pre-processing stages, multi-stepwise processing to deliver desired functionality to 3D-printed structure, toxicity, etc.

1.4.3 Parameter optimization by SLM

Besides the technical benefits of reduced tooling and freedom of design to rapidly prototype near-net-shape parts with near-theoretical densities, the SLM can have a viable economic benefit for novel ceramic and composite materials fabrication in the future (Yap et al., 2015). To achieve desirable density, morphology, and properties of fabricated components, some intrinsic characteristics of SLM and feedstock (e.g. rapid cooling rate, powder morphology, powder flowability, laser absorptivity of powder-bed) require the optimization of parameters optimization from a different perspective (D. Wang et al., 2017).

1.4.3.1 Scanning strategy

Scanning strategy is one of the necessary parameters affecting the porosity, microstructure, residual stress, and mechanical properties of the printed component. The length-, orientation-, order of the scan vector, and the rotation of subsequent layers can result in a considerable number of different combinations of scanning strategies. The alternating laser scan strategy has been proven to achieve minimum residual stress. However, it has already been shown that the 45° rotation strategy can result in a higher degree of porosity and residual stresses, while the 90° rotation can reduce the level of porosity and result in minimum residual stress (Ali et al., 2018). The effect of the scanning strategy (vector length and rotation) on residual stresses is complex and highly dependent on material and alloy. Nevertheless, shorter scan vectors, higher maximum temperature, and enhanced residual heat effect on the sides might cause higher porosity and residual stress at 45° compared with 90° rotation of the successive layers (Ali et al., 2018).

The scan vector length may furthermore affect the cooling rate and subsequently the phase transformation and microstructure. Studies on cooling rates have confirmed the complex correlation between scanning strategy and material behavior. Raising the powder bed temperature can also result in reduced residual stress for both scanning strategies (Ali et al., 2018).

1.4.3.2 Variation of exposure time

Although increased re-scanning exposure can directly influence the melt-pool size, no significant change in porosity or density of the samples might be observed (Ali et al., 2018). However, although porosity analysis may show nearly full density due to the reduction of cooling rates, precise examination of the micrographs can reveal considerable existence of micro-porosity to an extent that exceeds the porosity of non-rescanned 3D-printed samples (Kasperovich et al., 2015; Yasa et al., 2012). Accordingly, the elongation percentage can reach the maximum level in an optimum re-scanning exposure time due to a reduction in microporosity (Leuders et al., 2013). However, the improvement in elongation can also be attributed to phase transformation and microstructural changes (Simonelli et al., 2014).

Re-scanning in terms of variation of exposure time can be considered as another parameter that can affect the porosity, cooling rate, microstructure, relative residual stress, and mechanical properties of SLM-processed components (Ali et al., 2018). An increased re-scanning exposure time can directly result in an increased size of the melt-pool of the re-melted material and subsequently in a reduction of the cooling rate. Based on the temperature gradient and cool-down phase model (Ali et al., 2018; Shiomi et al., 2004), residual stresses can be imposed which might be increased upon re-scanning exposure (Ali et al., 2018).

1.4.4 Crack mitigation in SLM processes

Today, several standard metal powders (Al, Cu, Ni, etc.) have been processed by SLM to produce different metallic and/or composite parts. It has been shown that selected SLM process parameters affect not only the defect formation of the fabricated materials (e.g. porosity and cracks) but also the microstructure and the mechanical properties, due to variations in melting pool temperatures and cooling rates (B. Cheng et al., 2016; Hooper, 2018). However, the formation of solidification cracks is still a challenge in SLM-based processing of both brittle and high-temperature materials (J. H. Martin et al., 2017).

SLM processing of some materials is challenging due to the inherent properties of the materials including crystallographic structure, high laser reflection ratio, high thermal conductivity, and susceptibility to crack formation. In several SLM-processed materials, insufficient density, lack of wettability, balling effects, low fracture toughness, brittleness, and grain boundary crack growth are some of the drawbacks that need to be considered. It has been studied and shown that hatch space reduction can positively affect the instability of the melt pool, though it might result in reduced efficiency and increased residual stresses (Xin Zhou, Wang, et al., 2015). Furthermore, exceeding the hatch overlap/width ratio can cause thermal deformation of printed layers and larger numbers of structural defects (Faidel et al., 2015). Shrinkage of the added molten layers can also lead to ascending residual tensile stresses on the top layer, resulting in crack initiation (D. Wang et al., 2017).

Higher volumetric energy density can improve productivity, elimination of fusion porosities, and enhance the density of SLM printed parts (Faidel et al., 2015; Leitz et al., 2017; Xin Zhou, Liu, et al., 2015; Xin Zhou, Wang, et al., 2015). Keyhole formation can,

however, occur as a result of increased volumetric energy density (Higashi et al., 2020). An engineered/simulated support structure and layer-wise scan strategy can alleviate solidification cracks via affecting grain boundary interlocking, grain morphology, and distribution of residual stress throughout the SLM-processed parts (Higashi et al., 2020; D. Wang et al., 2017). The modified scan orientation might not be the only alternative to fabricate crack-free alloys (D. Wang et al., 2017), whereas an improved packing density, flowability, fluidity of the powder bed, and subsequently mean laser absorptivity can result in wettability of the molten pool and finer grain boundaries (Körner et al., 2011; D. Wang et al., 2017). Crack formation and residual porosities can be associated with the oxidation of the molten material (Braun et al., 2019). Low-melting-point oxide phases, located at the grain boundaries, can result in cold cracks during rapid solidification and hot cracks at planar grain boundaries (Braun et al., 2019). Hence, the elimination or control of impurities by alloying (e.g. with carbon) can alleviate the Marangoni effect and enable the fabrication of porosity- and crack-free components (Kaserer et al., 2019).

1.4.5 Processing of molybdenum by SLM: difficulties and solutions

SLM processing of molybdenum (Mo) with a melting point of 2623 °C has recently attracted considerable attention for high-temperature applications. Such processing is though challenging due to the inherent properties of Mo including its body-centered cubic (BCC) crystallographic structure, high laser reflection ratio, high melting point, high thermal conductivity, small melt pool, and high crack susceptibility (D. Wang et al., 2017). Insufficient density, lack of wettability, balling effects, low fracture toughness, brittleness, and grain boundary crack growth are some of the drawbacks that need to be considered (D. Wang et al., 2017). A hatch overlap/width ratio exceeding 60% can cause heat accumulation, thermal deformation of printed layers, and a larger number of defects in SLM-processed Mo structures (Faidel et al., 2015). Shrinkage of added molten layers of Mo can cause residual tensile stresses in the top layer, and ascending residual stresses exceeding the fracture strength can result in crack initiation (D. Wang et al., 2017).

Several solutions have been examined and suggested to mitigate structural defects such as a higher volumetric energy density as a function of higher laser power and lower layer thickness. This is accomplished by exposing the pulsed laser output and increasing laser scanning sequences to improve the productivity and the density of SLM printed components of Mo (Faidel et al., 2015; Leitz et al., 2017; Xin Zhou, Liu, et al., 2015; Xin Zhou, Wang, et al., 2015). A layer-wise scan strategy and clever designed support structures can effectively influence grain morphology, residual stress distribution, interlocking of parallel columnar grain boundaries, and subsequently alleviate solidification cracking (Paper I; Higashi et al., 2020; D. Wang et al., 2017). However, modification of the scan strategy (scan orientation) may not be sufficient to fabricate crack-free Mo and Mo-based alloys (D. Wang et al., 2017). An increased packing density of the powder bed has already been shown to improve the wettability of the Mo molten pool, which leads to an almost half-circular geometry of the molten pool and a higher density of manufactured components (Körner et al., 2011). The improvement of packing density, fluidity, and subsequently mean laser absorptivity can result in finer grain boundaries (D. Wang et al., 2017).

The formation of cracks and residual porosities has been correlated to the oxygen content in the melting atmosphere and the oxidation of Mo (Braun et al., 2019). Segregation of MoO_x of the lower melting point at the grain boundaries can cause hot cracking at planar solidified grain boundaries, cold cracking during rapid solidification,

and higher DBTT (Braun et al., 2019). Hence, elimination or control of impurities by alloying (e.g. with carbon) can alleviate the Marangoni effect and enable the fabrication of porosity- and crack-free Mo parts (Kaserer et al., 2019). Literature findings show correlations between the direct texture of the microstructure and the porosity sensitivity of SLM-processed Mo on changes in grain growth direction within the melt pool as a function of scan speed parameter (Higashi et al., 2020).

1.4.6 Addition of MoS₂ to Mo feedstock

MoS₂, a widespread advanced material as molybdate in nature, can be classified as a sort of material called transition metal dichalcogenides (TMDCs) possessing weak van der Waals force between the layers and strong covalent bonds between the Mo and S atoms (Chhowalla et al., 2013; Lu et al., 2016). Regarding the distinctive characteristics of MoS₂ and unique properties of Mo, additions of MoS₂ to refractory hard Mo metal can significantly facilitate the printability of different Mo-MoS₂ mixture feedstock.

Different crystallographic structures, strong covalent bonds, and weak van der Waals force between the MoS₂ layers allow them to be mechanically separated to form 2D nanostructures (Figure 6b) (Lu et al., 2016). Despite the significant electrochemical characteristics of MoS₂, the weak van der Waals force makes the direct SLM processing of pure MoS₂ structures difficult. The *ex-situ* addition of Mo powder can, hence, significantly facilitate the printability of Mo_(x)S_(x+1)-incorporated structures.

Firstly, MoS₂ raw material consists of non-spherical micro-sized particles formed via stacking of 2D layered structures (Figure 6a). Due to the non-spherical morphology of the nanoparticles and the wide particle size distribution, the pure MoS₂ feedstock shows weak flowability. Hence, the addition of metallic Mo powder can significantly improve the flowability of the feedstock mixture. The presence and simultaneous melting of pure Mo and MoS₂ can form a composite structure that positively overcomes the weak van der Waals force and mechanical properties of pure MoS₂. The presence of pure Mo particles in the mixture of Mo-MoS₂ feedstock can also lead to the formation of Mo₂S₃ nanostructures during the SLM process. The promising catalytic performance and the stability of Mo₂S₃ nanostructures, owing to Mo–Mo zigzag atomic bonds, enhance the electron and hole mobility between and within the Mo and S layers (Xiaowen Zhou et al., 2018).

Based on the above-mentioned aspects, compositional mixing of Mo and MoS₂ powders can be considered both *ex-situ* during mixing and *in-situ* via chemical and thermodynamic reactions during SLM processing of materials.

1.4.7 Processing of composites by SLM: difficulties and solutions

Aside from the versatile capability of the SLM technique for AM of pure metals and alloys, its potential has recently been focused on AM of high-performance composites, especially metal matrix composites (MMCs). The complex-shaped structure possessing comprehensive properties can meet the expectations of rapid tooling, biomedical-, aerospace-, and automotive industries. Towards preparation of MMCs production by SLM techniques, two different strategies (*ex-situ* and *in-situ*) can proceed.

The *ex-situ* strategy has been considered to manufacture ceramic-reinforced MMCs via combining metal and ceramic powders, the fracturing of powders, cold-welding of the metallic matrix and stiffer ceramic particle components to each other, and repeatedly re-fracturing during the milling (D. D. Gu et al., 2012). Some important cases can be addressed for *ex-situ* processing of MMCs with SLM. For instance, gas entrapment,

aggregation, and interfacial micro-cracks can be mentioned as constraints of obtaining dense and homogenous microstructures in MMCs. This can be governed by the strength and stability of the interfacial region between the ceramic reinforcement and the metal matrix (D. D. Gu et al., 2012). For example, ductile fracture in the metal matrix can occur alongside brittle fracture and debonding around ceramic reinforcing elements due to the pure wettability between the ceramic and the metal. The improvement of the wettability can be done via *ex-situ* encapsulation of ceramic components with the metal coating (D. D. Gu et al., 2012). Moreover, Ni-coated TiC has been shown to reinforce the matrices of the Inconel 625 and Ti6Al4V alloys and effectively reduce the formation of voids or cracks (Bi et al., 2013; B. Zheng et al., 2010). Improved homogeneous particulate dispersions, laser processibility, and microstructural refinement of WC/Cu MMCs can be achieved via the addition of rare earth (RE) compounds such as La_2O_3 and RE–Si–Fe. The addition of the RE can reduce the surface tension of the melt pool, limit grain growth coarsening, and increase the heterogeneous nucleation rate (D. Gu et al., 2009).

The *In-situ* strategies have recently been developed based on the thermodynamic synthesis of composite via a chemical reaction between elements during SLM processing, which is generally cleaner and more compatible (D. D. Gu et al., 2012). The formation of the *in-situ* reaction system needs complete melting of feedstock, which is supported by the SLM technique, and bottom-up phase formation in the liquid to create unique microstructures (D. D. Gu et al., 2012). The preheating temperature, powder density, and scan speed are three prominent parameters that can control the volume fraction, phase formation, and composition in 3D-printed MMCs (J. Choi et al., 1994). The microstructure can consist of some partially melted reinforcement components, metastable phases, and even amorphous structures in microstructure of MMCs. These issues can be alleviated by controlling the thermal gradient and the solidification rate by preheating the powder bed (Zhong et al., 2010). SLM processing of *in-situ* prepared MMCs still encounters some challenges such as partial controllability over the crystallization, successive change in morphology, formation of *in-situ* microstructures, and the final mechanical properties due to the non-equilibrium process (Xi et al., 2018; Yap et al., 2015). The *in-situ* study on SLM-processed Al-12Si/TiB₂ composites has shown that the wettability and distribution of TiB₂ ceramics can be enhanced by pre-heating of the mixture powder resulting in higher hardness and stronger bonding between the matrix and the reinforcement components (Xi et al., 2018).

2 Aim and objectives

In this research, I have investigated and proposed the capability of a novel AM approach (SLM) for *in-situ* processing of enhanced additively manufactured $\text{Mo}_{(x)}\text{S}_{(x+1)}$ -incorporated nanocomposite structures directly from the commercial feedstock. This research aimed to provide outstanding electrochemical properties for sustainable engineering and advanced electrochemical applications, i.e., corrosion-resistive composites and energy storage systems. This thesis has included five objectives (Figure 8).

1. Considering the literature, it may be assumed that the optimization of SLM parameters based on laser scan strategy and scan orientation may not be an effective approach toward fabricating crack-free Mo and Mo-based alloys. According to objective 1, the effect of the laser rescanning strategy was, hence, considered to process low-defect pure Mo (Paper I).

2. On the other hand, MoS_2 can be considered as a multifunctional candidate for different applications. Thus, objective 2 was to address and compare different conventional and AM techniques used for processing of MoS_2 , review the literature related to laser-based thinning of MoS_2 , and finally explore the capabilities of SLM and suggest the laser-based processing of MoS_2 and $\text{Mo}_{(x)}\text{S}_{(x+1)}$ -incorporated composites structures for electrochemical energy storage applications (Paper II).

3. According to objective 3 (SLM-assisted fabrication of sustainable $\text{Mo}/\text{Mo}_{(x)}\text{S}_{(x+1)}$ composite structures for EECSSs), $\text{Mo}_{(x)}\text{S}_{(x+1)}$ -incorporated micro-lattice structures were fabricated to electrochemically evaluate the sustainability of the structure of composite at Na^+ -rich media as an important criterion to be addressed by employing electrochemical and corrosion studies. Therefore, obtaining a corrosion-resistive and sustainable $\text{Mo}_{(x)}\text{S}_{(x+1)}$ -incorporated structure was the third objective to get assured that the 3D-printed composites are effectively sustainable to get utilized for Na-ion EECSS.

4. Moreover, under objective 4, $\text{Mo}/\text{Mo}_{(x)}\text{S}_{(x+1)}$ electrodes were fabricated to verify the capability of SLM to fabricate $\text{Mo}_{(x)}\text{S}_{(x+1)}$ -incorporated composites and to evaluate its capability from different aspects of the properties (crystallography, morphologies, microstructure, etc.) of the additively manufactured electrodes for application in Na-ion EECSS (Paper III).

5. Also, research on the electrodes fabricated by SLM from different $\text{Mo}:\text{MoS}_2$ ratios of feedstock were conducted to understand the effect of the composition of feedstock on the crystallographic properties, morphology, and phase transformation toward enhancement of the pseudocapacitance performance of SLM-processed $\text{Mo}/\text{Mo}_{(x)}\text{S}_{(x+1)}$ electrodes under objective 5.

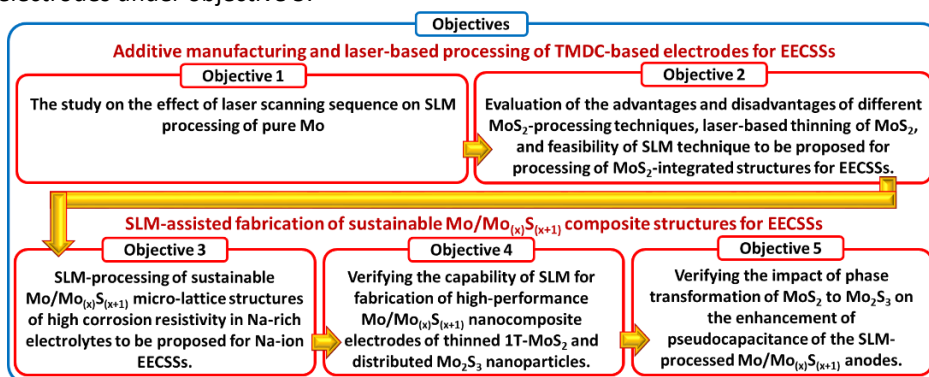


Figure 8. The schematic structure of the thesis is based on two objectives and five stages of research.

3 Materials and methods

3.1 SLM processing

3.1.1 Materials

Commercial gas atomized pure Mo (99.99%) and MoS₂ (99.99%, Sigma Aldrich) powders were mixed by a rotating mixer for 6 h at 20 rpm to prepare the different compositions of feedstock containing 2, 10, 20, 30, and 50 wt.% of MoS₂ to fabricate functional composites.

3.1.2 Method

A stainless steel 316L platform, a Nd:YAG laser source, and a Realizer GmbH SLM-50 instrument were utilized for SLM-based processing of pure Mo current collector and electroactive MoS₂/Mo₂S₃ composite structure at ambient temperature. The LDS and LSS parameters, as a function of energy density, were altered to optimize printing parameters for different pure Mo and composite samples. The laser energy density is calculated by Eq. 1:

$$E_d = \frac{P}{(v \times h \times t)} \quad \text{Eq. 1}$$

where P is the laser power (W), v is the laser scan speed (mm/s), h is the hatch distance (mm), and t is the layer thickness (mm). The $h = 45 \mu\text{m}$ and $t = 25$ were maintained unchanged for all samples. To print pure Mo samples, three different energy densities

of 1300 J/mm^3 ($P = 85$, $v = 58 \text{ mm/s}$), 900 J/mm^3 ($P = 85 \text{ W}$, $v = 84 \text{ mm/s}$), and 70 ($P = 42.5 \text{ W}$, $v = 540 \text{ mm/s}$)+ 900 ($P = 85 \text{ W}$, $v = 84 \text{ mm/s}$) J/mm^3 were employed. [Figure 9a](#) depicts a schematic illustration of single laser scanning on a powder bed to form a single hatch. In addition, the distribution of Mo-MoS₂ mixture feedstock onto the previously solidified layer to coat a layer of powder bed ([Figure 9b](#)) and subsequent laser scanning and melting of the loose powder bed ([Figure 9c](#)) are schematically illustrated. The scan speed and the laser power varied between 65-450 mm/s and 25-75 W, respectively ([Figure 9d](#)). Three different kinds of defects were observed in the single-layer laser scan of the powder bed; (i) the LOF defects (purple area), improved by a reduced scan speed and an increased laser power, (ii) balling defects (blue area) due to the insufficient energy densities either at low scan speed or high laser power, (iii) over-melting (red area) of the powder bed at excessive energy densities due to both low scan speed and high laser power. As a higher volumetric energy density can cause keyhole formation, the optimized parameters (yellow area) were selected for the SLM processing of some samples. The different composite electrodes were fabricated from the mixture feedstock of MoS₂ and Mo by using the optimized SLM parameters. Energy densities of 400 J/mm^3 ($P = 37.5 \text{ W}$, $v = 85 \text{ mm/s}$), 650 J/mm^3 ($P = 62.5 \text{ W}$, $v = 85 \text{ mm/s}$), and 850 J/mm^3 ($P = 62.5 \text{ W}$, $v = 65 \text{ mm/s}$) were employed in a normal scan direction and a hatch rotation of 60° to print SLM-Mo/Mo_{(x)S_(x+1)} lattice structures, disc-shaped electrodes (Paper III), and cube-shaped electrodes, respectively.

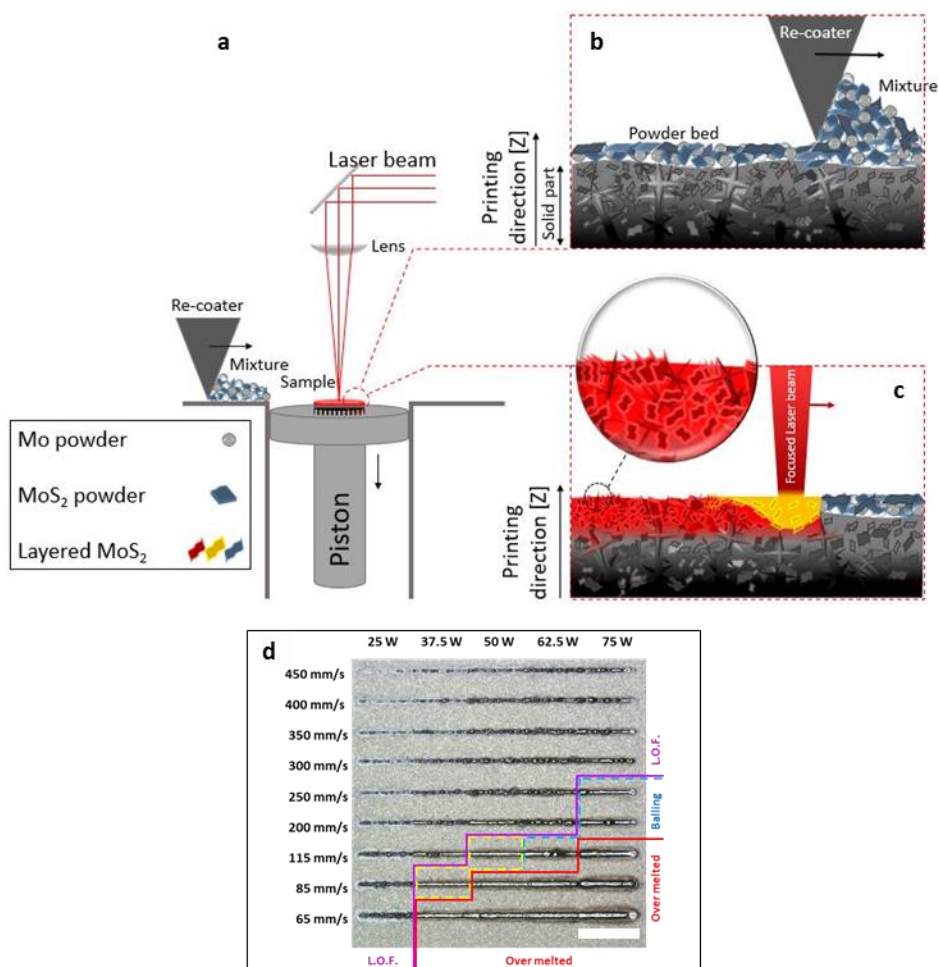


Figure 9. Schematic illustration of (a) SLM process, (b) distribution of feedstock by re-coater to coat loose powder bed, and (c) laser scanning and melting of the powder bed to consolidate a new layer of composite; (d) a stereomicroscope image of laser single-layer scan as a function of scan speed and laser power. The scale bar in (d) equals 1 mm and the different colored areas denote: purple – lack of fusion (L.O.F.); blue – balling effects; red – over melted power bed; yellow – optimized conditions.

3.1.3 SLM parameter optimization for composites

To study the sustainability of the electrodes and the mechanism of the enhancement of corrosion resistivity in Na-rich electrolytes, the lowest optimum energy density (400 J/mm^3) was applied to reduce the size of the melt pool and print the struts with the least possible diameter, the most accumulated lattice strain, and the highest residual stress in the structure of Mo matrix (Higashi et al., 2020; D. Wang et al., 2017). To fabricate solid structures and study the electrochemical properties of nanocomposites, two different laser energy densities (650 and 850 J/mm^3) were applied. The lower laser energy density is considered and applied with the aim of sublimation, thinning, transforming the phase of MoS_2 from 2H to 1T, and having 2H/1T phase in the 3D printed structure (Paper III). The higher laser energy density, however, is applied to completely melt the feedstock

and get assured of creation of a melt pool of dissociated MoS₂ and a more complete reaction and phase transformation from MoS₂ to Mo₂S₃ (Paper III; Pan et al., 2020). (For more details, see Paper III).

3.2 Electrochemical characterization

3.2.1 Materials

An ultra-pure water with a conductivity of 18.2 MΩcm and a pH of 6.5±0.1 at 25 °C, and the NaCl, Na₂SO₄, and H₂SO₄ (Merck) with a purity of ≥99.0% were used to prepare aqueous electrolytes of 0.1 M NaCl (pH = 5.4±0.02), 0.1 M Na₂SO₄ (pH = 5.47±0.02), and 0.1 M H₂SO₄ (pH = 1.05±0.02).

3.2.2 Methods

Degassing and preparation of electrolytes and cleaning the surface of the 3D-printed electrodes were carried out by using an ultrasonic bath (USC300TH, VWR, Malaysia). The pH values of the electrolytes were measured by using a standard pH meter (PHM210, Radiometer Analytical, France). An Ag/AgCl-, 3M-, or saturated KCl reference electrode (AMETEK, Princeton Applied Research, USA), a Pt wire counter electrode (CHI115, CH Instruments Inc., USA), a VersaStudio 2.61.3 software, and a PARSTAT MC multichannel potentiostat (AMETEK, Princeton Applied Research, USA) were used for the electrochemical characterizations at room temperature (25 °C).

3.2.2.1 Electrochemical energy conversion/storage studies

The scan rates between 10 and 100 mV s⁻¹ in a potential window between -1.1 and 0.2 V were adopted for CV characterizations. The frequency range between 10⁻¹ Hz and 10 kHz was adopted for EIS measurements. The GCD measurements were carried out at different current densities from 4 to 10 mA cm⁻².

3.2.2.2 Electrochemical polarization and corrosion studies

For the OCP vs. time, a scan rate of 1 mV s⁻¹ for 1 h was adopted to relatively stabilizing and determine the surfaces of SLM-processed Mo (SLM-Mo) and SLM-Mo/Mo_(x)S_(x+1) in the different electrolytes. Cyclic potentiodynamic polarization (CPP) was carried out starting from -0.8 V vs. OCP, ending at 1.2 V, and cycling back from 1.2 to 0 V. CPP was carried out with a low scan rate of 0.25 mV s⁻¹ in 0.1 M NaCl, 0.1 M Na₂SO₄, and 0.1 M H₂SO₄ electrolytes, respectively, to determine anodic and cathodic corrosion potentials and corrosion currents. Electrochemical impedance spectroscopy measurements (EIS) were carried out in the frequency range between 10⁻¹ Hz and 10 kHz by applying an alternating current (AC) with an amplitude of 10 mV. The corrosion current (*I*_{corr}), corrosion potential (*E*_{corr}), cathodic (β_c) and anodic (β_a) Tafel constants, pitting potential (*E*_{pp}), and pitting current (*I*_{pp}) were calculated by Tafel fitting of the polarization curve using the VersaStudio software. The corrosion current densities (*i*_{corr}) and pitting current density (*i*_{pp}) were calculated from *I*_{corr} and *I*_{pp} respectively normalized to the exposed geometric surface area (Karimi et al., 2020). The polarization resistance (*R*_p), was calculated according to Eq. 2:

$$R_p = \beta_c \times \beta_a / (2.3 \times (\beta_c + \beta_a) \times i_{corr}) \quad \text{Eq. 2}$$

3.3 Physical characterization

3.3.1 Methods

A wet laser scattering particle size distribution analyzer (LPSA, LA-950, HORIBA, Japan) was used to evaluate the particle size distribution of the Mo and MoS₂ powders. To study the effect of LSS on the stability of the melt pool and to optimize the laser parameters, a stereomicroscope (V20, Zeiss, Germany) was used (Figure 9d). The densities of as-printed (unpolished) samples were measured by the Archimedes principle using a Metler Toledo ME240 instrument. Room temperature microhardness was determined by using a Buehler Micromet 2001 device with a load of 100 gf for 10 s.

X-ray diffraction (XRD) studies were carried out by using a Smartlab (Rigaku, Japan) diffractometer with Cu-K α 1 radiation ($\lambda = 1.5406 \text{ \AA}$), and a silicon strip detector D/teX Ultra. The coherent domain size (D) and lattice strain (ε) were calculated based on the Scherrer formula shown in Eq. 3 and Eq. 4:

$$D = K\lambda/(\beta \times \cos\theta) \quad \text{Eq. 3}$$

$$\varepsilon = \beta/(4\tan\theta) \quad \text{Eq. 4}$$

where β is the structural broadening of the peaks (FWHM) (Rabiei et al., 2020). The ICDD card numbers 1527605, 9008543, and 1531960 were used to identify the XRD patterns of Mo₂S₃, Mo, and MoS₂, respectively. To show the crystallographic preference of growth in Mo matrix and evaluate its correlation with lattice strain, the texture coefficient (T.C.) of the samples was calculated using Eq. 5:

$$TC_{(hkl)} = (I_{(hkl)}/I_{(hkl)}^0) \times \{1/n \sum I_{(hkl)}/I_{(hkl)}^0\}^{-1} \quad \text{Eq. 5}$$

where $I_{(hkl)}$ is the intensity of the XRD peak of the (hkl) plane, $I_{(hkl)}^0$ is the intensity of the (hkl) plane in the standard pattern of XRD, and n is the peak number (Alinejadian et al., 2021). The dislocation density (δ) was calculated using Eq. 6:

$$\delta = 1/D^2 \quad \text{Eq. 6}$$

X-ray photoelectron spectroscopy (XPS, Kratos Axis SUPRA, Kratos Analytical) equipped with UltraDLD spectrometer and monochromatic 150W Al x-ray source was used to determine the chemical composition of the outermost surface of unexposed and exposed printed samples. Survey scans and detailed spectra (pass energy 80 eV) were acquired for Mo 3d, S 2p, and C 1s to calculate relative S to Mo ratios in the outermost surface of printed surfaces prior to and after exposure to the different electrolytes. The binding energy of adventitious carbon was used as a reference (285.0 eV).

A Horiba LabRAM HR800 micro-Raman system equipped with the Nd:YAG laser (wavelength $\lambda = 532 \text{ nm}$) with a spectral resolution of 1 cm^{-1} was used for Raman studies through excitation with a laser spot diameter size of approximately $5 \text{ }\mu\text{m}$.

The study on the surface morphology of samples in both secondary electron (SE) and back-scattered (BSE) modes were carried out by means of a Zeiss Axioskop 40 optical microscope, a Hitachi TM-1000 scanning electron microscope (SEM), a Philips/FEI XL30 ESEM, and a field emission scanning electron microscope (FE-SEM, Zeiss MERLIN, Germany).

4 Results and discussion

4.1 Phase transformation and crystallographic studies

XRD diffraction patterns of the powder feedstock and the SLM-processed parts are presented in Figure 10. The Mo and MoS₂ powders show their corresponding peaks without any peaks originating from any impurity elements (Figure 10a,b). Similarly, no other impurities or undesirable crystalline phases were observed in the Mo-MoS₂ feedstock powder after mixing. However, the increase in the fraction of MoS₂ resulted in a significant increase in the intensity of the MoS₂ main crystallographic (002) plane as well as a significant decrease in the intensity of both Mo and other MoS₂ corresponding peaks (Figure 10b). According to Bragg's law, this can be attributed to higher alignment and orientation of the MoS₂ basal plane. The diffraction pattern of the SLM-Mo lattice sample revealed only peaks assigned to Mo metal (Figure 10c). The fabricated SLM-Mo/Mo_(x)S_(x+1) sample showed peaks assigned to Mo, MoS₂, and Mo₂S₃. The low intensities of the characteristic (002) and (103) peaks of MoS₂ were attributed to the small fraction of MoS₂ embedded on the surface of Mo (Figure 10c,d). Since MoS₂ can react with Mo to form Mo₂S₃ at temperatures greater than 1300 °C (Alexaki et al., 2018), Mo₂S₃ peaks were observed in the SLM printed struts as well (Figure 10d). The increase in the fraction of MoS₂ in the feedstock resulted in an increase in the intensity of Mo₂S₃ peaks meanwhile a decrease in the intensity of MoS₂ corresponding peaks due to higher laser absorption and higher transformation of MoS₂ to Mo₂S₃ during the SLM process (Figure 10d). The XRD patterns of the Mo powder, SLM-Mo sample, and SLM-Mo/Mo_(x)S_(x+1) composite are presented in Figure 10e with peaks between 40.0° < 2θ < 40.8° and 58.4° < 2θ < 58.8°. As illustrated in Figure 10e, the intensity, width, and peak position of the Mo peaks varied between the samples. This may be connected to effects induced by rapid cooling associated with complex thermal solidification cycles, as this is reported to result in a high degree of defect density in SLM samples and hence peak broadening along with changes in the crystallite size and internal strain (G. Wang et al., 2020; Z. Wang et al., 2020). (For more details, see Papers III)

As shown in Figure 10f, the specific E_{2g}¹ and A_g¹ peaks of MoS₂, attributed to in-plane opposite vibrations of Mo and S and out-of-plane vibration of S atoms, were located at 384 and 410 cm⁻¹, respectively (Alexaki et al., 2018). In general, laser-based thinning down of the MoS₂ can lead to a blue shift in A_g¹ and red shift in E_{2g}¹ peaks in few-layered two-dimensional MoS₂, freestanding or deposited onto the surface of Si/SiO₂ substrates (Castellanos-Gomez et al., 2012). However, in our 3D composite structure including Mo and MoS₂, the Raman peaks of laser-exposed MoS₂ showed blue shifts (2 cm⁻¹) to 382 and 408 cm⁻¹, which can be attributed to partial Nd:YAG laser-assisted thinning and the turning of MoS₂ from a bulk to a few-layered structure (Alexaki et al., 2018) in the sample containing 20 wt.% of MoS₂. It has already been studied that in a constant value of MoS₂ in the exposure of laser, the lower laser energy can cause sublimation and thinning-down of the 2D layered structure (Pan et al., 2020). However, the higher laser energy can provide higher fluence, resulting in both sublimation and melting (Pan et al., 2020). In the sample containing a low fraction of MoS₂ (2 wt.%) no peak of MoS₂ was observed while the blue shift in both A_g¹ and red shift in E_{2g}¹ indicated the complete phase transformation of MoS₂ in the feedstock to Mo₂S₃ incorporated in the 3D structure (Alexaki et al., 2018; Pan et al., 2020). Nanostructures of Mo₂S₃ have previously been shown to form in argon atmospheres at temperatures exceeding 1300 °C (Alexaki et al.,

2018), and possibly be enhanced in the presence of molten Mo during the SLM process (Xiaowen Zhou et al., 2018). The thermal decomposition of Mo(VI) in MoS_2 into Mo(III) in Mo_2S_3 and S also takes place at temperatures close to 1100 °C alongside a change in the stoichiometric ratio of Mo/S can cause a lattice strain mostly arise and accumulate in the interface between laser-thinned MoS_2 and Mo_2S_3 nanostructures, resulting in a blue shift in E_{2g}^1 peak (Alexaki et al., 2018; L. Hu et al., 2017). (For more details, see Paper III).

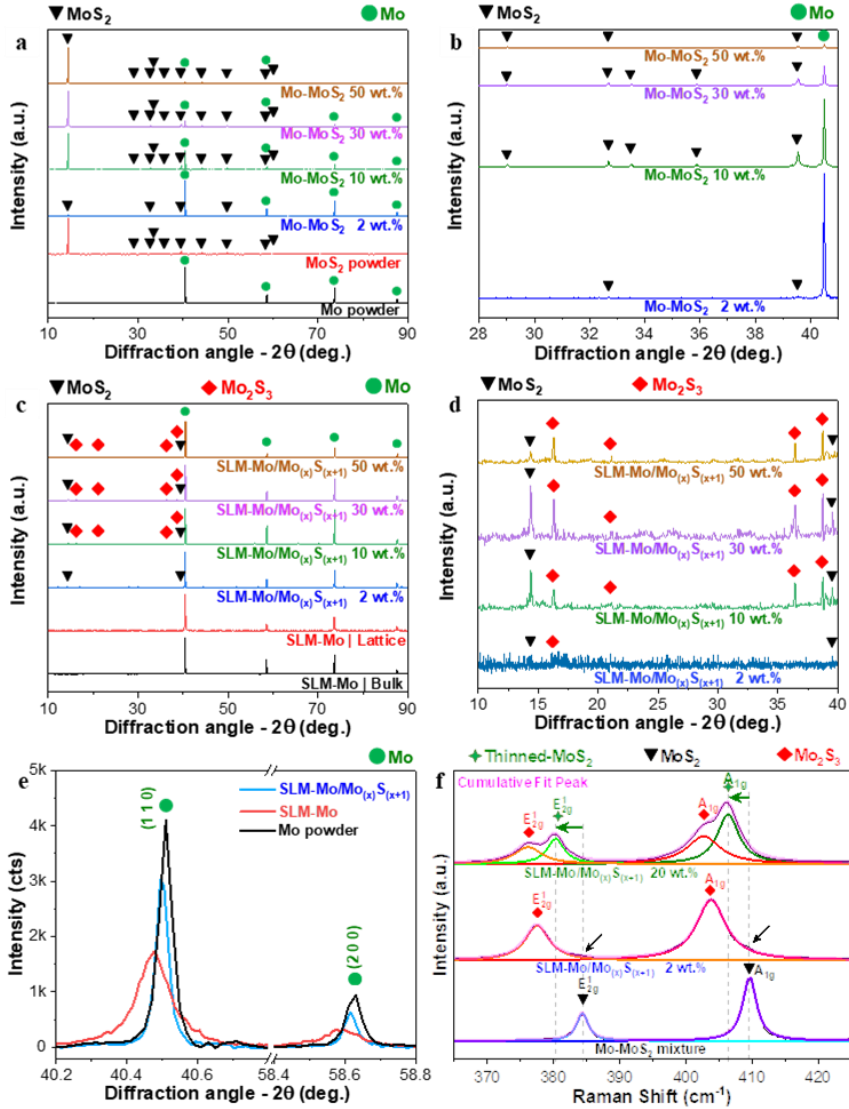


Figure 10. X-ray diffraction patterns of (a) the different raw materials (Mo, MoS_2 , Mo- MoS_2 powder feedstock with the compositions of 2, 10, 30, 50 wt.%, (b) the magnified XRD patterns of the Mo- MoS_2 powder feedstock between $28^\circ < 2\theta < 40^\circ$, (c) SLM-processed bulk and lattice structures of SLM-Mo and SLM-Mo/ $\text{Mo}_{(x)}\text{S}_{(x+1)}$ of different compositions, (d) the magnified XRD patterns of the SLM-Mo/ $\text{Mo}_{(x)}\text{S}_{(x+1)}$ micro-lattice structure between $10^\circ < 2\theta < 40^\circ$, (e) peaks between $40.2^\circ < 2\theta < 40.8^\circ$ and $58.4^\circ < 2\theta < 58.8^\circ$ variations in full width half maximum (FWHM) and intensities of the two main (110) and (200) XRD peaks of Mo; (f) Raman spectra variations of MoS_2 before and after SLM processing of feedstock containing 2 wt.% and 20 wt.% of MoS_2 (Paper III).

The information shortlisted in [Table 2](#) indicates that the preferential growth (texture) of SLM-processed samples occurs along the (110) plane, whereas the texture coefficient (110/200) alters from 0.90 to 1.08. As a result of the complex solidification conditions and cooling rates, such changes in preferential grain growth direction or texture are commensurately normal in the SLM-based fabricated samples (Xin Zhou, Liu, et al., 2015). Nucleation of new randomly oriented grains alongside higher lattice strain (0.092% compared to 0.04% for Mo powder) due to rapid solidification can result in the formation of brittle cracks in SLM-Mo ([Figure 13a](#)) (Higashi et al., 2020).

Table 2. Structural information was calculated from XRD patterns for the Mo feedstock, SLM-Mo, and SLM-Mo/Mo_(x)S_(x+1) samples. (FWHM-full width half maximum; T.C.-texture coefficient).

Sample	Crystallographic plane (110)					Crystallographic plane (200)					T.C. (110/200)
	2 θ (°)	Intensity (counts)	FWHM (°)	Coherent domain size (nm)	Lattice strain (%)	2 θ (°)	Intensity (counts)	FWHM (°)	Coherent domain size (nm)	Lattice strain (%)	
Mo Powder	40.51	4112	0.045	188	0.053	58.63	959	0.051	176	0.04	0.90
SLM-Mo	40.47	1728	0.108	79	0.13	58.57	334	0.117	77	0.09	1.08
SLM-Mo/Mo _(x) S _(x+1)	40.49	3051	0.042	199	0.05	58.61	654	0.044	203	0.044	0.97

4.2 Microstructural studies

SEM micrographs ([Figure 11a,b](#)) illustrate the spherical shape of the gas atomized commercial Mo powder with an average particle size (d_{50}) of 35 μm , the planar-shaped MoS₂ with a d_{50} of approximately 5 μm , and the mixture feedstock consisting of both Mo and MoS₂ powders. It is evident that the increasing addition (from 2 to 50 wt.%) of the smaller sized MoS₂, a commonly used solid lubricant semiconductor material (Krishnan et al., 2019), to the Mo powder can improve the flowability of the feedstock at lower compositions (Kumar, 2014), due to the inherent rheological properties of MoS₂ (Furlan et al., 2018; Yao et al., 2012). It can also increase the packing density at higher compositions (Körner et al., 2011) enhancing the mean laser absorptivity (Alexaki et al., 2018; D. Wang et al., 2017) of the powder bed by covering the Mo powders and filling interspaces between the spherical Mo particles ([Figure 11c–f](#)). The considerably smaller particle size distribution of MoS₂ compared with the Mo powders is presented in [Figure 11g](#). In [Figure 11h](#), the solidified region (red arrow), the loose powder bed region (yellow arrow), and the sintered particles in the boundary between those two regions as well as the overlapping of hatches (vertical lines indicated by the blue arrow) are evident.

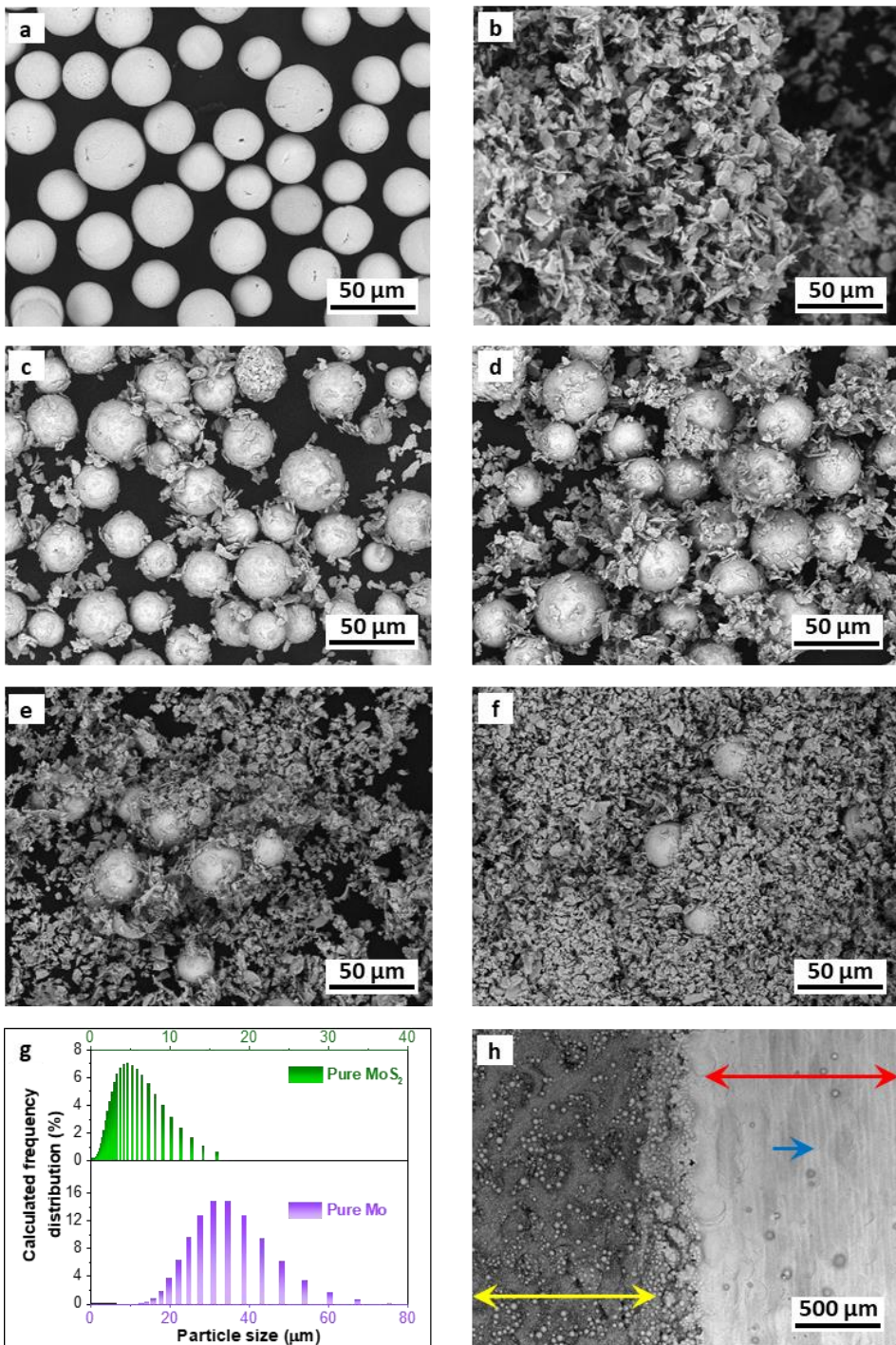


Figure 11. (a) SEM micrograph of pure Mo, (b) SEM micrograph of layered MoS₂, and SEM micrographs of Mo-MoS₂ mixture powder feedstock with (c) 2 wt.%, (d) 10 wt.%, (e) 30 wt.%, and (f) 50 wt.% of MoS₂; (g) Particle size distribution plot of Mo and MoS₂ powders; (h) SEM micrograph showing the edge between the solidified zone (red arrow) and powder bed (yellow arrow), as well as the hatch overlap during continues single laser scanning process (blue arrow) (Paper III).

Microscopy images of the SLM-Mo samples (fabricated with $E_d = 900 \text{ J/mm}^3$) are presented in [Figure 12a–c](#). The density and hardness values for each SLM parameter applied for printing the pure Mo samples were listed in [Table 3](#). It may be observed from [Figure 12a,b](#) that using laser single scan (LSS) and decreasing the E_d from 1300 to 900 J/mm^3 resulted in an increased density and hardness from 97.5% to 98.7% and 203 HV to 220 HV, respectively. From [Figure 12a,b](#) it is evident that using LSS and decreasing the E_d from 1300 to 900 J/mm^3 , result in a reduction in both the size and number of pores. In addition, the number of micro-cracks present in the microstructure also decreased with a decreased E_d . This is because a higher E_d results in a larger size of the melt pool with high-temperature gradients, which leads to the formation of coarser shrinkage pores (S. Liu et al., 2019). The high-temperature gradients also result in an increased amount of internal stresses, which lead to solidification cracking in the sample. On the other hand, a reduction of the E_d also decreases the size of the melt pool, from which follows lower temperature gradients and hence smaller and a less number of pores (D. Gu et al., 2012). (For more details, see Paper I).

Table 3. Variation of the density and hardness of the SLM-processed bulk pure Mo samples prepared with different laser energy densities (Paper I).

Melting strategy	Energy Density [J/mm^3]	Density [%]	Hardness [HV0.1/10]
Laser single scanning	1300	97.5±0.7	203±5
Laser single scanning	900	98.7±0.2	220±2
Laser double scanning	1 st scan	99.0±0.1	222±2
	2 nd scan		

By employing LDS, both porosity and hardness show a marginal increase from 97.5 ± 0.7 to $99\pm0.1\%$ and from 203 ± 0.5 to 222 ± 2 HV, respectively ([Table 3](#)). However, it was noted that LDS can eliminate the cracks that were observed when using LSS ([Figure 12c](#)) counterpart. Using LDS, the powder bed is heated during the first scan, where the laser scan speed is kept very high (increased nearly six times), and the laser power is reduced by 50%. In addition, the heated powder bed undergoes melting during the second scan which could selectively increase the temperature of the powder bed and the stability of the molten pool. This may lead to reduced residual stresses and reduced temperature gradient (Saunders, 2018; Yadroitsev et al., 2013). Moreover, LDS resulted in a larger proportion of columnar grain growth due to the 0° scan rotation, a decreased degree of supercooling, and reduced cooling rates ([Figure 12c](#)) (Saunders, 2018; D. Wang et al., 2017). However, only some micro-cracks were observed for the LDS treated sample. The grain size distribution in the laser re-scanned sample is displayed in [Figure 12e](#). The presence of elongated grains and some fine grains between the elongated grains suggest a bimodal distribution. A higher-resolution image of the grain size distribution is shown in [Figure 12f](#) and the corresponding high-resolution secondary image in [Figure 12g](#). From [Figure 12g](#) it is evident that no cracks are observed though some submicron pores exist. (For more details, see Paper I).

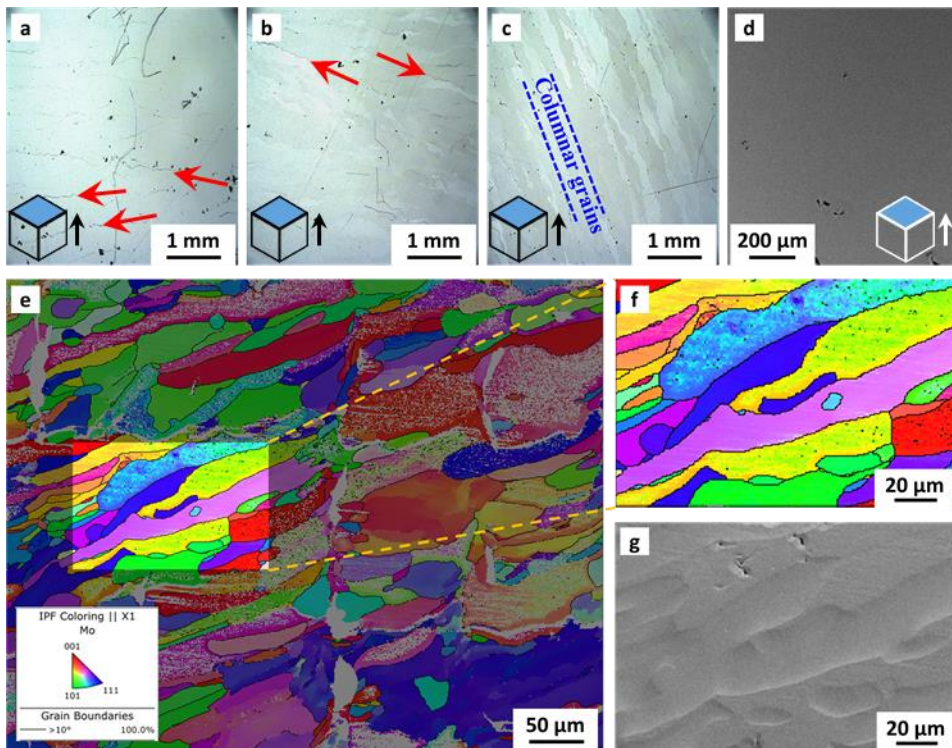


Figure 12. Optical microscopy images of the SLM-processed bulk pure Mo samples with a laser single scan and the energy density of (a) 1300 J/mm³, and (b) 900 J/mm³, respectively; (c) optical image of the SLM-Mo sample with a laser double scan and an energy density of 70+900 J/mm³; (d) scanning electron microscopy (SEM) image of a laser double scan sample with an energy density of 900 J/mm³; (e) energy back scattered dispersion (EBSD) image showing the distribution of pure Mo grains, (f) higher magnification energy back scattered dispersed image showing the orientation of grains, and (g) the corresponding high resolution back scattered image of the columnar Mo grains (Paper I). Inset cubes in (a)-(d) illustrate the characterized top surface, perpendicular to the printing direction.

From the SEM micrograph, despite optimization of the SLM parameters, the brittleness of Mo resulted in the formation and initiation of brittle micro-cracks from the hatch boundaries of the micro-lattice, indicated by red arrows (Figure 13a) (Kaserer et al., 2019; D. Wang et al., 2017). It was further evident that SLM fabrication of the Mo micro-lattice was unsuccessful (Figure 13c). Despite previous discussions related to crack formation in bulk Mo, the high melting point, the thermal conductivity, the DBTT of Mo, and the rapid cooling rate can intensify the thermal gradient in the small molten pool surrounded by the powder bed of lower thermal conductivity in SLM processing of micro-lattice Mo structures (Leitz et al., 2017; Chao Zhao et al., 2020). This can ease the thermal stress accumulation in the structure (especially at the intersection points) and result in the formation of cracks within the microstructure of SLM-Mo (Xin Zhou, Liu, et al., 2015).

A fine equiaxial microstructure of the SLM-Mo/Mo_(x)S_(x+1) composite consisting of the Mo₂S₃ phase in the Mo matrix is observed in Figure 13b. The results imply that the addition of a small proportion of MoS₂ (2 wt.%) to the Mo feedstock powder reduces crack formation in the SLM fabricated micro-lattices of small unit cell sizes

(750 μm) and tiny strut diameters (approximately 85 μm). The SEM micrograph of the SLM-Mo/Mo_(x)S_(x+1) micro-lattice in Figure 13d shows that the low-diameter SLM-fabricated struts remained undamaged during the process.

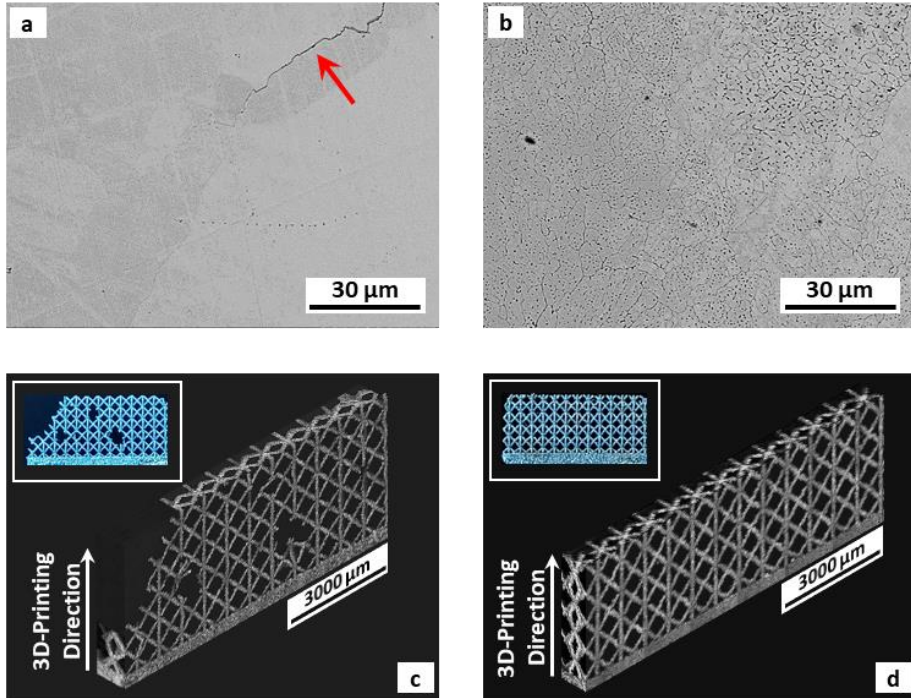
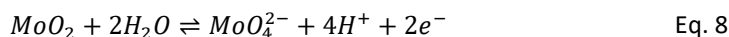
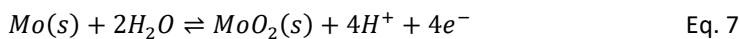


Figure 13. SEM micrographs illustrating (a) crack formation in the brittle microstructure of Mo, (b) near crack-free microstructure of SLM-Mo/Mo_(x)S_(x+1); assembly SEM micrographs of (c) Mo micro-lattice structure (inset image – optical image of the printed lattice), and (d) SLM-Mo/Mo_(x)S_(x+1) micro-lattice structure (inset image – optical image of the printed lattice). Shown in (b) and (d) are the characterized SLM-Mo/Mo_(x)S_(x+1) samples printed from the feedstock containing 2 wt.% of MoS₂.

SEM micrographs of the SLM-Mo and SLM-Mo/Mo_(x)S_(x+1) samples after potentiodynamic polarization in 0.1 M NaCl, 0.1 M Na₂SO₄, and 0.1 M H₂SO₄ solutions are presented in Figure 14. As previously discussed, residual stresses can accumulate at the grain boundaries. The unique properties of Mo can alongside a high cooling and intensive thermal gradient at the interface between the melt pool result in a higher dislocation density ($\delta = 5.2 \times 10^{-6} \text{ m}^{-2}$) than the conventional counterpart ($\delta = 5.85 \times 10^{-7} \text{ m}^{-2}$), which can result in the formation of micro-cracks in the microstructure (Figure 14a). The longitudinal grain boundaries can be considered as local high-energy zones, which can reduce the corrosion resistance via the oxidation of Mo to Mo(IV) and the formation of different oxides, Eq. 7, Eq. 8 (E. J. Martin et al., 2013; Rodriguez et al., 2018). The local oxidation of Mo, forming MoO₂ and MoO₄²⁻ in an aqueous NaCl solution, the presence of grain boundaries and micro-cracks, and the diffusion of Cl⁻ ions within the cracks can result in a brittle surface susceptible to longitudinal stress corrosion cracking (SCC, blue arrows in Figure 14a) (Ren et al., 2020). Diffusion of hydrogen atoms (up to 12 atoms) into interstitial octahedral sites of the microstructure can result in increased local plasticity, grain boundary weakening, and especially in the embrittlement of the surface and tips of microcracks within the BCC structure of Mo (Pereira et al., 2019; You et al., 2013).



Comparing different zones (e.g., struts and unfused Mo particles attached to the struts), the SCC observed in the SLM-fabricated Mo struts can be a result of strains accumulated during rapid solidification conditions. However, the non-melted Mo particles attached to the struts did not get affected at the same rate as the solidified struts.

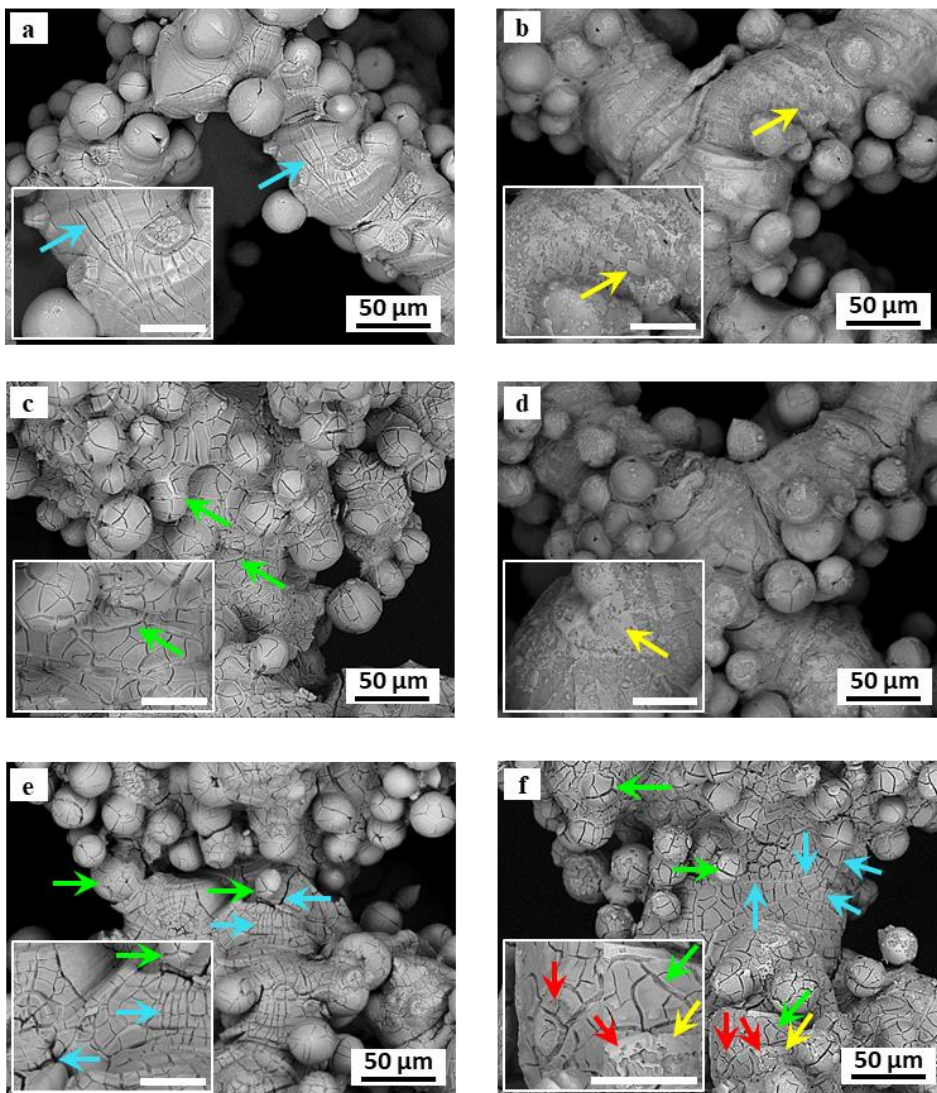


Figure 14. SEM micrographs of 3D-printed micro-lattices after potentiodynamic polarization: (a,b) SLM-Mo and SLM-Mo/Mo_(x)S_(x+1) at 0.1 M NaCl electrolyte, (c,d) SLM-Mo and SLM-Mo/Mo_(x)S_(x+1) at 0.1 M Na₂SO₄ electrolyte, (e,f) SLM-Mo and SLM-Mo/Mo_(x)S_(x+1) at 0.1 M H₂SO₄ electrolyte. Scale bars in the insets equal 25 µm. The coloured arrows denote different corrosion types: blue – SCC; green – surface cracking due to oxidized surfaces of different PBR; yellow – the presence of Mo₂S₃ in the corroded structures of SLM-Mo/Mo_(x)S_(x+1); red – pitting zones. Shown in (b), (d), and (f) are the characterized SLM-Mo/Mo_(x)S_(x+1) samples printed from the feedstock containing 2 wt.% of MoS₂.

The formation of MoO₂ has been shown to efficiently hinder corrosion of Mo-based alloys (Ha et al., 2018; Lutz et al., 2017; Lyon, 2010; E. J. Martin et al., 2013; Rodriguez et al., 2018). Other oxides such as MoO₃ have lower protective properties as indicated by their Pilling–Bedworth ratios (PBR), which is greater than 2 (Bradford, n.d.; Du et al., 2021). Despite a very similar pH of the NaCl and the Na₂SO₄ electrolytes, SLM-Mo was more corroded in Na₂SO₄ (Figure 14c) forming H₂S (Eq. 9) compared with its behavior in NaCl (Figure 14a) (Sridhar et al., 2018). This uniform cracking and corrosion, observed in both attached Mo particles and struts regardless of localized residual stress, may be attributed to the formation of MoO₃ which enables the initiation of cracks all over the sample (green arrows in Figure 14c). The possible transformation of MoO₃ to Na₂MoO₄ (Eq. 10) can take place along with a volume increase, which leads to the pilling of Na₂MoO₄ from the surface of both attached particles and struts (Lutz et al., 2017; Schofield, 2005). However, no evidence for such an oxide or the presence of Na (by means of XPS) at the outermost surface was obtained even though Na₂MoO₄ in the presence of H₂S (Eq. 11) can result in the formation of MoS₃ (Jin et al., 2020; Lutz et al., 2017; Lyon, 2010).

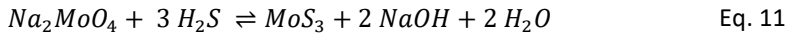
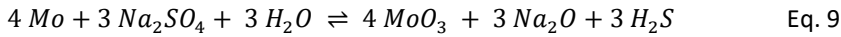


Figure 14e illustrates the corrosion performance of SLM-Mo in 0.1 M H₂SO₄. It has been reported that Mo in sulfurizing media (H₂SO₄) can be transformed into stable MoS₂ which reduces the corrosion rate (Lyon, 2010). As previously discussed, SLM-Mo, however, has structural defects and micro-cracks on the surface of the struts (Figure 13c). In the acidic H₂SO₄ electrolyte (pH ≈ 1), diffusion of H atoms into the cracks can intensify the embrittlement and SCC susceptibility. Therefore, compared to findings in Figure 14a, the SCC (blue arrows) cracks were deeper (Figure 14e). On the other hand, compared with Figure 14c, oxidation cracks (green arrows) also occurred due to the presence of SO₄²⁻ and the possible transformation of MoO₂ to MoO₃ (PBR≈3.4, Eq. 7-Eq. 9). However, due to the lack of Na in the solution, the remaining MoO₃ layer was more stable and protective against H₂S, without any change in oxide volume and less pilling from the surface of both Mo particles and struts.

The addition of 2 wt.% MoS₂ considerably increased the corrosion resistance of SLM-Mo/Mo_(x)S_(x+1) in both the NaCl and the Na₂SO₄ electrolyte. The yellow arrows in Figure 14b,d,f indicate the presence of Mo₂S₃ on the surface of the 3D-printed struts after cyclic potentiodynamic polarization. Comparing Figure 14a,b, the incorporation of Mo₂S₃ into the Mo matrix can hence in this way positively influence the resistance towards SCC (Figure 14b) in NaCl.

The surface structures of SLM-Mo and SLM-Mo/Mo_(x)S_(x+1) after potentiodynamic polarization in Na₂SO₄ are displayed in Figure 14c,d. Similar to the observations made in the NaCl solution, the incorporation of Mo₂S₃ into the SLM-Mo/Mo_(x)S_(x+1) structure substantially reduced the extent of surface oxidation cracking by preventing the Na⁺ accessibility to MoO₃ and hence a reduced formation rate of Na₂MoO₄ (Figure 14d).

Extremely low defect stoichiometric structures of MoS₂ can, as earlier discussed, improve the corrosion resistance of Mo_(x)S_(x+1)-incorporated structures (S. Hu et al., 2020; Mujib et al., 2020). However, other studies show that the existence of bulk or few-layered MoS₂ can be removed from the surface under strongly oxidizing conditions, but that a

monolayer can remain on the surface still acting as a barrier for corrosion (Schulman et al., 2018). In an H_2SO_4 electrolyte, the Mo matrix is exposed to both oxidizing (SO_4^{2-}) and sulfurizing (H_2S) species. Oxidation of Mo and the H^+ -rich media can hence result in SCC, specifically in the solidification direction and within grain boundaries (Eq. 7, Eq. 8). SEM micrographs of the samples polarized in H_2SO_4 (Figure 14e,f) revealed in contrast that the addition of 2 wt.% MoS_2 and the subsequent incorporation of Mo_2S_3 into the Mo matrix could neither prevent SLM-Mo/ $\text{Mo}_{(x)}\text{S}_{(x+1)}$ from SCC (blue arrows) nor surface oxidation cracking (green arrows). In H^+ -rich media, the process can be intensified since the processing of MoS_2 by high-energy Nd:YAG lasers and the incorporation of Mo_2S_3 into the composite can impose structural crystallographic defects into the SLM-Mo/ $\text{Mo}_{(x)}\text{S}_{(x+1)}$ structure. According to the Pourbaix diagrams of Mo–H–O–S systems, all phases (MoO_2 , MoO_3 , and Mo_2S_3) can be transformed to H_2MoO_4 at $\text{pH} \approx 1$ (Davoodi et al., 2011; Schulman et al., 2018). The formation of H_2MoO_4 with a $\text{PBR} > 2$ and the depletion of Mo_2S_3 from the structure during interactions with H_2S result in higher susceptibility for SCC. Thus, SCC on the struts (blue arrows), deeper oxidation cracks on struts and attached particles (green arrows), as well as the different extent of pitting corrosion of varying pit morphology (red arrows) can be associated with the crystallographic plane corroded by H_2S during cyclic potentiodynamic polarization. These types of corrosion, which can occur simultaneously, can lead to lower corrosion resistance for SLM-Mo/ $\text{Mo}_{(x)}\text{S}_{(x+1)}$ compared to SLM-Mo in aqueous H_2SO_4 (Figure 14e,f).

Variations in surface morphology by increasing the MoS_2 fraction in SLM-Mo/ $\text{Mo}_{(x)}\text{S}_{(x+1)}$ samples are illustrated in Figure 15. As expected from the XRD results, embedded bulk MoS_2 to the surface (red arrows in Figure 15a) can arise from lower packing density and subsequently a lower mean laser absorptivity of the feedstock, which lead to a lack of complete integration of MoS_2 into the structure of composite.

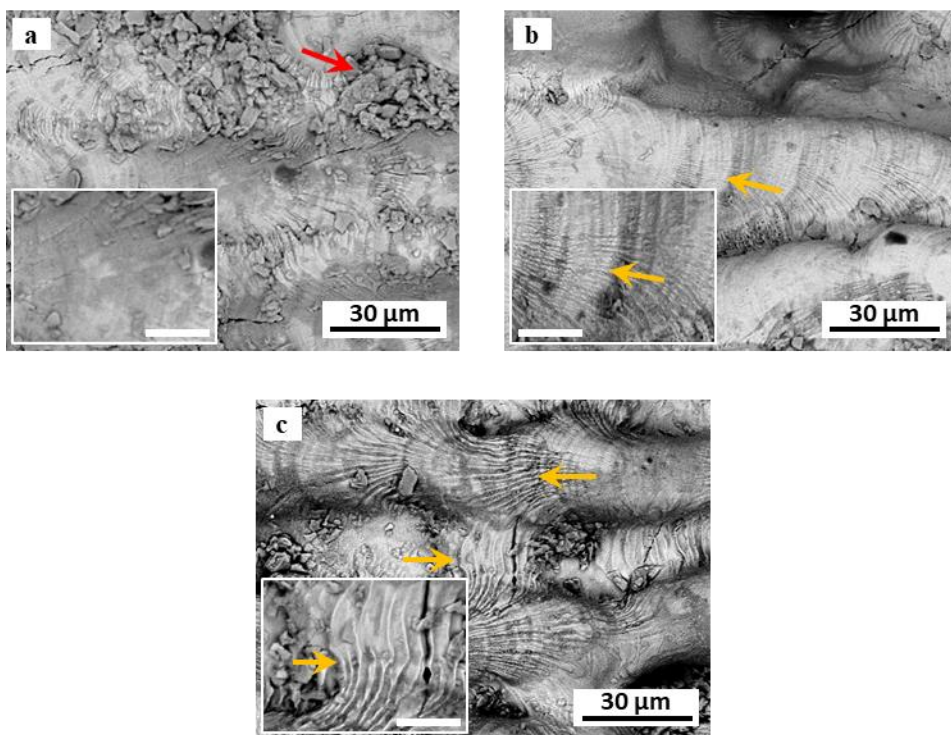


Figure 15. SEM micrographs obtained from the surface of SLM-Mo/Mo_(x)S_(x+1) printed of the mixture feedstock containing (a) 10 wt.% MoS₂, (b) 30 wt.% MoS₂, and (c) 50 wt.% MoS₂. The colored arrows denote: red – surface embedded MoS₂; yellow – laser-thinned MoS₂ integrated into the structure of SLM-Mo/Mo_(x)S_(x+1) composite. The scale bars in the insets equal 10 µm.

The gradually increased fraction of MoS₂ up to 50 wt.% not only resulted in an increased laser absorptivity but also integrated the MoS₂ layers into the structure of nanocomposite and changed the surface topology to a lamellar shape (yellow arrows in Figure 15b,c). The layered morphology can intensively increase the electroactivity of SLM-Mo/Mo_(x)S_(x+1) although the weak van der Waals force of MoS₂ in the higher fractions (50 wt.%) led to the appearance of microcracks in the structure. This was attributed to a higher thermal gradient in a larger metastable melt pool consisting of two different components as well as delamination of the layered structure of MoS₂ due to weak interlayer van der Waals force.

As shown in different polished sections in Figure 16a, a similar microstructure of SLM-Mo_(x)S_(x+1) can be attributed to the optimized LSS and a nearly constant thermal gradient in stable melt-pool during the SLM process (Leitz et al., 2017; Yuan et al., 2020). The presence of MoS₂ layers of low density was elucidated by both the secondary-electron (SE) and the back-scattered electron (BSE) micrographs (Figure 16b,c). The presence of Mo₂S₃ nanoparticles separated at the top surface- and coalesced at the lower parts of the nanocomposite, delimited by a transparent laser-thinned layer attributed to MoS₂, is identified by both yellow arrows in Figure 16b and the yellow dashed lines in Figure 16c. The coalescence of the nanoparticles at the lower layers can occur via partial and layer-wise re-melting of the subsequent layers during the SLM process. A uniform distribution of Mo₂S₃ nanoparticles (25 and 50 nm) was revealed by FE-SEM micrographs (Figure 16d). The variation of Mo/S ratios and the high surface tension between MoS₂

and Mo_2S_3 can result in the formation of spherical particle morphology due to the tendency of re-solidified nanostructures to reduce their surface energies (Alexaki et al., 2018). (For more details and information, see Paper III).

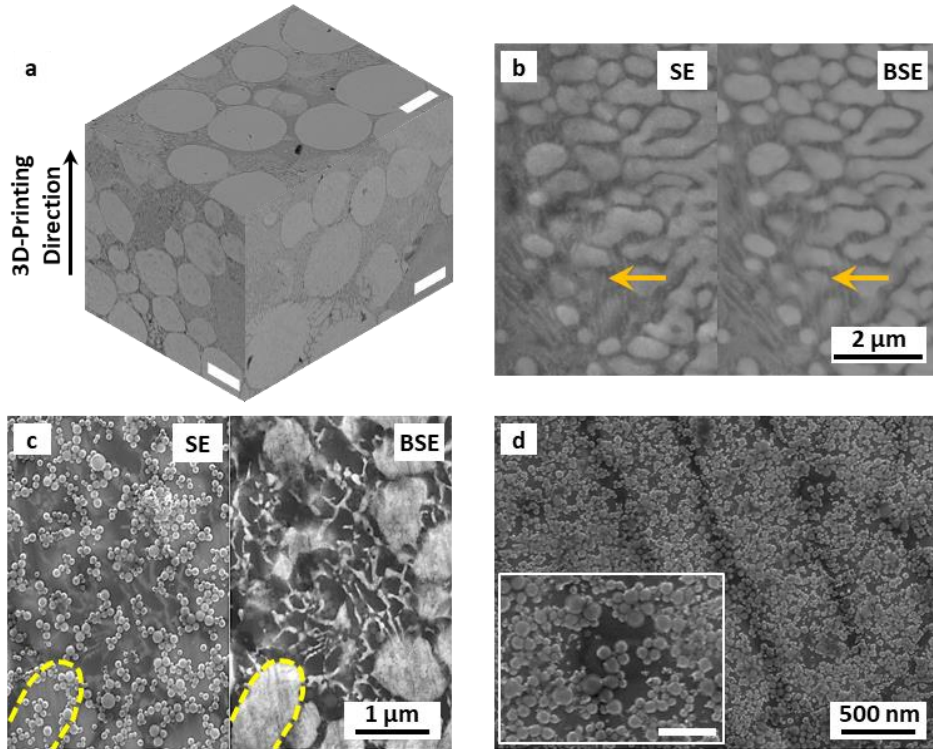


Figure 16. (a) SEM image from different polished surfaces of SLM- $\text{Mo}_{(x)}\text{S}_{(x+1)}$, (b) BSE and SE micrographs of a cross-section showing the transparent laser-thinned MoS_2 layers alongside coalesced Mo_2S_3 nanoparticles, (c) BSE and SE modes of FE-SEM micrographs of SLM- $\text{Mo}_{(x)}\text{S}_{(x+1)}$ indicating coalescence zones of Mo_2S_3 nanoparticles, and (d) magnified FE-SEM micrograph showing the distribution of Mo_2S_3 nanoparticles in the structure of the nanocomposite. The scale bar in (a) equals 25 μm and the characterized samples were printed from the feedstock containing 20 wt.% of MoS_2 (Paper III).

4.3 Physical characterization of phase transformation

Compositional analysis of the outermost surface (top 5-10 nm) of the SLM-Mo and SLM-Mo/ $\text{Mo}_{(x)}\text{S}_{(x+1)}$ samples was performed by means of XPS before and after polarization in the different electrolytes. The results are compiled in Table 4. As discussed above, SCC was the dominant corrosion mechanism of pure Mo in NaCl due to the diffusion of atomic hydrogen into the structure. This resulted in grain boundary weakening and especially in the embrittlement of the surface and tips of microcracks, being intensified by the presence of Cl^- ions. The presence of Na^+ ions in the NaCl and Na_2SO_4 solutions has been shown to result in an increased corrosion rate of SLM-Mo due to the intermediate formation of Na_2MoO_4 and its transformation into MoS_3 (Eq. 11) at the same time as Na^+ is dissolved into the solution to form NaOH. However, none of the SLM-Mo surfaces revealed any presence of Na upon polarization, which supports a complete transformation. However, the extent of this formation seems small as indicated

by the low S^{2-} to Mo (3s) atomic ratios observed for SLM-Mo (0.01-0.02) in the solutions. The relative fraction of Mo(VI) on the surface decreased in the following order; $Na_2SO_4 \geq un-pol. > NaCl > H_2SO_4$, at the same time as the relative fraction of Mo(IV) increased according to $un-pol. \leq NaCl < Na_2SO_4 < H_2SO_4$, indicative of the presence of MoO_3 and MoO_2 (Baltrusaitis et al., 2015), respectively. Exposure in both NaCl and H_2SO_4 indicated the presence of large amounts of Mo(VI). The presence of S (as S^{2-}), even though in minor amounts, after polarization in Na_2SO_4 and H_2SO_4 (Table 4) implied the formation of MoS_2 .

Table 4. Binding energies of oxidized Mo ($Mo_{(ox)}$) and S (as S^{2-} and/or SO_4^{2-}) and atomic $S^{2-}/Mo_{(ox)}$ ratio determined by means of XPS for SLM-Mo and SLM-Mo/ $Mo_{(x)}S_{(x+1)}$ before (Un-pol.) and after polarization in 0.1 M electrolytes of NaCl, Na_2SO_4 and H_2SO_4 . $S^{2-}/Mo_{(ox)}$ atomic ratios were calculated using the Mo 3s to avoid any possible influence of peak overlap with S 2s. The reported data were obtained from micro-lattice samples, printed from the feedstock containing 2 wt.% of MoS_2 .

XPS characteristic data	SLM-Mo				SLM-Mo/ $Mo_{(x)}S_{(x+1)}$			
	Un-pol.	NaCl	Na_2SO_4	H_2SO_4	Un-pol.	NaCl	Na_2SO_4	H_2SO_4
Mo(0)* / at. – %	6.9-7.1	-	-	-	-	-	-	-
Mo(IV)* / at. – %	5.4-5.6	0.1-2.3	7.4-8.8	26.9-27.1	4.9-10.3	28.2-37.1	7.7-8.2	21.1-28.1
Mo(V)* / at. – %	-	40.3-55.5	-	55.9-56.3	-	-	38.1-54.1	52.6-53.2
Mo(VI)* / at. – %	87.3-87.7	42.2-59.7	91.2-91.3	16.6-17.2	89.7-95.1	62.9-71.8	37.6-53.7	19.2-19.7
S 2p / eV	-	162.6	162.6	162.6 : 168.5	161.7	161.6	162.7	162.6
$S^{2-} / Mo_{(ox)}$ – atomic ratio	-:-	0.01;0.02	-:-	0.02;0.02	0.12;0.13	0.95;0.36	0.18-0.20	0.42;0.45

* Mo(0): 228.5±0.1 eV; Mo(IV): 229.5±0.2 eV; Mo(V): 232.2±0.2 eV; Mo(VI): 233.3±0.5 eV
 S^{2-} / Mo 3s (atomic ratio)

As shown in Table 4, $S^{2-}/Mo_{(ox)}$ ratios were calculated using the Mo 3s to avoid any possible influence of peak overlap with S 2s. Increased $S^{2-}/Mo_{(ox)}$ ratios after polarization were observed for SLM-Mo/ $Mo_{(x)}S_{(x+1)}$, with ratios increasing from (0.12-0.13) for the non-polarized surface to 0.18-0.20 in Na_2SO_4 , 0.42-0.45 in H_2SO_4 and 0.36-0.95 in NaCl. The high $S^{2-}/Mo_{(ox)}$ ratios observed upon polarization in H_2SO_4 and NaCl may correlate with the highest relative fraction of Mo(IV), which may indicate the presence of Mo_2S_3 . The relative fraction of Mo(VI) on the surface decreased in the following order; $un-pol. > NaCl > Na_2SO_4 > H_2SO_4$, whereas the relative fraction of Mo(IV) increased according to $un-pol. \approx Na_2SO_4 < NaCl \approx H_2SO_4$. Polarization in both Na_2SO_4 and H_2SO_4 indicated the presence of large amounts of Mo(VI). As previously mentioned, the observed values of Mo(V) can be attributed to the formation of MoS_3 as a by-product alongside MoS_2 . Less stable MoS_3 can be formed as a mixture of MoS_2 and nanocrystalline sulfur (Weber et al., 1995). Therefore, the increase in the relative fraction of Mo(V) up to 52.6-53.2 may be correlated with the formation of a less stable MoS_3 structure in the highly H_2S -rich 0.1 M H_2SO_4 solution. This could support the low polarization resistance (R_p) observed for the SLM-Mo/ $Mo_{(x)}S_{(x+1)}$ sample due to general surface corrosion and corrosion in the grain boundaries (Eq. 13Eq. 16).

4.4 Electrochemical characterization

4.4.1 Corrosion studies

The CPP results of SLM-Mo and SLM-Mo/Mo_(x)S_(x+1) in the different electrolytes are presented in Figure 17a,c,e. Corrosion potentials (E_{corr}), corrosion current densities (i_{corr}), polarization resistance (R_p), pitting potentials (E_{pp}), and pitting current densities (i_{pp}) of the AM samples are summarized in Table 5. At the first glance, i_{corr} for all samples seems to increase in the following order of electrolytes; NaCl < Na₂SO₄ < H₂SO₄. The presence of a small cathodic reaction peak/shoulder in the active region, which is more obvious in the Tafel curves of SLM-Mo rather than of SLM-Mo/Mo_(x)S_(x+1), can be attributed to hydrogen formation (green arrows in Figure 17a,c,e) (Sridhar et al., 2018). Thus, hydrogen embrittlement, and consequently SCC, can occur due to diffusion of H⁺ as a result of cathodic polarization through galvanic coupling with more active Mo (Pereira et al., 2019; Sridhar et al., 2018; You et al., 2013). It is evident that the cathodic reaction peak/shoulder (green arrows) became more evident with increasing H⁺ concentration. Since the presence of reduced sulfur species (SO₄²⁻) also can promote the diffusion of atomic hydrogen into the Mo matrix (Sridhar et al., 2018), the cathodic reaction peak/shoulder became more evident in the Na₂SO₄ electrolyte. The integration of Mo₂S₃ into the structure of the Mo matrix resulted in a reduced cathodic reaction due to limited active sites for galvanic coupling onto the surface of the Mo matrix in both the NaCl and the Na₂SO₄ electrolyte. However, in the H⁺-rich and SO₄²⁻-rich aqueous electrolyte (H₂SO₄), a wide area of H⁺-dominant cathodic reactions resulting from hydrogen generation lead to the excessive hydrogen embrittlement (Davoodi et al., 2011; Sridhar et al., 2018) as observed in the Tafel curves of both SLM-Mo and SLM-Mo/Mo_(x)S_(x+1) (green arrow in Figure 17e).

When comparing the corrosion findings of the two samples (SLM-Mo and SLM-Mo/Mo_(x)S_(x+1) composite), it was evident that the presence of 2 wt.% MoS₂, which resulted in the formation of Mo₂S₃, resulted in a considerably increased polarization resistance (R_p), i.e., improved corrosion resistance in both NaCl and Na₂SO₄. A reduced E_{corr} , observed for SLM-Mo/Mo_(x)S_(x+1) in all electrolytes, can be attributed to the lower crystallographic lattice strain resulting from the incorporation of laser-treated Mo₂S₃ into the metallic Mo matrix. An almost constant E_{pp} (red arrows indicating the interface between the passive and the transpassive regions of the Tafel curves in Figure 17a,c,e) before and after the addition of MoS₂ to Mo can be attributed to pitting and the consequential initiation of corrosion cracking on the surface, and the possible subsequent formation of MoO₄ (Eq. 8) (Rodriguez et al., 2018). Lower i_{corr} and i_{pp} and higher $\Delta E_{(corr-pp)}$ may reflect the positive effect of Mo₂S₃ on R_p in SLM-Mo/Mo_(x)S_(x+1) in both NaCl and Na₂SO₄. In contrast, exposure to H₂SO₄ of lower pH compared with NaCl and Na₂SO₃ resulted in increased E_{corr} and E_{pp} for both SLM-Mo and SLM-Mo/Mo_(x)S_(x+1). Higher i_{corr} and i_{pp} , as well as reduced $\Delta E_{(corr-pp)}$, were observed for SLM-Mo/Mo_(x)S_(x+1).

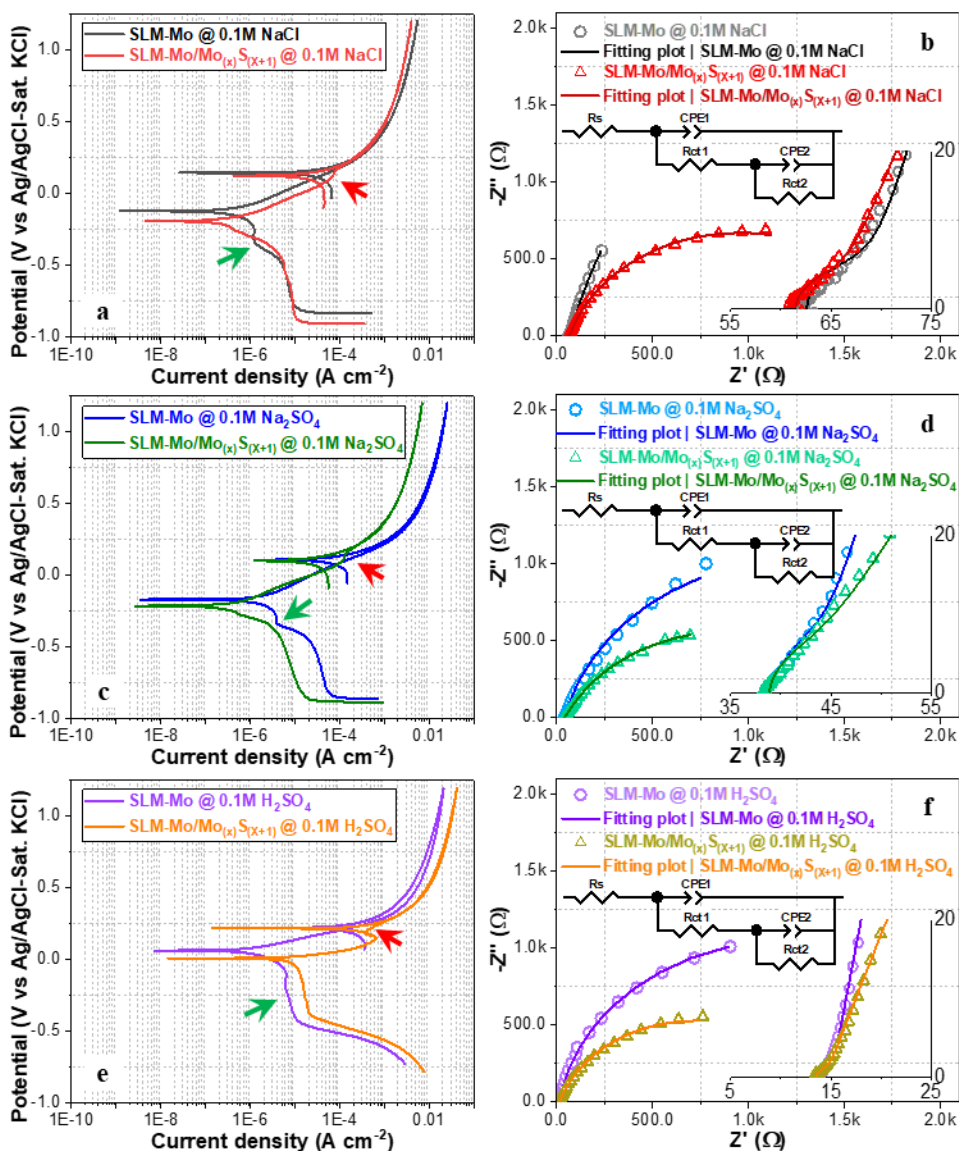


Figure 17. Cyclic potentiodynamic polarization curves of SLM-Mo and SLM-Mo/Mo_(x)S_(x+1) in (a) 0.1 M NaCl, (c) 0.1 M Na₂SO₄, (e) 0.1 M H₂SO₄; EIS plots recorded at OCP for SLM-Mo and SLM-Mo/Mo_(x)S_(x+1) in (b) 0.1 M NaCl, (d) 0.1 M Na₂SO₄, (f) 0.1 M H₂SO₄. The different coloured arrows denote; green – cathodic polarization reaction peak/shoulder; red – pitting and transformation of Mo₂S₃ to MoO₃ and production of H₂S.

As shown in Figure 14e,f, a lower R_p can be attributed to the degradation of Mo₂S₃ in an H⁺-rich medium, which increases the susceptibility to pitting and SCC, and finally cracking and corrosion of SLM-Mo/Mo_(x)S_(x+1) by H⁺ and SO₄²⁻ (Eq. 13). According to Eq. 12, the more evident E_{pp} peak in the passive region (red arrow in Figure 17e) can be attributed to pitting corrosion (red arrows in Figure 14f) and oxidation of defect-rich laser-exposed Mo₂S₃ which will result in the formation of H₂S (Davoodi et al., 2011). On the other hand, according to Eq. 13, exposure of the Mo matrix to H⁺ and SO₄²⁻ can

result in the formation of MoO₃ and H₂S, which subsequently can be transformed to H₂MoO₄, preferentially in the grain boundaries possessing higher residual stress, leading to SCC (Eq. 14). An obvious E_{pp} peak was observed for SLM-Mo/Mo_(x)S_(x+1). According to Eq. 14, the structure of the Mo/Mo₂S₃ can be degraded via SCC and pitting, which can promote the transformation of MoO₃ to H₂MoO₄ resulting in the oxidation cracking of the micro-lattice structure. An obvious E_{pp} peak was therefore observed for SLM-Mo/Mo_(x)S_(x+1). On the other hand, according to Eq. 15 and Eq. 16, the final product on the surface of SLM-Mo/Mo_(x)S_(x+1) may be MoS₂ and MoS₃ that can be peeled off from the surface of the structures during cyclic potential sweeping from +1.2 V to 0 V.

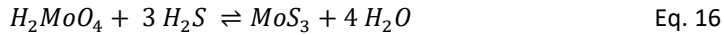
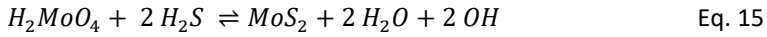
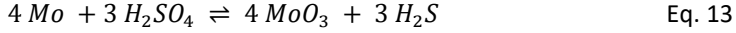
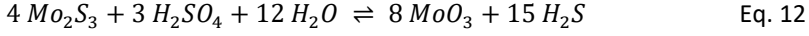


Table 5. Comparison of crystallographic and corrosion parameters for SLM-Mo and SLM-Mo/Mo_(x)S_(x+1) samples exposed in 0.1 M NaCl, 0.1 M Na₂SO₄, and 0.1 M H₂SO₄. The reported data were obtained from micro-lattice samples, printed from the feedstock containing 2 wt.% of MoS₂.

Sample	Electrolyte (0.1 M)	Lattice strain (%)		T.C. Ratio (110/200)	Corrosion							
		(110)	(200)		E _{corr} (mV)	i _{corr} (μA cm ⁻²)	B _c (mV)	B _a (mV)	R _p (kΩ cm ²)	E _{pp} (mV)	i _{pp} (μA cm ²)	ΔE _(corr-pp) (mV)
SLM-Mo	NaCl				-122.1	1.3	615.7	159.7	42.3	144.5	55.13	266.6
	Na ₂ SO ₄	0.13	0.092	1.08	-170.3	2.17	279.2	145.8	19.2	106.5	125.7	276.8
	H ₂ SO ₄				57.89	1.22	175	75	18.6	214.7	147.25	156.8
SLM-Mo/Mo _(x) S _(x+1)	NaCl				-202.9	0.06	128.2	143.3	437	127.7	33.07	330.7
	Na ₂ SO ₄	0.05	0.035	0.97	-260.6	0.26	74.08	132.4	78.2	97.8	35.24	358.4
	H ₂ SO ₄				4.48	10.2	260.5	49.1	1.76	212.6	324.5	208.1

Figure 17b,d,f show Nyquist plots at OCP recorded for SLM-Mo and SLM-Mo/Mo_(x)S_(x+1) in the different electrolytes. EIS is a non-destructive method to study the characteristic of surface layers and prevailing corrosion mechanisms. The size of the semi-circle arc (R_{ct}) accounts for the corrosion resistance of the electrode, i.e., the larger R_{ct}, the higher R_p at given conditions (Atapour et al., 2020). The R_{ct} can also be directly attributed to the charge transfer at the electrode-electrolyte interface (Pal et al., 2018). In all investigated samples and electrolytes, no straight Warburg line was observed in the low-frequency range. This implies an insufficient ion (Na⁺, Cl⁻, etc.) exchange between the structure of the Mo lattice and the electrolytes within the timeframe of the experiment. For all samples, the semi-circle diameters were reduced in the following order NaCl > Na₂SO₄ > H₂SO₄. However, when comparing SLM-Mo and SLM-Mo/Mo_(x)S_(x+1) in the different electrolytes, an opposite correlation between the corrosion mechanism and the semi-circle diameter was observed. In comparison with SLM-Mo, R_{ct} of SLM-Mo/Mo_(x)S_(x+1) changed from 7.00 to 1.79 kΩ in NaCl, from 2.55 to 1.75 kΩ in Na₂SO₄, and from 2.43 to 1.43 kΩ in H₂SO₄. This could have various explanations, e.g., a heterogeneous structure of SLM-Mo/Mo_(x)S_(x+1) including Mo₂S₃ with a 2D structure, different oxidation potentials, and the formation of protective surface layer, different crystallographic characteristics, a variety of Faradic

charge transfer resistance, etc. Despite a lower i_{corr} and considerably higher R_p for SLM-Mo/Mo_{(x)S_(x+1)}, the smaller R_{ct} values observed in the different electrolytes could be attributed to faster interface kinetics between H⁺ and Mo₂S₃. The 2D semi-layered structure of Mo₂S₃ with an atomic interlayer space of 8.6 Å can provide preferable sites for the diffusion of more H⁺ protons (Junke Li et al., 2022; D. Liu et al., 2019). On the other hand, the generation of a highly interlocked equiaxial microstructure of SLM-Mo/Mo_{(x)S_(x+1)}, aside from higher coherent domain size and lower crystallographic lattice strain, can further reduce the diffusion of H⁺ into the Mo structure (Pereira et al., 2019). As shown in Figure 13, a lower number of micro-cracks in SLM-Mo/Mo_{(x)S_(x+1)} compared to SLM-Mo can also reduce the SCC susceptibility of the micro-lattice structure (Pereira et al., 2019). However, during the rapid melting and cooling process in the Ar atmosphere, a defect-implanted MoS₂ can subsequently be transformed to Mo₂S₃, a highly potential material for hydrogen evolution reactions (L.-F. Zhang et al., 2016; Xiaowen Zhou et al., 2018). Therefore, induction of more active sites can result in absorption of H⁺ and preferably transforming to H₂ (a lower R_{ct} at a high-frequency range) at the interface of Mo₂S₃-electrolyte (L.-F. Zhang et al., 2016; Xiaowen Zhou et al., 2018). This can result in a lower ionic diffusion of H⁺ into the structure of the Mo matrix. Hence, less extent of hydrogen embrittlement of the Mo matrix can result in a lower R_{ct} and a higher R_p , which leads to further mitigation of SCC in SLM-Mo/Mo_{(x)S_(x+1)} in NaCl (Figure 17b). The same mechanism is suggested for the oxidation and corrosion resistance of SLM-Mo and SLM-Mo/Mo_{(x)S_(x+1)} in Na₂SO₄. Since the effect of hydrogen-induced corrosion, hydrogen embrittlement, and oxidation cracking can take place in the presence of sulfur-containing species (SO₄²⁻), higher R_{ct} and R_p values were observed for both SLM-Mo and SLM-Mo/Mo_{(x)S_(x+1)} in NaCl compared with Na₂SO₄ (Figure 17d). In H₂SO₄ of low pH (~1) and very high concentration of H⁺ and SO₄²⁻, both SLM-Mo and SLM-Mo/Mo_{(x)S_(x+1)} were in different stages corroded via SCC, oxidation cracking, and pitting corrosion (Eq. 12-Eq. 16). As a by-product of chemical reaction (Eq. 16), an amorphous MoS₃ structure can also be derived during the interaction of H₂MoO₄ with H₂S, which is less stable than MoS₂ and results in increased corrosion rate (Weber et al., 1995). As a result, both R_p and R_{ct} were considerably reduced in H₂SO₄ for both SLM-processed materials compared to their performance in NaCl and Na₂SO₄ (Figure 17f and Table 5).

4.4.2 Study on energy conversion/storage

The SLM-Mo/Mo_{(x)S_(x+1)} samples were studied by different electrochemical characterization techniques to understand the electrochemical energy conversion/storage performance of 3D-printed electrodes. As shown in Figure 18, CV curves revealed the variation of electrochemical behavior with the increased amount of MoS₂ from 10 to 50 wt.%. The CV loops in each sample maintained their specific shape at different scan rates from 10 to 100 mV s⁻¹. The addition of the lower amount (10 wt.%) of MoS₂ to the structure of SLM-Mo/Mo_{(x)S_(x+1)} resulted in higher negative currents at potentials lower than -0.85 V. This can be ascribed to water electrolysis and hydrogen evolution/reduction reactions in the presence of embedded bulk MoS₂ on the surface of the electrodes (Figure 15a). A small fraction of MoS₂ and transformed electroactive Mo₂S₃ can however contribute to the pseudocapacitance performance of the electrode (Figure 18a and Figure 10d). Higher loading of MoS₂ (30 wt.%) into the structure resulted both in the formation of a higher fraction of electroactive Mo₂S₃ (Figure 10d) and in a gradual reduction in the current related to hydrogen evolution/reduction reactions, small faradic oxidation peaks located at -0.25 V, and a more pseudocapacitance shape and higher oxidation currents

(Figure 18b). Interestingly, SLM-Mo/Mo_{(x)S_(x+1)} containing 50 wt.% of MoS₂ demonstrated a nearly rectangular supercapacitance shape for all scan rates (Figure 18c).

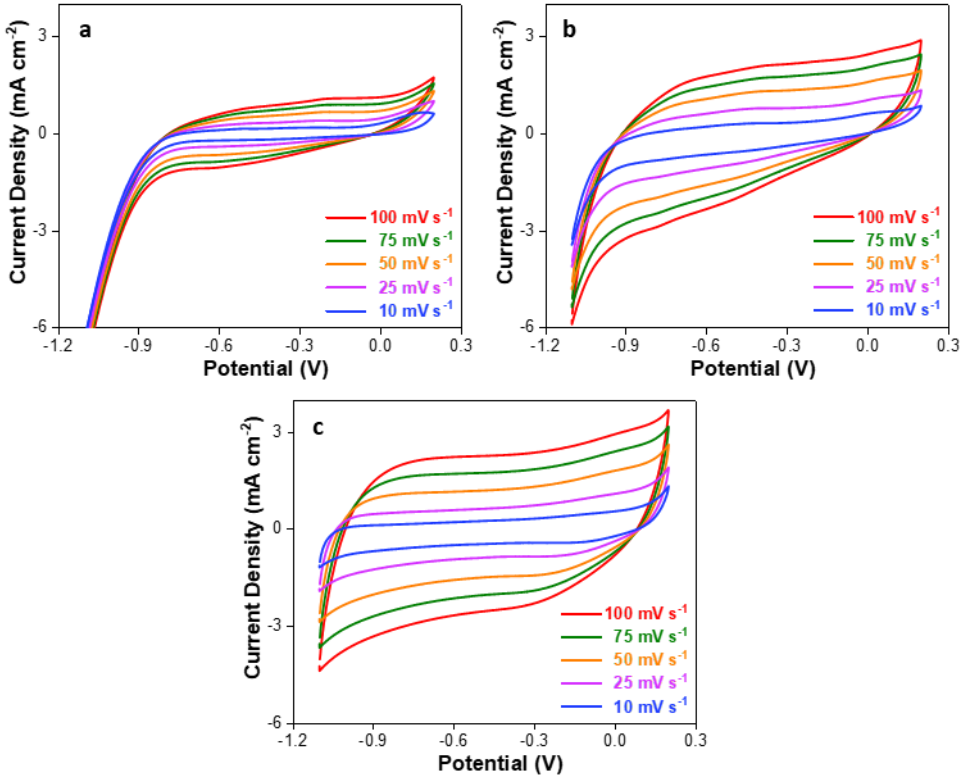


Figure 18. Cyclic voltammograms in a 0.5 M Na₂SO₄ for different scan rates from 10 to 100 mV s⁻¹ associated with (a) SLM-Mo/Mo_{(x)S_(x+1)} 10 wt.%, (b) SLM-Mo/Mo_{(x)S_(x+1)} 30 wt.%, and (c) SLM-Mo/Mo_{(x)S_(x+1)} 50 wt.%.

Compared to SLM-Mo, the considerable improvement in current density and rectangular shape of the CV curves by increasing the fraction of MoS₂ displayed in Figure 19a can be attributed to a higher amount of transformed Mo₂S₃ and a lamellar-shaped morphology facilitating the intercalation of Na⁺ ions and charge transfer performance of the SLM-Mo/Mo_{(x)S_(x+1)} electrodes. The Nyquist plots (Figure 19b) show an approximately equivalent series resistance (ESR) of 16 Ω for all electrodes, which can be attributed to the aqueous Na-rich electrolyte resistance. The quasi-semicircles, at the high-frequency region, indicate a considerably lowering R_{ct} from 193 to 85 Ω by increasing the fraction of MoS₂ from 10 to 50 wt.% at the SLM-Mo/Mo_{(x)S_(x+1)}, compared to solid and dense SLM-Mo. This can be attributed to faster interface kinetics offered by the laser-thinned layered MoS₂, separated by Mo₂S₃ nanoparticles (Figure 15c and Figure 16). Moreover, an increased fraction of MoS₂ from 10 to 50 wt.% resulted in a higher slope of the Warburg line and a lower diameter of the quasi-semicircle region in SLM-Mo/Mo_{(x)S_(x+1)}. This confirms the facilitated diffusion of Na⁺ into the laser-thinned MoS₂ on the surface (Figure 15c) (Y. Li et al., 2019). Regardless of a rate performance of almost 56.7%, the increased fraction of MoS₂ resulted in an increased areal capacitance of 112 mF cm⁻² at 10 mV s⁻¹, compared to 63 mF cm⁻² at a scan rate of 100 mV s⁻¹. The achieved areal

capacitances of SLM-Mo/Mo_(x)S_(x+1) were considerably higher than their counterpart electrodes processed by different additive manufacturing (Giannakou et al., 2020; Jiantong Li et al., 2017; Y. Lin et al., 2017; Shao et al., 2020; Sollami Delekta et al., 2020; Teng Wang et al., 2019) (Figure 19c) and conventional techniques (Bissett et al., 2015a; Cao et al., 2013; S. Wang et al., 2017; Winchester et al., 2014; Yang et al., 2014) (Figure 19d).

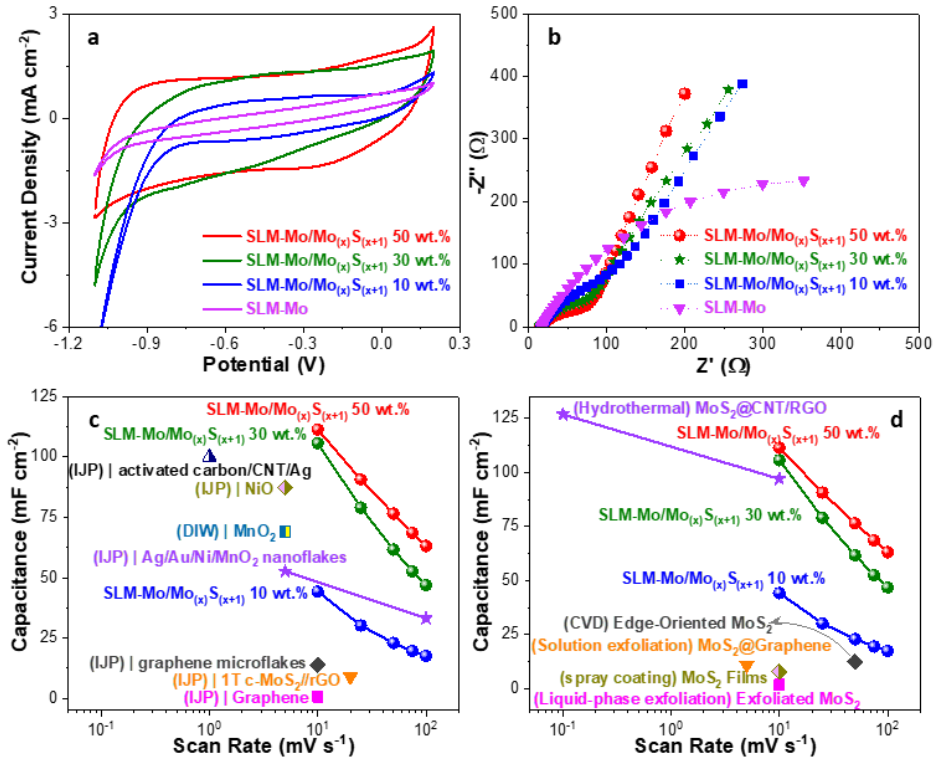


Figure 19. (a) Cyclic voltammograms comparing SLM-Mo and SLM-Mo/Mo_(x)S_(x+1) samples with different MoS₂ compositions (10 - 50 wt.%) by using a scan rate of 50 mV s⁻¹; (b) Nyquist plot of SLM-Mo and SLM-Mo/Mo_(x)S_(x+1) samples with different MoS₂ compositions in the frequency range between 10⁻¹ Hz to 10 kHz; Areal capacitance vs. scan rate comparing SLM-Mo/Mo_(x)S_(x+1) samples with (c) different 3D-printed materials and (d) different Mo_(x)S_(x+1)-incorporated nanocomposites processed by conventional methods for energy storage applications.

Figure 20 shows quasi-symmetrical triangle GCD plots indicating nearly 1.0 V output voltage even at high current densities (10 mV cm⁻²) in SLM-Mo/Mo_(x)S_(x+1) electrodes printed from the mixture feedstock containing 30 to 50 wt.% MoS₂ (Figure 20b,c). The electrodes offered an areal power density of 1.67 mW cm⁻² and energy density of 3.92 μWh cm⁻². However, the SLM-Mo/Mo_(x)S_(x+1) electrode was printed using a feedstock containing 10 wt.% MoS₂, the discharge curves leveled off at potentials lower than -0.85 V. This is due to the hydrogen reduction reaction which limits the output voltage to values less than 1.0 V and commensurately reduced the areal power density and energy density to 1.36 mW cm⁻² and 3.18 μWh cm⁻², respectively (Figure 20a).

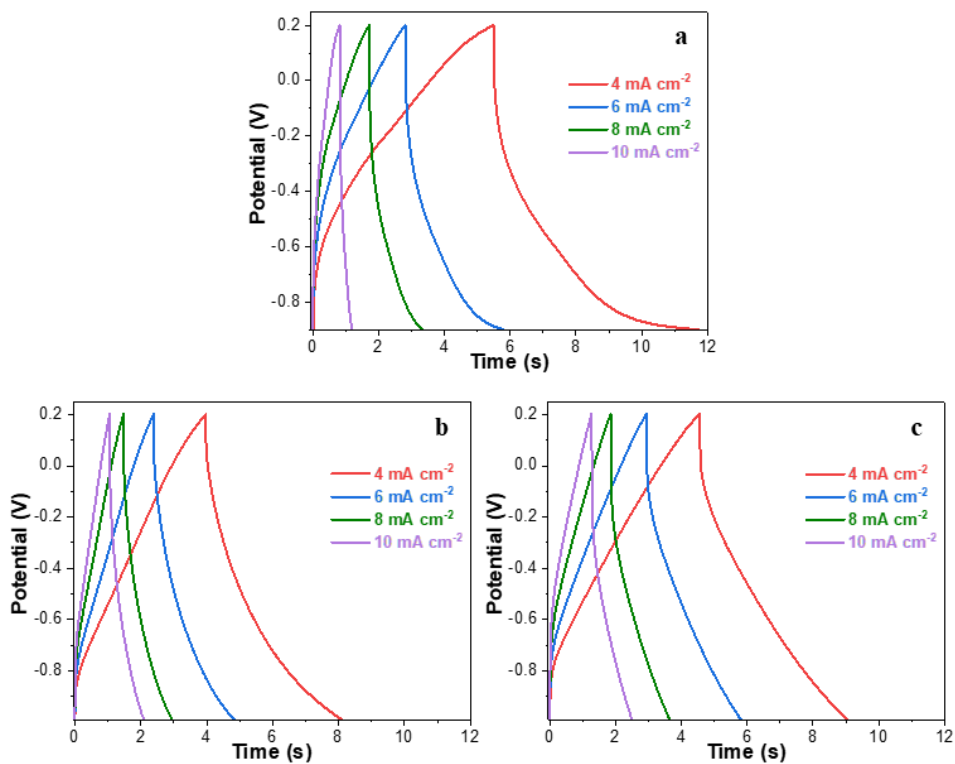


Figure 20. Galvanostatic charge-discharge curves for SLM-Mo/Mo_(x)S_(x+1) with different MoS₂ content (10, 30, 50 wt.%) in the printing powder at different current densities from 4 to 10 mA cm⁻² associated with (a) SLM-Mo/Mo_(x)S_(x+1) (10 wt.% MoS₂), (b) SLM-Mo/Mo_(x)S_(x+1) (30 wt.% MoS₂), and (c) SLM-Mo/Mo_(x)S_(x+1) (50 wt.% MoS₂).

5 Conclusion

Employing novel AM processes like laser-based powder bed fusion can overcome the drawbacks observed for both conventional manufacturing processes and AM approaches to fabricate functional 3D structures for the engineering applications extended to electrocatalytic devices and electrochemical energy storage electrodes.

1. We demonstrated that although the SLM processing of pure Mo can be challenging, due to its intrinsic properties, the double laser scanning strategy can positively affect the reduction of accumulated stress, DBTT, and crack susceptibility of bulk SLM-processed Mo. However, it has been shown that the SLM processing of micro-lattice structures of pure Mo has still been challenging as a result of the high cooling rate, thermal conductivity, thermal gradient, and less stable melt pool.

2. MoS₂, possessing multifunctional properties, is a promising candidate for being processed by laser-based powder bed fusion for a wide range of applications. In this thesis, It has been shown that the laser beam is a versatile source for thinning of MoS₂ and simultaneously delivering the functionality *in-situ* to the sustainable and functional additively manufactured components.

3. The addition of a small amount of MoS₂ to the Mo feedstock for the SLM-based fabrication of Mo-based composite structures positively influences the microstructure, crystallographic properties, and electrochemical performance. The transformation of MoS₂ to Mo₂S₃ considerably increases coherent domain, changes preferential solidification conditions and hence texture, decreases structural lattice strain, crystallographic defects, and the extent of crack formation in SLM fabricated micro-lattices of small unit cell sizes (750 μm) and tiny strut diameters (approximately 85 μm). Furthermore, It was also demonstrated that the phase transformation from MoS₂ to Mo₂S₃ considerably decreased the corrosion rate mainly via decreasing the residual stress to alleviate SCC susceptibility in NaCl electrolyte, hindering the Na⁺ accessibility to Mo components in Na₂SO₄ electrolyte to reduce oxidation corrosion, and finally increased polarization resistance values upon exposure in both Na-rich aqueous solutions.

4. Employing Nd:YAG laser source, it is elucidated that in-situ thinning and tuning of the structure of MoS₂, as well as distribution of electroactive Mo₂S₃ nanoparticles into the structure, can considerably enhance the areal energy density and power density of 3D-printed composite structures. The successful fabrication of SLM-processed Mo/MoS₂/Mo₂S₃ electrodes, compared to other 3D-printed counterparts, showed a remarkable capacitive behavior, promoting a novel manufacturing approach for the next generation of additively manufactured electrochemical components and devices. The initiative results propose an innovative research line on laser-assisted processing of 2D material-incorporated structures with a wide range of functionality applied in high-temperature solid-state energy conversion/storage systems, EECSS, aerospace parts, and more eco-friendly energy storage devices fabrication.

5. Also, it has been demonstrated that a higher load of MoS₂ (up to 50 wt.%) into the powder feedstock can increase the packing density of feedstock, laser absorptivity, and more stable melt pool, serving for phase transformation of MoS₂ to higher fractions of Mo₂S₃, resulted in higher rate capacitance and lower resistance (R_{ct}) of printed anodes.

6 Outlook

According to the research output and achievements, having been presented in this dissertation, a novel and innovative research path have been proposed on the basis of laser-based AM of 2D-materials-incorporated functional 3D structures, paving the way for the applications extended to electrocatalytic, electrochemical, and engineering devices and components. However, since this research field is in its very initial stages, further in-depth studies on the mechanisms are highly required for SLM-processed functional composites.

Moreover, limited attention to the processing of TMDCs-based composites by L-PBF techniques urges scientists to extensively research in the above-mentioned fields should be conducted to develop the functional benefits of $\text{Mo}_{(x)}\text{S}_{(x+1)}$ -incorporated structures and expand their applications, especially for electrochemical sensors and actuators, hydrogen evolution cells, biomedical implants, and sustainable electrochemical applications.

Overall, SLM of $\text{Mo}_{(x)}\text{S}_{(x+1)}$ -incorporated electroactive structures can generate promising advanced energy conversion/storage system components based on the present industrial and economic demands, such as Li-ion and Na-ion batteries, supercapacitors, etc. Hence, extensive research on the academic development of the above-mentioned achievements must be carried out along with the LCA, environmental, and economic investigations, simultaneously, to pave the way for scaling up or industrial fabrication of SLM-processed TMDCs-incorporated functional components.

Beyond the stated outlook, it is worth noticing that laser-based AM techniques have yet to fully reach their groundbreaking potential in the fabrication of 3D structures from 2D nanomaterials, and it would be a promising approach for the next-generation technologies.

References

- Acerce, M., Voiry, D., & Chhowalla, M. (2015). Metallic 1T phase MoS₂ nanosheets as supercapacitor electrode materials. *Nature Nanotechnology*, *10*(4), 313–318. doi: 10.1038/nnano.2015.40
- Advanced Energy Storage Systems Market Size, Share, Trends & Forecast*. (n.d.). Retrieved from <https://www.verifiedmarketresearch.com/product/advanced-energy-storage-systems-market/>
- Alexaki, K., Kostopoulou, A., Sygletou, M., Kenanakis, G., & Stratakis, E. (2018). Unveiling the structure of MoS_x nanocrystals produced upon laser fragmentation of MoS₂ platelets. *ACS Omega*, *3*(12), 16728–16734. doi: 10.1021/acsomega.8b01390
- Ali, H., Ghadbeigi, H., & Mumtaz, K. (2018). Effect of scanning strategies on residual stress and mechanical properties of Selective Laser Melted Ti6Al4V. *Materials Science and Engineering A*, *712*(December 2017), 175–187. doi: 10.1016/j.msea.2017.11.103
- Alinejadian, N., Nasirpour, F., Yus, J., & Ferrari, B. (2021). Reduction-based engineering of three-dimensional morphology of Ni-rGO nanocomposite. *Materials Science and Engineering B: Solid-State Materials for Advanced Technology*, *271*(April), 115259. doi: 10.1016/j.mseb.2021.115259
- Ambrosi, A., & Pumera, M. (2016). 3D-printing technologies for electrochemical applications. *Chemical Society Reviews*, *45*(10), 2740–2755. doi: 10.1039/c5cs00714c
- Atapour, M., Wang, X., Färnlund, K., Odnevall Wallinder, I., & Hedberg, Y. (2020). Corrosion and metal release investigations of selective laser melted 316L stainless steel in a synthetic physiological fluid containing proteins and in diluted hydrochloric acid. *Electrochimica Acta*, *354*, 136748. doi: 10.1016/j.electacta.2020.136748
- Babu, B. R., Bhanu, S. U., & Meera, K. S. (2009). Waste minimization in electroplating industries: A review. *Journal of Environmental Science and Health - Part C Environmental Carcinogenesis and Ecotoxicology Reviews*, *27*(3), 155–177. doi: 10.1080/10590500903124158
- Balasingam, S. K., Lee, J. S., & Jun, Y. (2015). Few-layered MoSe₂ nanosheets as an advanced electrode material for supercapacitors. *Dalton Transactions*, *44*(35), 15491–15498. doi: 10.1039/c5dt01985k
- Baltrusaitis, J., Mendoza-Sanchez, B., Fernandez, V., Veenstra, R., Dukstiene, N., Roberts, A., & Fairley, N. (2015). Generalized molybdenum oxide surface chemical state XPS determination via informed amorphous sample model. *Applied Surface Science*, *326*, 151–161. doi: 10.1016/j.apsusc.2014.11.077
- Bermúdez Agudelo, M. C., Hampe, M., Reiber, T., & Abele, E. (2020). Investigation of Porous Metal-Based 3D-Printed Anode GDLs for Tubular High Temperature Proton Exchange Membrane Fuel Cells. *Materials*, *13*(9), 2096. doi: 10.3390/ma13092096
- Bi, G., Sun, C. N., Nai, M. L., & Wei, J. (2013). Micro-structure and mechanical properties of nano-TiC reinforced Inconel 625 deposited using LAAM. *Physics Procedia*, *41*, 828–834. doi: 10.1016/j.phpro.2013.03.155
- Bissett, M. A., Kinloch, I. A., & Dryfe, R. A. W. (2015a). Characterization of MoS₂-Graphene Composites for High-Performance Coin Cell Supercapacitors. *ACS Applied Materials and Interfaces*, *7*(31), 17388–17398. doi: 10.1021/acsmi.5b04672
- Bissett, M. A., Kinloch, I. A., & Dryfe, R. A. W. (2015b). Characterization of MoS₂ – Graphene Composites for High-Performance Coin Cell Supercapacitors. *ACS Applied Materials & Interfaces*, *7*(31), 17388–17398. doi: 10.1021/acsmi.5b04672
- Bradford, S. A. (n.d.). Corrosion. In *Corrosion* (pp. 761–778). University of Alberta.

- Braun, J., Kaserer, L., Stajkovic, J., Leitz, K.-H., Tabernig, B., Singer, P., Leibenguth, P., Gspan, C., Kestler, H., & Leichtfried, G. (2019). Molybdenum and tungsten manufactured by selective laser melting: Analysis of defect structure and solidification mechanisms. *International Journal of Refractory Metals and Hard Materials*, 84(June), 104999. doi: 10.1016/j.ijrmhm.2019.104999
- Brown, E., Yan, P., Tekik, H., Elangovan, A., Wang, J., Lin, D., & Li, J. (2019). 3D printing of hybrid MoS₂-graphene aerogels as highly porous electrode materials for sodium ion battery anodes. *Materials & Design*, 170, 107689. doi: 10.1016/j.matdes.2019.107689
- Cao, L., Yang, S., Gao, W., Liu, Z., Gong, Y., Ma, L., Shi, G., Lei, S., Zhang, Y., Zhang, S., Vajtai, R., & Ajayan, P. M. (2013). Direct Laser-Patterned Micro-Supercapacitors from Paintable MoS₂ Films. *Small*, 9(17), 2905–2910. doi: 10.1002/smll.201203164
- Castellanos-Gomez, A., Barkelid, M., Goossens, A. M., Calado, V. E., van der Zant, H. S. J., & Steele, G. A. (2012). Laser-Thinning of MoS₂ : On Demand Generation of a Single-Layer Semiconductor. *Nano Letters*, 12(6), 3187–3192. doi: 10.1021/nl301164v
- Chang, P., Mei, H., Tan, Y., Zhao, Y., Huang, W., & Cheng, L. (2020). A 3D-Printed Stretchable Structural Supercapacitor with Active Stretchability/Flexibility and Remarkable Volumetric Capacitance. *Journal of Materials Chemistry A*, 8(27), 13646–13658. doi: 10.1039/d0ta04460a
- Chang, P., Mei, H., Zhou, S., Dassios, K. G., & Cheng, L. (2019). 3D printed electrochemical energy storage devices. *Journal of Materials Chemistry A*, 7(9), 4230–4258. doi: 10.1039/c8ta11860d
- Cheng, B., Shrestha, S., & Chou, K. (2016). Stress and deformation evaluations of scanning strategy effect in selective laser melting. *Additive Manufacturing*, 12, 240–251. doi: 10.1016/j.addma.2016.05.007
- Cheng, M., Deivanayagam, R., & Shahbazian-Yassar, R. (2020). 3D Printing of Electrochemical Energy Storage Devices: A Review of Printing Techniques and Electrode/Electrolyte Architectures. *Batteries & Supercaps*, 3(2), 130–146. doi: 10.1002/batt.201900130
- Chhowalla, M., Shin, H. S., Eda, G., Li, L. J., Loh, K. P., & Zhang, H. (2013). The chemistry of two-dimensional layered transition metal dichalcogenide nanosheets. *Nature Chemistry*, 5(4), 263–275. doi: 10.1038/nchem.1589
- Choi, J., & Mazumder, J. (1994). Non-equilibrium synthesis of Fe-Cr-C-W alloy by laser cladding. *Journal of Materials Science*, 29(17), 4460–4476. doi: 10.1007/BF00376268
- Choi, W., Choudhary, N., Han, G. H., Park, J., Akinwande, D., & Lee, Y. H. (2017). Recent development of two-dimensional transition metal dichalcogenides and their applications. *Materials Today*, 20(3), 116–130. doi: 10.1016/j.mattod.2016.10.002
- Cohen, E., Menkin, S., Lifshits, M., Kamir, Y., Gladkikh, A., Kosa, G., & Golodnitsky, D. (2018). Novel rechargeable 3D-Microbatteries on 3D-printed-polymer substrates: Feasibility study. *Electrochimica Acta*, 265(2018), 690–701. doi: 10.1016/j.electacta.2018.01.197
- Coleman, J. N., Lotya, M., O'Neill, A., Bergin, S. D., King, P. J., Khan, U., Young, K., Gaucher, A., De, S., Smith, R. J., Shvets, I. V., Arora, S. K., Stanton, G., Kim, H.-Y., Lee, K., Kim, G. T., Duesberg, G. S., Hallam, T., Boland, J. J., ... Nicolosi, V. (2011). Two-Dimensional Nanosheets Produced by Liquid Exfoliation of Layered Materials. *Science*, 331(6017), 568–571. doi: 10.1126/science.1194975
- Corrales-sánchez, T., Ampurdanés, J., & Urakawa, A. (2014). MoS₂-based materials as alternative cathode catalyst for PEM electrolysis. *International Journal of Hydrogen Energy*, 39(35), 20837–20843. doi: 10.1016/j.ijhydene.2014.08.078

- David, L., Bhandavat, R., & Singh, G. (2014). MoS₂/graphene composite paper for sodium-ion battery electrodes. *ACS Nano*, *8*(2), 1759–1770. doi: 10.1021/nn406156b
- Davoodi, A., Pakshir, M., Babaiee, M., & Ebrahimi, G. R. (2011). A comparative H₂S corrosion study of 304L and 316L stainless steels in acidic media. *Corrosion Science*, *53*(1), 399–408. doi: 10.1016/j.corsci.2010.09.050
- Dawson, R. J., Patel, A. J., Rennie, A. E. W., & White, S. (2015). An investigation into the use of additive manufacture for the production of metallic bipolar plates for polymer electrolyte fuel cell stacks. *Journal of Applied Electrochemistry*, *45*(7), 637–645. doi: 10.1007/s10800-015-0832-1
- Du, J., Li, Y., Li, F., Ran, X., Zhang, X., & Qi, X. (2021). Research on the high temperature oxidation mechanism of Cr₃C₂-NiCrCoMo coating for surface remanufacturing. *Journal of Materials Research and Technology*, *10*, 565–579. doi: 10.1016/j.jmrt.2020.12.049
- Elibol, K., Susi, T., Argentero, G., Reza Ahmadpour Monazam, M., Pennycook, T. J., Meyer, J. C., & Kotakoski, J. (2018). Atomic Structure of Intrinsic and Electron-Irradiation-Induced Defects in MoTe₂. *Chemistry of Materials*, *30*(4), 1230–1238. doi: 10.1021/acs.chemmater.7b03760
- Faidel, D., Jonas, D., Natour, G., & Behr, W. (2015). Investigation of the selective laser melting process with molybdenum powder. *Additive Manufacturing*, *8*, 88–94. doi: 10.1016/j.addma.2015.09.002
- Fleischmann, S., Mitchell, J. B., Wang, R., Zhan, C., Jiang, D. E., Presser, V., & Augustyn, V. (2020). Pseudocapacitance: From Fundamental Understanding to High Power Energy Storage Materials. *Chemical Reviews*, *120*(14), 6738–6782. doi: 10.1021/acs.chemrev.0c00170
- Furlan, K. P., de Mello, J. D. B., & Klein, A. N. (2018). Self-lubricating composites containing MoS₂: A review. *Tribology International*, *120*(December 2017), 280–298. doi: 10.1016/j.triboint.2017.12.033
- Gallardo, A., Pereyra, Y., Martínez-Campos, E., García, C., Acitores, D., Casado-Losada, I., Gómez-Fatou, M. A., Reinecke, H., Ellis, G., Acevedo, D., Rodríguez-Hernández, J., & Salavagione, H. J. (2017). Facile one-pot exfoliation and integration of 2D layered materials by dispersion in a photocurable polymer precursor. *Nanoscale*, *9*(30), 10590–10595. doi: 10.1039/c7nr03204h
- Gao, M. R., Xu, Y. F., Jiang, J., & Yu, S. H. (2013). Nanostructured metal chalcogenides: Synthesis, modification, and applications in energy conversion and storage devices. *Chemical Society Reviews*, *42*(7), 2986–3017. doi: 10.1039/c2cs35310e
- Ge, Q., Li, Z., Wang, Z., Kowsari, K., Zhang, W., He, X., Zhou, J., & Fang, N. X. (2020). Projection micro stereolithography based 3D printing and its applications. *International Journal of Extreme Manufacturing*, *2*(2), 022004. doi: 10.1088/2631-7990/ab8d9a
- Giannakou, P., Tas, M. O., Le Borgne, B., & Shkunov, M. (2020). Water-Transferred, Inkjet-Printed Supercapacitors toward Conformal and Epidermal Energy Storage. *ACS Applied Materials and Interfaces*, *12*(7), 8456–8465. doi: 10.1021/acsami.9b21283
- Gogotsi, Y., & Penner, R. M. (2018). Energy Storage in Nanomaterials - Capacitive, Pseudocapacitive, or Battery-like? *ACS Nano*, *12*(3), 2081–2083. doi: 10.1021/acsnano.8b01914

- Gu, D. D., Meiners, W., Wissenbach, K., & Poprawe, R. (2012). Laser additive manufacturing of metallic components: materials, processes and mechanisms. *International Materials Reviews*, *57*(3), 133–164. doi: 10.1179/1743280411Y.0000000014
- Gu, D., Hagedorn, Y. C., Meiners, W., Meng, G., Batista, R. J. S., Wissenbach, K., & Poprawe, R. (2012). Densification behavior, microstructure evolution, and wear performance of selective laser melting processed commercially pure titanium. *Acta Materialia*, *60*(9), 3849–3860. doi: 10.1016/j.actamat.2012.04.006
- Gu, D., & Shen, Y. (2009). Microstructures and properties of direct laser sintered tungsten carbide (WC) particle reinforced Cu matrix composites with RE - Si - Fe addition: A comparative study. *Journal of Materials Research*, *24*(11), 3397–3406. doi: 10.1557/jmr.2009.0419
- Gulzar, U., Glynn, C., & O'Dwyer, C. (2020). Additive manufacturing for energy storage: Methods, designs and material selection for customizable 3D printed batteries and supercapacitors. *Current Opinion in Electrochemistry*, *20*, 46–53. doi: 10.1016/j.coelec.2020.02.009
- Gunasekaran, J., Sevel, P., & John Solomon, I. (2021). Metallic materials fabrication by selective laser melting: A review. *Materials Today: Proceedings*, *37*(Part 2), 252–256. doi: 10.1016/j.matpr.2020.05.162
- Guo, Z., Sun, T., Li, Y., Kang, H., Che, Y., Zhang, Y., & Lu, J. (2018). Large surface and pore structure of mesoporous WS₂ and RGO nanosheets with small amount of Pt as a highly efficient electrocatalyst for hydrogen evolution. *International Journal of Hydrogen Energy*, *43*(51), 22905–22916. doi: 10.1016/j.ijhydene.2018.10.150
- Ha, H. Y., Lee, T. H., Bae, J. H., & Chun, D. W. (2018). Molybdenum effects on pitting corrosion resistance of FeCrMnMoNC austenitic stainless steels. *Metals*, *8*(8), 1–13. doi: 10.3390/met8080653
- Hasani, A., Nguyen, T. P., Tekalgne, M., Van Le, Q., Choi, K. S., Lee, T. H., Jung Park, T., Jang, H. W., & Kim, S. Y. (2018). The role of metal dopants in WS₂ nanoflowers in enhancing the hydrogen evolution reaction. *Applied Catalysis A: General*, *567*(June), 73–79. doi: 10.1016/j.apcata.2018.09.008
- Herzog, D., Seyda, V., Wycisk, E., & Emmelmann, C. (2016). Additive manufacturing of metals. *Acta Materialia*, *117*, 371–392. doi: 10.1016/j.actamat.2016.07.019
- Higashi, M., & Ozaki, T. (2020). Selective laser melting of pure molybdenum: Evolution of defect and crystallographic texture with process parameters. *Materials and Design*, *191*, 108588. doi: 10.1016/j.matdes.2020.108588
- Hooper, P. A. (2018). Melt pool temperature and cooling rates in laser powder bed fusion. *Additive Manufacturing*, *22*(May), 548–559. doi: 10.1016/j.addma.2018.05.032
- Hu, L., Shan, X., Wu, Y., Zhao, J., & Lu, X. (2017). Laser Thinning and Patterning of MoS₂ with Layer-by-Layer Precision. *Scientific Reports*, *7*(1), 15538. doi: 10.1038/s41598-017-15350-4
- Hu, S., Fan, Y., Muhammad, M., Wang, M., Ma, R., Du, A., Zhao, X., & Cao, X. (2020). Corrosion resistance performance of nano-MoS₂-containing zinc phosphate coating on Q235 steel. *Materials Letters*, *265*, 6–9. doi: 10.1016/j.matlet.2019.127256
- Hu, Y., & Chua, D. H. C. (2016). Synthesizing 2D MoS₂ Nanofins on carbon nanospheres as catalyst support for Proton Exchange Membrane Fuel Cells. *Scientific Reports*, *6*(May), 1–10. doi: 10.1038/srep28088
- Huang, Y., Guo, J., Kang, Y., Ai, Y., & Li, C. M. (2015). Two dimensional atomically thin MoS₂ nanosheets and their sensing applications. *Nanoscale*, *7*(46), 19358–19376. doi: 10.1039/C5NR06144J

- Hunt, G. E. (1988). Hazardous waste minimization: Part IV. Waste reduction in the metal finishing industry. *Journal of the Air Pollution Control Association*, 38(5), 672–680. doi: 10.1080/08940630.1988.10466410
- Jewel, M. U., Monne, M. A., Mishra, B., & Chen, M. Y. (2020). Inkjet-printed molybdenum disulfide and nitrogen-doped graphene active layer high on/off ratio transistors. *Molecules*, 25(5), 1–7. doi: 10.3390/molecules25051081
- Jin, Y., Cheng, M., Liu, H., Ouzounian, M., Hu, T. S., You, B., Shao, G., Liu, X., Liu, Y., Li, H., Li, S., Guan, J., & Liu, S. (2020). Na₂SO₄-Regulated High-Quality Growth of Transition Metal Dichalcogenides by Controlling Diffusion. *Chemistry of Materials*, 32(13), 5616–5625. doi: 10.1021/acs.chemmater.0c01089
- Karimi, P., Sadeghi, E., Ålgårdh, J., Harlin, P., & Andersson, J. (2020). Effect of build location on microstructural characteristics and corrosion behavior of EB-PBF built Alloy 718. *International Journal of Advanced Manufacturing Technology*, 106(7–8), 3597–3607. doi: 10.1007/s00170-019-04859-9
- Kaserer, L., Braun, J., Stajkovic, J., Leitz, K.-H., Tabernig, B., Singer, P., Letofsky-Papst, I., Kestler, H., & Leichtfried, G. (2019). Fully dense and crack-free molybdenum manufactured by Selective Laser Melting through alloying with carbon. *International Journal of Refractory Metals and Hard Materials*, 84(June), 105000. doi: 10.1016/j.ijrmhm.2019.105000
- Kasperovich, G., & Hausmann, J. (2015). Journal of Materials Processing Technology Improvement of fatigue resistance and ductility of TiAl6V4 processed by selective laser melting. *Journal of Materials Processing Tech.*, 220, 202–214. doi: 10.1016/j.jmatprotec.2015.01.025
- Kim, K. H. S., Kim, K. H. S., Nam, Y., Jeon, J., Yim, S., Singh, E., Lee, J. Y., Lee, S. J., Jung, Y. S., Yeom, G. Y., & Kim, D. W. (2017). Atomic Layer Etching Mechanism of MoS₂ for Nanodevices. *ACS Applied Materials and Interfaces*, 9(13), 11967–11976. doi: 10.1021/acsami.6b15886
- Kong, D., Wang, H., Cha, J. J., Pasta, M., Koski, K. J., Yao, J., & Cui, Y. (2013). Synthesis of MoS₂ and MoSe₂ films with vertically aligned layers. *Nano Letters*, 13(3), 1341–1347. doi: 10.1021/nl400258t
- Körner, C., Attar, E., & Heinl, P. (2011). Mesoscopic simulation of selective beam melting processes. *Journal of Materials Processing Technology*, 211(6), 978–987. doi: 10.1016/j.jmatprotec.2010.12.016
- Krishnan, U., Kaur, M., Singh, K., Kumar, M., & Kumar, A. (2019). A synoptic review of MoS₂: Synthesis to applications. *Superlattices and Microstructures*, 128(December 2018), 274–297. doi: 10.1016/j.spmi.2019.02.005
- Kumar, S. (2014). Selective Laser Sintering/Melting. In *Comprehensive Materials Processing* (Vol. 10, pp. 93–134). Elsevier. doi: 10.1016/B978-0-08-096532-1.01003-7
- Lee, H., Bak, S., Cho, Y., Kim, M., Kang, S. H., Bui, V. Q., Le, H. M., Kim, S. W., & Lee, H. (2018). Hydrogen adsorption engineering by intramolecular proton transfer on 2D nanosheets. *NPG Asia Materials*, 10(5), 441–454. doi: 10.1038/s41427-018-0037-2
- Lehnert, T., Ghorbani-Asl, M., Köster, J., Lee, Z., Krasheninnikov, A. V., & Kaiser, U. (2019). Electron-Beam-Driven Structure Evolution of Single-Layer MoTe₂ for Quantum Devices. *ACS Applied Nano Materials*, 2(5), 3262–3270. doi: 10.1021/acsanm.9b00616
- Leitz, K. H., Singer, P., Plankensteiner, A., Tabernig, B., Kestler, H., & Sigl, L. S. (2017). Multi-physical simulation of selective laser melting. *Metal Powder Report*, 72(5), 331–338. doi: 10.1016/j.mprp.2016.04.004

- Leuders, S., Thöne, M., Riemer, A., Niendorf, T., Tröster, T., Richard, H. A., & Maier, H. J. (2013). On the mechanical behaviour of titanium alloy TiAl6V4 manufactured by selective laser melting: Fatigue resistance and crack growth performance. *International Journal of Fatigue*, *48*, 300–307. doi: 10.1016/j.ijfatigue.2012.11.011
- Li, F., & Zhou, Z. (2018). Micro/Nanostructured Materials for Sodium-Ion Batteries and Capacitors. *Small*, *14*(6), 1702961. doi: 10.1002/smll.201702961
- Li, Jiantong, Lemme, M. C., & Östling, M. (2014). Inkjet Printing of 2D Layered Materials. *ChemPhysChem*, *1*(16), 408–412. doi: 10.1002/cphc.200
- Li, Jiantong, Naiini, M. M., Vaziri, S., Lemme, M. C., & Östling, M. (2014). Inkjet printing of MoS₂. *Advanced Functional Materials*, *24*(41), 6524–6531. doi: 10.1002/adfm.201400984
- Li, Jiantong, Sollami Delekta, S., Zhang, P., Yang, S., Lohe, M. R., Zhuang, X., Feng, X., & Östling, M. (2017). Scalable Fabrication and Integration of Graphene Microsupercapacitors through Full Inkjet Printing. *ACS Nano*, *11*(8), 8249–8256. doi: 10.1021/acsnano.7b03354
- Li, Junke, Li, M., & Jin, Z. (2022). ZIF-67 derived hierarchical hollow Co₃S₄@Mo₂S₃ dodecahedron with an S-scheme surface heterostructure for efficient photocatalytic hydrogen evolution. *Catalysis Science & Technology*, *12*(4), 1144–1158. doi: 10.1039/D1CY01757H
- Li, Xiao, & Zhu, H. (2015). Two-dimensional MoS₂: Properties, preparation, and applications. *Journal of Materiomics*, *1*(1), 33–44. doi: 10.1016/j.jmat.2015.03.003
- Li, Xiaodan, Wu, G., Chen, J., Li, M., Li, W., Wang, T., Jiang, B., He, Y., & Mai, L. (2017). Low-crystallinity molybdenum sulfide nanosheets assembled on carbon nanotubes for long-life lithium storage: Unusual electrochemical behaviors and ascending capacities. *Applied Surface Science*, *392*, 297–304. doi: 10.1016/j.apsusc.2016.09.055
- Li, Y., Zhang, R., Zhou, W., Wu, X., Zhang, H., & Zhang, J. (2019). Hierarchical MoS₂ Hollow Architectures with Abundant Mo Vacancies for Efficient Sodium Storage. *ACS Nano*, *13*(5), 5533–5540. doi: 10.1021/acsnano.9b00383
- Lin, H., Chen, X., Li, H., Yang, M., & Qi, Y. (2010). Hydrothermal synthesis and characterization of MoS₂ nanorods. *Materials Letters*, *64*(15), 1748–1750. doi: 10.1016/j.matlet.2010.04.032
- Lin, L., Lei, W., Zhang, S., Liu, Y., Wallace, G. G., & Chen, J. (2019). Two-dimensional transition metal dichalcogenides in supercapacitors and secondary batteries. *Energy Storage Materials*, *19*(February), 408–423. doi: 10.1016/j.ensm.2019.02.023
- Lin, Y., Gao, Y., & Fan, Z. (2017). Printable Fabrication of Nanocoral-Structured Electrodes for High-Performance Flexible and Planar Supercapacitor with Artistic Design. *Advanced Materials*, *29*(43), 1–8. doi: 10.1002/adma.201701736
- Lin, Z., Liu, Y., Halim, U., Ding, M., Liu, Y., Wang, Y., Jia, C., Chen, P., Duan, X. X., Wang, C., Song, F., Li, M., Wan, C., Huang, Y., & Duan, X. X. (2018). Solution-processable 2D semiconductors for high-performance large-area electronics. *Nature*, *562*(7726), 254–258. doi: 10.1038/s41586-018-0574-4
- Liu, D., Du, W., Liu, X., Tian, R., & Li, H. (2019). To Distinguish Electrostatic, Coordination Bond, Nonclassical Polarization, and Dispersion Forces on Cation–Clay Interactions. *The Journal of Physical Chemistry C*, *123*(4), 2157–2164. doi: 10.1021/acs.jpcc.8b08133
- Liu, S., & Shin, Y. C. (2019). Additive manufacturing of Ti6Al4V alloy: A review. *Materials and Design*, *164*, 107552. doi: 10.1016/j.matdes.2018.107552

- Liu, Y., Cui, C., Liu, Y., Liu, W., & Wei, J. (2020). Application of MoS₂ in the cathode of lithium-sulfur batteries. *RSC Advances*, *10*(13), 7384–7395. doi: 10.1039/C9RA09769D
- Lu, J., Liu, H., Tok, E. S., & Sow, C.-H. H. (2016). Interactions between lasers and two-dimensional transition metal dichalcogenides. *Chemical Society Reviews*, *45*(9), 2494–2515. doi: 10.1039/c5cs00553a
- Lutz, B. S., Alvarado-Orozco, J. M., Garcia-Fresnillo, L., & Meier, G. H. (2017). Na₂SO₄-Deposit-Induced Corrosion of Mo-Containing Alloys. *Oxidation of Metals*, *88*(5–6), 599–620. doi: 10.1007/s11085-017-9746-0
- Lyon, S. B. (2010). Corrosion of Molybdenum and its Alloys. In Shreir's Corrosion (pp. 2157–2167). Elsevier. doi: 10.1016/B978-044452787-5.00106-2
- Martin, E. J., Pourzal, R., Mathew, M. T., & Shull, K. R. (2013). Dominant Role of Molybdenum in the Electrochemical Deposition of Biological Macromolecules on Metallic Surfaces. *Langmuir*, *29*(15), 4813–4822. doi: 10.1021/la304046q
- Martin, J. H., Yahata, B. D., Hundley, J. M., Mayer, J. A., Schaedler, T. A., & Pollock, T. M. (2017). 3D printing of high-strength aluminium alloys. *Nature*, *549*(7672), 365–369. doi: 10.1038/nature23894
- Mortazavi, M., Wang, C., Deng, J., Shenoy, V. B., & Medhekar, N. V. (2014). Ab initio characterization of layered MoS₂ as anode for sodium-ion batteries. *Journal of Power Sources*, *268*, 279–286. doi: 10.1016/j.jpowsour.2014.06.049
- Mujib, S. Bin, Mukherjee, S., Ren, Z., & Singh, G. (2020). Assessing corrosion resistance of two-dimensional nanomaterial-based coatings on stainless steel substrates. *Royal Society Open Science*, *7*(4), 200214. doi: 10.1098/rsos.200214
- Mukherjee, S., Ren, Z., & Singh, G. (2018). Beyond Graphene Anode Materials for Emerging Metal Ion Batteries and Supercapacitors. *Nano-Micro Letters*, *10*(4). doi: 10.1007/s40820-018-0224-2
- Mukherjee, S., Turnley, J., Mansfield, E., Holm, J., Soares, D., David, L., & Singh, G. (2019). Exfoliated transition metal dichalcogenide nanosheets for supercapacitor and sodium-ion battery applications. *Royal Society Open Science*, *6*(8), 190437. doi: 10.1098/rsos.190437
- Ning, H., Pikul, J. H., Zhang, R., Li, X., Xu, S., Wang, J., Rogers, J. A., King, W. P., & Braun, P. V. (2015). Holographic patterning of high-performance on-chip 3D lithium-ion microbatteries. *Proceedings of the National Academy of Sciences*, *112*(21), 6573–6578. doi: 10.1073/pnas.1423889112
- Pal, S., & Kumar Chattopadhyay, K. (2018). Fabrication of Molybdenum Trioxide Nanobelts as High-Performance Supercapacitor. *Materials Today: Proceedings*, *5*(3), 9776–9782. doi: 10.1016/j.matpr.2017.10.166
- Pan, C., Jiang, L., Sun, J., Wang, Q., Wang, F., Wang, K., Lu, Y., Wang, Y., Qu, L., & Cui, T. (2020). Ultrafast optical response and ablation mechanisms of molybdenum disulfide under intense femtosecond laser irradiation. *Light: Science & Applications*, *9*(1), 80. doi: 10.1038/s41377-020-0318-8
- Pang, Y., Cao, Y., Chu, Y., Liu, M., Snyder, K., MacKenzie, D., & Cao, C. (2020). Additive Manufacturing of Batteries. *Advanced Functional Materials*, *30*(1), 1–22. doi: 10.1002/adfm.201906244
- Pereira, H. B., Panossian, Z., Baptista, I. P., & De Farias Azevedo, C. R. (2019). Investigation of stress corrosion cracking of austenitic, duplex and super duplex stainless steels under drop evaporation test using synthetic seawater. *Materials Research*, *22*(2), 5–8. doi: 10.1590/1980-5373-MR-2018-0211

- Prashanth, K. G., Scudino, S., & Eckert, J. (2017). Defining the tensile properties of Al-12Si parts produced by selective laser melting. *Acta Materialia*, *126*, 25–35. doi: 10.1016/j.actamat.2016.12.044
- Prashanth, K. G., Scudino, S., Klauss, H. J., Surreddi, K. B., Löber, L., Wang, Z., Chaubey, A. K., Kühn, U., & Eckert, J. (2014). Microstructure and mechanical properties of Al-12Si produced by selective laser melting: Effect of heat treatment. *Materials Science and Engineering A*, *590*, 153–160. doi: 10.1016/j.msea.2013.10.023
- Prashanth, K. G., Scudino, S., Maity, T., Das, J., & Eckert, J. (2017). Is the energy density a reliable parameter for materials synthesis by selective laser melting? *Materials Research Letters*, *5*(6), 386–390. doi: 10.1080/21663831.2017.1299808
- Prashanth, K. G., Shakur Shahabi, H., Attar, H., Srivastava, V. C., Ellendt, N., Uhlenwinkel, V., Eckert, J., & Scudino, S. (2015). Production of high-strength Al 85 Nd 8 Ni 5 Co 2 alloy by selective laser melting. *Additive Manufacturing*, *6*, 1–5. doi: 10.1016/j.addma.2015.01.001
- Pumera, M. (2019). Three-dimensionally printed electrochemical systems for biomedical analytical applications. *Current Opinion in Electrochemistry*, *14*, 133–137. doi: 10.1016/j.coelec.2019.02.001
- Putra, Y. P., Soemantojo, R. W., & Hamzah, U. S. (2019). Evaluation of waste minimization in electroplating for cost-saving. *AIP Conference Proceedings*, *2202*(December), 020072. doi: 10.1063/1.5141685
- Rabiei, M., Palevicius, A., Monshi, A., Nasiri, S., Vilkauskas, A., & Janusas, G. (2020). Comparing methods for calculating nano crystal size of natural hydroxyapatite using X-ray diffraction. *Nanomaterials*, *10*(9), 1–21. doi: 10.3390/nano10091627
- Reis, M. T. A., & Ismael, M. R. C. (2019). Electroplating wastes. *Physical Sciences Reviews*, *3*(6), 1–24. doi: 10.1515/psr-2018-0024
- Ren, Z., & Ernst, F. (2020). Stress–Corrosion Cracking of AISI 316L Stainless Steel in Seawater Environments: Effect of Surface Machining. *Metals*, *10*(10), 1324. doi: 10.3390/met10101324
- Rodriguez, A. A., Tylczak, J. H., Gao, M. C., Jablonski, P. D., Detrois, M., Ziomek-Moroz, M., & Hawk, J. A. (2018). Effect of Molybdenum on the Corrosion Behavior of High-Entropy Alloys CoCrFeNi₂ and CoCrFeNi₂Mo_{0.25} under Sodium Chloride Aqueous Conditions. *Advances in Materials Science and Engineering*, *2018*. doi: 10.1155/2018/3016304
- Rowley-Neale, S. J., Fearn, J. M., Brownson, D. A. C., Smith, G. C., Ji, X., & Banks, C. E. (2016). 2D molybdenum disulphide (2D-MoS₂) modified electrodes explored towards the oxygen reduction reaction. *Nanoscale*, *8*(31), 14767–14777. doi: 10.1039/C6NR04073J
- Sajedi-Moghaddam, A., Rahmanian, E., & Naseri, N. (2020). Inkjet-Printing Technology for Supercapacitor Application: Current State and Perspectives. *ACS Applied Materials & Interfaces*, *12*(31), 34487–34504. doi: 10.1021/acsami.0c07689
- Salman, O. O., Brenne, F., Niendorf, T., Eckert, J., Prashanth, K. G., He, T., & Scudino, S. (2019). Impact of the scanning strategy on the mechanical behavior of 316L steel synthesized by selective laser melting. *Journal of Manufacturing Processes*, *45*(July), 255–261. doi: 10.1016/j.jmapro.2019.07.010
- Samadi, M., Sarikhani, N., Zirak, M., Zhang, H., Zhang, H.-L., & Moshfegh, A. Z. (2018). Group 6 transition metal dichalcogenide nanomaterials: synthesis, applications and future perspectives. *Nanoscale Horizons*, *3*(2), 90–204. doi: 10.1039/C7NH00137A

- Saunders, M. (2018). The Magazine For The Metal Additive Manufacturing Industry. *Inovar Commun. Ltd., Vol. 04, N, Vol. 4*, 129-131. Retrieved from www.metal-am.com
- Schofield, K. (2005). New method to minimize high-temperature corrosion resulting from alkali sulfate and chloride deposition in combustion systems. II. Molybdenum salts. *Energy and Fuels*, *19*(5), 1898–1905. doi: 10.1021/ef050069y
- Schulman, D. S., May-Rawding, D., Zhang, F., Buzzell, D., Alem, N., & Das, S. (2018). Superior Electro-Oxidation and Corrosion Resistance of Monolayer Transition Metal Disulfides. *ACS Applied Materials and Interfaces*, *10*(4), 4285–4294. doi: 10.1021/acsami.7b17660
- Scotti, G., Kanninen, P., Matilainen, V. P., Salminen, A., & Kallio, T. (2016). Stainless steel micro fuel cells with enclosed channels by laser additive manufacturing. *Energy*, *106*, 475–481. doi: 10.1016/j.energy.2016.03.086
- Scudino, S., Unterdörfer, C., Prashanth, K. G., Attar, H., Ellendt, N., Uhlenwinkel, V., & Eckert, J. (2015). Additive manufacturing of Cu-10Sn bronze. *Materials Letters*, *156*, 202–204. doi: 10.1016/j.matlet.2015.05.076
- Seo, J. W. T., Zhu, J., Sangwan, V. K., Secor, E. B., Wallace, S. G., & Hersam, M. C. (2019). Fully Inkjet-Printed, Mechanically Flexible MoS₂ Nanosheet Photodetectors. *ACS Applied Materials and Interfaces*, *11*(6), 5675–5681. doi: 10.1021/acsami.8b19817
- Shao, Y., El-Kady, M. F., Sun, J., Li, Y., Zhang, Q., Zhu, M., Wang, H., Dunn, B., & Kaner, R. B. (2018). Design and Mechanisms of Asymmetric Supercapacitors. *Chemical Reviews*, *118*(18), 9233–9280. doi: 10.1021/acs.chemrev.8b00252
- Shao, Y., Fu, J. H., Cao, Z., Song, K., Sun, R., Wan, Y., Shamim, A., Cavallo, L., Han, Y., Kaner, R. B., & Tung, V. C. (2020). 3D Crumpled Ultrathin 1T MoS₂ for Inkjet Printing of Mg-Ion Asymmetric Micro-supercapacitors. *ACS Nano*, *14*(6), 7308–7318. doi: 10.1021/acs.nano.0c02585
- Shiomi, M., Osakada, K., Nakamura, K., Yamashita, T., & Abe, F. (2004). Residual stress within metallic model made by selective laser melting process. *CIRP Annals - Manufacturing Technology*, *53*(1), 195–198. doi: 10.1016/S0007-8506(07)60677-5
- Simonelli, M., Tse, Y. Y., & Tuck, C. (2014). *The formation of a 1 b microstructure in as-fabricated selective laser melting of Ti – 6Al – 4V*. doi: 10.1557/jmr.2014.166
- Sollami Delekt, S., Laurila, M.-M., Mäntysalo, M., & Li, J. (2020). Drying-Mediated Self-Assembly of Graphene for Inkjet Printing of High-Rate Micro-supercapacitors. *Nano-Micro Letters*, *12*(1), 40. doi: 10.1007/s40820-020-0368-8
- Sridhar, N., Thodla, R., Gui, F., Cao, L., & Anderko, A. (2018). *Corrosion-resistant alloy testing and selection for oil and gas production*. 2782. doi: 10.1080/1478422X.2017.1384609
- Stephenson, T., Li, Z., Olsen, B., & Mitlin, D. (2014). Lithium-ion battery applications of molybdenum disulfide (MoS₂) nanocomposites. *Energy Environ. Sci.*, *7*(1), 209–231. doi: 10.1039/C3EE42591F
- Tian, X., Jin, J., Yuan, S., Chua, C. K., Tor, S. B., & Zhou, K. (2017). Emerging 3D-Printed Electrochemical Energy Storage Devices: A Critical Review. *Advanced Energy Materials*, *7*(17), 1–17. doi: 10.1002/aenm.201700127
- Tian, X., & Zhou, K. (2020). 3D printing of cellular materials for advanced electrochemical energy storage and conversion. *Nanoscale*, *12*(14), 7416–7432. doi: 10.1039/d0nr00291g
- Tran, X. T., Poorahong, S., & Siaj, M. (2017). One-pot hydrothermal synthesis and selective etching method of a porous MoSe₂ sand rose-like structure for electrocatalytic hydrogen evolution reaction. *RSC Advances*, *7*(82), 52345–52351. doi: 10.1039/c7ra10001a

- United Nations. (2015). *THE 17 GOALS - Sustainable Development Goals*. United Nations. Retrieved from <https://sdgs.un.org/goals>
- Wang, B., Yang, X.-H., Zeng, D.-J., Yang, J.-F., Ishizaki, K., & Niihara, K. (2014). Effect of glassy bonding materials on the properties of LAS/SiC porous ceramics with near zero thermal expansion. *Journal of the European Ceramic Society*, *34*(1), 91–95. doi: 10.1016/j.jeurceramsoc.2013.08.008
- Wang, D., Yu, C., Ma, J., Liu, W., & Shen, Z. (2017). Densification and crack suppression in selective laser melting of pure molybdenum. *Materials & Design*, *129*(April), 44–52. doi: 10.1016/j.matdes.2017.04.094
- Wang, G., Ouyang, H., Fan, C., Guo, Q., Li, Z., Yan, W., & Li, Z. (2020). The origin of high-density dislocations in additively manufactured metals. *Materials Research Letters*, *8*(8), 283–290. doi: 10.1080/21663831.2020.1751739
- WANG, S., LI, G., DU, G., JIANG, X., FENG, C., GUO, Z., & KIM, S.-J. (2010). Hydrothermal Synthesis of Molybdenum Disulfide for Lithium-Ion Battery Applications. *Chinese Journal of Chemical Engineering*, *18*(6), 910–913. doi: 10.1016/S1004-9541(09)60147-6
- Wang, S., Zhu, J., Shao, Y., Li, W., Wu, Y., Zhang, L., & Hao, X. (2017). Three-Dimensional MoS₂@CNT/RGO Network Composites for High-Performance Flexible Supercapacitors. *Chemistry - A European Journal*, *23*(14), 3438–3446. doi: 10.1002/chem.201605465
- Wang, Teng, Li, L., Tian, X., Jin, H., Tang, K., Hou, S., Zhou, H., & Yu, X. (2019). 3D-printed interdigitated graphene framework as superior support of metal oxide nanostructures for remarkable micro-pseudocapacitors. *Electrochimica Acta*, *319*, 245–252. doi: 10.1016/j.electacta.2019.06.163
- Wang, Tianyi, Chen, S., Pang, H., Xue, H., & Yu, Y. (2017). MoS₂-Based Nanocomposites for Electrochemical Energy Storage. *Advanced Science*, *4*(2). doi: 10.1002/advs.201600289
- Wang, X., Li, T., Ma, H., Zhai, D., Jiang, C., Chang, J., Wang, J., & Wu, C. (2017). A 3D-printed scaffold with MoS₂ nanosheets for tumor therapy and tissue regeneration. *NPG Asia Materials*, *9*(4). doi: 10.1038/am.2017.47
- Wang, Y., Gao, L., Fan, S., Zhou, W., Li, X., & Lu, Y. (2019). 3D printed micro-mechanical device (MMD) for in situ tensile testing of micro/nanowires. *Extreme Mechanics Letters*, *33*, 100575. doi: 10.1016/j.eml.2019.100575
- Wang, Z., Xie, M., Li, Y., Zhang, W., Yang, C., Kollo, L., Eckert, J., & Prashanth, K. G. (2020). Premature failure of an additively manufactured material. *NPG Asia Materials*, *12*(1). doi: 10.1038/s41427-020-0212-0
- Weber, T., Muijsers, J. C., & Niemantsverdriet, J. W. (1995). Structure of amorphous MoS₃. *Journal of Physical Chemistry*, *99*(22), 9194–9200. doi: 10.1021/j100022a037
- Winchester, A., Ghosh, S., Feng, S., Elias, A. L., Mallouk, T., Terrones, M., & Talapatra, S. (2014). Electrochemical characterization of liquid phase exfoliated two-dimensional layers of molybdenum disulfide. *ACS Applied Materials and Interfaces*, *6*(3), 2125–2130. doi: 10.1021/am4051316
- Winter, M., & Brodd, R. J. (2004). What are batteries, fuel cells, and supercapacitors? *Chemical Reviews*, *104*(10), 4245–4269. doi: 10.1021/cr020730k
- Wu, M. H., Lee, J. T., Chung, Y. J., Srinivaas, M., & Wu, J. M. (2017). Ultrahigh efficient degradation activity of single- and few-layered MoSe₂ nanoflowers in dark by piezo-catalyst effect. *Nano Energy*, *40*(August), 369–375. doi: 10.1016/j.nanoen.2017.08.042

- Wu, Y., Chen, Y. X., Yan, J., Yang, S., Dong, P., & Soman, P. (2015). Fabrication of conductive polyaniline hydrogel using porogen leaching and projection microstereolithography. *Journal of Materials Chemistry B*, 3(26), 5352–5360. doi: 10.1039/C5TB00629E
- Xi, L. X., Zhang, H., Wang, P., Li, H. C., Prashanth, K. G., Lin, K. J., Kaban, I., & Gu, D. D. (2018). Comparative investigation of microstructure, mechanical properties and strengthening mechanisms of Al-12Si/TiB₂ fabricated by selective laser melting and hot pressing. *Ceramics International*, 44(15), 17635–17642. doi: 10.1016/j.ceramint.2018.06.225
- Xu, R. C., Xia, X. H., Wang, X. L., Xia, Y., & Tu, J. P. (2017). Tailored Li₂S-P₂S₅ glass-ceramic electrolyte by MoS₂ doping, possessing high ionic conductivity for all-solid-state lithium-sulfur batteries. *Journal of Materials Chemistry A*, 5(6), 2829–2834. doi: 10.1039/c6ta10142a
- Yadroitsev, I., Krakhmalev, P., Yadroitsava, I., Johansson, S., & Smurov, I. (2013). Energy input effect on morphology and microstructure of selective laser melting single track from metallic powder. *Journal of Materials Processing Technology*, 213(4), 606–613. doi: 10.1016/j.jmatprotec.2012.11.014
- Yang, Y., Fei, H., Ruan, G., Xiang, C., & Tour, J. M. (2014). Edge-oriented MoS₂ nanoporous films as flexible electrodes for hydrogen evolution reactions and supercapacitor devices. *Advanced Materials*, 26(48), 8163–8168. doi: 10.1002/adma.201402847
- Yao, Y., Lin, Z., Li, Z., Song, X., Moon, K. S., & Wong, C. P. (2012). Large-scale production of two-dimensional nanosheets. *Journal of Materials Chemistry*, 22(27), 13494–13499. doi: 10.1039/c2jm30587a
- Yap, C. Y., Chua, C. K., Dong, Z. L., Liu, Z. H., Zhang, D. Q., Loh, L. E., & Sing, S. L. (2015). Review of selective laser melting: Materials and applications. *Applied Physics Reviews*, 2(4). doi: 10.1063/1.4935926
- Yasa, E., & Kruth, J. (2012). Procedia Engineering Microstructural investigation of Selective Laser Melting 316L stainless steel parts exposed to laser re-melting. *Procedia Engineering*, 19, 389–395. doi: 10.1016/j.proeng.2011.11.130
- Yelgel, C., Yelgel, C., & Gülseren, O. (2017). Structural and electronic properties of MoS₂, WS₂, and WS₂/MoS₂ heterostructures encapsulated with hexagonal boron nitride monolayers. *Journal of Applied Physics*, 122(6). doi: 10.1063/1.4998522
- You, Y.-W., Kong, X.-S., Wu, X.-B., Xu, Y.-C., Fang, Q. F., Chen, J. L., Luo, G.-N., Liu, C. S., Pan, B. C., & Wang, Z. (2013). Dissolving, trapping and detrapping mechanisms of hydrogen in bcc and fcc transition metals. *AIP Advances*, 3(1), 012118. doi: 10.1063/1.4789547
- Yu, Z., Song, J., Wang, D., & Wang, D. (2017). Advanced anode for sodium-ion battery with promising long cycling stability achieved by tuning phosphorus-carbon nanostructures. *Nano Energy*, 40(August), 550–558. doi: 10.1016/j.nanoen.2017.08.019
- Yuan, W., Chen, H., Cheng, T., & Wei, Q. (2020). Effects of laser scanning speeds on different states of the molten pool during selective laser melting: Simulation and experiment. *Materials and Design*, 189, 108542. doi: 10.1016/j.matdes.2020.108542
- Zhang, F., Wei, M., Viswanathan, V. V., Swart, B., Shao, Y., Wu, G., & Zhou, C. (2017). 3D printing technologies for electrochemical energy storage. *Nano Energy*, 40(May), 418–431. doi: 10.1016/j.nanoen.2017.08.037

- Zhang, H., Yu, X., & Braun, P. V. (2011). Three-dimensional bicontinuous ultrafast-charge and-discharge bulk battery electrodes. *Nature Nanotechnology*, 6(5), 277–281. doi: 10.1038/nnano.2011.38
- Zhang, L.-F., Ou, G., Gu, L., Peng, Z.-J., Wang, L.-N., & Wu, H. (2016). A highly active molybdenum multisulfide electrocatalyst for the hydrogen evolution reaction. *RSC Advances*, 6(109), 107158–107162. doi: 10.1039/C6RA18106F
- Zhang, Y., Yan, J., Ren, X., Pang, L., Chen, H., & Liu, S. (Frank). (2017). 2D WS₂ nanosheet supported Pt nanoparticles for enhanced hydrogen evolution reaction. *International Journal of Hydrogen Energy*, 42(8), 5472–5477. doi: 10.1016/j.ijhydene.2016.08.225
- Zhao, Chao, Wang, Z., Li, D., Kollo, L., Luo, Z., Zhang, W., & Prashanth, K. G. (2020). Cu-Ni-Sn alloy fabricated by melt spinning and selective laser melting: A comparative study on the microstructure and formation kinetics. *Journal of Materials Research and Technology*, 9(6), 13097–13105. doi: 10.1016/j.jmrt.2020.09.047
- Zhao, Chen, Wang, C., Gorkin, R., Beirne, S., Shu, K., & Wallace, G. G. (2014). Three dimensional (3D) printed electrodes for interdigitated supercapacitors. *Electrochemistry Communications*, 41, 20–23. doi: 10.1016/j.elecom.2014.01.013
- Zhao, Y., Luo, X., Li, H., Zhang, J., Araujo, P. T., Gan, C. K., Wu, J., Zhang, H., Quek, S. Y., Dresselhaus, M. S., & Xiong, Q. (2013). Interlayer breathing and shear modes in few-trilayer MoS₂ and WSe₂. *Nano Letters*, 13(3), 1007–1015. doi: 10.1021/nl304169w
- Zheng, B., Topping, T., Smugeresky, J. E., Zhou, Y., Biswas, A., Baker, D., & Lavernia, E. J. (2010). The influence of Ni-coated TiC on laser-deposited IN625 metal matrix composites. *Metallurgical and Materials Transactions A: Physical Metallurgy and Materials Science*, 41(3), 568–573. doi: 10.1007/s11661-009-0126-5
- Zheng, X., Zhu, Y., Sun, Y., & Jiao, Q. (2018). Hydrothermal synthesis of MoS₂ with different morphology and its performance in thermal battery. *Journal of Power Sources*, 395(April), 318–327. doi: 10.1016/j.jpowsour.2018.05.092
- Zhong, M., & Liu, W. (2010). Laser surface cladding: The state of the art and challenges. *Proceedings of the Institution of Mechanical Engineers, Part C: Journal of Mechanical Engineering Science*, 224(5), 1041–1060. doi: 10.1243/09544062JMES1782
- Zhou, J., Fang, G., Pan, A., & Liang, S. (2016). Oxygen-Incorporated MoS₂ Nanosheets with Expanded Interlayers for Hydrogen Evolution Reaction and Pseudocapacitor Applications. *ACS Applied Materials and Interfaces*, 8(49), 33681–33689. doi: 10.1021/acsami.6b11811
- Zhou, Xiaoping, Xu, B., Lin, Z., Shu, D., & Ma, L. (2014). Hydrothermal synthesis of flower-like MoS₂ nanospheres for electrochemical supercapacitors. *Journal of Nanoscience and Nanotechnology*, 14(9), 7250–7254. doi: 10.1166/jnn.2014.8929
- Zhou, Xiaowen, Zhao, W., Pan, J., Fang, Y., Wang, F., & Huang, F. (2018). Urchin-like MoS₂ prepared via a molten salt-assisted method for efficient hydrogen evolution. *Chemical Communications*, 54(90), 12714–12717. doi: 10.1039/C8CC06714G
- Zhou, Xin, Liu, X., Zhang, D., Shen, Z., & Liu, W. (2015). Balling phenomena in selective laser melted tungsten. *Journal of Materials Processing Technology*, 222, 33–42. doi: 10.1016/j.jmatprotec.2015.02.032

- Zhou, Xin, Wang, D., Liu, X., Zhang, D. D., Qu, S., Ma, J., London, G., Shen, Z., & Liu, W. (2015). 3D-imaging of selective laser melting defects in a Co-Cr-Mo alloy by synchrotron radiation micro-CT. *Acta Materialia*, *98*, 1–16. doi: 10.1016/j.actamat.2015.07.014
- Zhou, Z., Lin, Y., Zhang, P., Ashalley, E., Shafa, M., Li, H., Wu, J., & Wang, Z. (2014). Hydrothermal fabrication of porous MoS₂ and its visible light photocatalytic properties. *Materials Letters*, *131*, 122–124. doi: 10.1016/j.matlet.2014.05.162
- Zhu, C., Liu, T., Qian, F., Chen, W., Chandrasekaran, S., Yao, B., Song, Y., Duoss, E. B., Kuntz, J. D., Spadaccini, C. M., Worsley, M. A., & Li, Y. (2017). 3D printed functional nanomaterials for electrochemical energy storage. *Nano Today*, *15*, 107–120. doi: 10.1016/j.nantod.2017.06.007

Acknowledgments

First and foremost, infinite praises and millions of thanks to the Almighty for the comprehension, awareness, and cognitions throughout every second of the valuable journey of life.

I am pleased to express my special appreciation to Prof. Prashanth Konda Gokuldoss and Dr. Lauri Kollo at the Tallinn University of Technology, who gave me this opportunity to intensively work on my initiative ideas and enabled me to propose a new field of research to the academic and industrial atmospheres. Dr. Lauri Kollo is worthy of appreciation for his technical consultation, facilitating the processes, and kindly easing this research in different stages. It was a great honor and privilege to research under their guidance.

Besides my supervisors, it is worthwhile to express my deep and sincere gratitude to my co-supervisor, Prof. Inger Charlotta Odnevall at the KTH Royal Institute of Technology, for giving me such a golden opportunity to extensively develop my research in her labs and for providing me with invaluable support despite her tightly busy schedule. Her dynamism, vision, honesty, sincerity, respectfulness, and motivation have deeply inspired me to endeavor tirelessly, think optimistically, and behave responsibly to make the world a better place for life.

I would also like to warmly appreciate Dr. Sayed Habib Kazemi, the Institute for Advanced Studies in Basic Sciences, for all his friendship, empathy, genuine support, and great sense of punctiliousness throughout this research work. He is worthy of warm appreciation due to his 24/7 responsibility for technical consultation during this research.

All my family members have always been my truly supporting pillars. Besides my parents and brother who have always encouraged and inspired me compassionately, I am extremely grateful to my wife, Marzieh Mahtabi, for her love, understanding, continuous support, and encouraging me for my shiny and glorious future. I want to dedicate my thesis to my wife because of her non-stop support and round-the-clock companionship throughout these four years of my Ph.D. study and research.

I am extending my gratitude to TalTech and all authorities, Prof. Maarja Kruusmaa, Prof. Kristo Karjust, Prof. Fjodor Sergejev, Prof. Jakob Kübarsepp, Prof. Maarja Grossberg-Kuusk, Prof. Irina Hissainova, Prof. Ilona Oja Acik, Ms. Anu Johannes, and Ms. Kaire Kaljuvee. My Ph.D. studies and research could have never been accomplished without their trust. Also, I am grateful to Dr. Maksim Antonov and Dr. Rocio Estefania Rojas Hernandez for their meticulous review and valuable comments on my dissertation.

My heartfelt thanks go to my colleagues (Dr. Olga Volobujeva, Dr. Mart Viljus, Dr. Gunilla Herting, Dr. Xuying Wang, Dr. Tingru Chang, Dr. Aliaksandr Kohort, Dr. Vitali Sõritski, Mr. Rainer Traksmäa, Mr. Hans Vallner, Ms. Laivi Väljaots, Ms. Sirje Roosme, and Ms. Ruth Kulbas) and all my dear friends for their friendship and kind scientific help.

Last, but not least, I want to thank myself for believing in myself as well as for my creativity, self-motivation, perseverance, patience, courage, accountability, honesty, and truthfulness. Soon, there will be a new world of shining hopes to flourish the dreams.

This research work was funded by European Regional Development Fund (Grant: ASTRA6-6), Tallinn University of Technology (Grant: MOBERC15), the Estonian Education and Youth Board and the Estonian Government (Contract No.: 5.10-6.1/21/23-4 and 5.10-6.1/21/327-2).

Abstract

Additive Manufacturing of Mo-Mo_(x)S_(x+1) Functional Structures: Engineering and Electrochemical Applications

MoS₂-based/-incorporated structures are well-known candidates for various engineering and electrochemical applications having been processed by a wide range of conventional- and AM techniques. As an initiative and innovative research field, selective laser melting (SLM), as a novel approach, has been employed for the first time to simultaneously thin the bulk MoS₂ down and tune its crystallographic structure to a 2H/1T phase. Having been elaborated in this dissertation, the SLM technique is able to *in-situ* distribute Mo₂S₃ nanoparticles in Mo_(x)S_(x+1)-incorporated electroactive nanocomposites to boost the electrochemical performance of the generated composite for energy conversion/storage applications. As an outstanding achievement of the research activities, substantial enhancement of areal power density, areal energy density, rate capacitance, and charge-discharge stability was obtained through direct SLM processing of 3D-printed Mo/MoS₂/Mo₂S₃ nanocomposite structures (SLM-Mo/Mo_(x)S_(x+1)) from commercial raw materials without any complex or costly pre-processing or post-processing stages.

Regarding the distinctive characteristics of MoS₂ and unique properties of Mo, additions of MoS₂ to refractory hard Mo metal can significantly facilitate the printability of different Mo-MoS₂ mixture feedstock and remarkably mitigate the crack formation and defects in the microstructure of the micro-lattice Mo/MoS₂/Mo₂S₃ composite structures processed by SLM technique. Dissociated MoS₂ in the melt pool and a more complete reaction and phase transformation from MoS₂ to Mo₂S₃ can result in fine interlocked equiaxial grains. The refinement of the microstructure and alleviation of lattice strains, along with constant maintenance of the texture coefficient (T.C.), resulted in nearly crack-free micro-lattice structures. These structures hindered stress-corrosion cracking (SCC) and surface oxidation corrosion of the micro-lattice Mo/MoS₂/Mo₂S₃ composite structures upon exposure in 0.1 M NaCl (pH = 5.4) and 0.1 M Na₂SO₄ (pH = 5.4).

These preliminary results propose an in-depth investigation of laser-assisted processing of 2D materials for fabrication of a wide range of sustainable and functional 3D-printed components of improved corrosion resistance and high-temperature durability, particularly for solid-state energy conversion/storage systems, novel sodium-ion energy storage applications, power semiconductor heat sinks, offshore-, aerospace-, defense-, and electronic applications.

Lühikokkuvõte

Lisandustehnoloogia teel valmistatud Mo-Mo_(x)S_(x+1) funktsionaalsed struktuurid inseneri- ja elektrokeemilistele rakendustele

MoS₂-põhised/integreeritud struktuurid on tuntud kandidaadid erinevatele elektrokeemilistele ja inseneritehnilistele kasutusvaldkondadele, mida on valmistatud paljude tavapärase ja ka lisandustehnikatega (AM). Uuendusliku uurimisvaldkonnana kasutatakse käesolevas töös esmakordselt selektiivset lasersulatamist (SLM), et üheaegselt kihistada MoS₂ ja häälestada selle kristallograafilist struktuuri 2H/1T faasile. Pärast käesolevas väitekirjas väljatöötamist on SLM-tehnika abil võimalik in situ dispergeerida Mo₂S₃ nanoosakesi Mo_(x)S_(x+1)-ga integreeritud elektroaktiivsetesse nanokomposiitidesse, et tõsta genereeritud komposiidi elektrokeemilist jõudlust energia muundamise/salvestamise rakendustes. Teadustegevuse silmapaistva saavutusena saavutati 3D-prinditud Mo/MoS₂/Mo₂S₃ nanokomposiitstruktuuride (SLM-Mo/Mo_(x)S_(x+1)) üheaastmelise SLM-töötusega materjalide võimsustiheduse, pindala energiatiheduse, mahtuvuse ja laengu-tühjenemise stabiilsuse oluline paranemine.) kaubanduslikust toorainest ilma keerukate või kulukate eel- või järeltöötusetappideta.

Seoses MoS₂ iseloomulike omaduste ja Mo ainulaadsete omadustega võib MoS₂ lisamine kõrgtemperatuursele ja kõvale Mo metallile oluliselt hõlbustada erinevate Mo-MoS₂ segude prinditavust ja märkimisväärselt leevendada pragude teket ja defekte SLM-tehnikaga töödeldud Mo/MoS₂/Mo₂S₃ mikrovõre komposiitstruktuuride mikrostruktuuris. Sulavannis dissotsieerunud MoS₂ ja reaktsioon ning faasimuutus MoS₂-st Mo₂S₃-ks võivad põhjustada peeneid omavahel haakuvaid ekviaksiaalseid terasid. Mikrostruktuuri peenenemine ja võrepingete leevenemine koos tekstuuri koefitsiendi (TC) pideva säilitamisega andsid tulemuseks peaaegu pragudeta mikrovõre struktuurid. Need struktuurid olid vastupidavad 0.1 M NaCl (pH = 5.4) ja 0.1 M Na₂SO₄ (pH = 5.4) mikrovõrestiku Mo/MoS₂/Mo₂S₃ komposiitstruktuuride pinge-korrosioonipragunemisele (SCC) ja pinna oksüdatsioonikorrosioonile.

Need esialgsed tulemused annavad aluse põhjalikule uurimisele 2D-materjalide laseri abil töötlemise kohta, et toota mitmesuguseid jätkusuutlikke ja funktsionaalseid 3D-prinditud komponente, millel on parem korrosioonikindlus ja vastupidavus kõrgele temperatuurile, eriti energia muundamiseks/salvestamiseks, uudseteks naatriumioonide energiasalvestusrakendusteks, pooljuhtide baasil jahutusradiaatoriteks ning, avamere-, kosmose-, kaitse- ja elektroonikarakendusteks.

Appendix 1

Publication I

N. Alinejadian, P. Wang, L. Kollo, K.G. Prashanth, Selective Laser Melting of Commercially Pure Molybdenum by Laser Rescanning, 3D Print. Addit. Manuf. 00 (2022) 1–7.
<https://doi.org/10.1089/3dp.2021.0265>.



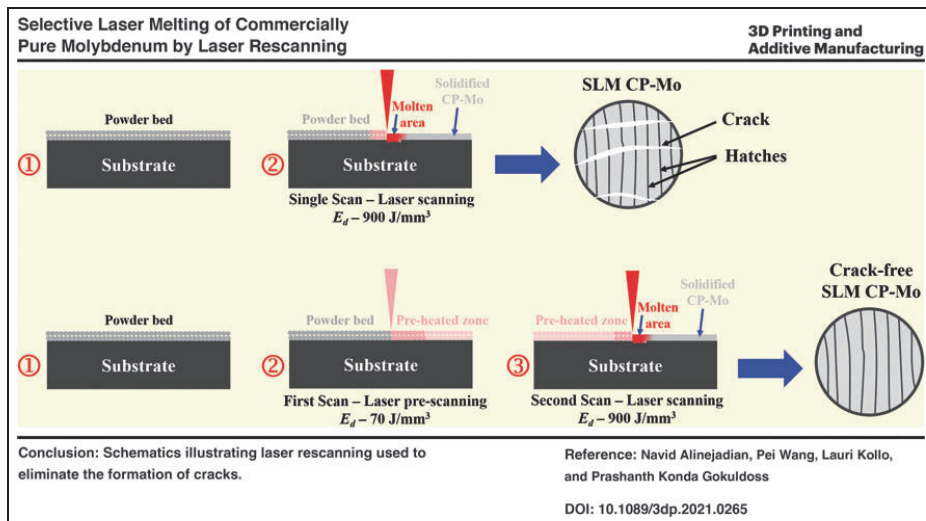
Selective Laser Melting of Commercially Pure Molybdenum by Laser Rescanning

Navid Alinejadian,^{1,j} Pei Wang,² Lauri Kollo,¹ and Konda Gokuldoss Prashanth^{1,3,4,ii}

Abstract

Commercially pure (cp) molybdenum (Mo) is one of the high-temperature materials of immense potential. It has a body-centered cubic (bcc) structure so it is hard to fabricate using nonequilibrium processes such as the selective laser melting (SLM) without the formation of cracks due to its inherent brittleness. This study deals with the fabrication of dense and near crack-free cp-Mo samples produced by the SLM. The laser scan strategy is adjusted from a single scan to a double scan to reduce the solidification cracks. Samples produced with a laser double scan strategy show a density of $\sim 99\%$ with a hardness of ~ 222 HV.

Keywords: additive manufacturing, selective laser melting, molybdenum, porosity, properties



Color images are available online.

¹Department of Mechanical and Industrial Engineering, Tallinn University of Technology (TalTech), Tallinn, Estonia.

²Additive Manufacturing Institute, Shenzhen University, Shenzhen, P.R. China.

³Erich Schmid Institute of Materials Science, Austrian Academy of Sciences, Leoben, Austria.

⁴CBCMT, School of Mechanical Engineering, Vellore Institute of Technology, Vellore, India.

^jORCID ID (<https://orcid.org/0000-0003-2316-7869>).

ⁱⁱORCID ID (<https://orcid.org/0000-0001-5644-2527>).

Introduction

SELECTIVE LASER MELTING (SLM) is a powder bed fusion process that uses the laser as a high energy source to melt and fuse the powder selectively, layer by layer, defined by computer-aided design data.^{1–3} Moreover, this is one of the established additive manufacturing processes that can fabricate most of the metals/alloys without significant difficulties.^{4–8} Still, the processing of high-temperature materials and brittle materials is quite a challenge due to the formation of solidification cracks.^{9,10} When a brittle material solidifies from its molten state, due to extreme cooling rates observed during the SLM process, the solidifying material cannot accommodate excessive stress.

When the internal stresses (tensile stress) in the material exceed the ductility of the alloy, it will lead to cracking in the material.^{11–13} In general, brittle material does not show appreciable ductility and cannot accommodate excessive internal strain and hence results in cracking during rapid solidification.^{11–13} Several strategies have been adopted to eliminate solidification cracking during the SLM process. Martin *et al.*¹⁰ used the conventional metallurgical approach of inoculation to suppress cracks in 7075 alloy, where the crystal structure of the material and the nanoinoculant were held the same. Similarly, alloy design was effectively used as a strategy to suppress the cracking tendency in Al7070 by Montero Sistiaga *et al.*¹⁴

Substrate plate heating was used as another strategy for the suppression of cracks in high-strength Al-based alloys.^{15,16} Solid solution strengthening was used as a strategy to eliminate cracking in Ni-based superalloys.¹⁷ Even though there exist several strategies, there is no universal strategy adopted for eliminating the cracking tendency in SLM-processed brittle/ceramic materials.¹⁸ Molybdenum (Mo) is one of the high-temperature refractory materials with a body-centered cubic (bcc) structure.

In general, materials with a bcc crystal structure display inherent brittleness compared with materials with a face-centered cubic crystal structure. In addition, Mo is susceptible to cracks because its ductile-to-brittle transition temperature is rather high (375 K). Hence, the shrinkage associated with solidification leads to cracking in the material. In addition, due to the high melting point, it is not easy to fabricate Mo and Mo-based alloys by a conventional casting process. Joining these materials is difficult since they are not weldable. It has been considered that the non-weldable alloys are not suitable for the SLM process, since they may lead to solidification cracking.^{19–22}

Faidel *et al.* initially proposed the fabrication of Mo by the SLM process, where a theoretical density of 82.5% was achieved.²³ They have varied the process parameters largely (including layer thickness, the influence of overlap/hatch distance, and laser scan speed). The effective volumetric energy density was varied between 200 and 1100 J/mm³. Nevertheless, a maximum relative density of only 92.5% was achieved with cracks in the SLM-fabricated Mo samples.

Wang *et al.* during SLM processing of Mo have observed two types of cracks: (1) longitudinal cracks—parallel to the molten tracks and (2) transverse cracks—perpendicular to the surface ripples.²⁴ Moreover, they have employed scan rotation (67°) or hatch rotation between two layers to effectively eliminate the presence of longitudinal cracks. However, the

transverse cracks still exist. The presence of transverse cracks was further eliminated by adopting properly designed support structures. A relative density of ~99.1% was observed in these samples.

Kaserer *et al.* later demonstrated both grain refinement and suppression of cracks in the SLM-processed Mo by the addition of 0.45 wt.% C.²⁵ They showed that addition of a small amount of carbon leads to the formation of a dual microstructure (cellular microstructure with α -Mo and surrounding Mo₂C network). Relative densities >99% were achieved with complete crack suppression observed. This may be attributed to the addition of carbon, which transforms the planar solidification mode to cellular solidification mode. At the same time, it refines the microstructure by acting as nucleation sites, thereby avoiding the possibility of epitaxial growth.

Only interlocked grains are observed.²⁵ Similarly, polymer-coated Mo powders were used for the SLS process to avoid cracking and excess deformation.^{26,27} In contrast, Higashi and Ozaki performed experiments by changing the process parameters such as laser power, laser scan speed, hatch distance, and layer thickness with the aim of evaluating the defect formation and crystallographic texture generation.²⁸ A nearly dense sample (99.2% theoretical density) was observed with the presence of pores (both keyhole and/or lack of fusion).

A combination of higher laser power, lower scan speed, and smaller layer thickness leads to highly dense samples. The laser scan speed influences the crystallographic texture in the material where <001>, <110>, and <111> fiber textures were obtained as a function of process parameters.²⁸

Laser strategy may involve laser rescanning, double melting, and/or remelting. However, there exist minor differences in these three terminologies.^{7,29,30} Laser rescanning defines that the same surface would be scanned for the second time without any addition of powder. It may or may not include melting during both scans. In contrast, the terminology double scan suggests that the powder bed will be melted during both the first and second scans, respectively, without the addition of any powder between the two melting sequences. Finally, the terminology laser remelting suggests that the first scan may or may not involve melting but the second scan involves melting of the powder bed.

From the published reports it may be clear that, just modifying the scan strategy (scan orientation) may not be an effective alternative³¹ and hence there exists a need to further explore the strategies of fabricating crack-free Mo and Mo-based alloys by SLM. Hence, the present article focuses on the fabrication of commercially pure (cp) Mo by SLM. The cracking tendency of Mo will be tested by changing the scan strategy (laser rescanning) during the SLM process rather than employing just scan rotation. The phases, microstructure, and hardness of the samples will be examined accordingly.

Materials and Methods

Gas atomized (GAP) cp-Mo powder was used to fabricate both bulk samples and structures using a Realizer GmbH SLM-50 device equipped with Nd-YAG laser. The powder characteristics (Fig. 1a, b) show that the GAP cp-Mo is

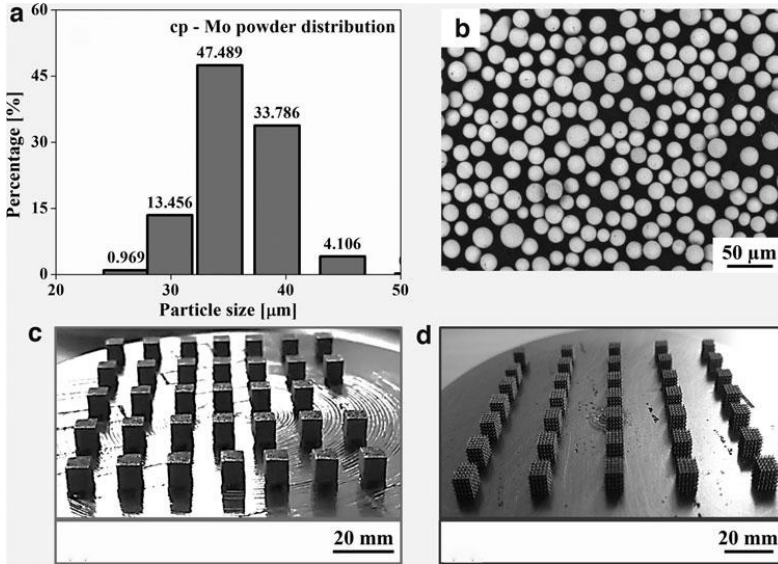


FIG. 1. (a) Plot showing the particle size distribution for the GAP cp-Mo powder and (b) SEM image of the GAP cp-Mo powder. Images showing the SLM Mo cubes ($8 \times 8 \times 8 \text{ mm}^3$) (c) bulk samples and (d) lattice structures. GAP cp-Mo, gas atomized commercially pure molybdenum; SEM, scanning electron microscopy; SLM, selective laser melting.

spherical in shape with an average particle size of $33 \pm 5 \mu\text{m}$. The laser single scanning (LSS) process parameters were varied as a function of energy density ($E_d = P/[v \cdot h \cdot t]$), where P is laser power, v is laser scan speed, h is hatch distance, and t is layer thickness). Two different energy densities 900 J/mm^3 ($p = 85 \text{ W}$, $v = 84 \text{ mm/s}$, $h = 45 \mu\text{m}$, and $t = 25 \mu\text{m}$) and 1300 J/mm^3 ($p = 85 \text{ W}$, $v = 58 \text{ mm/s}$, $h = 45 \mu\text{m}$, and $t = 25 \mu\text{m}$) were employed.³²

In addition, laser double scanning (LDS) was carried out, where two scans on the same layer were performed. The first scan was performed with an E_d of 70 J/mm^3 ($p = 42.5 \text{ W}$, $v = 540 \text{ mm/s}$, $h = 45 \mu\text{m}$, and $t = 25 \mu\text{m}$) and the second scan at an E_d of 900 J/mm^3 ($p = 85 \text{ W}$, $v = 84 \text{ mm/s}$, $h = 45 \mu\text{m}$, and $t = 25 \mu\text{m}$). A 316 L substrate plate was used to fabricate the samples at ambient conditions. The densities of the samples were measured by the Archimedes principle using a Metler Toledo ME240 and also using the volume and weight method.

Room temperature microhardness was measured by using a Buehler Micromet 2001 device with a load of 100 gf for 10 s. The micrographs were taken by a Zeiss Axioskope 40 optical microscope and Hitachi TM-1000 scanning electron microscope. X-ray diffraction (XRD) was obtained using a Rigaku SmartLab SE instrument equipped with Cu K α radiation ($\lambda = 1.5406 \text{ \AA}$). Texture coefficient ($T_c(hkl)$) of the samples was calculated by

$$T_c(hkl) = \frac{I(hkl)/I_o(hkl)}{(1/N) \left[\sum_N I(hkl)/I_o(hkl) \right]}, \quad (1)$$

where $I(hkl)$ is the measured intensity from the XRD pattern, $I_o(hkl)$ is the reference, and n is the number of the

diffraction peaks.³³ The coherent domain size and dislocation density were calculated using the Williamson–Smallman and Williamson–Hall equations.³⁴

Results and Discussion

The SLM-fabricated cp-Mo samples (both bulk and structures fabricated with $E_d = 900 \text{ J/mm}^3$) are shown in Figure 1c and d and their corresponding microscopy images of the bulk samples are shown in Figure 2. Structures were fabricated because generally, they do not result in solidification cracking, unlike the bulk material. Since the walls of these structures are thin and isolated, during solidification there is not enough bulk surface that resists the solidification compressive stresses and hence does not lead to cracking.^{35,36} Hence, these structures can be processed at different process parameters as long as the parameters can completely melt the powder particles.

The process parameters, density, and hardness values of the bulk cp-Mo samples are tabulated in Table 1. It may be observed from Table 1 and Figure 2 that using LSS and decreasing the E_d from 1300 to 900 J/mm^3 have led to an increase of both density and hardness from 97.5% to 98.7% and from 203 HV to 220 HV, respectively. With employing LDS, both porosity and hardness show a marginal increase of $\sim 99\%$ and 222 HV, respectively. However, it has to be noted that LDS can completely eliminate the cracks that were observed using LSS.

From Figure 2a and b using the LSS and decreasing the E_d from 1300 to 900 J/mm^3 , a decrease in both the size and number of pores is observed. In addition, the amount of microcracks present in the microstructure also decreases with

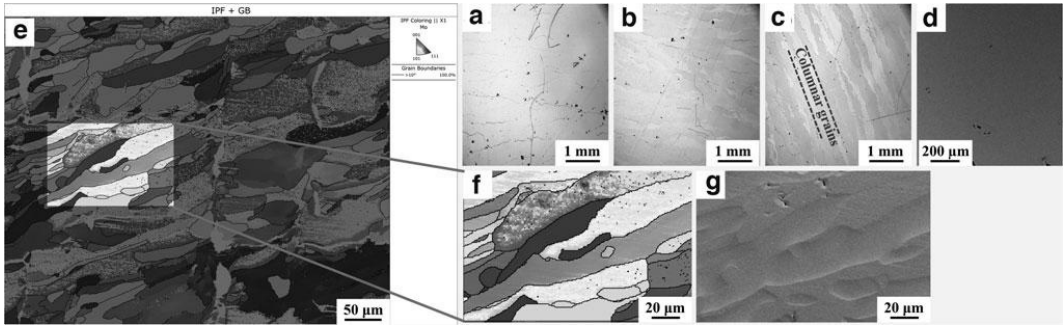


FIG. 2. Optical microscopy images of the bulk SLM samples with a laser single scan and the energy density of (a) 1300 J/mm³ and (b) 900 J/mm³, respectively. (c) Optical image of the SLM sample with a laser double scan and an energy density of 900 J/mm³. (d) SEM image of a laser double scan sample with an energy density of 900 J/mm³. (e) Energy back-scattered dispersion image showing the distribution of grains. (f) Higher magnification energy back-scattered dispersed image showing the orientation of grains and (g) its corresponding high-resolution back-scattered image.

a decrease in the E_d . This is because with higher E_d the size of the melt pool will be bigger with high-temperature gradients, leading to the formation of coarser shrinkage pores.³⁷ The high-temperature gradients also lead to an increased amount of internal stresses leading to solidification cracking in the sample. In contrast, decreasing the E_d decreases the size of the melt pool, resulting in lower surface tension and temperature gradients and hence smaller and lesser pores.³⁸

Using LDS, the powder bed is heated during the first scan, where the laser scan speed is kept very high (increased nearly six times) and the laser power is reduced to half. In addition, during the second scan, the heated powder bed undergoes melting. This could selectively increase the temperature of the powder bed and the stability of the molten pool leading to a decrease in the residual stresses and the temperature gradient.^{39,40} The LDS sample shows a marginal increase in the density and hardness levels compared with the sample fabricated with LSS (Table 1).

Moreover, a higher proportion of columnar grains grows due to 0° scan rotation, the decreased degree of supercooling, and reduced cooling rates observed during LDS (Fig. 2c).^{24,40} However, only some microcracks are observed in the LDS sample. Figure 2e shows the grain size distribution in the laser rescanned sample. There exists the presence of elongated grains and the presence of some fine grains between the two elongated grains, clearly showing the presence of bimodal distribution. A high-resolution grain size distribution image is shown in Figure 2f and the

corresponding high-resolution secondary image is shown in Figure 2g. Figure 2g shows no cracks, but some submicron pores are observed.

In addition, solidification cracking is significantly reduced with the LDS due to the availability of metal to backfill during solidification because of the decreased solidification rates. Both bulk samples and structures show similar porosity levels with LDS. Figure 3a and b shows the XRD pattern of the GAP and SLM prepared samples (bulk and structures). All the samples show the four diffraction peaks corresponding to the bcc-Mo phase. However, the SLM samples (bulk and structure) show a shift in their peaks to lower angles along with peak broadening compared with the GAP.

This may be attributed to the increased cooling rates leading to significant residual stresses in the SLM samples. The SLM-fabricated structure has a higher degree of peak broadening than the SLM bulk sample (Fig. 3b), suggesting the structures may have a high degree in internal stresses and reduced crystallite size (Fig. 3c) due to the differences in the conditions existing during the solidification of the structure and the bulk sample. In addition, the crystallographic texture is also observed in the SLM samples (Fig. 3a, c).

Similar to most of the SLM-fabricated samples,⁴¹ the degree of internal defects such as the dislocation density in the SLM bulk sample and the SLM structures are $\sim 1 \times 10^{14} \text{ m}^{-2}$ and $\sim 5 \times 10^{14} \text{ m}^{-2}$, respectively, which also leads to a broadening of the XRD peaks. After laser remelting, the dislocation density decreases to $\sim 8 \times 10^{13} \text{ m}^{-2}$, which may be attributed to the decreased solidification rates and subsequent decrease in the internal strain.

In this study, a laser rescanning/LDS (with low E_d during the first scan and relatively higher E_d during the second scan) was used to eliminate the cracking tendency of the cp-Mo. Even though a laser double scan is extensively used during SLM processing, laser rescanning (or remelting) has been extensively used to alter the surface topology, microstructure, residual stresses, and/or their properties.^{29,30,42–45} However, in this study inspired by the metallurgical practices carried out during electron beam melting (EBM) and welding processes, the LDS strategy was used. In an EBM process, the powder bed was generally heated to high temperatures by prescanning (a raster scan) before the melting event.⁴⁶

TABLE 1. VARIATION OF THE DENSITY AND HARDNESS OF THE SAMPLES PREPARED WITH DIFFERENT LASER ENERGY DENSITIES

Melting strategy	Energy density (J.mm ⁻²)	Density (%)	Hardness (HV ₁₀₀)
Laser single scanning	1300	97.5 ± 0.7	203 ± 5
Laser single scanning	900	98.7 ± 0.2	220 ± 2
Laser double scanning			
1st scan	70	99.0 ± 0.1	222 ± 2
2nd scan	900		

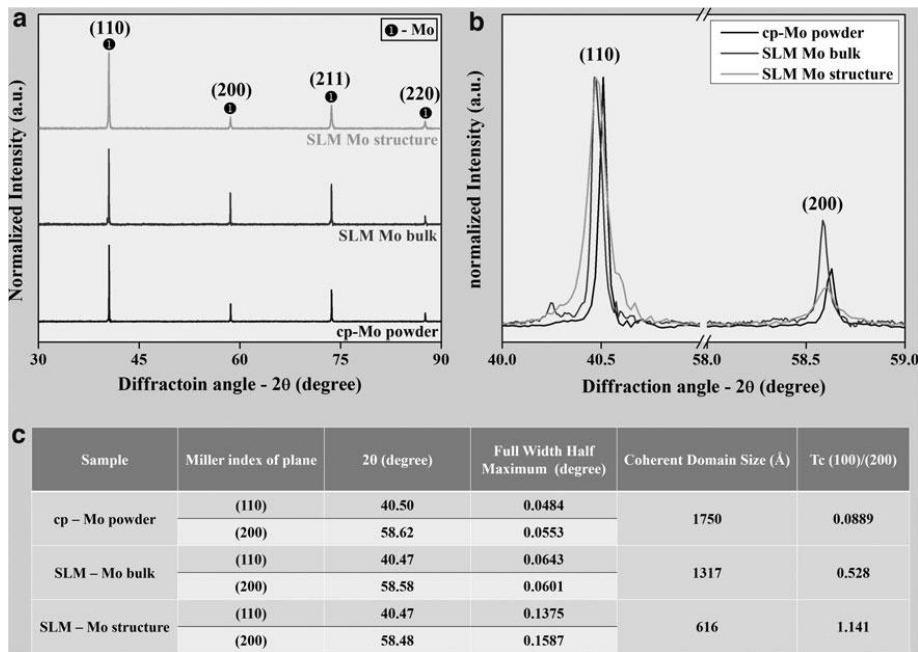


FIG. 3. XRD results of the pure Mo powder and SLM samples (bulk and lattice structure) in the range (a) 2θ between 30° and 90° , (b) 2θ between 40° and 59° , and (c) table furnishing the miller indices, position, full width half maximum, coherent domain size, and texture coefficient of the powder and SLM samples. XRD, X-ray diffraction.

The pre-scanning strategy in the EBM process reduces the cooling rate of the process and avoids cracking in the brittle materials processed by EBM. Similarly, in conventional welding processes, preheating of the substrate is used as a strategy to avoid cracking of the weldment.⁴⁷ With inspiration from the metallurgical practices carried out from EBM and welding processes, a similar analogy was employed in the SLM process to fabricate cp-Mo. Substrate heating during SLM can reduce the cooling rate and the cracking tendency. However, special setups are required to heat the substrate plate and all the commercial SLM devices do not have such an option.

As an alternative, the LDS strategy was effectively employed for the first time to fabricate nearly crack-free cp-Mo. The first scan with low power and fast scan speed effectively heats the powder bed (selectively) and the second scan (with higher energy density) will fuse the powders as the laser power is doubled and the laser scan speed is reduced drastically. The selective heating during the first scan may be compared with the preheating (welding) or pre-scanning/raster scan (EBM process) and can effectively reduce the cooling rate. The results suggest that cp-Mo may be successfully fabricated by SLM with $\sim 99\%$ density by modifying the laser scan strategy. The solidification cracks may be completely eliminated using a suitable laser scan strategy.

Conclusions

In conclusion, dense cp-Mo samples were successfully fabricated by SLM using changes in the laser scan strategy. The following observations were made:

- Using LDS, the solidification rate may be reduced since the initial scan selectively heats the powder bed. Hence, a stable melt pool is achieved, leading to a reduced amount of internal stresses compared with the LSS samples.
- LDS with no scan rotation has led to coarse columnar grains with a higher density.
- The solidification cracks were nearly eliminated using the LDS strategy.

Authors' Contributions

Conceptualization of the study was done by N.A. and K.G.P.; methodology was carried out by N.A. and P.W.; validation was taken care of K.G.P.; formal analysis was carried out by N.A., P.W., L.K., and K.G.P.; investigation was done by N.A., P.W., L.K., and K.G.P.; resources were taken care of P.W. and K.G.P.; original draft preparation of the article was done by N.A. and K.G.P.; reviewing and editing were done by N.A., P.W., L.K., and K.G.P.; funding acquisition was taken care of K.G.P. All authors have read and agreed to the published version of the article.

Data Availability

The present data form a part of the ongoing study and the results may be shared upon reasonable request from the corresponding author(s).

Author Disclosure Statement

No competing financial interests exist.

Funding Information

P.W. gratefully acknowledges the support from the NTUT-SZU Joint Research Program (Grant No. 2019011) and Natural Science Foundation of SZU (Grant No. 2019040). Financial support from the European Regional Development Fund through ASTRA6-6 is acknowledged.

References

- Gokuldoss PK, Kolla S, Eckert J. Additive manufacturing processes: Selective laser melting, electron beam melting and binder jetting-selection guidelines. *Materials (Basel)* 2017;10:1–11.
- DebRoy T, Wei HL, Zuback JS, *et al.* Additive manufacturing of metallic components—Process, structure and properties. *Prog Mater Sci* 2018;92:112–224.
- Zhang S, Ma P, Jia Y, *et al.* Microstructure and mechanical properties of Al-(12-20)Si Bi-material fabricated by selective laser melting. *Materials (Basel)* 2019;12:2126.
- Jung HY, Choi SJ, Prashanth KG, *et al.* Fabrication of Fe-based bulk metallic glass by selective laser melting: A parameter study. *Mater Des* 2015;86:703–708.
- Qian B, Saeidi K, Kvetková L, *et al.* Defects-tolerant Co-Cr-Mo dental alloys prepared by selective laser melting. *Dent Mater* 2015;31:1435–1444.
- Attar H, Prashanth KG, Chaubey AK, *et al.* Comparison of wear properties of commercially pure titanium prepared by selective laser melting and casting processes. *Mater Lett* 2015;142:38–41.
- Prashanth KG, Scudino S, Eckert J. Defining the tensile properties of Al-12Si parts produced by selective laser melting. *Acta Mater* 2017;126:25–35.
- Scudino S, Unterdörfer C, Prashanth KG, *et al.* Additive manufacturing of Cu-10Sn bronze. *Mater Lett* 2015;156:202–204.
- Karg MCH, Ahuja B, Wiesenmayer S, *et al.* Effects of process conditions on the mechanical behavior of aluminium wrought alloy EN AW-2219 (AlCu6Mn) additively manufactured by laser beam melting in powder bed. *Micromachines* 2017;8:1–11.
- Martin JH, Yahata BD, Hundley JM, *et al.* 3D printing of high-strength aluminium alloys. *Nature* 2017;549:365–369.
- Carter LN, Martin C, Withers PJ, *et al.* The influence of the laser scan strategy on grain structure and cracking behaviour in SLM powder-bed fabricated nickel superalloy. *J Alloys Compd* 2014;615:338–347.
- Zhang C, Feng K, Kokawa H, *et al.* Cracking mechanism and mechanical properties of selective laser melted CoCr-FeMnNi high entropy alloy using different scanning strategies. *Mater Sci Eng A* 2020;789:139672.
- Shi X, Wang H, Feng W, *et al.* The crack and pore formation mechanism of Ti-47Al-2Cr-2Nb alloy fabricated by selective laser melting. *Int J Refract Met Hard Mater* 2020;91:105247.
- Montero Sistiaga ML, Mertens R, Vrancken B, *et al.* Changing the alloy composition of Al7075 for better processability by selective laser melting. *J Mater Process Technol* 2016;238:437–445.
- Ma P, Ji P, Jia Y, *et al.* Effect of substrate plate heating on the microstructure and properties of selective laser melted Al-20Si-5Fe-3Cu-1Mg alloy. *Materials (Basel)* 2021;14:330.
- Prashanth KG, Shakur Shahabi H, Attar H, *et al.* Production of high strength Al 85 Nd 8 Ni 5 Co 2 alloy by selective laser melting. *Addit Manuf* 2015;6:1–5.
- Harrison NJ, Todd I, Mumtaz K. Reduction of micro-cracking in nickel superalloys processed by Selective Laser Melting: A fundamental alloy design approach. *Acta Mater* 2015;94:59–68.
- Konda Gokuldoss P. Design of next-generation alloys for additive manufacturing. *Mater Des Process Commun* 2019;1:19–22.
- Prashanth KG, Eckert J. Formation of metastable cellular microstructures in selective laser melted alloys. *J Alloys Compd* 2017;707:27–34.
- Vilaro T, Kottman-Rexerodt V, Thomas M, *et al.* Direct fabrication of a Ti-47Al-2Cr-2Nb alloy by selective laser melting and direct metal deposition processes. *Adv Mater Res* 2010;89–91:586–591.
- Khmyrov RS, Safronov VA, Gusarov A V. Obtaining crack-free WC-Co alloys by selective laser melting. *Phys Proc* 2016;83:874–881.
- Zhang H, Zhu H, Nie X, *et al.* Effect of Zirconium addition on crack, microstructure and mechanical behavior of selective laser melted Al-Cu-Mg alloy. *Scr Mater* 2017;134:6–10.
- Faidel D, Jonas D, Natour G, *et al.* Investigation of the selective laser melting process with molybdenum powder. *Addit Manuf* 2015;8:88–94.
- Wang D, Yu C, Ma J, *et al.* Densification and crack suppression in selective laser melting of pure molybdenum. *Mater Des* 2017;129:44–52.
- Kaserer L, Braun J, Stajkovic J, *et al.* Fully dense and crack free molybdenum manufactured by Selective Laser Melting through alloying with carbon. *Int J Refract Met Hard Mater* 2019;84:105000.
- Liu B, Bai P, Li Y. Post treatment process and selective laser sintering mechanism of polymer-coated mo powder. *Open Mater Sci J* 2011;5:194–198.
- BAI P kang, WANG W feng. Selective laser sintering mechanism of polymer-coated molybdenum powder. *Trans Nonferrous Met Soc China (English Ed)* 2007;17:543–547.
- Higashi M, Ozaki T. Selective laser melting of pure molybdenum: Evolution of defect and crystallographic texture with process parameters. *Mater Des* 2020;191:108588.
- Karimi J, Suryanarayana C, Okulov I, *et al.* Selective laser melting of Ti6Al4V: Effect of laser re-melting. *Mater Sci Eng A* 2020;805:140558.
- Ali H, Ghadbeigi H, Mumtaz K. Effect of scanning strategies on residual stress and mechanical properties of Selective Laser Melted Ti6Al4V. *Mater Sci Eng A* 2018;712:175–187.
- Braun J, Kaserer L, Stajkovic J, *et al.* Molybdenum and tungsten manufactured by selective laser melting: Analysis of defect structure and solidification mechanisms. *Int J Refract Met Hard Mater* 2019;84:104999.
- Prashanth KG, Scudino S, Maity T, *et al.* Is the energy density a reliable parameter for materials synthesis by selective laser melting? *Mater Res Lett* 2017;5:386–390.
- Prashanth KG, Scudino S, Klaus HJ, *et al.* Microstructure and mechanical properties of Al-12Si produced by selective laser melting: Effect of heat treatment. *Mater Sci Eng A* 2014;590:153–160.
- Xi L, Gu D, Guo S, *et al.* Grain refinement in laser manufactured Al-based composites with TiB₂ ceramic. *J Mater Res Technol* 2020;9:2611–2622.
- Prashanth K, Löber L, Klaus HJ, *et al.* Characterization of 316L steel cellular dodecahedron structures produced by selective laser melting. *Technologies* 2016;4:34.

36. Sercombe TB, Xu X, Challis VJ, *et al.* Failure modes in high strength and stiffness to weight scaffolds produced by Selective Laser Melting. *Mater Des* 2015;67:501–508.
37. Liu S, Shin YC. Additive manufacturing of Ti6Al4V alloy: A review. *Mater Des* 2019;164:107552.
38. Gu D, Hagedorn YC, Meiners W, *et al.* Densification behavior, microstructure evolution, and wear performance of selective laser melting processed commercially pure titanium. *Acta Mater* 2012;60:3849–3860.
39. Yadroitsev I, Krakhmalev P, Yadroitsava I, *et al.* Energy input effect on morphology and microstructure of selective laser melting single track from metallic powder. *J Mater Process Technol* 2013;213:606–613.
40. Saunders M. The magazine for the metal additive manufacturing industry. *Inovar Commun Ltd* 2018;4:129–131.
41. Karimi J, Ma P, Jia YD, *et al.* Linear patterning of high entropy alloy by additive manufacturing. *Manuf Lett* 2020;24:9–13.
42. Mugwagwa L, Dimitrov D, Matope S, *et al.* Evaluation of the impact of scanning strategies on residual stresses in selective laser melting. *Int J Adv Manuf Technol* 2019;102:2441–2450.
43. Moussaoui K, Rubio W, Mousseigne M, *et al.* Effects of Selective Laser Melting additive manufacturing parameters of Inconel 718 on porosity, microstructure and mechanical properties. *Mater Sci Eng A* 2018;735:182–190.
44. Liu B, Li BQ, Li Z. Selective laser remelting of an additive layer manufacturing process on AISi10Mg. *Results Phys* 2019;12:982–988.
45. Valente EH, Gundlach C, Christiansen TL, *et al.* Effect of scanning strategy during selective laser melting on surface topography, porosity, and microstructure of additively manufactured Ti-6Al-4V. *Appl Sci* 2019;9:5554.
46. Körner C. Additive manufacturing of metallic components by selective electron beam melting—A review. *Int Mater Rev* 2016;61:361–377.
47. Peng F, Zhang B, Wang H, *et al.* Effect of pre-weld heat treatment on the microstructure and mechanical properties of electron beam welded IN738LC joint. *Vacuum* 2019;168:108857.

Address correspondence to:
Konda Gokuldoss Prashanth
Department of Mechanical
and Industrial Engineering
Tallinn University of Technology (TalTech)
Ehitajate tee 5
Tallinn 19086
Estonia

E-mail: kgprashanth@gmail.com

Appendix 2

Publication II

N. Alinejadian, L. Kollo, I. Odnevall, Progress in additive manufacturing of MoS₂-based structures for energy storage applications – A review, Mater. Sci. Semicond. Process. 139C (2022) 106331. <https://doi.org/10.1016/j.mssp.2021.106331>. [adapted with permission from Elsevier dated May 12, 2022 (Fleischmann et al., 2020)]



Contents lists available at ScienceDirect

Materials Science in Semiconductor Processing

journal homepage: www.elsevier.com/locate/mssp

Progress in additive manufacturing of MoS₂-based structures for energy storage applications – A review

Navid Alinejadian^{a,b,*}, Lauri Kollo^a, Inger Odnevall^{b,c,d}

^a Department of Mechanical and Industrial Engineering, Tallinn University of Technology (TalTech), Ehitajate tee 5, 19086, Tallinn, Estonia

^b KTH Royal Institute of Technology, Division of Surface and Corrosion Science, School of Engineering Sciences in Chemistry, Biotechnology and Health, SE-100 44, Stockholm, Sweden

^c AIMES - Center for the Advancement of Integrated Medical and Engineering Sciences at Karolinska Institutet and KTH Royal Institute of Technology, Stockholm, Sweden

^d Department of Neuroscience, Karolinska Institutet, SE-171 77, Stockholm, Sweden

ARTICLE INFO

Keywords:

Additive manufacturing
Laser-based powder bed fusion
Selective laser melting
Two-dimensional materials
MoS₂
Electrochemistry
Electrochemical energy conversion/storage
Novel energy storage systems
Electrochemical applications

ABSTRACT

Investigation of next-generation manufacturing methods for the processing of functional materials and offering products with improved performance/functionalities has always been a challenge in terms of energy efficiency, cost-effectiveness, and eco-friendliness. Additive manufacturing (AM) attributes to rapid prototyping techniques that provide new opportunities to test new concepts and design complex 3D structures from metals, ceramics, and composites. Moreover, as a well-known transition metal dichalcogenide, Molybdenum disulfide (MoS₂) is a two-dimensional (2D) material with outstanding electrochemical, physical, and mechanical properties that make it a potential candidate for energy storage electrodes via intercalation of different H⁺, Li⁺, Na⁺, and K⁺ cations. In this review, we discuss the existing conventional MoS₂-processing methodologies and compare them with the novel additive manufacturing processes (especially laser-based powder bed fusion). The authors are convinced that the processing of prominent MoS₂-based functional structures by the novel additive manufacturing processes can provide complex structures for different electrochemical applications, particularly for energy conversion/storage systems.

1. Introduction

Molybdenum disulfide (MoS₂), a widespread material as molybdate in nature, belongs to a class of advanced next-generation materials called transition metal dichalcogenides (TMDs) [1–4]. MoS₂ with different structures offers strong covalent bonds between the Mo and S atoms and weak van der Waals force between the layers, allowing them to be mechanically separated and forming 2D sheets of MoS₂. Recently, researchers have focused on the improvement of the functionalities and broadened the application of novel graphene-like 2D materials [4]. Due to the direct bandgap, MoS₂ has a great advantage over graphene in several applications such as photodetectors, solar cells, chemical sensors, supercapacitor electrodes, Valleytronic devices, optical sensors, and field-effect transistors [4]. 3D bulk materials may reveal similar properties corresponding to their 2D counterparts [5]. MoS₂ has a melting point of ~1185 °C and Young's modulus of 0.33 ± 0.007 TPa. Monolayer MoS₂ is a typical stable existing semiconductor material with

a direct bandgap of ~1.8 eV which makes it advantageous compared to graphene with zero bandgap [2,4,6]. This specific property makes MoS₂ a promising next-generation material in applications such as switching devices, optoelectronic devices, stretchable electronics, and energy conversion/storage [7–10].

Considering the advantages and potential of MoS₂ as a next-generation/benchmark material, especially in the field of energy storage, it has been widely processed and studied using a variety of conventional methods [11–26]. However, drawbacks related to the preparation and processing of MoS₂-based structures with conventional methods have limited their industrial applications. Several AM techniques have been introduced toward the elimination of drawbacks of conventional methods previously used for processing 2D materials [27–32] such as MoS₂-based parts and structures for energy storage systems [17,18,33–38]. However, there still exist some drawbacks regarding their mechanisms. AM processes such as laser-based powder bed fusion (L-PBF) can overcome some of the drawbacks (e.g., lack of

* Corresponding author. Department of Mechanical and Industrial Engineering, Tallinn University of Technology (TalTech), Ehitajate tee 5, 19086, Tallinn, Estonia.

E-mail addresses: n.alinejadian@outlook.com, navid.alinejadian@taltech.ee (N. Alinejadian).

<https://doi.org/10.1016/j.mssp.2021.106331>

Received 10 August 2021; Received in revised form 24 September 2021; Accepted 15 November 2021

Available online 26 November 2021

1369-8001/© 2021 Elsevier Ltd. All rights reserved.

mass production, expensive pre-processing stages, limitation of geometric and specific surface area, special chemical requirements, thermal treatment, acid treatment, multi-step-wise processing to deliver desired functionality to AM-printed structure, and post-processing stages) observed during both conventional processes and AM fabrication of MoS₂-based 3D structures.

This review deals with the general introduction of 2D materials, properties of MoS₂ including its electrochemical performance, state-of-the-art applications, and processing techniques for energy-based applications. This is followed by an introduction of AM techniques applicable for energy storage systems with a focus on AM of MoS₂ based structures. The advantages of using the laser-based powder bed fusion (L-PBF) of ceramics are discussed. An overview is also provided on L-PBF processes employed to fabricate structures and parts for energy-based applications and their future prospects.

2. MoS₂ – properties, applications, and processing

2.1. Two-dimensional (2D) nanomaterials

2D crystals such as MoS₂, MoTe₂, MoSe₂, NbSe₂, and TaSe₂ have properties (large surface area, high mechanical strength, high electrical and thermal conductivity) that can be utilized in a wide range of functional applications such as catalysis, energy storage, electronics, etc. [23,26,39]. Extensive research is currently focused on the development of cheap, efficient, environmentally safe, and reliable electrochemical energy storage systems. The use of 2D materials as negative electrodes in ever-emerging non-Li battery systems (e.g. the Na-ion batteries (SIB) and the K-ion batteries (KIB)) has gained increased attentions [26]. However, the large size of ions such as Na⁺ and K⁺ may challenge the intercalation process and result in reduced ionic mobility and poor kinetics. A careful configuration of the microstructure and the adaptation of the next-generation electrode design (based on AM technologies) are therefore of outermost importance. The rather large interlayer spacing of MoS₂ (0.65 nm) provides as an example a conducive possibility for accommodating large-sized alkali metal ions (e.g. Na⁺, K⁺) [18,40].

2.2. MoS₂ properties

TMDs consist of hexagonal layers of metal atoms (M) sandwiched between two layers of chalcogen atoms (X) with a stoichiometry of MX₂

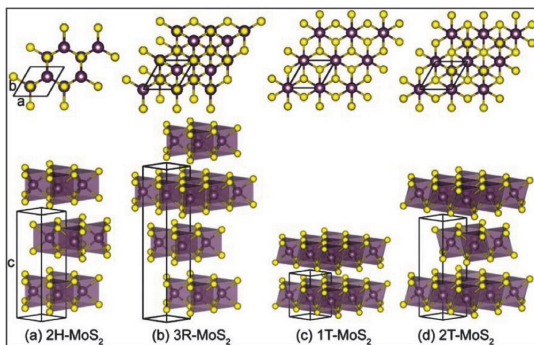


Fig. 1. Layered MoS₂ of different structural polytypes: (a) 2H, (b) 3R, (c) 1T, and (d) 2T. *a*, *b* and *c* denote the lattice constants of the hexagonal close-packed (HCP) unit cell <https://www.sciencedirect.com/topics/chemistry/hexagonal-sp-ace-group>. Yellow and purple spheres represent S and Mo atoms, respectively [adapted with permission from Elsevier under the license number 5147890462147 dated Sep. 14th, 2021 [41]]. (For interpretation of the references to colour in this figure legend, the reader is referred to the Web version of this article.)

(Fig. 1). The transition metal – M and the chalcogen atom – X exhibit the oxidation states of +4 and –2, respectively [11]. Among the various layered TMDs reported, MoS₂ is one of the most studied materials and has attracted huge attention during the last decade because of its excellent energy harvesting, nanoelectronic, and optoelectronic properties [11,26]. MoS₂ exhibits Young's modulus of 330 ± 7 GPa and is mechanically flexible. The structural characterization reveals that the single layer consists of a honeycomb lattice structure with a lattice parameter of 3.12 Å. The vertical separation between the Sulfur layers is 3.11 Å with a thickness of 6.5 Å [4,11]. The bulk form of MoS₂ acts as a semiconductor with an indirect bandgap of ~1.29 eV whereas a monolayer shifts upwards in energy to ~1.8 eV [11,41]. The differences between the bulk and monolayer MoS₂ in terms of atomic structure and bandgap have been demonstrated by Huang et al. [11]. Such differences between single- and few-layered forms, compared to their bulk counterpart, and their surface properties can though be optimized to enhance the electrochemical performance [4,11,26]. Chhowalla et al. studied the suitability of different crystallographic structures of MoS₂ as supercapacitor electrodes [3]. MoS₂ nanosheets aligned vertically exhibit for example a higher capacity and active surface area compared with horizontally aligned sheets [42]. Efficient intercalation of ions is a prerequisite in the layered materials used as EES devices such as batteries and supercapacitors. The electrochemical performance as a function of morphologies and physical properties needs optimization as this is of large importance for the applicability of TMDs (e.g. MoS₂ and MoS₂-based composites) in sensors to various EES devices.

2.3. Applications of MoS₂

MoS₂ is, due to its extraordinary properties and electrochemical performance, an outstanding candidate for different energy storage applications [2,7–18] and a wide range of future applications as described below.

2.3.1. Optic, electronic, and sensors

Yao et al. demonstrated a prototype of a MoS₂-based gas sensor able to detect ammonia gas even in small amounts [23], and Huang et al. investigated the applicability of MoS₂ electrodes for sensing applications (such as electrochemical biosensing, MoS₂ FET-based biosensing, fluorescence-based biosensing, gas sensing, and chemical sensing) [11]. In a similar study, Zhang et al. elaborated on the potential of using MoS₂ and MoS₂-based nanocomposites for sensing applications (in FET sensors, optical sensors, and electrochemical sensors) [52]. Barua et al. investigated the potential of using MoS₂ structures (0D, 1D, 2D, and 3D) in optic, electronic, and electrochemical biosensors [53] and showed that different optical and electrochemical attributes may be achieved by varying the dimension of the MoS₂ samples [53]. Electrochemical detection of non-enzymatic glucose was another application of MoS₂ introduced by Zhai et al. [54]. Its synergistic electrocatalytic activity alongside a high sensitivity for glucose ($570.71 \text{ mA mM}^{-1}$) and precise linear detection capability (in the range from 0 to 30 mM), illustrated its applicability in a wide range of sensing applications ranging from clinical diagnosis to food analysis and biotechnology [54]. Pan et al. studied the interaction mechanism between MoS₂ and intense ultrafast femtosecond laser, as well as the optical response and ablation mechanism of laser-processed MoS₂ and its applications [49]. Castellanos-Gomez et al. demonstrated the possibility of using laser-assisted exfoliated MoS₂ for transistor applications due to its beneficial mechanical properties, large in-plane mobilities ($200\text{--}500 \text{ cm}^2 \text{ V}^{-1} \text{ s}^{-1}$), and high current on/off ratios (>108) [12]. Zhang et al. proved the potential of using a 2D self-aligned MoS₂-based heterostructure Schottky diode for Wi-Fi-band wireless energy harvesting [55]. Tan et al. demonstrated strong photoluminescence in the visible range by modifying the crystallinity of MoS₂ [56]. Wu et al. investigated an oscillating piezoelectric current and voltage provided by MoS₂ with an odd number of atomic layers. The output increased with decreased thickness whereas no piezoelectric

response was observed for flakes with an even number of layers. These characteristics could be exploited in future adaptive bio-probes and tunable/stretchable electronics/optoelectronics [10].

2.3.2. Hydrogen reduction reaction (HER) and fuel cells

Yang et al. have studied the hydrogen evolution reactions (HER) and supercapacitor applications of edge-oriented nano-porous MoS₂ films [42]. They successfully demonstrated cation intercalation and reversible redox reactions between different valence states of Mo ($+4 \leftrightarrow +3$). Lee et al. demonstrated that COOH-functionalized MoS₂ provides a very high hydrogen evolution reaction (HER) performance due to its intramolecular proton transfer, characteristics that enables its use for hydrogen adsorption engineering [57]. Zhou et al. showed that defect-rich oxygen-incorporated MoS₂ nanosheets demonstrate excellent HER and long-term stability up to 20,000 cycles [25]. Rowley-Neale et al. proved for the first time MoS₂ to be an electrocatalyst candidate for oxygen reduction reactions (ORR) in acidic electrolytes in hydrogen fuel cells. Since the performance was the same as for proton exchange membrane fuel cells (PEMFCs), MoS₂ was considered to be a highly applicable candidate for industrial applications [58]. Corrales-Sanchez et al. investigated MoS₂/carbon-based nanomaterial nanocomposites as cost-effective cathode catalysts for HER [59]. Hu et al. showed that the composition of MoS₂ with carbon-based nanomaterials can serve as a catalyst for PEMFCs cathodes [60].

2.3.3. Battery and supercapacitor

David et al. studied the mechanical properties and electrochemical response of crumpled MoS₂/rGO composite flakes for Na-ion batteries [43]. They obtained the first cycle electrochemical capacity of 338 mAh g⁻¹ and the final gravimetric charge capacity of 230 mAh g⁻¹. They also performed static uniaxial tensile tests to demonstrate the average ultimate tensile strain of approximately 2% for the crumpled composite paper [43]. Li et al. widely reviewed recent achievements of a wide range of micro- and nanostructured materials processed for sodium-ion based energy storage systems, i.e., batteries and capacitors [44]. They introduced MoS₂ and MoS₂-based structures as potential candidates for Na-ion energy storage systems. They showed that 2D heterostructures of CC@CN@MoS₂ are able to deliver high mechanical strength and electrical conductivity. They demonstrated the high capacity of 265 mAh g⁻¹ even after 1000 GCD cycles at 1 A g⁻¹. Furthermore, they demonstrated that MoS₂-based structures can play a promising role in Na-S batteries [44]. Zheng et al. studied the influence of MoS₂ morphology for thermal battery applications [45]. They showed that a flower-like porous microsphere structure offered a low weight loss, outstanding thermal stability, and excellent electrolyte compatibility. Compared to FeS₂ or CoS₂, MoS₂ offered a longer discharge time of improved capacity when used as a cathode material in thermal battery applications [45]. Liu et al. widely investigated the recent progress in the processing of MoS₂ cathodes for Li-S batteries and showed the advantage of MoS₂ due to reducing the shuttle effect [46]. They showed high absorptivity of polysulfides inside of the structure of MoS₂, leading to the storage capacity of 670 mAh g⁻¹ and better stability up to several thousands of GCD cycles [46]. Lin et al. introduced monolayered 1T-MoS₂ with its high electrical conductivity of 10–100 S cm⁻¹, volumetric capacitances between 400 to 700 F cm⁻³, and 95% capacity retention after 5000 GCD cycles [47]. They, moreover, showed that the rich coordination sites, large electroactive surface area, flexibility, and charge transport of 1T-MoS₂ between stacked forms and cross-linked networks can shift its electrochemical behaviors from faradaic to non-faradaic. This turns MoS₂ into an extraordinary 2D TMD applicable for supercapacitors and secondary batteries [47]. Bissett et al. investigated the performance of MoS₂/graphene in symmetrical coin cell supercapacitors by using an aqueous Na₂SO₄ electrolyte [51]. They showed that partial re-exfoliation of 2D structures via GCD can lead to a significant increase in the performance of supercapacitor up to 800%. They showed that a small mass loading of 1 mg cm⁻² can achieve a specific capacitance of 11

mF cm⁻² at the scan rate of 5 mV s⁻¹ [51]. Stephenson et al. reviewed the applicability of using MoS₂-based composites as both anode and cathode in secondary Li-ion batteries [61]. The high reversible capacity and excellent rate capability of MoS₂ were attributed to its microstructural and electrochemical performance. The pseudo-capacitance, induced by the intercalation and redox reactions, contributes to improved supercapacitor performance and electric double-layer capacitance (EDLC). An excellent pseudo-capacitive behavior was observed without any appearance of the charge transfer resistance. The edge-oriented MoS₂ films showed an increased areal capacitance (C_A) from 2.2 to 10.5 mF cm⁻² after 10,000 testing cycles at a current density of 10 mA cm⁻². The charge/discharge curves obtained after the cycling test were in the form of quasi-triangular shape and did not change significantly with the increase of the number of cycles [42]. Acerce et al. showed that a high concentration of the metallic phase of exfoliated 1T-MoS₂ with an extraordinary efficiency can electrochemically intercalate ions (e.g., H⁺, Li⁺, Na⁺, and K⁺). Capacitance values ranging between ~400 and ~700 F cm⁻³ were observed in a variety of aqueous electrolytes in which MoS₂ was introduced at high-voltage (3.5 V) operation. They further demonstrated differences in the crystallographic structure of the 1T and 2H phases of MoS₂. Cyclic voltammograms of MoS₂ in different scan rates and 0.5 M Na₂SO₄ demonstrated that the 1T electrodes retained their high capacitance values even at high scan rates >200 mV s⁻¹ [40]. The wide range of applications of MoS₂ and MoS₂-based structures illustrates that these 2D TMDs can be considered to be processed by cutting-edge manufacturing techniques which are utilized in the next generation of novel technologies.

2.4. Processing of MoS₂ for electrochemical applications

As previously mentioned, conventional techniques that process MoS₂ as a 2D nanomaterial include different stages. These process stages are elaborated in the following paragraphs divided into exfoliation and fabrication of MoS₂, including different techniques, to create electrodes for specific applications.

2.4.1. Exfoliation

2.4.1.1. Chemical vapor deposition (CVD) and atomic layer deposition (ALD).

CVD [11,62] and ALD [56,63,64] are two of the most important bottom-up approaches that have been employed to fabricate monolayered or few-layered high-quality MoS₂ nanosheets in a controlled way [65] with different growth orientations and morphologies applicable for a wide range of applications [66]. These 2D fabrication techniques are advantageous since they allow optimization of the morphological, mechanical, and electronic properties, and chemical stability [26]. The CVD method can generate layered heterostructures in which interfacial contamination is avoided. CVD-processed MoS₂ can be made based on Mo-based compound powders and ammonium molybdate [67]. These bottom-up techniques have capabilities to tune the morphology as well as the alignment of 2D TMDs from horizontal to vertical directions. Choudhary et al. used the CVD process to prepare 1D/2D core/shell h-WO₃/WS₂ nanowires for flexible supercapacitor applications [68]. Their designed structure showed high charge-discharge retention over 30,000 cycles with the retention higher than 100% at a scan rate of 100 mV s⁻¹. This was attributed to the structural stability which facilitates its application for unconventional energy storage technologies [68]. Chen et al. utilized a modified CVD method to synthesize MoS₂ crystals in a process that was capable to control the number of layers [65]. In another study, Kong et al. used CVD in a horizontal tube furnace to vertically grow thin films of MoS₂ and MoSe₂ to reach the maximum edge of nanolayers onto the surface for the HER [66]. Recently, Demirtas et al. reported CVD-assisted deposition and simultaneous sulfurization of MoO₃ to obtain uniform MoS₂ structures with an edge length of ~40 μm and a thickness of

~0.78 nm for optoelectronic applications [69]. These strengths of the CVD technique show its ability to directly assembling of 2D TMDs structures with different morphologies onto substrates. However, the employment of such techniques to fabricate the structures are not favorable for electrochemical energy storage applications due to high costs and scalability issues [26]. Another disadvantage of the CVD technique in this context is the discontinuous production of thin films [70].

2.4.1.2. Liquid-phase exfoliation. Another commonly used exfoliation technique is liquid-phase exfoliation using alcohols, ketones, and acids which minimize the energy required for the exfoliation process [20]. This method, coupled with the sonication process can effectively be used to overcome the relatively weak van der Waals bonding existing between the layers of the bulk material [11,26]. Sonication offers several positive effects on exfoliated materials (2D nanosheets and layered materials), where it helps in breaking larger crystallites into smaller ones [23]. Recently, Jin et al. reported an inkjet-printed humidity sensor on the basis of MoS₂/PVP which was prepared by liquid-phase exfoliation with high sensitivity, ultrafast response behavior, and good reproducibility [71]. Regarding the weaknesses, Lin et al. demonstrated that Li-intercalation and exfoliation can be tortured by the presence of a metallic 1T phase of MoS₂, result in poor electrical performance, and provide broad thickness distribution of exfoliated MoS₂ nano-layers [72]. They illustrated a process leading to the preparation of a uniform, solution-processable, and pure-phase 2H-MoS₂ nanosheets via precise control of electrochemical intercalation of quaternary ammonium molecules (such as tetraheptylammonium bromide) into 2D crystals. Liquid-phase exfoliated MoS₂-based materials can be utilized for healthcare monitoring, large-scale sensors, and flexible sensing devices that can be fabricated by inkjet printing. Etching is another top-down technique that is used to preferentially leach out the selective atom(s) from the precursor or vice-versa [22,26].

2.4.1.3. Mechanical delamination (ball-milling). Top-down techniques (Fig. 2) are preferred because of their ease of processing, the low cost associated with the materials and technique, and the production of large surface area sheets with reasonable scalability. Ball-milling is a process that can effectively generate both shear and compressive forces that can both shear and weld materials [73–75]. Recently, such techniques have widely been employed in electrochemical energy storage applications. One of the most widely used straightforward top-down approaches for fabricating 2D materials is mechanical exfoliation [23,26]. The ball milling mechanism can be helpful in the fabrication of thin 2D nanosheets from the edge of layered materials. Low-energy ball milling does not induce any significant damage to the crystallographic structure of the 2D nanosheets and generates fewer internal defects as compared to sonication [23]. Krishnamoorthy et al. exfoliated bulk MoS₂ to obtain a

few-layered MoS₂ for solid-state double-layer supercapacitors [76]. The exfoliated MoS₂ showed rectangular-shaped CV curves and the near-triangular shaped charge-discharge provided a capacitance of 119 mF cm⁻¹ and an energy density of 8.1 nWh cm⁻¹ [76]. Pazhamalai et al. applied a liquid-medium ball-milling process to exfoliate MoS₂ in tetraethylammonium tetrafluoroborate (TEABF₄) for symmetric supercapacitors [77]. In a wide-range potential window from -3 to 3 V and a scan rate of 250 mV s⁻¹, they showed rectangular-shaped CV curves that possess a specific capacitance of 14.75 F g⁻¹, an energy density of 18.43 Wh kg⁻¹, and a power density of 1125 W kg⁻¹. Recently, Wang et al. utilized a planetary ball-mill machine to prepare few-layered MoS₂/Graphene-based ink for a sandwiched supercapacitor [78]. The low-cost and environmental-friendly ink showed a specific capacitance of 76 F g⁻¹ and areal capacitance of 58.5 mF cm⁻². The weakness of ball-milling is that it may be unreliable from a scalability perspective even though high purity sheets can be produced [26]. As an innovative insight, ball-milled MoS₂ ink can be utilized as a feedstock for ink-jet printing if its drawbacks can be eliminated.

2.4.1.4. Electrochemical exfoliation. Electrochemical exfoliation carried out by electrochemical Li-intercalation and exfoliation can be used to produce MoS₂ nanosheets during the discharge process using a bulk cathode (MoS₂ crystal) and a Li foil anode followed by ultrasonication and exfoliation of Li_xMoS₂ in H₂O or C₆H₅OH. This results in the fabrication of single-layer MoS₂ nanosheets on a large scale with an extremely high output (92% yield), even at room temperature [11].

2.4.1.5. Hydrothermal and solvothermal. Due to the processing simplicity, efficient performance, and high-yield, both hydrothermal [13,15,19,24] and solvothermal [16,25] processes have been reported extensively to engineer the interlayer spacing, exfoliation, and synthesis of novel MoS₂. The hydrothermal and solvothermal reactions are carried out in an autoclave at high temperatures (180–250 °C) and pressure. As one of the strengths, the morphology of the material, physical, chemical, and electrochemical properties can be manipulated by controlling the time, temperature, type, and concentration of solvent [16,25,48,79].

2.4.1.6. Laser thinning and exfoliation. The above-mentioned studies and techniques show that mechanical and chemical-based exfoliation methods can hence be used to fabricate high-quality MoS₂, which is an important prerequisite to obtain desired properties of the processed MoS₂. However, drawbacks such as the lack of reliable large-scale production techniques and difficulties in precise morphology control limits though their applications [12,23]. Moreover, the entire process chain further includes multiple complex steps with pollutant residues [80–83], and the resultant materials need post-processing purification to obtain high-quality (relatively pure) MoS₂ products.

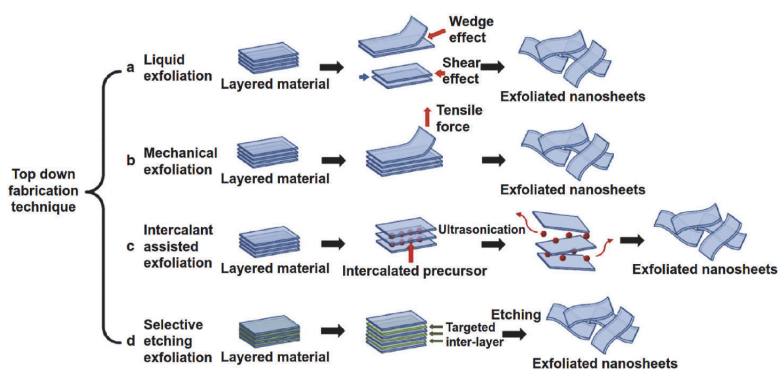


Fig. 2. Schematic representation of the different 'top-down' approaches for large-scale synthesis of electrode materials: (a) liquid exfoliation, where sonication of the bulk material is carried out in a liquid medium, (b) mechanical exfoliation carried out using tensile forces, (c) intercalant-assisted exfoliation where the sonication of the bulk precursor is carried out in a liquid media followed by intercalation of metal ion (usually Li⁺) between the sheets, and (d) selective etching to remove one or more constituent atoms resulting in the formation of sheets [adapted from Springeropen under the open access policy [26]].

The novel, green, low-cost, and highly efficient laser-assisted techniques have been investigated to overcome the cons of conventional preparation and MoS₂ exfoliation methods. For instance, Castellanos-Gomez et al. successfully used a laser-based top-down approach to fabricate a single-layer 2D MoS₂ crystal in arbitrary shapes and patterns with features in the range of 200 nm [12]. The two-dimensional exfoliated MoS₂ crystals showed comparable electronic and optical properties as pristine exfoliated MoS₂ single layers. In addition, the authors demonstrated that the laser beam can effectively reduce the thickness of MoS₂ layers down to a single layer [12]. In a similar study, Hu et al. conducted the same procedure and evaluated in detail the thermal conductivity of MoS₂ by thinning the layers. They demonstrated that MoS₂ films with designed layer numbers can be fabricated precisely by controlling the laser parameters and exposure time [14]. Laser-assisted thinning of MoS₂ sheets can be considered the most promising approach. Laser-assisted exfoliation not only overcomes the limitation of existing conventional bottom-up and top-down preparation methods but can also enable patterning of MoS₂ based structures and thinning of TMDs for a wide spectrum of applications [14,21]. Despite the laser-assisted patterning of MoS₂, laser modification could be considered as a capable means toward modification or manipulation of the physical and chemical properties of MoS₂ via the introduction of defects into its structure [1].

2.4.2. Fabrication

2.4.2.1. Cladding and paste methods. Despite the advantages and disadvantages of different MoS₂ exfoliation methods discussed above, there exist several conventional methods to process exfoliated MoS₂ nanosheets towards the fabrication of electrodes for various functional applications. The exfoliated MoS₂ or MoS₂-based composite is deposited onto a conductive substrate for characterizations and electrochemical measurements. One of the simplest and fastest methods is to clad a conductive substrate with a MoS₂-based paste compound which may also contain conductive carbon-based materials to reduce the resistivity of the paste and simultaneously increase the electrode performance [11, 20,25,84–86]. Recently, Lu et al. used the paste method for cladding a coin cell with CNTs@MoS₂/MoO₂ for in-situ synchrotron XRD studies of the electrochemical capability of the nanocomposite [87]. A simple paste method was shown capable to prepare the electrodes and the results indicated synergistic Li storage within the three components during charge/discharge reactions. However, this method can though result in reduced geometric and specific surface areas of exfoliated MoS₂-based materials and nanocomposites.

2.4.2.2. Hydrothermal and solvothermal. Another high-yield production method is the deposition of nanomaterials by hydrothermal or solvothermal methods. This can either be a one-pot strategy for the synthesis and simultaneous deposition of materials onto the substrate [88–90] or be separately employed to deposit already synthesized materials onto a substrate [91,92]. Moreover, the hydrothermal method is capable to prepare different types of pure and composites materials with a variety of morphologies and structures. For instance, Mukherji et al. synthesized and grew MoS₂-wrapped MnCO₃ on graphite paper in-situ under hydrothermal conditions [93]. An asymmetric two-electrode system including the above-mentioned negative electrode along with its NiCo₂O₄ positive counterpart illustrated a high specific energy density of 48.97 Wh kg⁻¹ and power density of 600 W kg⁻¹. Wang et al. directly deposited V-doped 1T-MoS₂ with a large layer spacing on carbon cloth by using an in-situ hydrothermal technique with the aim of Na⁺ storage [94]. Their high-performance electrode showed a specific capacity of 1235 mAh g⁻¹ at the first cycle, 1000 mAh g⁻¹ after 100 cycles, and 453.2 mAh g⁻¹ after 200 cycles of constant-current charge-discharge. As an innovative insight, they showed that a high specific surface area of the carbon substrate can inhibit aggregation of 1T-MoS₂

nanosheets and reduce the ion diffusion resistance. These studies have also shown that the hydrothermal method can be applied for the one-step growth of complex nanostructures onto the electrodes. However, hydro/solvothermal methods limit the mass-production of nanomaterials and cannot be considered for large-scale industrial production. Nevertheless, extensive research is undertaken for scaling up the products [20].

2.4.2.3. Layer-by-layer deposition. Layer-by-layer deposition methods include spray-coating [23,39], spin-coating [57,72], and/or deep-coating [95]. Lin et al. applied spin coating to uniformly deposit 2H-MoS₂ thin film onto SiO₂/Si wafer [72]. In another study, Paul et al. demonstrated that spray coating can be considered as a method capable of good dispersion of metal ions droplets on the surface of carbon cloth to impose accessible active sites for the electrochemical reaction [96]. These layer-by-layer deposition methods need pre-processing steps to generate a suitable solution able to generate material with desirable properties and subsequent post-processing able to stabilize the deposited materials onto the substrate. In order to achieve the desired performance and to produce a continuous and reasonable thick film, the ink concentration and the parameters of the spin coating procedure need to be optimized for different types of substrates [72].

2.4.2.4. Electrochemical deposition (electrodeposition). Electrochemical co-/deposition methods are generally considered as a low-energy and low-cost way to deposit materials of a wide dimensional range from the nano to the microscale. Recently, Dam et al. applied the electrodeposition method to grow MoS₂ thin film on In-Sn oxide coated glass (ITO). They approved the amorphous nature of the as-deposited thin film and its high orientation along the <002> crystallographic direction after annealing [97]. When using electrophoretic deposition [101,102] and electrodeposition [103], the process parameters can be adjusted to control the morphology of deposited layers or materials. However, due to scalability issues, large-scale manufacturing can be limited by using these electrochemical methods. They further have complex handling procedures, special chemical requirements, and difficulties in controlling the thickness, and uniformity of thin films.

2.4.2.5. Roll-to-roll processing. Conventional EES devices are fabricated through high-speed roll-to-roll processing technology, which normally includes chemical deposition, electrode rolling, roll cutting, followed by cell assembly with separator, electrolyte filling, and finally packaging with re-cutting [98,99]. This technology can be scaled up for large-scale industrial applications [98,99]. Mensah-Darkwa et al. reviewed the recent progress in MoS₂ for HER [100]. They elaborated on the effect of crystallinity, phases, and electrocatalytic site engineering of MoS₂ on the HER performance as well as on the enhanced impact of doping, functionalization, and composition of MoS₂ with other elements and nanomaterials [100].

2.4.2.6. Laser-based patterning. Several investigations have shown the capability of using laser for processing of MoS₂. Castellanos-Gomez et al. developed an approach for laser-assisted thinning of MoS₂ down to a few-layered nanosheet. They showed that the bandgap and semiconducting properties of laser-thinned MoS₂ were similar to its pristine single-layer nanosheet. Their results may lead to the development of MoS₂-based structures for future electronic, photovoltaic, and optoelectronic devices [12]. Cao et al. focused on direct laser patterning of MoS₂ with the aim of generating micro-supercapacitors from printable MoS₂. In their study, the laser exposure optimized h-MoS₂ film exhibited approximately 178 F cm⁻³ of volumetric capacitances as well as an excellent cycle performance. It was demonstrated that laser-assisted thinning and patterning provide a good opportunity to develop various micro-sized energy storage devices [21]. Hu et al. demonstrated that an increased temperature of MoS₂ depends on both laser power and

the substrate materials for the cooling and light absorption of MoS₂. Therefore, tuning of the laser power and exposure time could precisely affect the thinning of the MoS₂ down to a monolayer [14].

The above-mentioned physical fundamental interactions between the laser beam and TMDs show that the use of laser not only paves the way for one-step processing of MoS₂-based structures via novel AM approaches but also enables the improvement of its functional properties for the next generation of functional additively manufactured devices [1]. A schematic illustration comparing the different fabrication processes and types of materials (dry and wet) available for the fabrication of EES is presented in Fig. 3. The 3D printing/rapid prototyping processes denoted Additive Manufacturing (AM) technology, offer new bottom-up approaches that are versatile, rapid, flexible, efficient, and which can be economically feasible to generate novel energy storage devices/systems with added functionalities. The use of AM not only avoids the limitation of existing bottom-up and top-down fabrication methods but can also be used to rapidly prototype MoS₂-based structures for a wide spectrum of applications.

3. Additive manufacturing

3.1. General introduction of AM methods

According to the ASTM standard (F2792-10), available AM processes include (i) material jetting including jet printing (JP), poly jet printing (PJP), inkjet printing (IJP), multi-jet printing (MJP), direct ink writing (DIW), electrohydrodynamic (EHD), (ii) Vat photopolymerization (VP), stereolithography (SLA), (iii) fused deposition modeling (FDM), (iv)

binder jetting (BJ), (v) sheet lamination (laminated object manufacturing (LOM)), and (vi) powder bed fusion (metal AM processes like selective laser melting) [31,50,99,101].

Recently, several successful innovative attempts have resulted in novel AM methods developed for a wide range of applications including bio-engineering, robotics, aerospace, environment, automotive, electronics, energy, etc. Several state-of-the-art AM methods for polymers are able to generate functional structures to which an additional dimension, such as time, belongs (4D printing) toward the enhancement of functionalities [102]. Fig. 4 shows that the polymer-based AM processes having widely been progressed by using different types of polymers (as the feedstock), AM methods, and final applications (as the demand of end-users). Based on ASTM standard classification, The stability of polymer-based AM products, processed by different AM methods, would associate with the processing method, polymer properties, and the desired part properties [102].

Vat Photopolymerization (VP) is an accurate and high-resolution AM method based on UV-assisted selective polymerization of photosensitive resins to print 3D parts [102]. Development of this method led to introduction of several capable AM techniques such as stereolithography (SLA) [103], digital light processing (DLP) [104], continuous liquid interphase printing (CLIP) [105,106], high-area rapid printing (HARP) [107], computed axial lithography (CAL) [108], two-photon photopolymerization (2 PP) [109–112], femtosecond projection two-photon lithography (FP-TPL) [113–115]. VP-based techniques have successively been developed with the aims of increasing the manufacturing speed, dimensional precision of parts, production of complex parts, etc. Amongst AM methods, continuous extrusion of a wide range of polymer

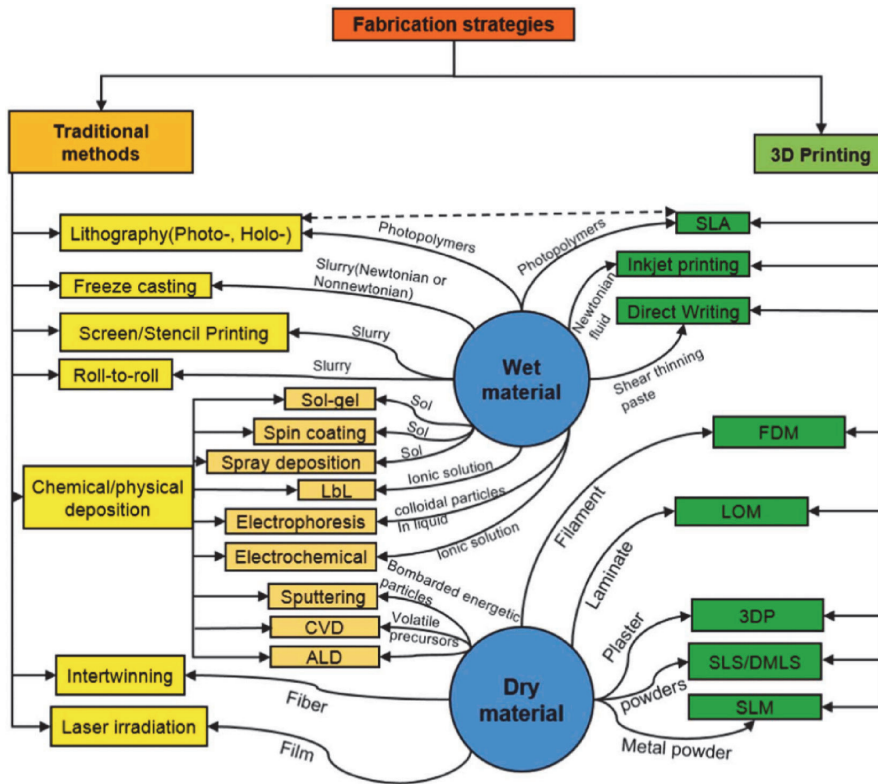


Fig. 3. Systematic illustration detailing the different fabrication strategies employed for the fabrication of energy storage systems [adapted with permission from Elsevier under the license number 5147871482683 dated Sep. 14th, 2021 [99]].

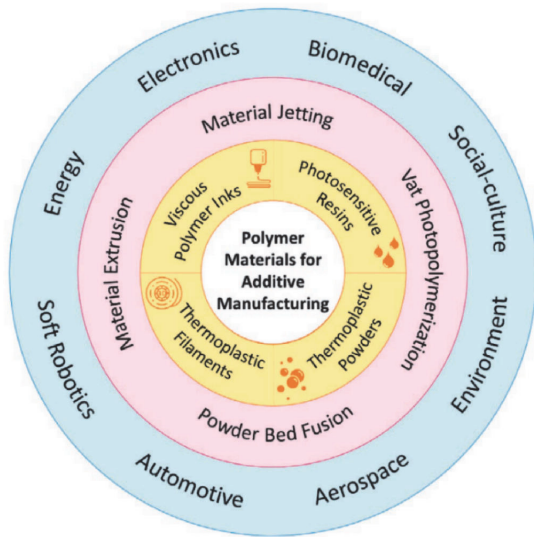


Fig. 4. Schematic illustration of the categorization of typical polymer AM techniques, relevant polymer materials, and applications [adapted with permission from John Wiley and Sons under the license number 5147890089467 dated Sep. 14th, 2021 [102]].

materials or viscous inks through a nozzle onto a platform and subsequently solidification introduces affordable AM systems so-called materials extrusion (ME) technique. Fused deposition modeling (FDM) is a type of ME technique based on the melting and extrusion of thermoplastic materials [116], while direct ink writing (DIW) plots viscous inks such as pastes and concentrated polymer solutions onto the platform [117,118]. In both methods, cooling, drying, or chemical reaction leads to solidification of the deposited materials [102]. Some of the above-mentioned techniques, which are able to be used for energy storage application, will be elaborated on in the following sections.

Unlike conventional subtractive manufacturing processes [119–121], AM fabricates parts layer-by-layer without design restrictions (theoretically) and with added functionalities [99,122–124]. Almost all kinds of materials can be processed using existing AM technologies. For instance, metals are fabricated by using selective laser melting (SLM), electron beam melting (EBM), direct energy deposition (DED), etc., and ceramics by using selective laser sintering (SLS), binder jetting, etc.

Binder jetting (BJ) is a powder-based AM technique in which a liquid binder (polymers) is deposited onto powder particles (metals or ceramics) to selectively stick them together to build 3D objects. As expensive laser sources are not required, BJ systems are significantly low-cost and capable to build much larger objects without support structures compared with typical PBF systems. However, the absence of sintering or melting processes results in porous and relatively fragile products, which can be recovered by high-temperature sintering and liquid infiltration [125,126]. Material jetting is another versatile AM method capable to produce multi-material parts via using multiple print-heads (MP) and different materials such as photosensitive resins, thermoplastics, wax, and reactive materials. This method can, due to the precise control of the material deposition, generate functional materials of high dimensional accuracy and low surface roughness. The main drawbacks are related to the lack of control over the formation and deposition of the droplets [102,127]. Electrohydrodynamic (EHD) jetting is another process governed by the electrostatic drawing of ink onto the substrate regardless of the nozzle size. This rapid method is able to fabricate thin-walled structures of high height-to-thickness ratios in

the submicron scales [102,128].

Powder bed fusion (PBF) builds 3D parts in successive layers by selective fusion of any materials in the form of powder particles that can be softened, sintered, or melted by a laser or an infrared beam [129–132]. The limitations include over-sintering of particles, reduced tensile strength, the finite size of the laser beam, and low-speed processing [102]. Integration of PBF with inkjet printing introduced multi-jet fusion (MJF), a method with a higher resolution, cost-effectiveness, and faster print speed [102]. The main characteristic of MJF is a selective deposition of a fusing agent (heat absorbent) and a detailing agent (heat impediment) as droplets onto powder particles and line-wise fusion employing an IR-beam across the powder bed layers [133].

3.2. AM and energy storage

AM processes have distinct advantages over conventional EES fabrication methods such as process flexibility, design freedom, and geometry controllability, which facilitate the incorporation of 0D, 1D, and 2D structures [73,111–113]. The ability to fabricate structures with defined spaces enhances ion transportation, charge/discharge speed, and energy storage capability in electrochemical devices. Layer-by-layer fabrication follows a possibility for precise control of the electrodes (in terms of thickness) from thin layers (for flexible/wearable devices) to thick electrodes, which promotes fast ion diffusion and energy density. Such cost-effective, energy-conservative, and environment-friendly AM technologies enable one-step fabrication and eliminate material waste and hence considered ideal fabrication processes for energy storage devices [99,134–136].

Due to the wide advances and progress in AM methods and materials to generate complex 3D shapes with superior electrochemical performance [31], advanced research is currently ongoing to use MoS₂-based ceramics as the solid-state electrolyte for batteries [137]. Table 1 shortlists different characteristics of AM methods applicable for AM of batteries and energy storage systems. A categorization of electrodes, electrolytes, and techniques applicable for the AM of batteries is presented in Fig. 5 [31].

3.2.1. Lithography

Lithography-based printing techniques apply photocurable materials, and the polymerization process generates complex high-resolution 3D structures with or without using masks.

3.2.1.1. Holographic lithography (HL). HL is a simple multi-beam and cost-efficient technique using single laser exposure [138,139]. Ning et al. adopted a complex procedure assisting the integration of HL and photolithography to print SU-8 3D on ITO to obtain a 3D porous Ni scaffold as the current collector [29]. The procedure included the infiltration of AZ9260 photoresist materials into the SU-8 lattice, electrodeposition of Ni, and removal of the photoresist template [29]. They used HL and photolithography to generate a 3D porous mesostructured lattice after which MnO₂ and Ni-Sn were electrodeposited onto 3D porous scaffolds to generate a cathode and an anode, respectively. They illustrated that 3D holographic patterning is able to control the structural parameters toward tuning the energy and power densities for specific applications. The HL-fabricated electrodes provided an energy density of 6.5 μWh cm⁻² μm⁻¹, a power density of 3600 μW cm⁻² μm⁻¹, and a retained capacity of 88% after 100 cycles of charge-discharge. The superior performance of their HL-processed electrodes was attributed to the well-optimization of size, shape, surface area, and porosity of the structure, precisely controlled by the HL process [29].

Relying on the overlapping single laser beams, the rapid fabrication of periodic structures in the whole area can be considered as an advantage of the HL technique [139]. Backed by the optical interference of coherent light beam, HL is a potential technique able to fabricate defect-free multidimensional periodic nanostructures with a variety of

Table 1
Categorized AM methods for 3D printing of batteries [adapted with permission from John Wiley and Sons under the license number 5147881275359 dated Sep. 14th, 2021 [31]].

AM method	Available materials	Printing resolution	Advantage	Disadvantage
FDM	Thermoplastic	50–200 μm	User-friendly, low cost, high speed, large size capabilities, and lack of necessity for chemical post-processing	Limited resolution on the z-axis, weak mechanical properties, high viscosity of the molten materials, and low surface quality
DIW	Plastic, metals, ceramic, and food	1 μm	Affordable cost, easy operation, large material diversity, and no mask requirement	Weak mechanical properties, high requirement of ink
TAE	Polymers, metals, oxides, and hydroxides	50 nm to 10 μm	High ordered macroporous structure, low cost, high efficiency, simplicity, versatility, and controllability	Weak mechanical properties and strength limitation in materials
IJP	Sol-gel, metals, conductive polymers, and carbon-based and protein materials	20 μm	Low cost, multi-material printing capability, able to print large areas	Low printing speed, not good for high-volume printing, and the print head is less durable
AJP	Nanoparticles, nanowires, CNTs, 2D materials, dielectric materials	10 μm	High-resolution, high efficiency, compactable with inks in different viscosities	Overspray, printing quality is not stable, high-cost of equipment
SLA	Photopolymers	0.25–10 μm	High resolution, high surface finish, and high efficiency	Strong limitation in multi-materials deposition

geometries and a high level of flexibility in 3D design [138]. On the other hand, the performance of HL-processed electrodes depends on the precise control and well-optimization of size, shape, surface area, and porosity of the structure [29]. To tackle some of the above-mentioned difficulties, splitting, and recombining of a single laser beam can produce a multiple-beam interference pattern [138].

3.2.1.2. Stereolithography (SLA). The SLA is a well-known layer-by-layer AM technique for the printing of porous 3D electrodes based on the selective solidification of acrylic- or epoxy-based photosensitized monomer by visible or UV light [103]. Previously, dispersion and one-pot processing of MoS_2 and graphene have been studied for facile and industrial mass production of functional polymer hydrogels, particularly vinylpyrrolidone (VP) and polyvinylpyrrolidone PVP, possible to be processed by AM methods [35]. Wang et al. processed MoS_2 by using the SLA technique to print a bioactive 3D scaffold for tumor therapy and tissue regeneration. The feedstock was prepared from a mixture of akermanite powder, alginate acid sodium, and Pluronic F127 solution. The MoS_2 -modified AM-processed bio-ceramic scaffold was prepared by means of a hydrothermal process. It was tough challenging to prepare a scaffold with similar surface roughness and properties, degradation control, pore size, and mechanical properties as bone tissue [36]. Chang et al. combined the SLA technique with electrodeposition for AM of stretchable (up to 55%) and flexible (up to up to 180°) thick supercapacitors with a capacitance of 46.2 F cm^{-3} , a power density of

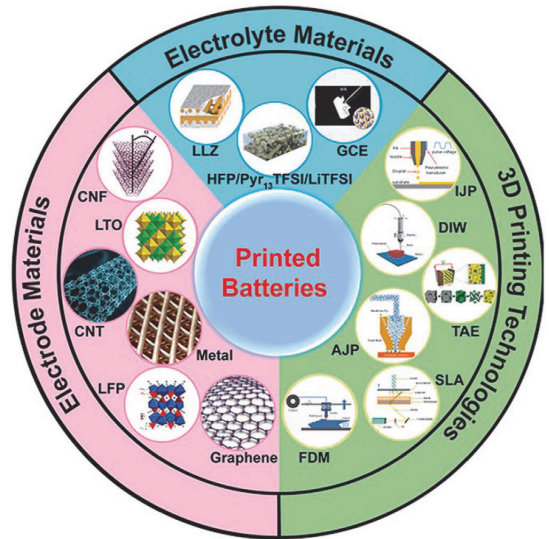


Fig. 5. Schematic illustration of AM-processed batteries by categorizing the electrolyte materials, electrode materials, and AM methods. The major AM methods for batteries include inkjet printing (IJP), direct ink writing (DIW), template-assisted electrodeposition (TAE), aerosol jet printing (AJP), lithography, and fused deposition modeling (FDM). carbon nanomaterials, LTO, LFP, metals, and graphene can be considered as electrode materials. $\text{Li}_7\text{La}_3\text{Zr}_2\text{O}_{12}$, *N*-Propyl-*N*-methylpyrrolidinium bis(trifluoromethanesulfonyl)imide (Pyr13TFSI)/lithium bis(trifluoromethanesulfonyl)imide (LiTFSI) salt, and gel composite electrolyte (GCE) are the most common feedstock acting as the electrolyte in additively manufactured ESS [adapted with permission from John Wiley and Sons under the license number 5147881275359 dated Sep. 14th, 2021 [31]].

85.81 mW cm^{-3} , and an energy density of $0.582 \text{ mWh cm}^{-3}$, and stability of 75.2% of the initial capacitance stability after 1000 periodic stretch/release cycles. The same study also attributed the energy density of $0.582 \text{ mWh cm}^{-3}$ and power density of 85.81 mW cm^{-3} to the well-designed 3D NPR multicellular electrode and novel architecting of the nanoflower-on-nanosheet nanocomposite. The improvement of the AM-processed electrode was attributed to negligible resistance due to the synergistic effect of electron/ion transport channels and low contact resistance. Besides, they stated that the electrochemical capacitance of the 3D NPR multicellular structure is sensitive to bending due to the high-stress accommodation capability. The long-term cycling stability of the electrodes was examined after 5000 cycles of GCD at 500 mA cm^{-3} . The capacitance of 28.5 F cm^{-3} and outstanding capacitance retention of 92.2% were achieved due to large surface area and strong adhesion between hierarchical porous nanocomposites and 3D structural current collectors [30]. Cohen et al. employed SLA to prepare perforated spherical, cylindrical, and cubic graphene-filled conducting polymer substrates with high surface area [27]. They used electrophoretic deposition to deposit Li-based compounds and turn the additively manufactured substrates into cathode, membrane, and anode. In terms of geometric surface area, the SLA-fabricated battery electrode offered an areal capacity of $400\text{--}500 \text{ mAh cm}^{-2}$ due to a higher geometrical area compared to its planar thin-film counterparts, which was improved up to three times. The study showed that the upward areal capacitance of AM-processed micro-battery, compared to its thin-film counterpart, is associated with and increased geometrical surface area [27].

The advantages of the SLA process include the highest resolution (even up to 100 nm) among other AM methods [103], easy creation of different 3D geometries [140], nozzle-free processing [141], and the

speed of the process [142]. Some disadvantages can also be addressed for the SLA process such as post-processing steps to deliver the functionality to the additively manufactured structure for specific applications [103]. Besides, a high-cost system, possible cytotoxicity, residual photo-initiator, and uncured resin can be mentioned as further struggles in the SLA process [141]. Post-processing such as photo-curing or heat treatment is though inevitable for subsequent solidification of the created 3D structures [27]. A schematic illustration of the mechanism of photopolymerization using the SLA technique is given in Fig. 6.

3.2.1.3. Projection micro-stereolithography (PμSL). The PμSL has been developed to fabricate high-resolution 3D polymer structures and devices [144]. Chen et al. applied PμSL to create a virtual photomask by digital micro-display technology and a focused ultraviolet (UV) light spot to directly print a 3D micro-battery [140]. They used poly(ethylene glycol) (PEG)-based polymer electrolyte of high ionic conductivity to fabricate current collectors, electrodes, and gel polymer electrolyte (GPE) of the battery. The PμSL-processed electrode showed a poor capacity of $1.4 \mu\text{Ah cm}^{-2}$ dropping to 40% after only 4 cycles of charge-discharge and half-cell failure after only 10 cycles of charge-discharge. Sub-micron sized surface channels of the GPE enabled ion exchangeability of the membrane and able to reduce the interfacial scattering. This method was presented as a low-speed and high-cost AM method. Considering the poor contact between the electrode and current collector, a large internal resistance was observed resulting in degraded capacity [140]. The capability of using PμSL in AM processing of a wide range of structures for micro-mechanical, biomedical, and high-precision applications is illustrated in Fig. 7.

3.2.2. Template-assisted electrodeposition (TAE)

The TAE is a technique capable to create macro-porous nano-structured electrodes of tunable pore sizes and large specific surface areas by changing the templates and electrodeposition parameters [146–148]. A schematic of TAE-based AM of a micro-spring is illustrated in Fig. 8 (a,b). Different 3D shapes, dimensions, and numbers of a microstructure can be printed by TAE even at the microscale are shown in Fig. 8(c–h) [149]. Zhang et al. designed a self-assembled 3D cathode including both ion conductive and electron transport pathways by deposition of polystyrene (PS) spheres and subsequently electrodeposition of a thin layer of Ni to form a 3D Ni scaffold [32]. They showed the short solid-state diffusion length can lead to a fast-charging process even in large volume manufacturing toward small- and large-scale applications. Their 3D electrode showed a gravimetric capacity of 286 mAh g^{-1} .

The advantages of TAE-designed electrodes include excellent electron conductivity, fast ion transportation, high specific surface area, and short-distance ion diffusion [32].

Some of the TAE advantages have compensated for the weakness of this technique. For instance, in energy storage electrodes, fast ion exchange via interconnected pore network, minimum sluggish solid-state ion transport, short ion diffusion distance, high electrode surface area, and excellent electron conductivity are the most prominent advantages of the TAE method [31]. However, poor mechanical strength, due to the high level of porosity existing in the structure of the electrodes, and lack of mass production have been considered as the drawbacks of these electrodes. Generally, the TAE technique has a sort of disadvantages such as convection in some narrow holes, template filling ratio, the influence of additives on trench filling, and macroscale feature density [149].

3.2.3. Inkjet printing (IJP)

The IJP can be considered as a high-resolution droplet-wise coating approach that directly deposits materials of tunable thickness via nozzles onto different substrates (Fig. 9) [150,151]. A wide range of materials such as metal, polymers, carbon-based, sol-gels, and proteins can be printed by IJP [152–160]. IJP has been widely suggested and discussed as a potential technique for printing 2D structures (graphene, MoS₂, etc.) for a wide range of applications such as supercapacitors and energy storage devices [28]. In terms of the formulation of 2D-material-content ink, 1T-MoS₂ can be stabilized in a mixture of polystyrene nanobead solution, IPA/2-butanol, and N,N,N',N'-tetramethyl-4,4'-diaminotriphenylcarbenium oxalate dissolved in IPA/2-butanol [161]. Li et al. used ethyl cellulose (EC) polymer to stabilize the MoS₂ solution exfoliated in DMF solution as well as toluene/ethanol solution for the adjustment of ink viscosity. They approved the high jetting performance of the formulated inks without degradation of the performance of AM-processed electrodes from 2D material nanosheets. For instance, their IJP-printed graphene/silver-based micro-supercapacitor showed capacitance of 0.6 mF cm^{-2} at the scan rate of 100 mV s^{-1} . The electrodes showed a reasonable capability for different applications such as photonics, optoelectronics, sensors, transparent conductors, supercapacitors, and energy storage [37,38]. The ink can be commonly prepared from a mixture of conducting agents, electroactive material, and polymer binder in water. Lawes et al. applied a desktop inkjet printer to create thin-film silicon anodes of improved specific surface areas [162]. Brown et al. developed a 3D freeze-printing method based on IJP to fabricate porous hybrid anodes from MoS₂/graphene aerogels for

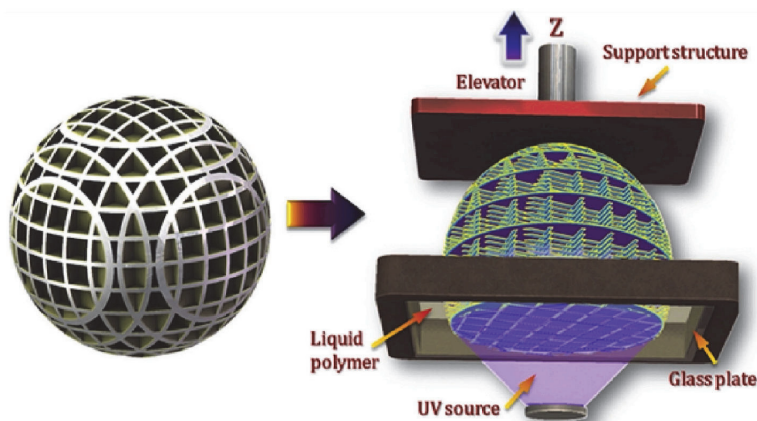


Fig. 6. Schematic illustration of the photopolymerization mechanism in the SL technique [adapted from Elsevier under the Creative Commons CC-BY-NC-ND license (<https://creativecommons.org/licenses/>) [143]].

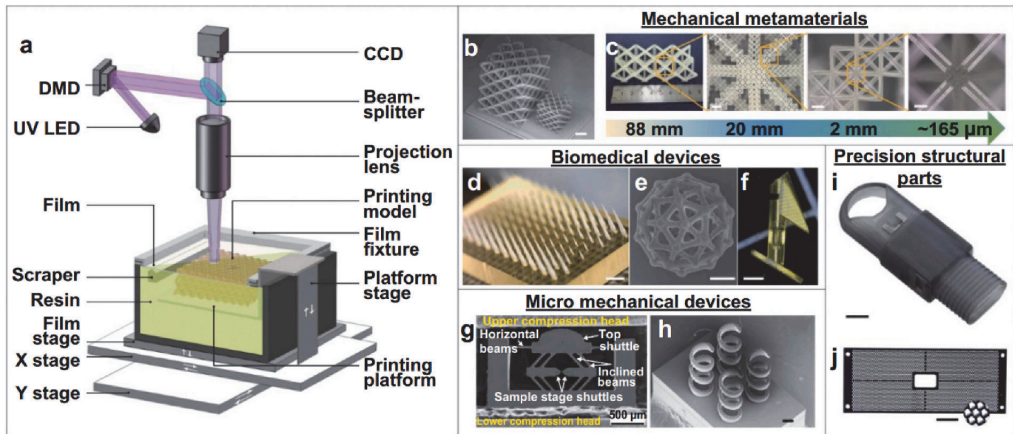


Fig. 7. (a) Schematic illustration of a high-resolution P μ SL system, (b) The AM-processed octet truss geometry from mechanical metamaterial (scale bar: 100 μ m), (c) hierarchical structure of AM-processed mechanical metamaterial with different scale bars, 2 mm, 200 μ m, and 500 μ m respectively from left to right, (d) tilted microneedles for drug injection (scale bar: 1 mm), (e) micro-buckyball for cell cultivation (scale bar: 50 μ m), (f) drainage nail for glaucoma (scale bar: 500 μ m), (g) a micro-mechanical device (MMD) for in-situ tensile testing of micro/nanowires, (h) micro spring array with 20 μ m diameter for each spring (scale bar: 100 μ m), (i) micro-fiber connector with a minimum groove edge thickness of 80 μ m (scale bar: 5 mm), (j) 1700 trapezoidal hole array in micro-socket (scale bar: 12.5 mm) [adapted from IOPscience under the terms of the Creative Commons Attribution 3.0 license (<https://creativecommons.org/licenses/by/3.0/>) [145]].

sodium-ion batteries at freezing temperatures below -25 $^{\circ}$ C [17]. Subsequent annealing of MoS₂/reduced graphene oxide aerogel at 600 $^{\circ}$ C generated several large micro-scale pores (3–5 μ m) in the structure of an AM-processed electrode that facilitated fast ion transport and resulted in a considerable specific capacity of 800 mAh g⁻¹ at 100 mA g⁻¹. However, the specific capacity value was, due to irreversible conversion of MoS₂ into Mo and reversible to Na⁺ insertion, dramatically reduced down to 429 mAh g⁻¹ in the first ten cycles [17]. Hu et al. controlled the width and height of an extruded ink prepared from carbon black, LiMn_xFe_{1-x}PO₄ (LMFP), and poly(vinylidene fluoride) (PVDF) dissolved in *N*-methylpyrrolidone (NMP), by micro-nozzle onto an Al foil [163]. Although the printed electrode demonstrated excellent electrochemical performance (specific capacities of 150.21 mAh g⁻¹ after the first cycle and 140.67 mAh g⁻¹ after 1000 cycles), under the same conditions, the specific capacities of the traditionally coated electrode only reached 103.38 mAh g⁻¹ and 90.64 mAh g⁻¹, respectively. They clearly showed that the thickness of the electrode can dramatically affect the electroactivity of the electrodes processed by the IJP method. They further stated that the porosity in electrodes can affect the Li-ion transport, change the diffusion coefficient in the electrolyte, and decrease the connectivity within the electrolyte. The higher the efficiency porosity, the larger the volume fraction of the electrolyte [163]. Recently, Seo et al. created flexible MoS₂-based photodetector electrodes by the IJP technique. They optimized the stability of MoS₂ by dispersing MoS₂/EC in v/v cyclohexanone/terpineol printed on a graphene substrate. IJP-printed MoS₂ was post-processed by thermal and photonic annealing and showed stability and invariant sensitivity (I_{pc}/I_{dark}) over 500 bending cycles at a radius of curvature of 8.1 mm. They illustrated that the fully IJP-processed electrode can provide a fast photoresponse of 150 μ s and high photoresponsivity of 50 mA W⁻¹. They stated that the improved contact interface between the intermixing surfaces of the photonic annealed MoS₂ and graphene layers can result in lower contact resistance and higher conductivity of dark bulk MoS₂-Gr PA [33]. Shao et al. prepared 3D crumpled 1T-MoS₂ by using an electro-hydrodynamic approach and printed the materials by the IJP technique for supercapacitor applications. The AM-processed 1T-C-MoS₂ and rGO interdigitated patterns directly act as both active electrodes and current collectors because of the high conductivity of the materials. By using reduced graphene oxide in MgSO₄ media, they printed 96

asymmetric micro-supercapacitors (AMSCs) by means of the IJP method, showing a high capacitance of 258 F g⁻¹, capacitance retention of 64% at the scan rate of 100 mV s⁻¹, and a stability of 96% over 20,000 cycles [18]. In summary, despite the advantages of IJP, such as cost-effectiveness of the method, capability of scaling up the products, good multi-material printing ability, and outstanding printing resolution, the use of IJP may be limited due to its requirements for ink formulation, low printing speed, and low durability of the printing head [31,134].

3.2.4. Direct ink writing (DIW)

The DIW, the most well-known AM approach due to its cost-effectiveness, user-friendliness, and ability to process a diversity of materials, is widely used to fabricate batteries, particularly for printing quantum dots (QDs) [165–171]. DIW extrudes ink materials meanwhile the printing resolution is compatible with the nozzle diameter [172, 173]. Pre-processing of DIW includes the preparation of shear-thinning gel-based viscoelastic inks, continuous extrusion of ink material on a substrate, replacement of even stage or nozzle, and layer-by-layer printing on the former layers. Tang et al. applied the advantages of DIW to generate a graphene-aerogels-based electrode shaped like a network with a complex geometry of a programmable feature and with a multi-components homogeneity [171]. They used the AM-processed electrode in symmetric micro-supercapacitor exhibiting enhanced areal capacitance of 639.56 mF cm⁻², retained capacitance of 71.4%, and sustained capacitance of approximately 90% after 10,000 GCD cycles. They illustrated that variation of the thicknesses of Graphene/MWCNT HA electrodes slightly affected the R_s and R_{ct} values. The ion and electron transport was hence not affected due to the highly interconnected network [171]. Chen et al. implemented the outstanding DIW method for processing of fully packaged single-wall carbon nanotube (SWCNTs)-based supercapacitors. They loaded a mixture of SWCNTs, distilled water, sodium n-dodecyl sulfate (SDS), PVA powder, silicon rubber, and Li chloride powder to prepare glue-like gel as the feedstock of the DIW method. Their electrode showed an energy density of 1.18 mWh cm⁻³ and a power density of 11.8 W cm⁻³ whereas the electrode retained ~96.5% of its initial capacitance after 5000 cycles of GCD at 1.32 A cm⁻³. They, furthermore, reported an increase of capacitance after a few cycles at the beginning of the cyclic test due to

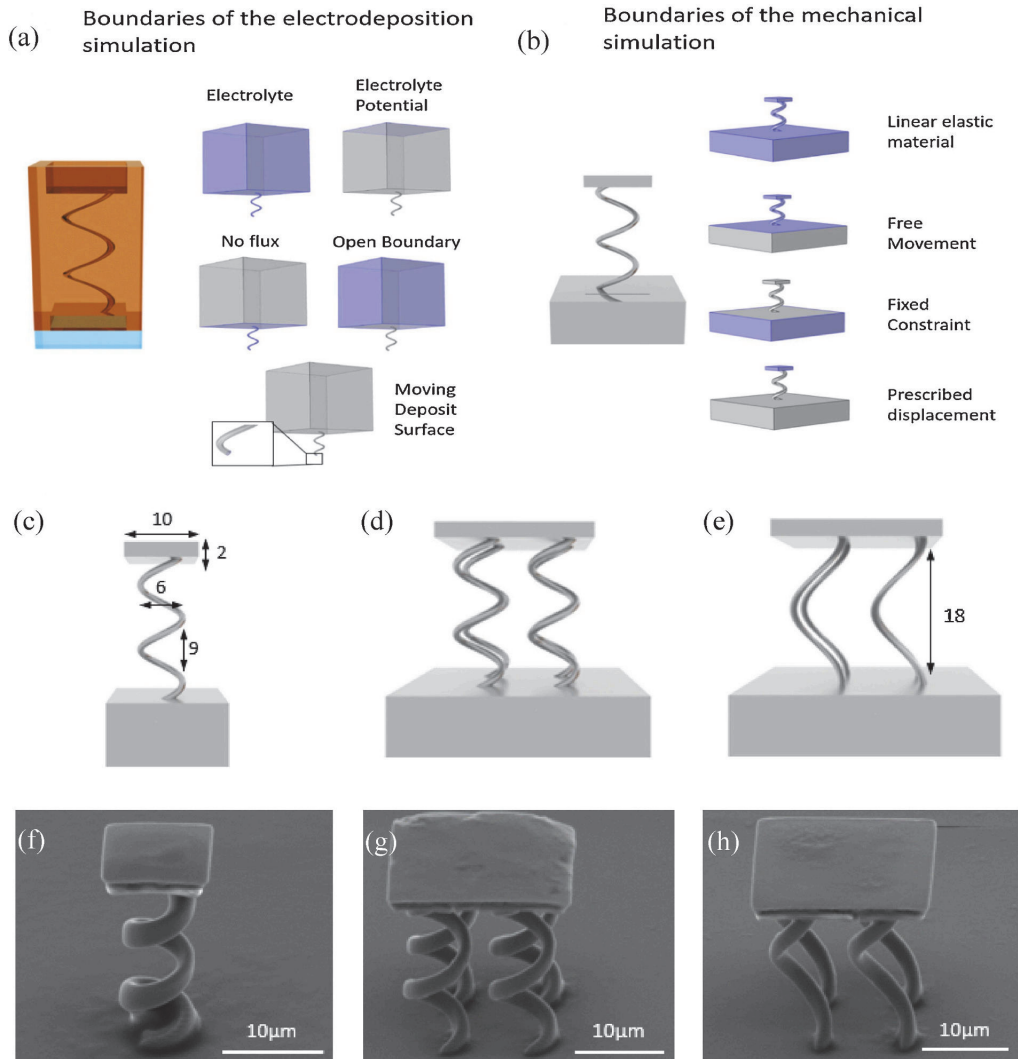


Fig. 8. Schematic illustration of (a) microscopic TAE model boundary definitions, (b) mechanical model boundary definition, (a, c, e) microscale micro-spring designs, (b, d, f) SEM micrographs of the deposited structures at 45° tilt [adapted with permission from Elsevier under the license number 5147880447161 dated Sep. 14th, 2020 [149]].

the increase of SW-CNT surface area induced by the surface activation effect of the charge/discharge process [174]. Wang et al. used DIW to print a 3D interdigitated graphene framework (IGF) support to fabricate NiO/MnO₂ nanostructures for quasi-solid-state planar micro pseudocapacitors. The fabricated electrode delivered a high specific capacity of 220.2 C g⁻¹, a high capacity up to 197.5 mC cm⁻², and stability during 10,000 charge-discharge cycles which were attributed to the superior ion- and electron-transport provided by the AM-processed structure [175]. Wang et al. further developed their electrodes by DIW printing of asymmetric micro-pseudocapacitor electrodes including Ni-Co-O nanosheets on 3D rGO for one electrode and MnO₂ nanosheets on 3D rGO for another counterpart. Fast electron transport and large ionic diffusion led to a specific capacity of 500 mC cm⁻², an energy density of 90 mWh cm⁻², and stability after 10,000 charge-discharge cycles. The growth of pseudocapacitive MnO₂ and NiCoO nanosheets on each side of

the interdigitated cellular microelectrodes led to a wider potential window of up to 1.3 V. On the other hand, the insufficient amount of electrolyte ions can limit the enhancement of electrical transport between the pseudocapacitive materials and current collectors in the AM of interdigitated packed graphene (IPG) microelectrode. Therefore, the AM-processed structure enables continued electrical transport and ionic diffusion which result in fast electrical transport as well as presence of a sufficient amount of diffused electrolyte ions [176]. Yao et al. processed a graphene aerogel/MnO₂ pseudocapacitor by the DIW method. They showed that the simultaneous increase in volumetric, areal, and gravimetric capacitance of the 3D G/MnO₂ electrode was three times higher than those for other electrodes fabricated based on e.g. Ni foam, wood, or carbon-based nanomaterials. They validated the increased areal capacitance by increasing the MnO₂ mass loading and thickness of the electrodes. They demonstrated that the AM-processed graphene aerogel

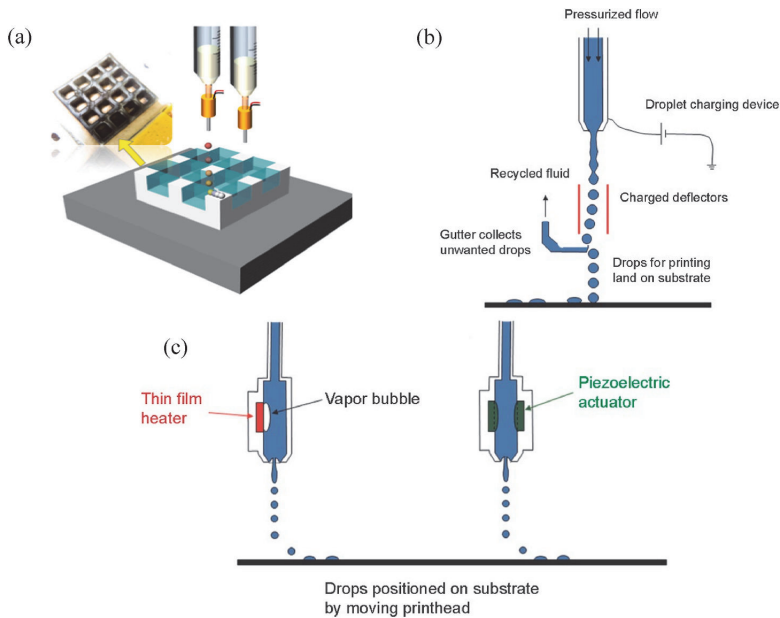


Fig. 9. Schematic illustration of (a) inkjet printing with freezing solidification [adapted with permission from Elsevier under the license number 5147871482683 dated Sep. 14th, 2021 [99]], (b) the operating principles of a continuous inkjet printer (CIJ), (c) the operating principles of a drop-on-demand inkjet printer (DOD) with thermal and piezoelectric actuation [adapted from Elsevier under the terms of the Creative Commons CC-BY 4.0 license (<https://creativecommons.org/licenses/by/4.0/>) [164]].

electrode is capable to load a higher amount of MnO_2 without sluggish ion diffusion observed in the bulk material. They achieved a record high-areal capacitance of 44.13 F cm^{-2} whereas the capacitance retention of 73.2% was recorded via increasing the scan rate from 0.5 to 10 mA cm^{-2} . The DIW-processed electrode showed the triangular shape at different scan rates from 1 to 20 mA cm^{-2} as well as capacitance retention of approximately 90% after 20,000 cycles of galvanostatic charge-discharge (GCD) [177]. Wei et al. printed thick electrodes, including all components, anode, cathode, and separator, by using a four-printing-ink-assisted DIW technique for Li-ion batteries. According to cyclic voltammograms, thick electrodes generated a ten-fold higher peak current at low scan rates. However, the broader redox peaks and peak-to-peak potential differences resulted from slower kinetics. Excellent Coulombic efficiencies and areal capacities over several months of continuous cycling were observed for both thin and thick electrodes. On the other hand, the energy efficiency of thick electrodes fell off considerably with increased number of cycles, probably due to increased voltage polarization. Their DIW-processed electrode delivered a capacity of 4.45 mAh cm^{-2} whereas the areal energy density of 20 mWh cm^{-2} and power density of 1 mW cm^{-2} were achieved for ultra-thick electrodes compared with thin electrodes [170]. Zhang et al. printed 3D electrodes by DIW from a mass of monodispersed sol-gel SnO_2 quantum dot (QD) ink mixed with GO and water [168]. The freeze-drying post-processing stage incorporated micro-pores which resulted in high charge capacity, reversible capacity, and excellent cycling stability. The AM-processed electrodes demonstrated an ultrahigh specific capacitance of 991.6 mAh g^{-1} due to improved kinetics for both electrons and ions. Moreover, the high areal capacity of 5.0 mAh cm^{-2} was achieved for 6-layer 3D-printed electrodes. The superior rheological properties of the hybrid ink led to the excellent structural integrity of micro-lattices which in turn lead to well-designed additively manufactured constructions with a porous structure able to maintain a liquid electrolyte within the 3D construction. This facilitated the access of electrolyte to the active materials, and subsequently in good rate capability of the 3DP- SnO_2 QDs/G architectures [168]. Yang et al., recently, directly processed an octadecane (OD)/graphene (BOG) phase change micro-lattices by DIW technique [178]. They showed that OD,

encapsulated and interconnected by graphene, is able to spread light into the interior structure of the micro-lattice, harvest, store, and transfer the solar-thermal energy. Furthermore, they achieved a phase change enthalpy of 190 J g^{-1} and stability at 1000 thermal cycles [178]. Lyu et al. processed a microporous metal-organic framework (MOF) derived carbon-based nanocomposite by DIW for subsequent deposition of Li_2O_2 for Li- O_2 batteries. They showed that the existence of micrometer-sized pores formed between Co-MOF-derived carbon flakes improved the efficient deposition and facilitated the decomposition of Li_2O_2 particles in presence of Co electrocatalysts. Hence, a self-standing porous structure could provide a high discharge capacity of 525 mAh g^{-1} , a specific power density of 5.5 W kg^{-1} , and a high specific energy density of 798 Wh kg^{-1} [165]. Li et al. applied a novel multiscale process combining DIW with applied electric field treatment to regulate its internal structure during printing of Li-ion batteries. The macro-controlled hybrid AM-processed structure illustrated a high areal capacity (3.1 mAh cm^{-2}) which was 200% higher than a conventional laminated structure. However, the reduction of capacity at high C-rates was attributed to high ohmic resistance in their macro-controlled 3D structure. The results verify that manipulating the microstructures via induction of an electric field (EF) can improve the electrocatalytic performance of macro-controlled 3D constructions. EF can positively affect the transport of Li-ions and the capability rate [179]. The drawbacks of DIW-processed 3D parts include weak mechanical strength, complex requirements for gel-based viscoelastic inks, insufficient yield stress, and insufficient storage modulus [134,135]. Three different mechanisms (pneumatic, piston, screw) of ink extrusion onto a substrate are illustrated in Fig. 10 (a). The ink can be heated up to improve the quality and resolution of the AM-processed structure (Fig. 10 (b)).

3.2.5. Aerosol jet printing (AJP)

The AJP is a novel contactless direct write approach that can aerosolize a wide range of functional materials with different bandgaps to form small ink droplets focused onto a substrate utilizing carrier gas flow (Fig. 11) [182–188]. 2D and 3D electronic circuits and devices can be printed due to the high-resolution, non-contact, and mask-free mechanism of AJP [187]. Saleh et al. applied AJP to print 3D porous

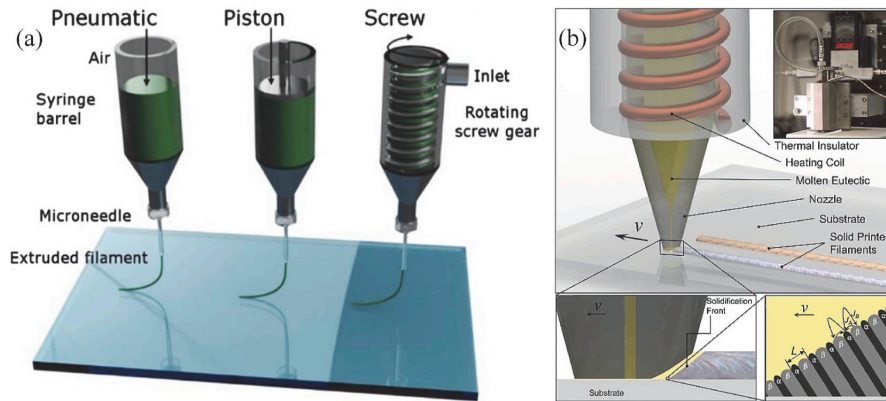


Fig. 10. (a) Schematic illustration comparing the mechanism of nozzle-based extrusion in DIW [adapted from AIMS Press under the terms of the Creative Commons Attribution Licence (<http://creativecommons.org/licenses/by/4.0>) [180]], (b) overview of HOT-DIW printing system and list of components for molten eutectic inks writing with a nozzle inner diameter of $\approx 200 \mu\text{m}$ which can print eutectic phase including the dark lamellae (α -phase) and the light gray lamellae (β -phase) [adapted with permission from John Wiley and Sons under the license number 5147870782811 dated Sep. 14th, 2021 [181]].

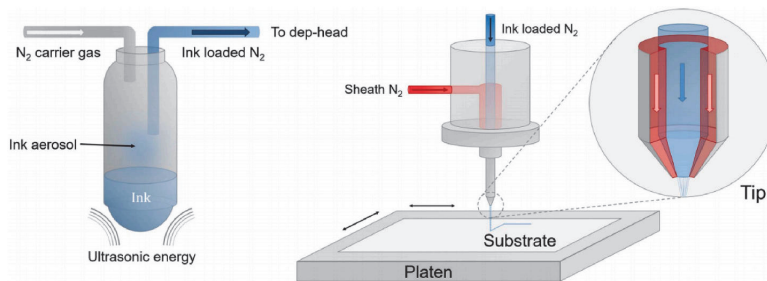


Fig. 11. Schematic illustration of the Aerosol-jet printing technique [adapted from IOPscience under the terms of the Creative Commons Attribution 3.0 license (<https://creativecommons.org/licenses/by/3.0/>) [190]].

micro-lattice electrodes of Ag nanoparticles with outstanding mechanical strength and considerably improved areal capacity and specific capacity up to 100% and 400%, respectively. Their AM-processed electrodes showed a stable maximum specific capacitance of 95 mAh g^{-1} , though that an increased thickness of lattice-shaped electrodes can result in a reduction in capacity down to 20% due to blocking of the channels, decreased geometric surface area as well decreased the ion-accessibility between electrode and electrolyte [189].

3.2.6. Fused deposition modeling (FDM)

The FDM is the most capable AM technology which is able to create complex shapes without any material waste. The feedstock of FDM can be thin thermoplastic filaments (polylactic acid (PLA), polycarbonate (PC), polystyrene (PS), acrylonitrile butadiene styrene (ABS), polyphenylsulfone (PPSF), and polyamide (PA)) that can be transformed into a semiliquid state at the nozzle head, be extruded, and immediately solidified onto the platform. Wei et al. applied FDM to print extruded filament of graphene-ABS [191]. They showed that the addition of 3.8 wt% of graphene considerably increased the conductivity up to $6.4 \times 10^{-5} \text{ S m}^{-1}$. However, their AM-processed structure showed a lower electrical conductivity of $2.5 \times 10^{-7} \text{ S m}^{-1}$ due to the generation of internal voids during the FDM process. Finally, the highest printable feedstock which contained 5.6 wt% graphene resulted in an increased electrical conductivity of $1.05 \times 10^{-3} \text{ S m}^{-1}$ [189]. Maurel et al. printed a 3D structure of graphite/PLA as a homogeneous negative electrode disk for Li-ion batteries [192]. They obtained a reversible capacity of

200 mAh g^{-1} after six cycles at a current density of 18.6 mA g^{-1} . However, the capacitance was reduced to 15 mAh g^{-1} by increasing the GCD current density up to 186 mA g^{-1} . The active materials (carbon black and carbon nanofiber) improved the conductivity of the filament, enhanced the electrochemical performance, and provided sufficient mechanical strength to AM-processed electrodes. The addition of active materials further electronically connected some isolated active particles to the percolating network [192]. Rohaizad et al. utilized the FDM method for relatively fast and simple AM of an Ag/AgCl pseudo-reference electrode. They printed PLA/graphene followed by electrodeposition of Ag onto the printed electrodes and bleached it to form AgCl. Cyclic voltammetry of two redox systems showed the similarity of shapes and intensities between printed electrodes and commercial reference electrodes [193]. Reyes et al. printed a full Li-ion battery cell, including separators, cathode, anode, current collectors, and frame from improved ion conductive PLA by using an FDM method [194]. They proposed a ratio of 80:20 of conductive to active material toward obtaining the maximum battery capacity. The highest specific capacitance of 7.48 mAh cm^{-3} was achieved by an additively manufactured LTO-graphene anode structure. In parallel to the AM-processed LMO-MWNT cathode structure, the highest specific capacity of 9.74 mAh cm^{-3} was achieved. Finally, the full-cell of the AM-processed Li-ion battery demonstrated a large reduction in capacitance from 22.96 to 9.4 mAh cm^{-3} after only 10 cycles and subsequently 5.32 mAh cm^{-3} after 50 cycles of charge-discharge. They approved the versatility of AM with customizable wearable electronics via integration of the printed

batteries with printed liquid crystal display (LCD) sunglasses and an LED bangle [194]. FDM can be considered as a user-friendly, cost-effective, and rapid method which does not demand chemical post-processing, and has large-size capabilities which can facilitate the integration of AM-processed batteries with different AM-processed electronics. However, some disadvantages of the FDM method include overall procedure complexity due to mixing electroactive materials with thermoplastics, heating the filament to glass transit state, low printing resolution, low printing accuracy and controllability, and low manufacturing speed [31, 134,135]. The principle of the FDM method is depicted in Fig. 12 (a) and the mechanism of the combination of hot-melt extrusion (HME) and the FDM technique for well-controlled AM of medical applications is illustrated in Fig. 12 (b).

3.2.7. Laser-based powder bed fusion (L-PBF)

The L-PBF processes are AM technologies that use a laser beam or an electron beam to fuse powder particles in a layer-by-layer fashion to fabricate complex three-dimensional (3D) structures dictated by a CAD design [123]. L-PBF is commonly known as selective laser melting (SLM) [197–201]. This technology completely fuses loose metal powders and converts them into near-net-shape parts. The density of the parts largely depends on given process parameters [202]. SLM is an AM process that

can fabricate a wide spectrum of materials such as Fe-based alloys [198, 203–205], Ti-based alloys [206–209], Al-based alloys [197,210–213], and Cu-based alloys [200,214] as well as crystalline [212,215,216], quasi-crystalline [217], and amorphous materials [218–220]. Recently, composites, high entropy alloys, and metal/ceramic composites (cermets) have also been fabricated by SLM [221–227]. On the other hand, SLS employs sintering (solid/liquid state) of the powder using a laser (as an energy source) and may include partial powder melting [228]. The laser slowly and steadily scans the powder bed and sinters a thin layer of powders. The powder is not sufficiently heated up to be melted completely [229]. Given process parameters not only dictate the defect level in the fabricated materials (like porosity, cracks, etc.) but also influence the microstructure and the mechanical properties [220, 230–232]. A schematic illustration describing the operating principle of the layer-by-laser SLM process is displayed in Fig. 13.

Processing of high-density ceramics with remarkable mechanical properties for different industrial and medical applications requires the use of advanced manufacturing processes like SLM/SLS. Even though several electroactive ceramics for electrochemical and energy-based applications have successfully been fabricated by the AM techniques [50,99,234,235], only a few reports are available. Scotti et al. printed 3D microfluidic-based micro fuel cells (MFCs) from stainless steel by

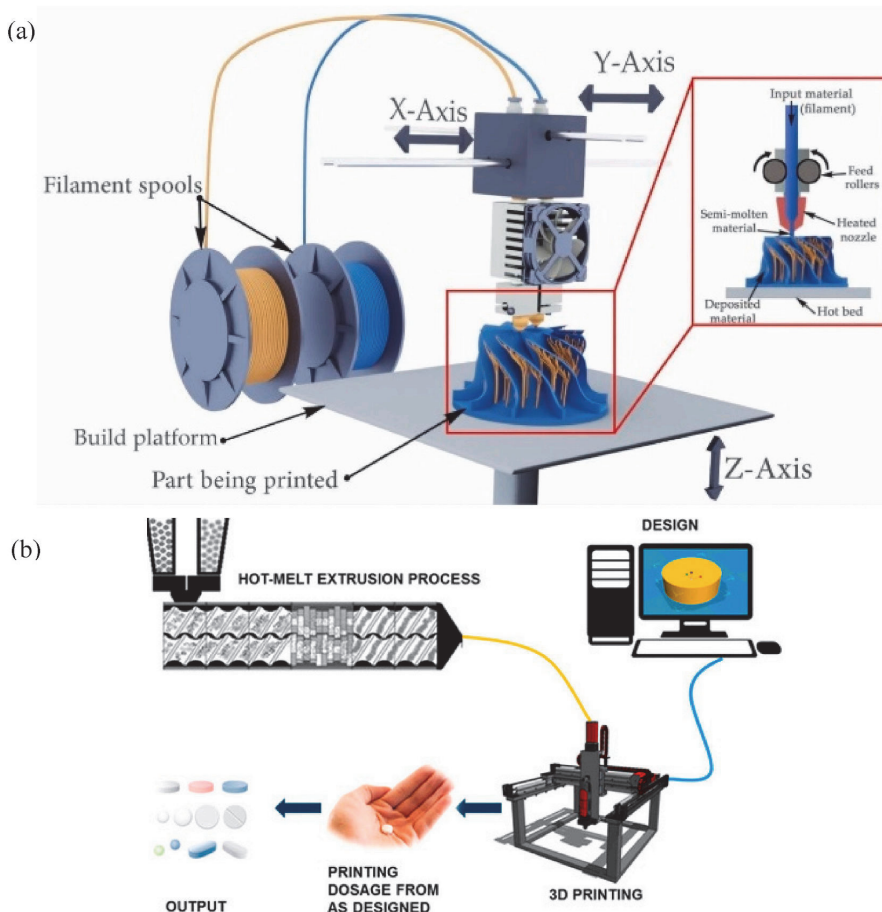


Fig. 12. Schematic illustration of (a) fused deposition modeling (FDM) [adapted from MDPI AG under an open access Creative Common CC BY license (<https://www.mdpi.com/openaccess>) [195]], (b) combination of hot-melt extrusion (HME) and FDM techniques [adapted from MDPI AG under an open access Creative Common CC BY license (<https://www.mdpi.com/openaccess>) [196]].

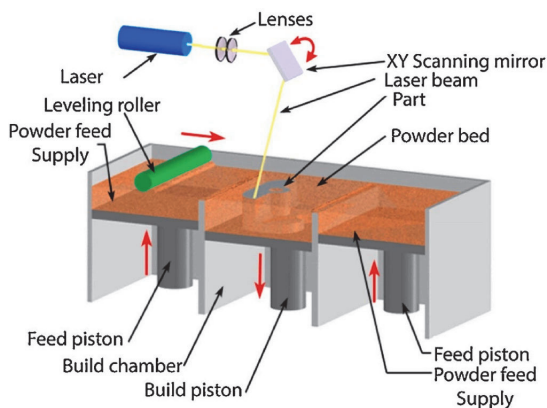


Fig. 13. Schematic illustration describing the operating principle of the SLM process [adapted with permission from Elsevier under the license number 5147820184620 dated Sep. 14th, 2021 [233].

using of SLM technique. Their miniaturized MFC with enclosed cavities obtained a current density of 1.515 A cm^{-2} and a power density of 363 mW cm^{-2} [236]. Dawson et al. applied SLM to fabricate metallic bipolar plates of stainless steel 316L for PEMFCs and approved the capability of SLM for AM of plates [237]. The electrochemical performance was the same as plates manufactured by CNC milling. The current density reported from the AM-processed device was only 200 mA cm^{-2} at a voltage of 0.5 V [237]. Bermúdez et al. applied the SLM process for printing of a porous gas diffusion layer of 316L stainless steel instead of carbon-based substrates in a multilayer tubular high-temperature proton exchange membrane fuel cell (HT-PEMFC) [238]. They showed that porosity of 16% resulted in a power density of 329.25 W m^{-2} in 160°C , H_2/air atmosphere at ambient pressure. The current density was 125.52 A m^{-2} after 5 h of operation [238]. Even though Jafari et al. highlighted the potential of using the SLM technology to fabricate heat transfer devices for thermal energy conversion applications, they have not addressed the SLM processing of ceramics [239]. Similarly, Nofal et al. fabricated phase change materials by SLS for thermal energy storage applications with thermal conductivity in the range between 1.4 and $1.9 \text{ W m}^{-1} \text{ K}^{-1}$ for single-layer and $0.75\text{--}0.80 \text{ W m}^{-1} \text{ K}^{-1}$ for multi-layer samples. Besides, the latent heat of fabricated samples was in the range of $161\text{--}166 \text{ kJ kg}^{-1}$ for both single-layer and multi-layer structures [240]. Zhao et al. fabricated and studied a 3D-Ti-based electrode created using SLM for supercapacitor applications [241] being comparable to electrodes fabricated by lithography. The assembled solid-state supercapacitor, in which the SLM-printed electrode was used as a charge delivering part of the supercapacitor and not as an electroactive part, delivered a volumetric capacitance of 2.4 F cm^{-3} , an energy density of 213.5 Wh m^{-3} , and a power density of 15.0 kW m^{-3} at a current density of 37.4 mA cm^{-3} [241]. Cheng et al. recently compared the potentials of the SLS, SLA, and DIW methods for the fabrication of EES and electrode/electrolyte architectures [134,136] and has elucidated the advantages of AM, including SLM.

Even though some AM technologies have been widely used for EES applications, laser-based powder bed processes such as SLM and SLM are barely used for polymers [99,134]. Despite the cost factors involved in the SLM and SLS processes (raw materials cost, installation cost, running costs, etc.), both processes can fabricate a wider spectrum of materials. These near-net-to-shape processes can fabricate intricate parts such as current collector, electroactive parts for EES devices, etc. directly from metal powders with added functionalities and without any additional additives or binders [134]. Aspects such as weight reduction, improved design characteristics, and improved functionality can compensate for

the cost factor and overcome the most of disadvantages of conventional EES fabrication methods. L-PBF-based processes can further eliminate deficiencies of other AM methods, such as expensive pre-processing stages, multi-step-wise processing to deliver desired functionality to AM-processed structures, post-processing, lack of mass production, etc. As any fusible powder can be directly processed by L-PBF methods, these non-contact methods can be used for rapid prototyping of energy storage systems [229].

3.3. An overview of AM techniques

Regarding the potentials of the AM techniques mentioned above, a majority of them have been widely studied for processing of 0D (nanoparticles, quantum dots, etc.), 1D (carbon nanotubes, etc.), 2D nanomaterials (graphene, graphene oxide, TMDs, MoS_2 , etc.), and cellular materials [31,134,135,242]. Although the strengths of various AM techniques have been progressed by the differentiation of printing mechanisms or the integration of AM methods with conventional methods, each technique still has its specific limitations which may hinder the scaling-up of AM products for industrial manufacturing. Several industries have though been founded based on L-PBF techniques. Despite differences in material and product scales, L-PBF-based methods can overcome many of the disadvantages of other AM techniques. For instance, preparation and formulation of feedstock are for most methods considered as complex, time-consuming, and expensive pre-processing stages. No pre-processing of the materials can be carried out before L-PBF processing of many powder materials. As previously discussed, several AM techniques (HL, SLA, DIW, IJP) can generate 3D structures (lattice, scaffold, etc.) and the functionality of the AM-processed structures can be subsequently added to the structures via other conventional methods such as electrodeposition or electrophoretic deposition. It means that the functionality, particularly the energy storage capability, is indirectly delivered to an AM-processed structure. L-PBF is, though, supposed to be able to directly print functional 3D structures. The photo-curing or heat treatment post-processing stage is inevitable for subsequent solidification of 3D structures created by the SLA technique, but not essential for certain kinds of L-PBF-processed parts. Disadvantages such as lack of mass production and poor mechanical properties of DIW-processed and TAE-processed parts can be solved by employing L-PBF-based methods.

4. Authors' view: processing of MoS_2 with laser-based powder bed fusion technique

The multifunctional properties of MoS_2 , an electroactive 2D TMDs, make the material a promising candidate for different applications. Preparation and processing of MoS_2 electrodes via conventional methods include several and complex pre-processing stages such as exfoliation, preparation, and deposition. Some drawbacks such as lack of reliable large-scale production and lack of precise morphology control can be considered as limitations of these pre-processing stages. On the other hand, expensive complementary post-processing stages can be accompanied by further drawbacks such as limitation of geometric and specific surface area, special chemical requirements, thermal treatment, and acid treatment. These drawbacks limit the possibility of conventional methods to scale up MoS_2 -based structures for industrial applications.

As previously described, some AM techniques have processed MoS_2 -based 3D structures for electrochemical and energy-based applications. However, there still exist several drawbacks regarding the mechanisms of the AM techniques such as expensive pre-processing stages, multi-step-wise processing to deliver desired functionality to AM-processed structure, post-processing stages, and lack of mass production.

Employing novel AM processes like laser-based powder bed fusion can though overcome the observed drawbacks of both conventional manufacturing processes and AM approaches to fabricate MoS_2 -based

3D structures. Their applications can be extended from electrocatalytic devices and electrodes to medical and bioactive parts if fabricated as AM-processed structures. Since there is limited attention related to the processing of MoS₂-based composites by SLS/SLM, extensive research should be carried out in the above-mentioned fields to reap the functional benefits of MoS₂-based structures, especially in (but not limited to) electrochemical sensing, battery, hydrogen evolution cell, self-lubrication applications.

5. Summary, prospects, and conclusion

MoS₂ owing to its multifunctional properties is promising for different applications. The conventional MoS₂ preparation includes several and complex pre-processing stages such as exfoliation, purification, deposition, etc. The lack of reliable large-scale production or lack of precise morphology control can be considered as the drawbacks of these pre-processing stages. On the other hand, further drawbacks such as limitation of geometric and specific surface area, special chemical requirements, thermal treatment, acid treatment, etc. can be considered as the expensive complementary post-processing stages.

The AM processes can fabricate the current collector, the electroactive components (anode and cathode), and even the porous separator. Some of the additive manufacturing techniques have processed MoS₂-based 3D structures for electrochemical and energy-based applications. However, there still exist several drawbacks regarding the mechanisms of AM techniques, such as expensive pre-processing stages, multi-step-wise processing to deliver desired functionality to AM-processed structure, post-processing stages, and lack of mass production.

As it has already been studied that laser is a good source for exfoliation of MoS₂, the effective use of novel AM processes like laser-based powder bed fusion (L-PBF) can overcome the drawbacks observed from both conventional manufacturing processes and AM approaches. toward the fabrication of highly porous MoS₂-based additively manufactured structures. It is suggested that processing of MoS₂-based structures by L-PBF not only can create complex porous 3D designs but also can simultaneously exfoliate the MoS₂ and change its phase from bulk 2H to metallic 1T; hence, the L-PBF technique will lead to rapid, low-cost (considering the functionality that the AM process can impart), energy-efficient, and eco-friendly production of MoS₂-based materials.

Since there is limited attention to the processing of MoS₂-based composites by L-PBF techniques, extensive research should be carried out in the above-mentioned fields to extend and reap the functional benefits of MoS₂-based structures, especially in (but not limited to) electrochemical sensing, energy storage, hydrogen evolution cell, medical and bioactive parts, and self-lubrication applications. Overall, SLM/SLS of MoS₂-based electroactive structures can generate promising advanced energy conversion/storage applications based on the present industrial demands such as Li-ion batteries, Na-ion batteries, supercapacitors, electric vehicles, etc. Beyond the scope of this review, it is noteworthy to consider that laser-based AM techniques have yet to fully reach their outstanding potential in the manufacturing of 3D structures from 2D TMDs, and it would be suggested as a promising method for the next generation systems and technologies.

CRedit authorship contribution statement

Navid Alinejadian: Validation, Conceptualization, Writing – review & editing, Writing – original draft. **Lauri Kollo:** Supervision, Validation, Writing – review & editing. **Inger Odneval:** Validation, Writing – review & editing.

Declaration of competing interest

The authors declare the following financial interests/personal relationships which may be considered as potential competing interests: This research was funded by European Regional Development Fund

[ASTRA6-6], the Estonian Education and Youth Board [contract number: 5.10-6.1/21/23-4], and Estonian Government.

Acknowledgment

This research was funded by European Regional Development Fund [ASTRA6-6], the Estonian Education and Youth Board and Estonian Government [contract number: 5.10-6.1/21/23-4]. Prof. Prashanth Konda Gokuldoss is appreciated for sharing his initial opinions.

References

- [1] J. Lu, H. Liu, E.S. Tok, C.-H.H. Sow, Interactions between lasers and two-dimensional transition metal dichalcogenides, *Chem. Soc. Rev.* 45 (2016) 2494–2515, <https://doi.org/10.1039/c5cs00553a>.
- [2] R. Ganatra, Q. Zhang, Few-layer MoS₂: a promising layered semiconductor, *ACS Nano* 8 (2014) 4074–4099, <https://doi.org/10.1021/nn405938z>.
- [3] M. Chhowalla, H.S. Shin, G. Eda, L.J. Li, K.P. Loh, H. Zhang, The chemistry of two-dimensional layered transition metal dichalcogenide nanosheets, *Nat. Chem.* 5 (2013) 263–275, <https://doi.org/10.1038/nchem.1589>.
- [4] X. Li, H. Zhu, Two-dimensional MoS₂: properties, preparation, and applications, *J. Mater.* 1 (2015) 33–44, <https://doi.org/10.1016/j.jmat.2015.03.003>.
- [5] A.K. Geim, I.V. Grigorieva, Van der Waals heterostructures, *Nature* 499 (2013) 419–425, <https://doi.org/10.1038/nature12385>.
- [6] C. Yelgel, C. Yelgel, O. Gülsüren, Structural and electronic properties of MoS₂, WS₂, and WS₂/MoS₂ heterostructures encapsulated with hexagonal boron nitride monolayers, *J. Appl. Phys.* 122 (2017), <https://doi.org/10.1063/1.4998522>.
- [7] S. Wi, H. Kim, M. Chen, H. Nam, L.J. Guo, E. Meyhofer, X. Liang, Enhancement of photovoltaic response in multilayer MoS₂ induced by plasma doping, *ACS Nano* 8 (2014) 5270–5281, <https://doi.org/10.1021/nn5013429>.
- [8] S. Ding, D. Zhang, J.S. Chen, X.W. Lou, Facile synthesis of hierarchical MoS₂ microspheres composed of few-layered nanosheets and their lithium storage properties, *Nanoscale* 4 (2012) 95–98, <https://doi.org/10.1039/c1nr11552a>.
- [9] Y. Li, H. Wang, L. Xie, Y. Liang, G. Hong, H. Dai, MoS₂ nanoparticles grown on graphene: an advanced catalyst for the hydrogen evolution reaction, *J. Am. Chem. Soc.* 133 (2011) 7296–7299, <https://doi.org/10.1021/ja201269b>.
- [10] W. Wu, L. Wang, Y. Li, F. Zhang, L. Lin, S. Niu, D. Chenet, X. Zhang, Y. Hao, T. F. Heinz, J. Hone, Z.L. Wang, Piezoelectricity of single-atomic-layer MoS₂ for energy conversion and piezotronics, *Nature* 514 (2014) 470–474, <https://doi.org/10.1038/nature13792>.
- [11] Y. Huang, J. Guo, Y. Kang, Y. Ai, C.M. Li, Two dimensional atomically thin MoS₂ nanosheets and their sensing applications, *Nanoscale* 7 (2015), <https://doi.org/10.1039/c5nr06144j>, 19358–19376.
- [12] A. Castellanos-Gomez, M. Barkelid, A.M. Goossens, V.E. Calado, H.S.J.J. Van Der Zant, G.A. Steele, Laser-Thinning of MoS₂: on Demand generation of a single-layer semiconductor, *Nano Lett.* 12 (2012) 3187–3192, <https://doi.org/10.1021/nl301164v>.
- [13] H. Lin, X. Chen, H. Li, M. Yang, Y. Qi, Hydrothermal synthesis and characterization of MoS₂ nanorods, *Mater. Lett.* 64 (2010) 1748–1750, <https://doi.org/10.1016/j.matlet.2010.04.032>.
- [14] L. Hu, X. Shan, Y. Wu, J. Zhao, X. Lu, Laser thinning and patterning of MoS₂ with layer-by-layer precision, *Sci. Rep.* 7 (2017) 1–9, <https://doi.org/10.1038/s41598-017-15350-4>.
- [15] Z. Zhou, Y. Lin, P. Zhang, E. Ashalley, M. Shafa, H. Li, J. Wu, Z. Wang, Hydrothermal fabrication of porous MoS₂ and its visible light photocatalytic properties, *Mater. Lett.* 131 (2014) 122–124, <https://doi.org/10.1016/j.matlet.2014.05.162>.
- [16] X. Li, G. Wu, J. Chen, M. Li, W. Li, T. Wang, B. Jiang, Y. He, L. Mai, Low-crystallinity molybdenum sulfide nanosheets assembled on carbon nanotubes for long-life lithium storage: unusual electrochemical behaviors and ascending capacities, *Appl. Surf. Sci.* 392 (2017) 297–304, <https://doi.org/10.1016/j.apsusc.2016.09.055>.
- [17] E. Brown, P. Yan, H. Tekik, A. Elangovan, J. Wang, D. Lin, J. Li, 3D printing of hybrid MoS₂-graphene aerogels as highly porous electrode materials for sodium ion battery anodes, *Mater. Des.* 170 (2019) 107689, <https://doi.org/10.1016/j.matdes.2019.107689>.
- [18] Y. Shao, J.H. Fu, Z. Cao, K. Song, R. Sun, Y. Wan, A. Shamim, L. Cavallo, Y. Han, R.B. Kaner, V.C. Tung, 3D crumpled ultrathin 1T MoS₂ for inkjet printing of Mg-ion asymmetric micro-supercapacitors, *ACS Nano* 14 (2020) 7308–7318, <https://doi.org/10.1021/acsnano.0c02585>.
- [19] S. Wang, G. Li, G. Du, X. Jiang, C. Feng, Z. Guo, S.J. Kim, Hydrothermal synthesis of molybdenum disulfide for lithium ion battery applications, *Chin. J. Chem. Eng.* 18 (2010) 910–913, [https://doi.org/10.1016/S1004-9541\(09\)60147-6](https://doi.org/10.1016/S1004-9541(09)60147-6).
- [20] M.R. Gao, Y.F. Xu, J. Jiang, S.H. Yu, Nanostructured metal chalcogenides: synthesis, modification, and applications in energy conversion and storage devices, *Chem. Soc. Rev.* 42 (2013) 2986–3017, <https://doi.org/10.1039/c2cs35310e>.
- [21] L. Cao, S. Yang, W. Gao, Z. Liu, Y. Gong, L. Ma, G. Shi, S. Lei, Y. Zhang, S. Zhang, R. Vajtai, P.M. Ajayan, Direct laser-patterned micro-supercapacitors from printable MoS₂ films, *Small* 9 (2013) 2905–2910, <https://doi.org/10.1002/sml.201203164>.

- [22] K.H.S. Kim, K.H.S. Kim, Y. Nam, J. Jeon, S. Yim, E. Singh, J.Y. Lee, S.J. Lee, Y. S. Jung, G.Y. Yeom, D.W. Kim, Atomic layer etching mechanism of MoS₂ for nanodevices, *ACS Appl. Mater. Interfaces* 9 (2017) 11967–11976, <https://doi.org/10.1021/acami.6b15886>.
- [23] Y. Yao, Z. Lin, Z. Li, X. Song, K.S. Moon, C.P. Wong, Large-scale production of two-dimensional nanosheets, *J. Mater. Chem.* 22 (2012) 13494–13499, <https://doi.org/10.1039/c2jm30587a>.
- [24] X. Zhou, B. Xu, Z. Lin, D. Shu, L. Ma, Hydrothermal synthesis of flower-like MoS₂ nanospheres for electrochemical supercapacitors, *J. Nanosci. Nanotechnol.* 14 (2014) 7250–7254, <https://doi.org/10.1166/jnn.2014.8929>.
- [25] J. Zhou, G. Fang, A. Pan, S. Liang, Oxygen-incorporated MoS₂ nanosheets with expanded interlayers for hydrogen evolution reaction and pseudocapacitor applications, *ACS Appl. Mater. Interfaces* 8 (2016) 33681–33689, <https://doi.org/10.1021/acami.6b11811>.
- [26] S. Mukherjee, Z. Ren, G. Singh, Beyond graphene anode materials for emerging metal ion batteries and supercapacitors, *Nano-Micro Lett.* 10 (2018), <https://doi.org/10.1007/s40820-018-0224-2>.
- [27] E. Cohen, S. Menkin, M. Lifshits, Y. Kamir, A. Gladkikh, G. Kosa, D. Golodnitsky, Novel rechargeable 3D-microbatteries on 3D-printed-polymer substrates: feasibility study, *Electrochim. Acta* 265 (2018) 690–701, <https://doi.org/10.1016/j.electacta.2018.01.197>.
- [28] A. Sajedi-Moghaddam, E. Rahmani, N. Naseri, Inkjet-Printing Technology for supercapacitor application: current state and perspectives, *ACS Appl. Mater. Interfaces* 12 (2020) 34487–34504, <https://doi.org/10.1021/acami.0c07689>.
- [29] H. Ning, J.H. Pikul, R. Zhang, X. Li, S. Xu, J. Wang, J.A. Rogers, W.P. King, P. V. Braun, Holographic patterning of high-performance on-chip 3D lithium-ion microbatteries, *Proc. Natl. Acad. Sci. U. S. A.* 112 (2015) 6573–6578, <https://doi.org/10.1073/pnas.1423889112>.
- [30] P. Chang, H. Mei, Y. Tan, Y. Zhao, W. Huang, L. Cheng, A 3D-printed stretchable structural supercapacitor with active stretchability/flexibility and remarkable volumetric capacitance, *J. Mater. Chem. A* 8 (2020) 13646–13658, <https://doi.org/10.1039/d0ta04460a>.
- [31] Y. Pang, Y. Cao, Y. Chu, M. Liu, K. Snyder, D. MacKenzie, C. Cao, Additive manufacturing of batteries, *Adv. Funct. Mater.* 30 (2020) 1–22, <https://doi.org/10.1002/adfm.201906244>.
- [32] H. Zhang, X. Yu, P.V. Braun, Three-dimensional bicontinuous ultrafast-charge and-discharge bulk battery electrodes, *Nat. Nanotechnol.* 6 (2011) 277–281, <https://doi.org/10.1038/nnano.2011.38>.
- [33] J.W.T. Seo, J. Zhu, V.K. Sangwan, E.B. Secor, S.G. Wallace, M.C. Hersam, Fully inkjet-printed mechanically flexible MoS₂ nanosheet photodetectors, *ACS Appl. Mater. Interfaces* 11 (2019) 5675–5681, <https://doi.org/10.1021/acami.8b19817>.
- [34] M.U. Jewel, M.A. Monne, B. Mishra, M.Y. Chen, Inkjet-printed molybdenum disulfide and nitrogen-doped graphene active layer high on/off ratio transistors, *Molecules* 25 (2020) 1–7, <https://doi.org/10.3390/molecules25051081>.
- [35] A. Gallardo, Y. Pereyra, E. Martínez-Campos, C. García, D. Acitores, I. Casado-Losada, M.A. Gómez-Fatou, H. Reinecke, G. Ellis, D. Acevedo, J. Rodríguez-Hernández, H.J. Salavagione, Facile one-pot exfoliation and integration of 2D layered materials by dispersion in a photocurable polymer precursor, *Nanoscale* 9 (2017) 10590–10595, <https://doi.org/10.1039/c7nr03204h>.
- [36] X. Wang, T. Li, H. Ma, D. Zhai, C. Jiang, J. Chang, J. Wang, C. Wu, A 3D-printed scaffold with MoS₂ nanosheets for tumor therapy and tissue regeneration, *NPG Asia Mater.* 9 (2017), <https://doi.org/10.1038/am.2017.47>.
- [37] J. Li, M.M. Nairini, S. Vaziri, M.C. Lemme, M. Östling, Inkjet printing of MoS₂, *Adv. Funct. Mater.* 24 (2014) 6524–6531, <https://doi.org/10.1002/adfm.201400984>.
- [38] J. Li, M.C. Lemme, M. Östling, Inkjet printing of 2D layered materials, *ChemPhysChem* 1 (2014) 408–412, <https://doi.org/10.1002/cphc.200>.
- [39] J.N. Coleman, M. Lotya, A. O'Neill, S.D. Bergin, P.J. King, U. Khan, K. Young, A. Gaucher, S. De, R.J. Smith, I.V. Shvets, S.K. Arora, G. Stanton, H.Y. Kim, K. Lee, G.T. Kim, G.S. Duesberg, T. Hallam, J.J. Boland, J.J. Wang, J.F. Donegan, J. C. Grunlan, G. Moriarty, A. Shmeliov, R.J. Nicholls, J.M. Perkins, E.M. Grievson, K. Theuvsissen, D.W. McComb, P.D. Nellist, V. Nicolosi, Two-dimensional nanosheets produced by liquid exfoliation of layered materials, *Science* 331 (80) (2011) 568–571, <https://doi.org/10.1126/science.1194975>.
- [40] M. Acerce, D. Voiry, M. Chhowalla, Metallic 1T phase MoS₂ nanosheets as supercapacitor electrode materials, *Nat. Nanotechnol.* 10 (2015) 313–318, <https://doi.org/10.1038/nnano.2015.40>.
- [41] M. Mortazavi, C. Wang, J. Deng, V.B. Shenoy, N.V. Medhekar, Ab initio characterization of layered MoS₂ as anode for sodium-ion batteries, *J. Power Sources* 268 (2014) 279–286, <https://doi.org/10.1016/j.jpowsour.2014.06.049>.
- [42] Y. Yang, H. Fei, G. Ruan, C. Xiang, J.M. Tour, Edge-oriented MoS₂ nanoporous films as flexible electrodes for hydrogen evolution reactions and supercapacitor devices, *Adv. Mater.* 26 (2014) 8163–8168, <https://doi.org/10.1002/adma.201402847>.
- [43] L. David, R. Bhandavat, G. Singh, MoS₂/graphene composite paper for sodium-ion battery electrodes, *ACS Nano* 8 (2014) 1759–1770, <https://doi.org/10.1021/nn406156b>.
- [44] F. Li, Z. Zhou, Micro/nanostructured materials for sodium on batteries and capacitors, *Small* 14 (2018) 1–25, <https://doi.org/10.1002/sml.201702961>.
- [45] X. Zheng, Y. Zhu, Y. Sun, Q. Jiao, Hydrothermal synthesis of MoS₂ with different morphology and its performance in thermal battery, *J. Power Sources* 395 (2018) 318–327, <https://doi.org/10.1016/j.jpowsour.2018.05.092>.
- [46] Y. Liu, C. Cui, Y. Liu, W. Liu, J. Wei, Application of MoS₂ in the cathode of lithium sulfur batteries, *RSC Adv.* 10 (2020) 7384–7395, <https://doi.org/10.1039/c9ra09769d>.
- [47] L. Lin, W. Lei, S. Zhang, Y. Liu, G.G. Wallace, J. Chen, Two-dimensional transition metal dichalcogenides in supercapacitors and secondary batteries, *Energy Storage Mater.* 19 (2019) 408–423, <https://doi.org/10.1016/j.ensm.2019.02.023>.
- [48] T. Wang, S. Chen, H. Pang, H. Xue, Y. Yu, MoS₂-based nanocomposites for electrochemical energy storage, *Adv. Sci.* 4 (2017), <https://doi.org/10.1002/advs.201600289>.
- [49] C. Pan, L. Jiang, J. Sun, Q. Wang, F. Wang, K. Wang, Y. Lu, Y. Wang, Ultrafast optical response and ablation mechanisms of molybdenum disulfide under intense femtosecond laser irradiation, *Light Sci. Appl.* (2020), <https://doi.org/10.1038/s41377-020-0318-8>.
- [50] A. Ambrosi, M. Pumera, 3D-printing technologies for electrochemical applications, *Chem. Soc. Rev.* 45 (2016) 2740–2755, <https://doi.org/10.1039/c5cs00714c>.
- [51] M.A. Bissett, I.A. Kinloch, R.A.W. Dryfe, Characterization of MoS₂/graphene composites for high-performance coin cell supercapacitors, *ACS Appl. Mater. Interfaces* 7 (2015) 17388–17398, <https://doi.org/10.1021/acami.5b04672>.
- [52] W. Zhang, P. Zhang, Z. Su, G. Wei, Synthesis and sensor applications of MoS₂-based nanocomposites, *Nanoscale* 7 (2015) 18364–18378, <https://doi.org/10.1039/c5nr06121k>.
- [53] S. Barua, H.S. Dutta, S. Gogoi, R. Devi, R. Khan, Nanostructured MoS₂-based advanced biosensors: a review, *ACS Appl. Nano Mater.* 1 (2018) 2–25, <https://doi.org/10.1021/acsnan.7b00157>.
- [54] Y.J. Zhai, J.H. Li, X.Y. Chu, M.Z. Xu, F.J. Jin, X. Li, X. Fang, Z.P. Wei, X.H. Wang, MoS₂ microflowers based electrochemical sensing platform for non-enzymatic glucose detection, *J. Alloys Compd.* 672 (2016) 600–608, <https://doi.org/10.1016/j.jallcom.2016.02.130>.
- [55] X. Zhang, J. Grajal, J.L. Vazquez-Roy, U. Radhakrishna, X. Wang, W. Chern, L. Zhou, Y. Lin, P.C. Shen, X. Ji, X. Ling, A. Zubair, Y. Zhang, H. Wang, M. Dubey, J. Kong, M. Dresselhaus, T. Palacios, Two-dimensional MoS₂-enabled flexible rectenna for Wi-Fi-band wireless energy harvesting, *Nature* 566 (2019) 368–372, <https://doi.org/10.1038/s41586-019-0892-1>.
- [56] L.K. Tan, B. Liu, J.H. Teng, S. Guo, H.Y. Low, K.P. Loh, Atomic layer deposition of a MoS₂ film, *Nanoscale* 6 (2014) 10584–10588, <https://doi.org/10.1039/c4nr02451f>.
- [57] H. Lee, S. Bak, Y. Cho, M. Kim, S.H. Kang, V.Q. Bui, H.M. Le, S.W. Kim, H. Lee, Hydrogen adsorption engineering by intramolecular proton transfer on 2D nanosheets, *NPG Asia Mater.* 10 (2018) 441–454, <https://doi.org/10.1038/s41427-018-0037-2>.
- [58] S.J. Rowley-Neale, J.M. Fearn, D.A.C. Brownson, G.C. Smith, X. Ji, C.E. Banks, 2D molybdenum disulphide (2D-MoS₂) modified electrodes explored towards the oxygen reduction reaction, *Nanoscale* 8 (2016) 14767–14777, <https://doi.org/10.1039/c6nr04073j>.
- [59] T. Corrales-sánchez, J. Ampuránés, A. Urakawa, MoS₂-based materials as alternative cathode catalyst for PEM electrolysis, *Int. J. Hydrogen Energy* 39 (2014) 20837–20843, <https://doi.org/10.1016/j.ijhydene.2014.08.078>.
- [60] Y. Hu, D.H.C. Chua, Synthesizing 2D MoS₂ nanoflakes on carbon nanospheres as catalyst support for proton exchange membrane fuel cells, *Sci. Rep.* 6 (2016) 1–10, <https://doi.org/10.1038/srep28088>.
- [61] T. Stephenson, Z. Li, B. Olsen, D. Mitlin, Lithium ion battery applications of molybdenum disulfide (MoS₂) nanocomposites, *Energy Environ. Sci.* 7 (2014) 209–231, <https://doi.org/10.1039/c3ee42591f>.
- [62] W. Choi, N. Choudhary, G.H. Han, J. Park, D. Akinwande, Y.H. Lee, Recent development of two-dimensional transition metal dichalcogenides and their applications, *Mater. Today Off.* 20 (2017) 116–130, <https://doi.org/10.1016/j.mattod.2016.10.002>.
- [63] T. Jurca, M.J. Moody, A. Henning, J.D. Emery, B. Wang, J.M. Tan, T.L. Lohr, L. J. Lauhon, T.J. Marks, Low-temperature atomic layer deposition of MoS₂ films, *Angew. Chem. Int. Ed.* 56 (2017) 4991–4995, <https://doi.org/10.1002/anie.201611838>.
- [64] J. Cai, P. Ruffieux, R. Jaafar, M. Bieri, T. Braun, S. Blankenburg, M. Muoth, A. P. Seitonen, M. Saleh, X. Feng, K. Müllen, R. Fasel, Atomically precise bottom-up fabrication of graphene nanoribbons, *Nature* 466 (2010) 470–473, <https://doi.org/10.1038/nature09211>.
- [65] F. Chen, Y. Yao, W. Su, S. Zhao, S. Ding, L. Fu, The synthesis of 2D MoS₂ flakes with tunable layer numbers via pulsed-Argon-flow assisted CVD approach, *Ceram. Int.* 46 (2020) 14523–14528, <https://doi.org/10.1016/j.ceramint.2020.02.251>.
- [66] D. Kong, H. Wang, J.J. Cha, M. Pasta, K.J. Koski, J. Yao, Y. Cui, Synthesis of MoS₂ and MoSe₂ films with vertically aligned layers, *Nano Lett.* 13 (2013) 1341–1347, <https://doi.org/10.1021/nl400258t>.
- [67] I.T. Bello, A.O. Oladipo, O. Adedokun, S.M. Dhlamini, Recent advances on the preparation and electrochemical analysis of MoS₂-based materials for supercapacitor applications: a mini-review, *Mater. Today Commun.* 25 (2020) 101664, <https://doi.org/10.1016/j.mtcomm.2020.101664>.
- [68] N. Choudhary, C. Li, H.S. Chung, J. Moore, J. Thomas, Y. Jung, High-performance one-body core/shell nanowire supercapacitor enabled by conformal growth of capacitive 2D WS₂ layers, *ACS Nano* 10 (2016) 10726–10735, <https://doi.org/10.1021/acsnano.6b06111>.
- [69] M. Demirtas, C. Odacı, Y. Shehu, N.K. Perkgöz, F. Ay, Layer and size distribution control of CVD-grown 2D MoS₂ using ALD-deposited MoO₃ structures as the precursor, *Mater. Sci. Semicond. Process.* 108 (2020), <https://doi.org/10.1016/j.mssp.2019.104880>.
- [70] U. Krishnan, M. Kaur, K. Singh, M. Kumar, A. Kumar, A synoptic review of MoS₂ : synthesis to applications, *Superlattice. Microst.* 128 (2019) 274–297, <https://doi.org/10.1016/j.spmi.2019.02.005>.

- [71] X.-F. Jin, C.-R.-L. Liu, L. Chen, Y. Zhang, X.-J. Zhang, Y.-M. Chen, J.-J. Chen, Inkjet-printed MoS₂/PVP hybrid nanocomposite for enhanced humidity sensing, *Sensors Actuators A Phys* (2020) 112388, <https://doi.org/10.1016/j.sna.2020.112388>.
- [72] Z. Lin, Y. Liu, U. Halim, M. Ding, Y. Liu, Y. Wang, C. Jia, P. Chen, X.X. Duan, C. Wang, F. Song, M. Li, C. Wan, Y. Huang, X.X. Duan, Solution-processable 2D semiconductors for high-performance large-area electronics, *Nature* 562 (2018) 254–258, <https://doi.org/10.1038/s41586-018-0574-4>.
- [73] K.G. Prashanth, Influence of mechanical activation on decomposition of titanium hydride, *Mater. Manuf. Process.* 25 (2010) 974–977, <https://doi.org/10.1080/10426911003720870>.
- [74] C. Suryanarayana, Mechanical alloying and milling, *Prog. Mater. Sci.* 46 (2001) 1–184, [https://doi.org/10.1016/S0079-6425\(99\)00010-9](https://doi.org/10.1016/S0079-6425(99)00010-9).
- [75] Z. Wang, K.G. Prashanth, S. Scudino, J. He, W.W. Zhang, Y.Y. Li, M. Stoica, G. Vaughan, D.J. Sordelet, J. Eckert, Effect of ball milling on structure and thermal stability of Al₈₄Gd₆Ni₇Co₃ glassy powders, *Intermetallics* 46 (2014) 97–102, <https://doi.org/10.1016/j.intermet.2013.11.005>.
- [76] K. Krishnamoorthy, P. Pazhamalai, G.K. Veerasubramani, S.J. Kim, Mechanically delaminated few layered MoS₂ nanosheets based high performance wire type solid-state symmetric supercapacitors, *J. Power Sources* 321 (2016) 112–119, <https://doi.org/10.1016/j.jpowsour.2016.04.116>.
- [77] P. Pazhamalai, K. Krishnamoorthy, S. Manoharan, S.J. Kim, High energy symmetric supercapacitor based on mechanically delaminated few-layered MoS₂ sheets in organic electrolyte, *J. Alloys Compd.* 771 (2019) 803–809, <https://doi.org/10.1016/j.jallcom.2018.08.203>.
- [78] H. Wang, D. Tran, M. Moussa, N. Stanley, T.T. Tung, L. Yu, P.L. Yap, F. Ding, J. Qian, D. Losic, Improved preparation of MoS₂/graphene composites and their inks for supercapacitors applications, *Mater. Sci. Eng. B Solid-State Mater. Adv. Technol.* 262 (2020), <https://doi.org/10.1016/j.mseb.2020.114700>.
- [79] K.D. Rasamani, F. Alimohammadi, Y. Sun, Interlayer-expanded MoS₂, *Mater. Today Off.* 20 (2017) 83–91, <https://doi.org/10.1016/j.mattod.2016.10.004>.
- [80] M.T.A. Reis, M.R.C. Ismael, Electroplating wastes, *Phys. Sci. Rev.* 3 (2019) 1–24, <https://doi.org/10.1515/psr-2018-0024>.
- [81] B.R. Babu, S.U. Bhanu, K.S. Meera, Waste minimization in electroplating industries: a review, *J. Environ. Sci. Health Part C Environ. Carcinog. Ecotoxicol. Rev.* 27 (2009) 155–177, <https://doi.org/10.1080/10590500903124158>.
- [82] Y.P. Putra, R.W. Soemantojo, U.S. Hamzah, Evaluation of waste minimization in electroplating for cost saving, *AIP Conf. Proc.* 2202 (2019), <https://doi.org/10.1063/1.5141685>.
- [83] G.E. Hunt, Hazardous waste minimization: Part IV. Waste reduction in the metal finishing industry, *J. Air Pollut. Control Assoc.* 38 (1988) 672–680, <https://doi.org/10.1080/08940630.1988.10466410>.
- [84] X. Zhao, G. Wang, X. Liu, X. Zheng, H. Wang, Ultrathin MoS₂ with expanded interlayers supported on hierarchical polypyrrole-derived amorphous N-doped carbon tubular structures for high-performance Li/Na-ion batteries, *Nano Res.* 11 (2018) 3603–3618, <https://doi.org/10.1007/s12274-017-1927-2>.
- [85] L. Wang, Q. Zhang, J. Zhu, X. Duan, Z. Xu, Y. Liu, H. Yang, B. Lu, Nature of extra capacity in MoS₂ electrodes: molybdenum atoms accommodate with lithium, *Energy Storage Mater.* 16 (2019) 37–45, <https://doi.org/10.1016/j.ensm.2018.04.025>.
- [86] R. Wang, S. Gao, K. Wang, M. Zhou, S. Cheng, K. Jiang, MoS₂/rGO nanoflakes as high performance anode materials in sodium ion batteries, *Sci. Rep.* 7 (2017) 1–9, <https://doi.org/10.1038/s41598-017-08341-y>.
- [87] H. Lu, K. Tian, L. Bu, X. Huang, X. Li, Y. Zhao, F. Wang, J. Bai, L. Gao, J. Zhao, Synergistic effect from coaxially integrated CNTs@MoS₂/MoO₂ composite enables fast and stable lithium storage, *J. Energy Chem.* 55 (2021) 449–458, <https://doi.org/10.1016/j.jechem.2020.07.033>.
- [88] P. Pazhamalai, K. Krishnamoorthy, S.J. Kim, Hierarchical copper selenide nanoneedles grown on copper foil as a binder free electrode for supercapacitors, *Int. J. Hydrogen Energy* 41 (2016) 14830–14835, <https://doi.org/10.1016/j.ijhydene.2016.05.157>.
- [89] S.H. Kazemi, F. Bahmani, H. Kazemi, M.A. Kiani, Binder-free electrodes of NiMoO₄/graphene oxide nanosheets: synthesis, characterization and supercapacitive behavior, *RSC Adv.* 6 (2016) 111170–111181, <https://doi.org/10.1039/c6ra23076h>.
- [90] W. Xu, Z. Lu, T. Zhang, Y. Zhong, Y. Wu, G. Zhang, J. Liu, H. Wang, X. Sun, An advanced zinc air battery with nanostructured superwetting electrodes, *Energy Storage Mater.* 17 (2019) 358–365, <https://doi.org/10.1016/j.ensm.2018.06.029>.
- [91] D. Li, G. Chang, L. Zong, P. Xue, Y. Wang, Y. Xia, C. Lai, D. Yang, From double-helix structured seaweed to S-doped carbon aerogel with ultra-high surface area for energy storage, *Energy Storage Mater.* 17 (2019) 22–30, <https://doi.org/10.1016/j.ensm.2018.08.004>.
- [92] S.K. Balasingam, J.S. Lee, Y. Jun, Few-layered MoSe₂ nanosheets as an advanced electrode material for supercapacitors, *Dalton Trans.* 44 (2015) 15491–15498, <https://doi.org/10.1039/c5dt01985k>.
- [93] A. Mukherji, L. Saikia, R. Srivastava, Few-layer MoS₂ wrapped MnCO₃ on graphite paper: a hydrothermally grown hybrid negative electrode for electrochemical energy storage, *Chem. Eng. J.* 373 (2019) 1233–1246, <https://doi.org/10.1016/j.cej.2019.05.133>.
- [94] L.-N.N. Wang, X. Wu, F.-T.T. Wang, X. Chen, J. Xu, K.-J.J. Huang, 1T-Phase MoS₂ with large layer spacing supported on carbon cloth for high-performance Na⁺ storage, *J. Colloid Interface Sci.* 583 (2020) 579–585, <https://doi.org/10.1016/j.jcis.2020.09.055>.
- [95] H.R. Byon, S.W. Lee, S. Chen, P.T. Hammond, Y. Shao-Horn, Thin films of carbon nanotubes and chemically reduced graphenes for electrochemical micro-capacitors, *Carbon N. Y.* 49 (2011) 457–467, <https://doi.org/10.1016/j.carbon.2010.09.042>.
- [96] S. Islam, S. Debnath, M.Y. Miah, Nanomaterials as electrocatalyst for hydrogen and oxygen evolution reaction : exploitation of challenges and current progressions, *Polyhedron* (2020) 114871, <https://doi.org/10.1016/j.poly.2020.114871>.
- [97] S. Dam, A. Thakur, S. Hussain, Valence band studies of MoS₂ thin films synthesised by electrodeposition method, *Mater. Today Proc.* (2020), <https://doi.org/10.1016/j.matpr.2020.03.722>.
- [98] K. Miettunen, M. Toivola, G. Hashmi, J. Salpakari, I. Asghar, P. Lund, A carbon gel catalyst layer for the roll-to-roll production of dye solar cells, *Carbon N. Y.* 49 (2011) 528–532, <https://doi.org/10.1016/j.carbon.2010.09.052>.
- [99] F. Zhang, M. Wei, V.V. Viswanathan, B. Swart, Y. Shao, G. Wu, C. Zhou, 3D printing technologies for electrochemical energy storage, *Nano Energy* 40 (2017) 418–431, <https://doi.org/10.1016/j.nanoen.2017.08.037>.
- [100] R. Gupta, K. Mensah-Darkwa, R.N. Tabi, M. Owusu, T. Ingels, P.K. Kahol, Recent advancement on MoS₂ for hydrogen evolution reactions, *Curr. Graphene Sci.* 4 (2020) 1–15, <https://doi.org/10.2174/245227320466200303124226>.
- [101] K.G. Prashanth, Selective laser melting: materials and applications, *J. Manuf. Mater. Process.* 4 (2020) 15–17, <https://doi.org/10.3390/jmmp4010013>.
- [102] L.J. Tan, W. Zhu, K. Zhou, Recent progress on polymer materials for additive manufacturing, *Adv. Funct. Mater.* (2020) 1–54, <https://doi.org/10.1002/adfm.202003062>, 2003062.
- [103] J.Z. Manapat, Q. Chen, P. Ye, R.C. Advincula, 3D printing of polymer nanocomposites via stereolithography, *Macromol. Mater. Eng.* 302 (2017) 1–13, <https://doi.org/10.1002/mame.201600553>.
- [104] G. Mitteramskogler, R. Gmeiner, R. Felzmann, S. Gruber, C. Hofstetter, J. Stampfl, J. Ebert, W. Wachter, J. Laubersheimer, Light curing strategies for lithography-based additive manufacturing of customized ceramics, *Addit. Manuf.* 1 (2014) 110–118, <https://doi.org/10.1016/j.addma.2014.08.003>.
- [105] K. Taki, A simplified 2D numerical simulation of photopolymerization kinetics and oxygen diffusion-reaction for the continuous liquid interface production (CLIP) system, *Polymers* 12 (2020), <https://doi.org/10.3390/POLYM12040875>.
- [106] R. Januszewicz, J.R. Tumbleston, A.L. Quintanilla, S.J. Mechem, J.M. DeSimone, Layerless fabrication with continuous liquid interface production, *Proc. Natl. Acad. Sci. U. S. A.* 113 (2016) 11703–11708, <https://doi.org/10.1073/pnas.1605271113>.
- [107] D.A. Walker, J.L. Hedrick, C.A. Mirkin, Supplementary Materials for using a mobile liquid interface, *Science* 366 (80) (2019) 360–364, <https://doi.org/10.1126/science.aax1562>.
- [108] B.E. Kelly, I. Bhattacharya, H. Heidari, M. Shusteff, C.M. Spadaccini, H.K. Taylor, Volumetric additive manufacturing via tomographic reconstruction, *Science* 363 (80) (2019) 1075–1079, <https://doi.org/10.1126/science.aau7114>.
- [109] C.N. LaPratta, D. Lim, K. O'Malley, T. Baldacchini, J.T. Fourkas, Direct laser patterning of conductive wires on three-dimensional polymeric microstructures, *Chem. Mater.* 18 (2006) 2038–2042, <https://doi.org/10.1021/cm0525306>.
- [110] K. Satoshi, S. Hong-Bo, T. Tomokazu, T. Kenji, Finer features for functional microdevices, *Nature* 412 (2001) 697–698.
- [111] S. Shoji, S. Kawata, Photofabrication of three-dimensional photonic crystals by multibeam laser interference into a photopolymerizable resin, *Appl. Phys. Lett.* 76 (2000) 2668–2670, <https://doi.org/10.1063/1.126438>.
- [112] S. Maruo, K. Ikuta, Three-dimensional microfabrication by use of single-photon-absorbed polymerization, *Appl. Phys. Lett.* 76 (2000) 2656–2658, <https://doi.org/10.1063/1.126742>.
- [113] S.K. Saha, D. Wang, V.H. Nguyen, Y. Chang, J.S. Oakdale, S.C. Chen, Scalable submicrometer additive manufacturing, *Science* 366 (80) (2019) 105–109, <https://doi.org/10.1126/science.aax8760>.
- [114] X.Y. Lee, S.K. Saha, S. Sarkar, B. Giera, Two photon lithography additive manufacturing: video dataset of parameter sweep of light dosages, photo-curable resins, and structures, *Data Brief* 32 (2020) 106119, <https://doi.org/10.1016/j.dib.2020.106119>.
- [115] H. Kim, S.K. Saha, Defect control during femtosecond projection two-photon lithography, *Procedia Manuf.* 48 (2020) 650–655, <https://doi.org/10.1016/j.promfg.2020.05.157>.
- [116] S. Singh, S. Ramakrishna, R. Singh, Material issues in additive manufacturing: a review, *J. Manuf. Process.* 25 (2017) 185–200, <https://doi.org/10.1016/j.jmpro.2016.11.006>.
- [117] R.L. Truby, J.A. Lewis, Printing soft matter in three dimensions, *Nature* 540 (2016) 371–378, <https://doi.org/10.1038/nature21003>.
- [118] M.A. Skylar-Scott, J. Mueller, C.W. Visser, J.A. Lewis, Voxellated soft matter via multimaterial multinozzle 3D printing, *Nature* 575 (2019) 330–335, <https://doi.org/10.1038/s41586-019-1736-8>.
- [119] W.S.W. Harun, M.S.I.N. Kamariah, N. Muhamad, S.A.C. Ghani, F. Ahmad, Z. Mohamed, A review of powder additive manufacturing processes for metallic biomaterials, *Powder Technol.* 327 (2018) 128–151, <https://doi.org/10.1016/j.powtec.2017.12.058>.
- [120] T.J. Horn, O.L.A. Harrysson, Overview of current additive manufacturing technologies and selected applications, *Sci. Prog.* 95 (2012) 255–282, <https://doi.org/10.3184/003685012X13420984463047>.
- [121] N. Li, S. Huang, G. Zhang, R. Qin, W. Liu, H. Xiong, G. Shi, J. Blackburn, Progress in additive manufacturing on new materials: a review, *J. Mater. Sci. Technol.* 35 (2019) 242–269, <https://doi.org/10.1016/j.jmst.2018.09.002>.
- [122] P.K. Gokuldoss, S. Kolla, J. Eckert, Additive manufacturing processes: selective laser melting, electron beam melting and binder jetting-selection guidelines, *Materials* 10 (2017), <https://doi.org/10.3390/ma10060672>.

- [123] D. Herzog, V. Seyda, E. Wycisk, C. Emmelmann, Additive manufacturing of metals, *Acta Mater.* 117 (2016) 371–392, <https://doi.org/10.1016/j.actamat.2016.07.019>.
- [124] E. MacDonald, R. Wicker, Multiprocess 3D printing for increasing component functionality, *Science* 80–(2016) 353, <https://doi.org/10.1126/science.aaf2093>.
- [125] S.Y. Chin, V. Dikshit, B.M. Priyadarshini, Y. Zhang, Powder-based 3D printing for the fabrication of device with micro and mesoscale features, *Micromachines* 11 (2020) 29–40, <https://doi.org/10.3390/M11070658>.
- [126] S. Mirzababaei, S. Pasebani, A review on binder jet additive manufacturing of 316L stainless steel, *J. Manuf. Mater. Process.* 3 (2019) 8–12, <https://doi.org/10.3390/jmmp3030082>.
- [127] D. Majumdar, M. Mandal, S.K. Bhattacharya, V2O5 and its carbon-based nanocomposites for supercapacitor applications, *ChemElectroChem* (2019) 1623–1648, <https://doi.org/10.1002/celec.201801761>.
- [128] I. Liashenko, J. Rosell-Llompart, A. Cabot, Ultrafast 3D printing with submicrometer features using electrostatic jet deflection, *Nat. Commun.* 11 (2020) 1–9, <https://doi.org/10.1038/s41467-020-14557-w>.
- [129] J.P. Kruth, X. Wang, T. Laoui, L. Froeyen, Lasers and materials in selective laser sintering, *Assemb. Autom.* 23 (2003) 357–371, <https://doi.org/10.1108/01445150310698652>.
- [130] M. Speirs, J. Van Humbeeck, J. Schrooten, J. Luyten, J.P. Kruth, The effect of pore geometry on the mechanical properties of selective laser melted Ti-13Nb-13Zr scaffolds, *Procedia CIRP* 5 (2013) 79–82, <https://doi.org/10.1016/j.procir.2013.01.016>.
- [131] M. Schmid, A. Amado, K. Wegener, Materials perspective of polymers for additive manufacturing with selective laser sintering, *J. Mater. Res.* 29 (2014) 1824–1832, <https://doi.org/10.1557/jmr.2014.138>.
- [132] R.D. Goodridge, C.J. Tuck, R.J.M. Hague, Laser sintering of polyamides and other polymers, *Prog. Mater. Sci.* 57 (2012) 229–267, <https://doi.org/10.1016/j.pmatsci.2011.04.001>.
- [133] Y. Wang, Z. Xu, D. Wu, J. Bai, Current status and prospects of polymer powder 3D printing technologies, *Materials* 13 (2020), <https://doi.org/10.3390/ma13102406>.
- [134] M. Cheng, R. Deivanayagam, R. Shahbazian-Yassar, 3D Printing of electrochemical energy storage devices: a review of printing techniques and electrode/electrolyte architectures, *Battery Supercapacitors* 3 (2020) 130–146, <https://doi.org/10.1002/batt.201900130>.
- [135] U. Gulzar, C. Glynn, C. O'Dwyer, Additive manufacturing for energy storage: methods, designs and material selection for customizable 3D printed batteries and supercapacitors, *Curr. Opin. Electrochem.* 20 (2020) 46–53, <https://doi.org/10.1016/j.coelec.2020.02.009>.
- [136] P. Chang, H. Mei, S. Zhou, K.G. Dossios, L. Cheng, 3D printed electrochemical energy storage devices, *J. Mater. Chem. A* 7 (2019) 4230–4258, <https://doi.org/10.1039/c8ta11860d>.
- [137] R.C. Xu, X.H. Xia, X.L. Wang, Y. Xia, J.P. Tu, Tailored Li2S-P2S5 glass-ceramic electrolyte by MoS2 doping, possessing high ionic conductivity for all-solid-state lithium-sulfur batteries, *J. Mater. Chem. A* 5 (2017) 2829–2834, <https://doi.org/10.1039/c6ta10142a>.
- [138] T. Jeon, D.H. Kim, S.G. Park, Holographic fabrication of 3D nanostructures, *Adv. Mater. Interfaces* 5 (2018) 1–13, <https://doi.org/10.1002/admi.201800330>.
- [139] E. Stankevicius, M. Gedvilas, B. Voisiat, M. Malinauskas, G. Raciukaitis, Fabrication of periodic micro-structures by holographic lithography, *Lith. J. Phys.* 53 (2013) 227–237, <https://doi.org/10.3952/lithophys.53406>.
- [140] Q. Chen, R. Xu, Z. He, K. Zhao, L. Panz, L. Pan, Printing 3D gel polymer electrolyte in Li-ion microbattery using stereolithography, *35th, Annu. Int. Batter. Semin. Exhib.* 2 (2018) 871–883, <https://doi.org/10.1149/2.0651709jes>, 2018.
- [141] X. Wang, M. Jiang, Z. Zhou, J. Gou, D. Hui, 3D printing of polymer matrix composites: a review and prospective, *Compos. B Eng.* 110 (2017) 442–458, <https://doi.org/10.1016/j.compositesb.2016.11.034>.
- [142] R.S. Jordan, Y. Wang, 3D printing of conjugated polymers, *J. Polym. Sci., Part B: Polym. Phys.* 57 (2019) 1592–1605, <https://doi.org/10.1002/polb.24893>.
- [143] Y. Gao, L. Xu, Y. Zhao, Z. You, Q. Guan, 3D printing preview for stereolithography based on photopolymerization kinetic models, *Bioact. Mater.* 5 (2020) 798–807, <https://doi.org/10.1016/j.bioactmat.2020.05.006>.
- [144] Y. Wu, Y.X. Chen, J. Yan, S. Yang, P. Dong, P. Soman, Fabrication of conductive polyaniline hydrogel using porogen leaching and projection microstereolithography, *J. Mater. Chem. B* 3 (2015) 5352–5360, <https://doi.org/10.1039/c5tb00629e>.
- [145] Q. Ge, Z. Li, Z. Wang, K. Kowsari, W. Zhang, X. He, J. Zhou, N.X. Fang, Projection micro stereolithography based 3D printing and its applications, *Int. J. Extrem. Manuf.* 2 (2020), 022004, <https://doi.org/10.1088/2631-7990/ab8d9a>.
- [146] I.C. Seung, B.L. Sang, Fast electrochemistry of conductive polymer nanotubes: synthesis, mechanism, and application, *Acc. Chem. Res.* 41 (2008) 699–707, <https://doi.org/10.1021/ar700294>.
- [147] Z. Liu, A. Prowald, S. Zein El Abedin, F. Endres, Template-assisted electrodeposition of highly ordered macroporous zinc structures from an ionic liquid, *J. Solid State Electrochem.* 17 (2013) 1185–1188, <https://doi.org/10.1007/s10008-012-1988-9>.
- [148] Y.F. Yuan, X.H. Xia, J.B. Wu, Y.B. Chen, J.L. Yang, S.Y. Guo, Enhanced electrochromic properties of ordered porous nickel oxide thin film prepared by self-assembled colloidal crystal template-assisted electrodeposition, *Electrochim. Acta* 56 (2011) 1208–1212, <https://doi.org/10.1016/j.electacta.2010.10.097>.
- [149] P. Schürch, R. Ramachandramoorthy, L. Pethő, J. Michler, L. Philippe, Additive manufacturing by template-assisted 3D electrodeposition: nanocrystalline nickel microspheres and microspring arrays, *Appl. Mater. Today* 18 (2020) 100472, <https://doi.org/10.1016/j.apmt.2019.100472>.
- [150] Y. Chu, C. Qian, P. Chahal, C. Cao, Printed Diodes: materials processing, fabrication, and applications, *Adv. Sci.* 6 (2019), <https://doi.org/10.1002/advs.201801653>.
- [151] K.H. Choi, D.B. Ahn, S.H. Lee, Current status and challenges in printed batteries: toward form factor-free, monolithic integrated power sources, *ACS Energy Lett.* 3 (2018) 220–236, <https://doi.org/10.1021/acsenenergylt.7b01086>.
- [152] R. Tortorich, J.-W. Choi, Inkjet printing of carbon nanotubes, *Nanomaterials* 3 (2013) 453–468, <https://doi.org/10.3390/nano3030453>.
- [153] Z. Zhan, J. An, Y. Wei, V.T. Tran, H. Du, Inkjet-printed optoelectronics, *Nanoscale* 9 (2017) 965–993, <https://doi.org/10.1039/c6nr08220c>.
- [154] B. Derby, Bioprinting: inkjet printing proteins and hybrid cell-containing materials and structures, *J. Mater. Chem.* 18 (2008) 5717–5721, <https://doi.org/10.1039/b807560c>.
- [155] S. Sumaiya, K. Kardel, A. El-Shahat, Organic solar cell by inkjet printing—an overview, *Technologies* 5 (2017) 53, <https://doi.org/10.3390/technologies5030053>.
- [156] J. Ding, K. Shen, Z. Du, B. Li, S. Yang, 3D-Printed hierarchical porous frameworks for sodium storage, *ACS Appl. Mater. Interfaces* 9 (2017) 41871–41877, <https://doi.org/10.1021/acsmi.7b12892>.
- [157] Y. Zhao, Q. Zhou, L. Liu, J. Xu, M. Yan, Z. Jiang, A novel and facile route of ink-jet printing to thin film SnO2 anode for rechargeable lithium ion batteries, *Electrochim. Acta* 51 (2006) 2639–2645, <https://doi.org/10.1016/j.electacta.2005.07.050>.
- [158] P.E. Delannoy, B. Riou, T. Brousse, J. Le Bideau, D. Guyomard, B. Lestriez, Ink-jet printed porous composite LiFePO4 electrode from aqueous suspension for microbatteries, *J. Power Sources* 287 (2015) 261–268, <https://doi.org/10.1016/j.jpowsour.2015.04.067>.
- [159] Y. Gu, A. Wu, H. Sohn, C. Nicoletti, Z. Iqbal, J.F. Federici, Fabrication of rechargeable lithium ion batteries using water-based inkjet printed cathodes, *J. Manuf. Process.* 20 (2015) 198–205, <https://doi.org/10.1016/j.jmapro.2015.08.003>.
- [160] J. Huang, J. Yang, W. Li, W. Cai, Z. Jiang, Electrochemical properties of LiCoO2 thin film electrode prepared by ink-jet printing technique, *Thin Solid Films* 516 (2008) 3314–3319, <https://doi.org/10.1016/j.tsf.2007.09.039>.
- [161] G. Hu, L. Yang, Z. Yang, Y. Wang, X. Jin, J. Dai, Q. Wu, S. Liu, X. Zhu, X. Wang, T.-C. Wu, R.C.T. Howe, T. Albroow-Owen, L.W.T. Ng, Q. Yang, L.G. Occhipinti, R. I. Woodward, E.J.R. Kelleher, Z. Sun, X. Huang, M. Zhang, C.D. Bain, T. Hasan, A general ink formulation of 2D crystals for wafer-scale inkjet printing, *Sci. Adv.* 6 (2020), <https://doi.org/10.1126/sciadv.aba5029> eaba5029.
- [162] S. Lawes, Q. Sun, A. Lushington, B. Xiao, Y. Liu, X. Sun, Inkjet-printed silicon as high performance anodes for Li-ion batteries, *Nano Energy* 36 (2017) 313–321, <https://doi.org/10.1016/j.nanoen.2017.04.041>.
- [163] J. Hu, Y. Jiang, S. Cui, Y. Duan, T. Liu, H. Guo, L. Lin, Y. Lin, J. Zheng, K. Amine, F. Pan, 3D-printed cathodes of LiMn1-xFePO4 nanocrystals achieve both ultrahigh rate and high capacity for advanced lithium-ion battery, *Adv. Energy Mater.* 6 (2016), <https://doi.org/10.1002/aem.201600856>.
- [164] B. Derby, Additive manufacture of ceramic components by inkjet printing, *Engineering* 1 (2015) 113–123, <https://doi.org/10.15300/J-ENG-2015014>.
- [165] Z. Lyu, G.J.H. Lim, R. Guo, Z. Kou, T. Wang, C. Guan, J. Ding, W. Chen, J. Wang, 3D-printed MOF-derived hierarchically porous frameworks for practical high-energy density Li-O2 batteries, *Adv. Funct. Mater.* 29 (2019) 1–8, <https://doi.org/10.1002/adfm.201806658>.
- [166] L. Zhou, W. Ning, C. Wu, D. Zhang, W. Wei, J. Ma, C. Li, L. Chen, 3D-printed microelectrodes with a developed conductive network and hierarchical pores toward high areal capacity for microbatteries, *Adv. Mater. Technol.* 4 (2019) 1–7, <https://doi.org/10.1002/admt.201800402>.
- [167] M. Cheng, Y. Jiang, W. Yao, Y. Yuan, R. Deivanayagam, T. Foroosan, Z. Huang, B. Song, R. Rojaee, T. Shokuhfar, Y. Pan, J. Lu, R. Shahbazian-Yassar, Elevated-temperature 3D printing of hybrid solid-state electrolyte for Li-ion batteries, *Adv. Mater.* 30 (2018) 1–10, <https://doi.org/10.1002/adma.201800615>.
- [168] C. Zhang, K. Shen, B. Li, S. Li, S. Yang, Continuously 3D printed quantum dot-based electrodes for lithium storage with ultrahigh capacities, *J. Mater. Chem. A* 6 (2018), <https://doi.org/10.1039/c8ta08559e>, 19960–19966.
- [169] K. Sun, T.S. Wei, B.Y. Ahn, J.Y. Seo, S.J. Dillon, J.A. Lewis, 3D printing of interdigitated Li-ion microbattery architectures, *Adv. Mater.* 25 (2013) 4539–4543, <https://doi.org/10.1002/adma.201301036>.
- [170] T.S. Wei, B.Y. Ahn, J. Grotto, J.A. Lewis, 3D printing of customized Li-ion batteries with thick electrodes, *Adv. Mater.* 30 (2018) 1–7, <https://doi.org/10.1002/adma.201703027>.
- [171] X. Tang, H. Zhou, Z. Cai, D. Cheng, P. He, P. Xie, D. Zhang, T. Fan, Generalized 3D printing of graphene-based mixed-dimensional hybrid aerogels, *ACS Nano* 12 (2018) 3502–3511, <https://doi.org/10.1021/acsnano.8b00304>.
- [172] J.A. Lewis, G.M. Gratson, Direct writing in three dimensions, *Mater. Today* 7 (2004) 32–39, [https://doi.org/10.1016/S1369-7021\(04\)00344-X](https://doi.org/10.1016/S1369-7021(04)00344-X).
- [173] J.A. Lewis, Direct ink writing of 3D functional materials, *Adv. Funct. Mater.* 16 (2006) 2193–2204, <https://doi.org/10.1002/adfm.200600434>.
- [174] B. Chen, Y. Jiang, X. Tang, Y. Pan, S. Hu, Fully packaged carbon nanotube supercapacitors by direct ink writing on flexible substrates, *ACS Appl. Mater. Interfaces* 9 (2017) 28433–28440, <https://doi.org/10.1021/acsmi.7b06804>.
- [175] T. Wang, L. Li, X. Tian, H. Jin, K. Tang, S. Hou, H. Zhou, X. Yu, 3D-printed interdigitated graphene framework as superior support of metal oxide nanostructures for remarkable micro-pseudocapacitors, *Electrochim. Acta* 319 (2019) 245–252, <https://doi.org/10.1016/j.electacta.2019.06.163>.
- [176] T. Wang, X. Tian, L. Li, L. Lu, S. Hou, G. Cao, H. Jin, 3D printing-based cellular microelectrodes for high-performance asymmetric quasi-solid-state micro-

- psudocapacitors, *J. Mater. Chem. A* 8 (2020) 1749–1756, <https://doi.org/10.1039/c9ta11386j>.
- [177] B. Yao, S. Chandrasekaran, J. Zhang, W. Xiao, F. Qian, C. Zhu, E.B. Duoss, C. M. Spadaccini, M.A. Worsley, Y. Li, Efficient 3D printed pseudocapacitive electrodes with ultrahigh MnO₂ loading, *Joule* 3 (2019) 459–470, <https://doi.org/10.1016/j.joule.2018.09.020>.
- [178] Z. Yang, S. Jia, Y. Niu, X. Lv, H. Fu, Y. Zhang, D. Liu, B. Wang, Q. Li, Bean-pod-inspired 3D-printed phase change microlattices for solar-thermal energy harvesting and storage, *Small* 17 (2021) 1–10, <https://doi.org/10.1002/sml.202101093>.
- [179] J. Li, X. Liang, F. Liou, J. Park, Macro-/micro-controlled 3D lithium-ion batteries via additive manufacturing and electric field processing, *Sci. Rep.* 8 (2018) 1–11, <https://doi.org/10.1038/s41598-018-20329-w>.
- [180] S. Turunen, S. Kaisto, I. Skovorodkin, V. Mironov, T. Kalpio, S. Vainio, A. Rak-Raszewska, 3D bioprinting of the kidney—hype or hope? *AIMS Cell Tissue Eng.* 2 (2018) 119–162, <https://doi.org/10.3934/celltissue.2018.3.119>.
- [181] J.W. Boley, K. Chaudhary, T.J. Ober, M. Khorasaninejad, W.T. Chen, E. Hanson, A. Kulkarni, J. Oh, J. Kim, L.K. Aagesen, A.Y. Zhu, F. Capasso, K. Thornton, P. V. Braun, J.A. Lewis, High-orientation-temperature direct ink writing of mesoscale eutectic architectures, *Adv. Mater.* 29 (2017) 1–8, <https://doi.org/10.1002/adma.2021604778>.
- [182] A. Mahajan, C.D. Frisbie, L.F. Francis, Optimization of aerosol jet printing for high-resolution, high-aspect ratio silver lines, *ACS Appl. Mater. Interfaces* 5 (2013) 4856–4864, <https://doi.org/10.1021/am400606y>.
- [183] M. Ha, J.W.T. Seo, P.L. Prabhuramirashi, W. Zhang, M.L. Geier, M.J. Renn, C. H. Kim, M.C. Hersam, C.D. Frisbie, Aerosol jet printed, low voltage, electrolyte gated carbon nanotube ring oscillators with sub-5 μs stage delays, *Nano Lett.* 13 (2013) 954–960, <https://doi.org/10.1021/nl303877z>.
- [184] C. Cao, J.B. Andrews, A.D. Franklin, Completely printed, flexible, stable, and hysteresis-free carbon nanotube thin-film transistors via aerosol jet printing, *Adv. Electron. Mater.* 3 (2017) 1–10, <https://doi.org/10.1002/aeml.201700057>.
- [185] M. Green, K. Emery, Y. Hishikawa, W. Warta, E. Dunlop, D. Barkhouse, O. Gunawan, T. Gokmen, T. Todrov, D. Mitzi, Solar cell efficiency tables (version 40), *IEEE Trans. Fuzzy Syst.* 20 (2012) 1114–1129, <https://doi.org/10.1002/pip.186>.
- [186] M.J. Catenacci, P.F. Flowers, C. Cao, J.B. Andrews, A.D. Franklin, B.J. Wiley, Fully printed memristors from Cu-SiO₂ core-shell nanowire composites, *J. Electron. Mater.* 46 (2017) 4596–4603, <https://doi.org/10.1007/s11664-017-5445-5>.
- [187] J.M. Hoey, A. Lutfurakhmanov, D.L. Schulz, I.S. Akhatov, A review on aerosol-based direct-write and its applications for microelectronics, *J. Nanotechnol.* 2012 (2012), <https://doi.org/10.1155/2012/324380>.
- [188] C. Cao, J.B. Andrews, A. Kumar, A.D. Franklin, Improving contact interfaces in fully printed carbon nanotube thin-film transistors, *ACS Nano* 10 (2016) 5221–5229, <https://doi.org/10.1021/acsnano.6b00877>.
- [189] M.S. Saleh, J. Li, J. Park, R. Panat, 3D printed hierarchically-porous microlattice electrode materials for exceptionally high specific capacity and areal capacity lithium ion batteries, *Addit. Manuf.* 23 (2018) 70–78, <https://doi.org/10.1016/j.addma.2018.07.006>.
- [190] M. Smith, Y.S. Choi, C. Boughey, S. Kar-Narayan, Controlling and assessing the quality of aerosol jet printed features for large area and flexible electronics, *Flex. Print. Electron.* 2 (2017), <https://doi.org/10.1088/2058-8585/aa5af9>.
- [191] X. Wei, D. Li, W. Jiang, Z. Gu, X. Wang, Z. Zhang, Z. Sun, 3D Printable graphene composite, *Sci. Rep.* 5 (2015) 1–7, <https://doi.org/10.1038/srep11181>.
- [192] A. Maurel, M. Courty, B. Fleutot, H. Tortajada, K. Prashantha, M. Armand, S. Grugeon, S. Panier, L. Dupont, Highly loaded graphite-poly(lactic acid) composite-based filaments for lithium-ion battery three-dimensional printing, *Chem. Mater.* 30 (2018) 7484–7493, <https://doi.org/10.1021/acs.chemmater.8b02062>.
- [193] N. Rohaizad, C.C. Mayorga-Martinez, F. Novotný, R.D. Webster, M. Pumera, 3D-printed Ag/AgCl pseudo-reference electrodes, *Electrochem. Commun.* 103 (2019) 104–108, <https://doi.org/10.1016/j.elecom.2019.05.010>.
- [194] C. Reyes, R. Somogyi, S. Niu, M.A. Cruz, F. Yang, M.J. Catenacci, C.P. Rhodes, B. J. Wiley, Three-dimensional printing of a complete lithium ion battery with fused filament fabrication, *ACS Appl. Energy Mater.* 1 (2018) 5268–5279, <https://doi.org/10.1021/acsaem.8b00885>.
- [195] F.F.F. Printing, A. Elkaseer, S. Schneider, G. Scholz, Experiment-based Process Modeling and Optimization for High-Quality and Resource-Efficient, applied sciences, 2020.
- [196] D.K. Tan, M. Maniruzzaman, A. Nokhodchi, Advanced pharmaceutical applications of hot-melt extrusion coupled with fused deposition modelling (FDM) 3D printing for personalised drug delivery, *Pharmaceutics* 10 (2018), <https://doi.org/10.3390/pharmaceutics10040203>.
- [197] K.G. Prashanth, S. Scudino, H.J. Klaus, K.B. Surreddi, L. Löber, Z. Wang, A. K. Chaubey, U. Kühn, J. Eckert, Microstructure and mechanical properties of Al-12Si produced by selective laser melting: effect of heat treatment, *Mater. Sci. Eng. A* 590 (2014) 153–160, <https://doi.org/10.1016/j.msea.2013.10.023>.
- [198] O.O. Salman, F. Brenne, T. Niendorf, J. Eckert, K.G. Prashanth, T. He, S. Scudino, Impact of the scanning strategy on the mechanical behavior of 316L steel synthesized by selective laser melting, *J. Manuf. Process.* 45 (2019) 255–261, <https://doi.org/10.1016/j.jmapro.2019.07.010>.
- [199] K.G. Prashanth, S. Scudino, J. Eckert, Defining the tensile properties of Al-12Si parts produced by selective laser melting, *Acta Mater.* 126 (2017) 25–35, <https://doi.org/10.1016/j.actamat.2016.12.044>.
- [200] S. Scudino, C. Unterderfer, K.G. Prashanth, H. Attar, N. Ellenndt, V. Uhlenwinkel, J. Eckert, Additive manufacturing of Cu-10Sn bronze, *Mater. Lett.* 156 (2015) 202–204, <https://doi.org/10.1016/j.matlet.2015.05.076>.
- [201] K.G. Prashanth, H.S. Sahabi, H. Attar, V.C. Srivastava, N. Ellenndt, V. Uhlenwinkel, J. Eckert, S. Scudino, Production of high strength Al85Ni5Co2 alloy by selective laser melting, *Addit. Manuf.* 6 (2015) 1–5.
- [202] K.G. Prashanth, S. Scudino, T. Maity, J. Das, J. Eckert, Is the energy density a reliable parameter for materials synthesis by selective laser melting? *Mater. Res. Lett.* 5 (2017) 386–390, <https://doi.org/10.1080/21663831.2017.1299808>.
- [203] O.O. Salman, C. Gammmer, J. Eckert, M.Z. Salih, E.H. Abdulsalam, K.G. Prashanth, S. Scudino, Selective laser melting of 316L stainless steel: influence of TiB₂ addition on microstructure and mechanical properties, *Mater. Today Commun.* 21 (2019), <https://doi.org/10.1016/j.mtcomm.2019.100615>.
- [204] J. Suryawanshi, K.G. Prashanth, U. Ramamurty, Mechanical behavior of selective laser melted 316L stainless steel, *Mater. Sci. Eng. A* 696 (2017) 113–121, <https://doi.org/10.1016/j.msea.2017.04.058>.
- [205] J. Suryawanshi, K.G. Prashanth, U. Ramamurty, Tensile, fracture, and fatigue crack growth properties of a 3D printed maraging steel through selective laser melting, *J. Alloys Compd.* 725 (2017) 355–364, <https://doi.org/10.1016/j.jallcom.2017.07.177>.
- [206] H. Attar, K.G. Prashanth, A.K. Chaubey, M. Calin, L.C. Zhang, S. Scudino, J. Eckert, Comparison of wear properties of commercially pure titanium prepared by selective laser melting and casting processes, *Mater. Lett.* 142 (2015) 38–41, <https://doi.org/10.1016/j.matlet.2014.11.156>.
- [207] K. Zhuravleva, M. Bönisch, K.G. Prashanth, U. Hempel, A. Helth, T. Gemming, M. Calin, S. Scudino, L. Schultz, J. Eckert, A. Gebert, Production of porous β-type Ti-40Nb alloy for biomedical applications: comparison of selective laser melting and hot pressing, *Materials* 6 (2013) 5700–5712, <https://doi.org/10.3390/ma6125700>.
- [208] H. Schwab, F. Palm, U. Kühn, J. Eckert, Microstructure and mechanical properties of the near-beta titanium alloy Ti-5553 processed by selective laser melting, *Mater. Des.* 105 (2016) 75–80, <https://doi.org/10.1016/j.matdes.2016.04.103>.
- [209] H. Attar, K.G. Prashanth, L.C. Zhang, M. Calin, I.V. Okulov, S. Scudino, C. Yang, J. Eckert, Effect of powder particle shape on the properties of in situ Ti-TiB composite materials produced by selective laser melting, *J. Mater. Sci. Technol.* 31 (2015) 1001–1005, <https://doi.org/10.1016/j.jmst.2015.08.007>.
- [210] L.X. Xi, H. Zhang, P. Wang, H.C. Li, K.G. Prashanth, K.J. Lin, I. Kaban, D.D. Gu, Comparative investigation of microstructure, mechanical properties and strengthening mechanisms of Al-12Si/TiB₂ fabricated by selective laser melting and hot pressing, *Ceram. Int.* 44 (2018) 17635–17642, <https://doi.org/10.1016/j.ceramint.2018.06.225>.
- [211] L. Xi, D. Gu, S. Guo, R. Wang, K. Ding, K.G. Prashanth, Grain refinement in laser manufactured Al-based composites with TiB₂ ceramic, *J. Mater. Res. Technol.* 9 (2020) 2611–2622, <https://doi.org/10.1016/j.jmrt.2020.04.059>.
- [212] P. Ma, Y. Jia, K.G. Prashanth, S. Scudino, Z. Yu, J. Eckert, Microstructure and phase formation in Al-20Si-5Fe-3Cu-1Mg synthesized by selective laser melting, *J. Alloys Compd.* 657 (2016) 430–435, <https://doi.org/10.1016/j.jallcom.2015.10.119>.
- [213] Y.D. Jia, L.B. Zhang, P. Ma, S. Scudino, G. Wang, J. Yi, J. Eckert, K.G. Prashanth, Thermal expansion behavior of Al-xSi alloys fabricated using selective laser melting, *Prog. Addit. Manuf.* 5 (2020) 247–257, <https://doi.org/10.1007/s40964-020-00130-w>.
- [214] C. Zhao, Z. Wang, D. Li, M. Xie, L. Kollo, Z. Luo, W. Zhang, K.G. Prashanth, Comparison of additively manufacturing samples fabricated from pre-alloyed and mechanically mixed powders, *J. Alloys Compd.* 830 (2020), <https://doi.org/10.1016/j.jallcom.2020.154603>.
- [215] K. Gokuldooss Prashanth, S. Scudino, J. Eckert, Tensile properties of Al-12Si fabricated via selective laser melting (SLM) at different temperatures, *Technologies* 4 (2016) 38, <https://doi.org/10.3390/technologies4040038>.
- [216] R. Baitimerov, P. Lykov, D. Zherebtsov, L. Radionova, A. Shults, K.G. Prashanth, Influence of powder characteristics on processability of AlSi12 alloy fabricated by selective laser melting, *Materials* 11 (2018) 1–14, <https://doi.org/10.3390/ma11050742>.
- [217] K.G. Prashanth, S. Scudino, Quasicrystalline composites by additive manufacturing, *Key Eng. Mater.* 818 KEM, 2019, pp. 72–76. www.scientific.net/KEM.818.72.
- [218] N. Li, J. Zhang, W. Xing, D. Ouyang, L. Liu, 3D printing of Fe-based bulk metallic glass composites with combined high strength and fracture toughness, *Mater. Des.* 143 (2018) 285–296, <https://doi.org/10.1016/j.matdes.2018.01.061>.
- [219] S. Pauly, L. Löber, R. Petters, M. Stoica, S. Scudino, U. Kühn, J. Eckert, Processing metallic glasses by selective laser melting, *Mater. Today* 16 (2013) 37–41, <https://doi.org/10.1016/j.matod.2013.01.018>.
- [220] H.Y. Jung, S.J. Choi, K.G. Prashanth, M. Stoica, S. Scudino, S. Yi, U. Kühn, D. H. Kim, K.B. Kim, J. Eckert, Fabrication of Fe-based bulk metallic glass by selective laser melting: a parameter study, *Mater. Des.* 86 (2015) 703–708, <https://doi.org/10.1016/j.matdes.2015.07.145>.
- [221] D. Gu, J. Ma, H. Chen, K. Lin, L. Xi, Laser additive manufactured WC reinforced Fe-based composites with gradient reinforcement/matrix interface and enhanced performance, *Compos. Struct.* 192 (2018) 387–396, <https://doi.org/10.1016/j.compstruct.2018.03.008>.
- [222] K.G. Prashanth, S. Scudino, A.K. Chaubey, L. Löber, P. Wang, H. Attar, F. P. Schimansky, F. Pyczak, J. Eckert, Processing of Al-12Si-TiN composites by selective laser melting and evaluation of compressive and wear properties, *J. Mater. Res.* 31 (2016) 55–65, <https://doi.org/10.1557/jmr.2015.326>.
- [223] N. Kang, M. El Mansori, X. Lin, F. Guittouneau, H.L. Liao, W.D. Huang, C. Coddet, In-situ synthesis of aluminum/nano-quasicrystalline Al-Fe-Cr composite by using selective laser melting, *Compos. B Eng.* 155 (2018) 382–390, <https://doi.org/10.1016/j.compositesb.2018.08.108>.

- [224] J. Karimi, P. Ma, Y.D. Jia, K.G. Prashanth, Linear patterning of high entropy alloy by additive manufacturing, *Manuf. Lett.* 24 (2020) 9–13, <https://doi.org/10.1016/j.mfglet.2020.03.003>.
- [225] Z. Xu, H. Zhang, W. Li, A. Mao, L. Wang, G. Song, Y. He, Microstructure and nanoindentation creep behavior of CoCrFeMnNi high-entropy alloy fabricated by selective laser melting, *Addit. Manuf.* 28 (2019) 766–771, <https://doi.org/10.1016/j.addma.2019.06.012>.
- [226] P.D. Niu, R.D. Li, T.C. Yuan, S.Y. Zhu, C. Chen, M.B. Wang, L. Huang, Microstructures and properties of an equimolar AlCoCrFeNi high entropy alloy printed by selective laser melting, *Intermetallics* 104 (2019) 24–32, <https://doi.org/10.1016/j.intermet.2018.10.018>.
- [227] A. Aramian, Z. Sadeghian, K.G. Prashanth, F. Berto, In situ fabrication of TiC-NiCr cermets by selective laser melting, *Int. J. Refract. Metals Hard Mater.* 87 (2020) 105171, <https://doi.org/10.1016/j.ijrmhm.2019.105171>.
- [228] S.L. Sing, W.Y. Yeong, F.E. Wiria, B.Y. Tay, Z. Zhao, L. Zhao, Z. Tian, S. Yang, Direct selective laser sintering and melting of ceramics: a review, *Rapid Prototyp. J.* 23 (2017) 611–623, <https://doi.org/10.1108/RPJ-11-2015-0178>.
- [229] C. Zhu, T. Liu, F. Qian, W. Chen, S. Chandrasekaran, B. Yao, Y. Song, E.B. Duoss, J.D. Kuntz, C.M. Spadaccini, M.A. Worsley, Y. Li, 3D printed functional nanomaterials for electrochemical energy storage, *Nano Today* 15 (2017) 107–120, <https://doi.org/10.1016/j.nantod.2017.06.007>.
- [230] Z. Sun, X. Tan, S.B. Tor, C.K. Chua, Simultaneously enhanced strength and ductility for 3D-printed stainless steel 316L by selective laser melting, *NPG Asia Mater.* 10 (2018) 127–136, <https://doi.org/10.1038/s41427-018-0018-5>.
- [231] Z. Wang, M. Xie, Y. Li, W. Zhang, C. Yang, L. Kollo, J. Eckert, K.G. Prashanth, Premature failure of an additively manufactured material, *NPG Asia Mater.* 12 (2020), <https://doi.org/10.1038/s41427-020-0212-0>.
- [232] J. Suryawanshi, K.G. Prashanth, S. Scudino, J. Eckert, O. Prakash, U. Ramamurty, Simultaneous enhancements of strength and toughness in an Al-12Si alloy synthesized using selective laser melting, *Acta Mater.* 115 (2016) 285–294, <https://doi.org/10.1016/j.actamat.2016.06.009>.
- [233] Q. Chen, G. Guillemot, C.A. Gandin, M. Bellet, Three-dimensional finite element thermomechanical modeling of additive manufacturing by selective laser melting for ceramic materials, *Addit. Manuf.* 16 (2017) 124–137, <https://doi.org/10.1016/j.addma.2017.02.005>.
- [234] X. Tian, J. Jin, S. Yuan, C.K. Chua, S.B. Tor, K. Zhou, Emerging 3D-printed electrochemical energy storage devices: a critical review, *Adv. Energy Mater.* 7 (2017) 1–17, <https://doi.org/10.1002/aenm.201700127>.
- [235] M. Pumera, Three-dimensionally printed electrochemical systems for biomedical analytical applications, *Curr. Opin. Electrochem.* 14 (2019) 133–137, <https://doi.org/10.1016/j.coelec.2019.02.001>.
- [236] G. Scotti, P. Kanninen, V.P. Mattilainen, A. Salminen, T. Kallio, Stainless steel micro fuel cells with enclosed channels by laser additive manufacturing, *Energy* 106 (2016) 475–481, <https://doi.org/10.1016/j.energy.2016.03.086>.
- [237] R.J. Dawson, A.J. Patel, A.E.W. Rennie, S. White, An investigation into the use of additive manufacture for the production of metallic bipolar plates for polymer electrolyte fuel cell stacks, *J. Appl. Electrochem.* 45 (2015) 637–645, <https://doi.org/10.1007/s10800-015-0832-1>.
- [238] M.C.B. Agudelo, M. Hampe, T. Reiber, E. Abele, Investigation of porous metal-based 3D-printed anode GDs for tubular high temperature proton exchange membrane fuel cells, *Materials (Basel)* 13 (2020) 1–12, <https://doi.org/10.3390/ma13092096>.
- [239] D. Jafari, W.W. Wits, The utilization of selective laser melting technology on heat transfer devices for thermal energy conversion applications: a review, *Renew. Sustain. Energy Rev.* 91 (2018) 420–442, <https://doi.org/10.1016/j.rser.2018.03.109>.
- [240] M. Nofal, Y. Pan, S. Al-Hallaj, Selective laser sintering of phase change materials for thermal energy storage applications, *Procedia Manuf.* 10 (2017) 851–865, <https://doi.org/10.1016/j.promfg.2017.07.071>.
- [241] C. Zhao, C. Wang, R. Gorkin, S. Beirne, K. Shu, G.G. Wallace, Three dimensional (3D) printed electrodes for interdigitated supercapacitors, *Electrochem. Commun.* 41 (2014) 20–23, <https://doi.org/10.1016/j.elecom.2014.01.013>.
- [242] X. Tian, K. Zhou, 3D printing of cellular materials for advanced electrochemical energy storage and conversion, *Nanoscale* 12 (2020) 7416–7432, <https://doi.org/10.1039/d0nr00291g>.

Appendix 3

Publication III

N. Alinejadian, S.H. Kazemi, I. Odnevall, SLM-processed MoS₂/Mo₂S₃ nanocomposite for energy conversion/storage applications, Sci. Rep. 12, 5030 (2022). <https://doi.org/10.1038/s41598-022-08921-7>.



OPEN

SLM-processed MoS₂/Mo₂S₃ nanocomposite for energy conversion/storage applications

Navid Alinejadian^{1,2}, Sayed Habib Kazemi³ & Inger Odnevall^{2,4,5}✉

MoS₂-based nanocomposites have been widely processed by a variety of conventional and 3D printing techniques. In this study, selective laser melting (SLM) has for the first time successfully been employed to tune the crystallographic structure of bulk MoS₂ to a 2H/1T phase and to distribute Mo₂S₃ nanoparticles in-situ in MoS₂/Mo₂S₃ nanocomposites used in electrochemical energy conversion/storage systems (EECSS). The remarkable results promote further research on and elucidate the applicability of laser-based powder bed processing of 2D nanomaterials for a wide range of functional structures within, e.g., EECSS, aerospace, and possibly high-temperature solid-state EECSS even in space.

Na-S energy conversion/storage devices have earlier been demonstrated as possible alternatives to mitigate thermal decomposition, short circuit, heat, fire, or explosion of Li-ion electrodes^{1,2}. Recently has a high thermal stable hexagonal boron nitride (h-BN) been introduced as a promising anode material, though its low electrical conductivity may limit its electrochemical performance¹. Molybdenum disulfide (MoS₂) belongs to a class of advanced next-generation materials called Transition Metal Dichalcogenides (TMDs) with a direct bandgap of ~1.8 eV and a melting point of 1185 °C in nonoxidizing environments³. MoS₂ with strong covalent S–Mo–S bonds and weak inter-layer van der Waals forces⁴, and its nanocomposites dominate electroactive layered structures due to their transitional structure from semiconductor 2H to metallic 1T, which is favorable in electrochemical applications^{5,6}. Similar to Li⁺, the accommodation of Na⁺ between 1T-MoS₂ results in considerable capacitance and interesting electrochemical properties⁷.

MoS₂-based nanocomposites have been widely studied using a variety of conventional methods^{8–12} which have different technical drawbacks such as complex expensive pre-processing (exfoliation, preparation, and large-scale production), processing (deposition or lack of precise morphology control), and complementary post-processing stages (thermal, acid treatment, and limitation of geometric and specific surface area)^{6,13}. Despite the mitigation of existing drawbacks, scientists have enhanced processing possibilities which have led to novel 3D printing techniques^{14–20}. The use of these techniques is still limited due to drawbacks such as restricted resolution, weak mechanical properties, low printing speed, or high cost of equipment^{6,21–23}.

Laser-based thinning can effectively exfoliate MoS₂ in a controlled manner²⁴ to enable green fabrication of 3D shapes from 2D nanomaterials^{25,26}, and improve the charge capacitance properties of Mo₂S₃ nanostructures²⁷. The thinning mechanism of MoS₂, with a high laser absorption coefficient due to the weak van der Waals forces between poorly coupled MoS₂ layers, can be attributed to localized temperature-dependent sublimation of upper layers of bulk 2H-MoS₂ lattice, arising through the absorption of high-energy laser^{24,25,28}. At the next steps, laser irradiation on thinned 2H-MoS₂ can lead to further photoinduced exfoliation to form few-layered nanosheets²⁵. On the other hand, the more laser reflection due to the high reflection ratio of Mo powder²⁸, the more thinning of 2H-MoS₂ existing nearby Mo powders²⁵.

2H-MoS₂ is the thermodynamically stable trigonal phase consisting of prismatic coordination of Mo atoms by six surrounding sulfur atoms, whereas metallic 1T-MoS₂, metastable octahedral coordination of Mo atoms in MoS₂, can be a result of the first-order phase transition due to the change in the density of states²⁹. It has already been shown that the exfoliated form consists of a 1T-MoS₂ phase with lattice distortions according to

¹Department of Mechanical and Industrial Engineering, Tallinn University of Technology, 19086 Tallinn, Estonia. ²KTH Royal Institute of Technology, Division of Surface and Corrosion Science, Department of Chemistry, School of Engineering Sciences in Chemistry, Biotechnology and Health, Drottning Kristinas väg 51, 100-44 Stockholm, Sweden. ³Department of Chemistry, Institute for Advanced Studies in Basic Sciences, Zanjan 45137-66731, Iran. ⁴AIMES-Center for the Advancement of Integrated Medical and Engineering Sciences, Karolinska Institutet, KTH Royal Institute of Technology, Stockholm, Sweden. ⁵Department of Neuroscience, Karolinska Institutet, 171 77 Stockholm, Sweden. ✉email: ingero@kth.se

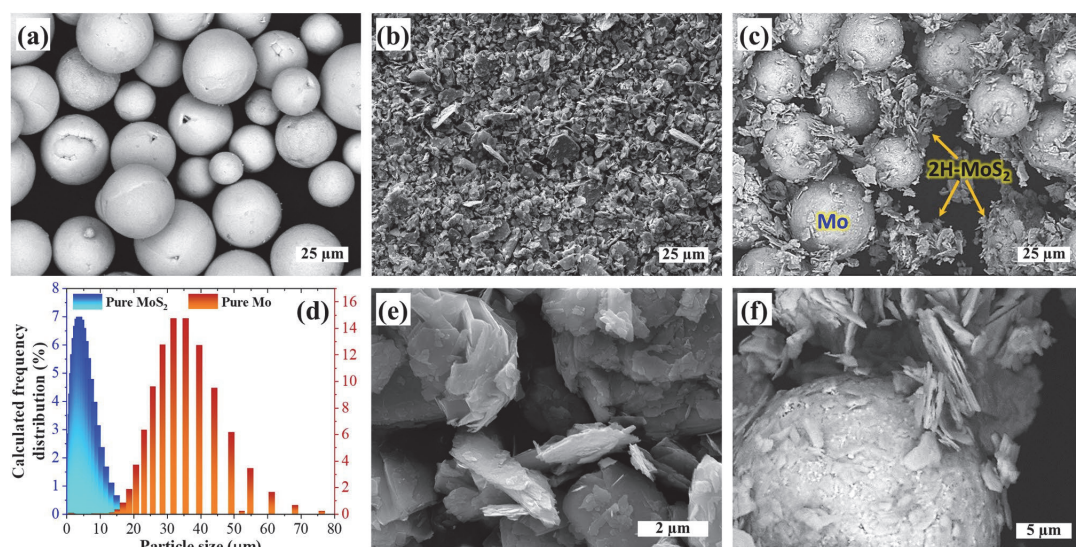


Figure 1. Scanning electron microscopy images of (a) pure Mo powder, (b) layered MoS₂ powder, and (c) Mo-MoS₂ powder mixture feedstock. (d) Particle size distribution plot of Mo and MoS₂ powders based on high-resolution scanning electron microscopy images of (e) layered MoS₂ powder and (f) the Mo-MoS₂ mixture feedstock.

the exfoliation technique. The annealing of metastable 1T-MoS₂ at temperatures lower than 300 °C can lead to restocking of the layers and restoration of 2H-MoS₂^{7,29,30}. Hence, generally, integrated hybrid 1T/2H-MoS₂ exists in which the 2H phase can stabilize the metastable 1T phase, avoiding restocking and restoration³⁰. It has though been proven that 2H-MoS₂ at temperatures higher than 600 °C can be transformed into 1T-MoS₂ via nucleation of an intermediate and subsequently 2H/1T boundaries migration over time³¹.

Accordingly, high-energy laser processing of MoS₂ can impose a highly localized temperature resulting in the thinning of MoS₂ as well as the creation of many α -phase nucleation sites for 2H to 1T phase transformation^{25,26,31}. Mo₂S₃ nanostructures can due to surface phase transformation also be formed through thermal annealing or sputtering of MoS₂ in an Ar-isolated atmosphere and at high temperatures above 1300 °C²⁵. Imposing sulfur vacancies into the structure of MoS₂ in the exposure of high-energy laser beam in the presence of melted Mo at a high temperature can also result in the formation of Mo₂S₃ nanostructures at the edges of laser-thinned 1T-MoS₂ and sulfur vacancies^{25,26}. Consequently, the rapid cooling rate of the SLM process as well as the presentation of Mo₂S₃ nanostructures can significantly prevent the restoration of 1T/2H-MoS₂.

Compared to other 3D printing methods, SLM relies on versatile high-energy Nd:YAG laser equipment which enables printing of parts of improved mechanical properties and better resolution. Since the SLM technique can overcome many of the demerits of both conventional and other 3D printing techniques^{6,21,23}, this technology can be used for rapid prototyping of future energy storage materials^{6,32}. Despite the specific characteristics of MoS₂ in electrochemical applications, the weak van der Waals forces make direct SLM processing of MoS₂ structures difficult. The addition of Mo powder, as a metallic additive, has been shown to both facilitate the printability of MoS₂ based structures and result in the formation of stable electrocatalytic Mo₂S₃ nanostructures via Mo-Mo zigzag chains, which enhance the electron transfer within and between the S-Mo-S layers²⁷.

This study reveals the extraordinary influence of the SLM technology not only on the crystallographic phase transformation of MoS₂ from bulk 2H to metallic 1T through one-step laser-based exfoliation but also on the simultaneous formation and uniform distribution of Mo₂S₃ nanoparticles in the nanocomposite structure. The unprecedented electroactivity of the one-step SLM-processed MoS₂/Mo₂S₃ nanocomposite (SLM-Mo_(x)S_(x+1)) is demonstrated, paving the way for the fabrication of the next generation EECSS. Our recent findings demonstrate that the SLM technique is able to directly utilize raw materials, exfoliate MoS₂ in-situ during fabrication of intricate parts, such as electroactive components of EECSS, and directly deliver parts of different functionalities without any special additives or binders.

Results

The spherical morphology of Mo and irregularly shaped MoS₂ particles can be ascertained from Fig. 1a,b,e, showing an average size (d_{50}) of 25–35 μm and 2.5–7.5 μm , respectively (Fig. 1d). Aside from slightly crushed pure MoS₂, its lamellar morphology was retained even after 6 h of mixing with pure Mo (Fig. 1c,f), enhancing the packing density³³ and the mean laser absorptivity^{25,28} of the Mo-MoS₂ mixture feedstock.

Illustrated in Fig. 6e (experimental), three types of defects were observed in the laser single scan (LSS) of powder bed; (i) lack of fusion (LOF) defects which were intensified by increased scan speed and reduced laser

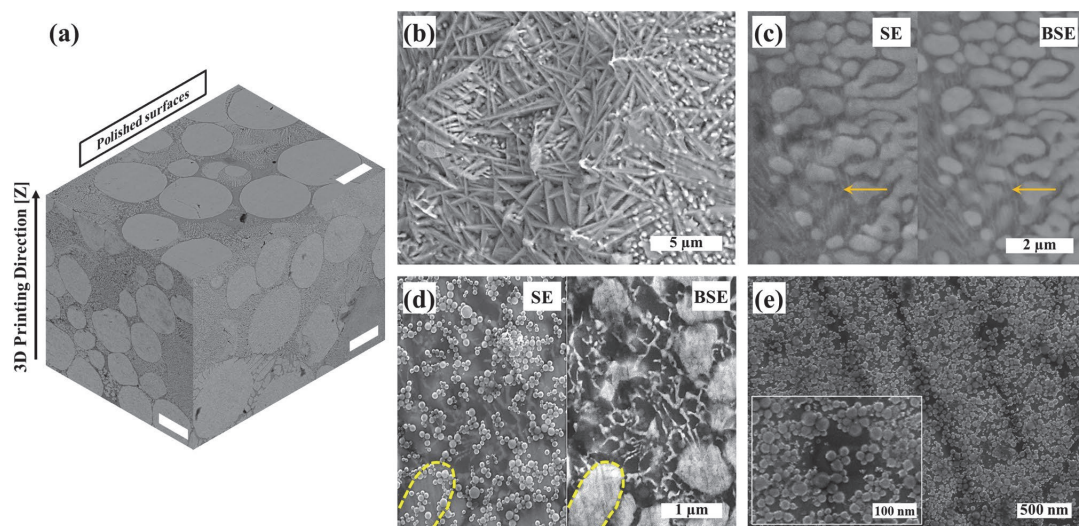


Figure 2. SEM micrographs of (a) polished surfaces of SLM- $\text{Mo}_{(x)}\text{S}_{(x+1)}$ (scale bar = 25 μm), (b) unpolished top-surface including laser-assisted exfoliated 1T- MoS_2 nanosheets and Mo_2S_3 nanoparticles, (c) high magnification secondary and backscattered electron micrographs acquired from the polished cross-section in which the arrows indicate thin transparent 1T- MoS_2 layers alongside coalesced Mo_2S_3 nanoparticles, (d) HR-SEM micrograph of the polished surface of SLM- $\text{Mo}_{(x)}\text{S}_{(x+1)}$ in which the yellow dashed lines indicate coalescence zones of Mo_2S_3 nanoparticles, and (e) high magnification HR-SEM micrograph of a cross-section showing Mo_2S_3 nanoparticles within the structure of the nanocomposite.

power, (ii) balling defects due to the insufficient imposed energy density either at high scan speeds or low laser powers, and (iii) over melting of the powder bed at high energy densities due to both high laser power and low scan speed²⁸. The 3D SEM micrograph from different polished sections of SLM- $\text{Mo}_{(x)}\text{S}_{(x+1)}$ indicated a similar microstructure which can be ascribed to the optimized LSS (laser power of 62.5 W and a laser scan speed of 85 mm s^{-1}) resulting in a relatively stable melt-pool with a nearly constant thermal gradient during the SLM process (Fig. 2a)^{34,35}. Scanning electron micrographs (SEM) illustrate the exfoliation of bulk 2H- MoS_2 into thin 1T- MoS_2 nanosheets and the distribution of Mo_2S_3 nanoparticles in the matrix (Fig. 2b). Both the back-scattered (BSE) and the secondary-electron (SE) micrographs elucidate the presence of 1T- MoS_2 layers of low density (Fig. 2c,d). Indicating identical zones, the arrows in Fig. 2c and the dashed lines in Fig. 2d, confirm the presence of Mo_2S_3 nanoparticles coalesced at the lower parts- and separated at the top surface of the nanocomposite, delimited by a transparent 1T- MoS_2 layer. The coalescence is attributed to partial remelting of the subsequent layers during the layer-wise SLM process. HR-SEM micrographs (Fig. 2e) reveal a uniform distribution of Mo_2S_3 nanoparticles sized between 25 and 50 nm. The spherical particle morphology is attributed to the high surface tension between MoS_2 and Mo_2S_3 due to varying Mo/S ratios and the tendency of resolidified nanostructures to reduce their surface energies²⁵.

The X-ray diffraction (XRD) patterns verified the purity of Mo and MoS_2 both before and after the mixing process (Fig. 3a). The low-intensity XRD peaks confirm the presence of Mo_2S_3 along with pure 1T/2H- MoS_2 crystallographic planes (Fig. 3b). Both the exfoliation and the phase transformation of 2H- MoS_2 resulted in diffraction peaks related to the 001 plane of 1T- MoS_2 ($2\theta = 10.495^\circ$)⁷. Illustrated in Fig. 3c, the broadening and blue shift of the E_{2g}^1 and A_{1g} Raman peaks from 384 cm^{-1} (E_{2g}^1) and 409 cm^{-1} to 380 cm^{-1} and 406 cm^{-1} , respectively, confirm the Nd:YAG laser-assisted thinning and transformation of 2H- MoS_2 to a few-layered 1T- MoS_2 at the temperature elevated above 650° K^{25,26}. Besides, the existence of Mo_2S_3 nanoparticles was verified by the appearance of two shoulders associated with E_{2g}^1 and A_{1g} Raman peaks of Mo_2S_3 at 376 cm^{-1} and 403 cm^{-1} , respectively²⁵.

Cyclic voltammograms (CV) show considerably enhanced current densities for the SLM- $\text{Mo}_{(x)}\text{S}_{(x+1)}$ sample compared to both pure Mo and MoS_2 electrodes (Fig. 4a). Due to the presence of the Mo_2S_3 nanoparticles as well as the laser-based thinning and crystallographic phase transformation of MoS_2 from 2H to 1T, it is evident that the CV loops retained their nearly rectangular shapes even at high scan rates (100 mV s^{-1}) (Fig. 4b)⁷. Quasi-symmetrical triangle plots of the galvanostatic charge-discharge (GCD) at different current densities revealed nearly 1.0 V in output voltage even at a current density of 15 mA cm^{-2} for the SLM- $\text{Mo}_{(x)}\text{S}_{(x+1)}$ electrodes (Fig. 4c). Herein, we observed considerable capacitance enhancement up to 2000 cycles of GCD at a current density of 8 mA cm^{-2} . This confirms an increased areal capacitance (from 41 to 121.2 mF cm^{-2}) and a decreased iR voltage drop. The enhanced capacitance induced by increasing the number of GCD cycles can be attributed to facilitated intercalation of Na^+ cations, activation of the electrode texture, and improved electrical conductivity (Fig. 4d). It can also be ascribed to the penetration of electrolyte into micro-holes of the structure,

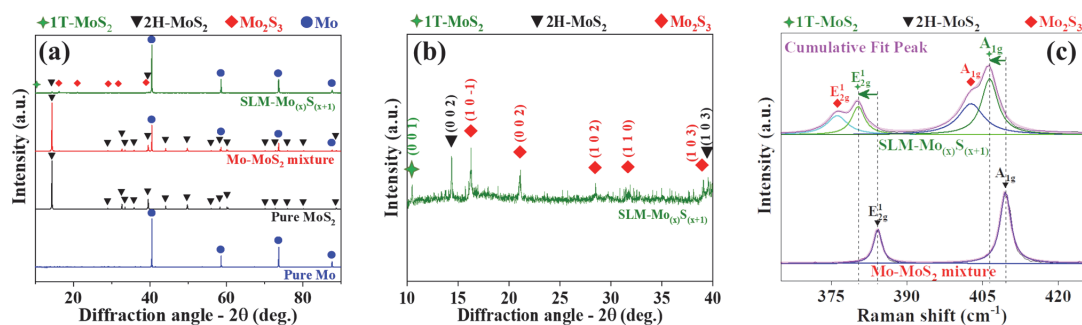


Figure 3. (a) XRD patterns of the pure Mo powder, MoS₂ powder, Mo-MoS₂ powder mixture, and SLM-Mo_(x)S_(x+1) samples, (b) magnified XRD peaks between $10 \leq 2\theta \leq 40$ showing the presence of 1T-MoS₂, 2H-MoS₂, and Mo₂S₃ phases in the nanocomposite and (c) Raman spectra with the deconvoluted profiles of 1T-MoS₂, 2H-MoS₂, and Mo₂S₃ nanoparticles showing the shift in their position.

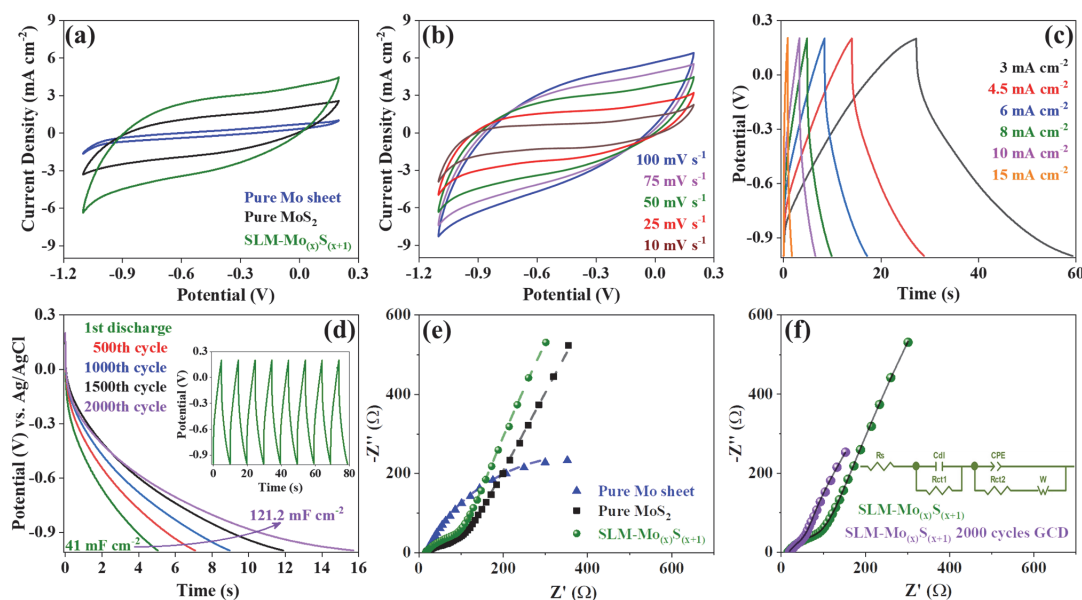


Figure 4. Electrochemical characterization in a 0.5 M Na₂SO₄: (a) CV curves of pure Mo sheet, pure MoS₂, and SLM-Mo_(x)S_(x+1) by using a scan rate of 50 mV s⁻¹, (b) cyclic voltammograms for different scan rates from 10 to 100 mV s⁻¹, (c) GCD curves for different current densities from 3 to 15 mA cm⁻², (d) discharge retention stability after 500, 1000, 1500, and 2000 cycles of GCD at a current density of 8 mA cm⁻², and (e) Nyquist plot of pure Mo sheet, pure MoS₂, and SLM-Mo_(x)S_(x+1) in the frequency range between 10⁻¹ Hz to 100 kHz, (f) Nyquist plot of SLM-Mo_(x)S_(x+1) in the frequency range between 10⁻¹ Hz to 100 kHz before and after 2000 cycles of GCD at a current density of 8 mA cm⁻².

successively activating deeper electro-active sites, and possibly a continued activation of sub-layers beneath the SLM-Mo_(x)S_(x+1) surface^{36,37}.

As shown in Fig. 4e, faster kinetic of the charge transfer at the interface offered by the layered 1T-MoS₂, separated by Mo₂S₃ nanoparticles, resulted in a considerably lower R_{ct} (75.36 Ω) and a quasi-semicircle shape of the Nyquist plot of SLM-Mo_(x)S_(x+1) compared to pure Mo. The higher slope of the diffusion impedance in the low-frequency region for SLM-Mo_(x)S_(x+1) compared to pure 2H-MoS₂, confirms facilitated diffusion and accumulation of Na⁺ charges into the defect-rich 1T-MoS₂ nanolayers within the porous surface (Fig. 4e)³⁸. Comparing the SLM-Mo_(x)S_(x+1) electrode before and after 2000 cycles GCD in Fig. 4f, showed a considerably decreased diameter of the quasi-semicircle of the Nyquist plot (charge transfer resistance) at high frequencies as well as an increased slope of the diffusion impedance in the low-frequency region. This further verify faster

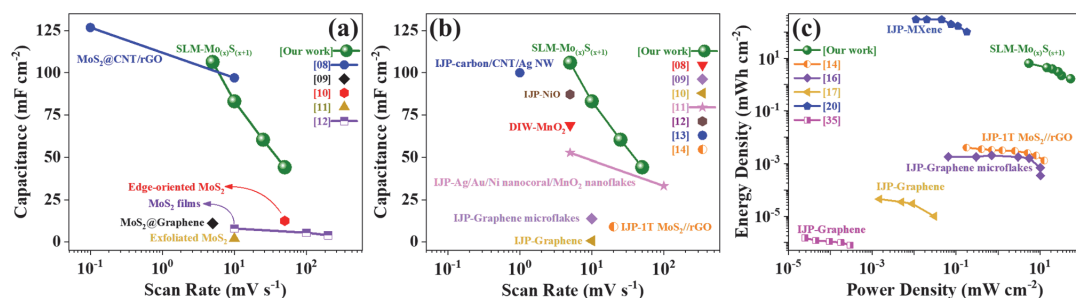


Figure 5. (a) Areal rate capacitance for different MoS₂-based structures processed by various conventional methods for energy storage devices (the weight percentage in parenthesis indicates the amount of MoS₂ in the structure); (b) areal rate capacitance for different materials processed with various 3D printing methods for energy storage applications and (c) Ragone plot comparing the areal power density versus areal energy density of 3D-printed electrodes intended for energy storage applications.

kinetics of the interface charge transfer and facilitated Na⁺ intercalation into the deeper active sites and spaces of electrode materials, respectively, by increasing the number of GCD cycles.

Areal rate capability studies of the SLM-Mo_(x)S_(x+1) electrode revealed capacitance retention of 53% even at a scan rate of 50 mV s⁻¹ (44.16 mF cm⁻²) compared to a low scan rate of 10 mV s⁻¹ (83.1 mF cm⁻²). This is considerably higher than their counterpart electrodes processed by different 3D printing techniques (Fig. 5a,b). Furthermore, according to the Ragone plot (Fig. 5c), the SLM-Mo_(x)S_(x+1) electrodes offered higher power (53.34 mW cm⁻²) and energy density (1.66 mWh cm⁻²) compared with ink-jet printed MXene³⁹, and graphene-based electrodes^{16,17,40}, as well as 1T-MoS₂/graphene-based electrodes¹⁴.

Concluding remarks

The successful fabrication of SLM-processed MoS₂/Mo₂S₃ electrodes with a remarkable capacitive behavior compared to other 3D-printed counterparts provides a new possibility to manufacture the next generation of 3D-printed electrochemical devices. In this study, we elucidated that a high-energy Nd:YAG laser can simultaneously exfoliate and tune the structure of MoS₂, distribute electroactive Mo₂S₃ nanoparticles into the structure of the nanocomposite, and therefore considerably enhance the power density and energy density of 3D-printed structures. The preliminary results promote further research on laser-based processing of 2D nanomaterials for a wide range of functional structures e.g., EECSS, high-temperature solid-state energy conversion/storage systems, aerospace parts, and green energy storage device fabrication, even in space.

Materials and methods

Gas atomized powder (GAP) of commercial pure molybdenum (Mo, 99.99%) was used as the feedstock to fabricate both the current collector and the electroactive nanocomposite. Pure molybdenum disulfide powder (2H-MoS₂, 99.99%, Sigma Aldrich) was used as feedstock for SLM processing of the electroactive nanocomposite. A mixture of Mo and MoS₂ (20 wt.%) was prepared by mixing for 6 h at 20 rpm to obtain a homogenous mixture (Fig. 6a,d). The Na₂SO₄ (≥ 99.0%, Merck) and ultrapure water, with a conductivity of 18.2 MΩcm and a pH of 6.5 ± 0.1 at 25 °C, was used to prepare the 0.5 M Na₂SO₄ (pH 5.5 ± 0.1) electrolyte for the electrochemical investigations.

A laser scattering particle size distribution analyzer (LPSA, LA-950, HORIBA, Japan) was used to evaluate the particle size distribution of the Mo and MoS₂ powders. A Realizer GmbH SLM-50 device equipped with Nd:YAG laser was used for SLM processing of pure Mo as a substrate/current collector and MoS₂/Mo₂S₃ nanocomposite as the electroactive structure. The 316L substrate platform was used to fabricate the samples at ambient conditions. Laser single scanning (LSS) was carried out as a function of energy density to obtain the optimized printing parameters, where the energy density is defined in Eq. (1):

$$E_d = P/(v.h.t) \quad (1)$$

where P is the laser power, v is the laser scan speed, h is the hatch distance, and t is the layer thickness. The hatch distance and layer thickness were kept constant at 0.045 mm and 0.025 mm, respectively. The schematic of single laser scanning on a powder bed to form a single hatch has been illustrated in Fig. 6b. commensurately shown in Fig. 6e, the laser power and scan speed were varied between 25 and 75 W and 65–550 mm s⁻¹, respectively. The disk-shaped electrodes were fabricated of a mixture of Mo and MoS₂ (20 wt.%) by using optimized SLM parameters (laser power – 62.5 W and scan speed – 85 mm s⁻¹). Figure 6c illustrates the continued scanning of powder-bed leading to consolidation and formation of one layer onto the previously printed and solidified sub-layers (Supplementary Information). Each layer can contain approximately 14 mg MoS₂. Shown in Fig. 6f, both the sintered particles in the boundary between melted/solidified region (red arrow) and un-melted powder bed (yellow arrow) and overlapping of hatches (vertical lines indicated by the blue arrow) are evident. Hatch size (a) and hatch overlap (a – Δx) have been illustrated in Fig. 6b,c, respectively.

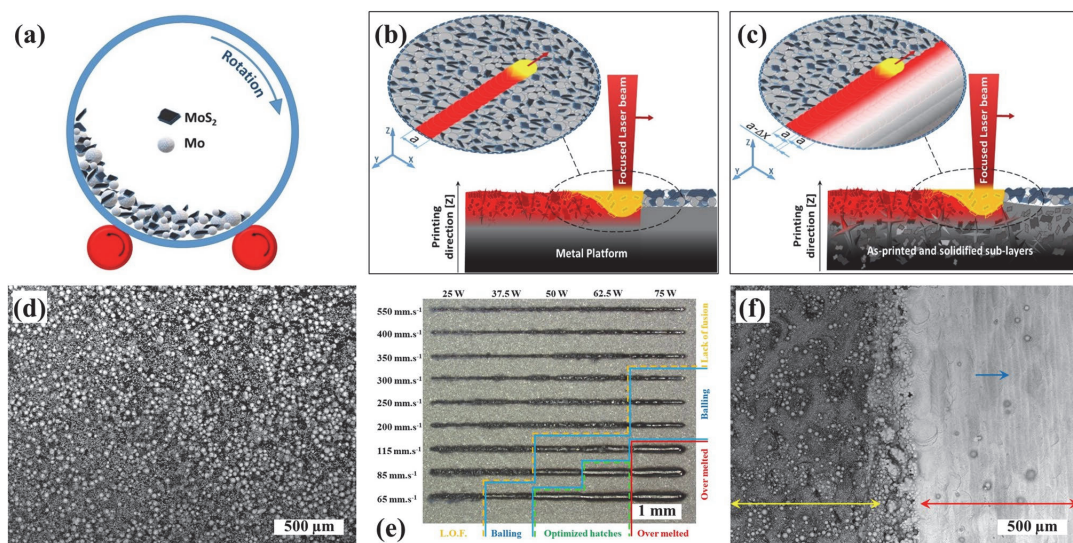


Figure 6. Schematic illustrating the (a) mixing of Mo and MoS₂ powders, (b) single laser scanning, and (c) laser-based fusion of the powder bed with partial remelting of the previously solidified layer. (d) SEM images of a homogenous mixture of Mo and MoS₂ powders, (e) stereomicrograph of laser single scan as a function of energy density, and (f) SEM image of the half-melted sample showing the boundary between the melted/solidified (red arrow), un-melted powder bed (yellow arrow), and hatch overlap during continues single laser scanning of powder bed (blue arrow).

A stereomicroscope (V20, Zeiss, Germany) was used to study the effect of different single laser scanning parameters on the stability of the melt pool to optimize the 3D printing parameters (Fig. 6e). An ultrasonic bath (USC300TH, VWR, Malaysia) was used to prepare and degas the 0.5 M Na₂SO₄ electrolyte as well as to clean the surface of the 3D-printed electrodes. A standard pH meter (PHM210, Radiometer Analytical-Hack, France) was used to measure the pH of the Na₂SO₄ electrolyte. A PARSTAT MC multichannel potentiostat (AMETEK, Princeton Applied Research, USA), an Ag/AgCl reference electrode (AMETEK, Princeton Applied Research, USA), and a Pt wire counter electrode (CHI115, CH Instruments Inc., USA) were used for the electrochemical studies. The surface area of the working electrode (anode) was 0.33 cm². Cyclic voltammetry (CV) was carried out using scan rates between 10 and 100 mV s⁻¹ in a potential window between -1.1 and 0.2 V. Electrochemical potentiostatic impedance (EIS) measurements were carried out in the frequency range between 10⁻¹ Hz and 100 kHz (Figure S4b). Galvanostatic charge-discharge (GCD) measurements were carried out at different current densities (3, 4.5, 6, 8, 10, and 15 mA cm⁻²). 2000 cycles of GCD at a current density of 8 mA cm⁻² were performed on the electrodes to evaluate their stability and capacity retention.

X-ray diffraction (XRD) studies were carried out by using a Smartlab (Rigaku, Japan) diffractometer equipped with a rotating 9 kW Cu anode X-ray tube with Cu-Kα1 radiation ($\lambda = 1.5406 \text{ \AA}$), and a silicon strip detector D/teX Ultra. Based on the Rigaku database, ICDD card numbers 9008543, 1531960, and 1531960 were selected to identify the XRD patterns of Mo, MoS₂, and Mo₂S₃, respectively. Raman measurements were carried out using a Horiba LabRAM HR800 micro-Raman system equipped with a cooled multichannel CCD detection system in the back-scattering configuration with a spectral resolution of 1 cm⁻¹. A Nd:YAG laser ($\lambda = 532 \text{ nm}$) was used for excitation with a laser spot size diameter of approximately 5 μm . A high-resolution scanning electron microscope (HR-SEM, Zeiss MERLIN, Germany) was employed to study the surface morphology of 3D-printed samples in both back-scattered (BE) and secondary (SE) electron modes (Supplementary Information).

Data availability

All data generated or analyzed during this study are included in this published article, and the datasets used and analyzed during the current study are available from the corresponding author on reasonable request.

Received: 2 February 2022; Accepted: 15 March 2022

Published online: 23 March 2022

References

- Mussa, Y., Ahmed, F., Arsalan, M. & Alsharaeh, E. Two dimensional (2D) reduced graphene oxide (RGO)/hexagonal boron nitride (h-BN) based nanocomposites as anodes for high temperature rechargeable lithium-ion batteries. *Sci. Rep.* **10**, 1–13 (2020).
- Yoo, H. D., Markevich, E., Salitra, G., Sharon, D. & Aurbach, D. On the challenge of developing advanced technologies for electrochemical energy storage and conversion. *Mater. Today* **17**, 110–121 (2014).

3. Chhowalla, M. *et al.* The chemistry of two-dimensional layered transition metal dichalcogenide nanosheets. *Nat. Chem.* **5**, 263–275 (2013).
4. Lu, J., Liu, H., Tok, E. S. & Sow, C.-H.H. Interactions between lasers and two-dimensional transition metal dichalcogenides. *Chem. Soc. Rev.* **45**, 2494–2515 (2016).
5. Fleischmann, S. *et al.* Pseudocapacitance: From fundamental understanding to high power energy storage materials. *Chem. Rev.* **120**, 6738–6782 (2020).
6. Alinejadian, N., Kollo, L. & Odneval, I. Materials science in semiconductor processing progress in additive manufacturing of MoS₂-based structures for energy storage applications—A review. *Mater. Sci. Semicond. Process.* **139**, 106331 (2022).
7. Acerce, M., Voiry, D. & Chhowalla, M. Metallic 1T phase MoS₂ nanosheets as supercapacitor electrode materials. *Nat. Nanotechnol.* **10**, 313–318 (2015).
8. Wang, S. *et al.* Three-dimensional MoS₂@CNT/RGO network composites for high-performance flexible supercapacitors. *Chem. A Eur. J.* **23**, 3438–3446 (2017).
9. Bissett, M. A., Kinloch, I. A. & Dryfe, R. A. W. Characterization of MoS₂-graphene composites for high-performance coin cell supercapacitors. *ACS Appl. Mater. Interfaces* **7**, 17388–17398 (2015).
10. Yang, Y., Fei, H., Ruan, G., Xiang, C. & Tour, J. M. Edge-oriented MoS₂ nanoporous films as flexible electrodes for hydrogen evolution reactions and supercapacitor devices. *Adv. Mater.* **26**, 8163–8168 (2014).
11. Winchester, A. *et al.* Electrochemical characterization of liquid phase exfoliated two-dimensional layers of molybdenum disulfide. *ACS Appl. Mater. Interfaces* **6**, 2125–2130 (2014).
12. Cao, L. *et al.* Direct laser-patterned micro-supercapacitors from paintable MoS₂ films. *Small* **9**, 2905–2910 (2013).
13. Lin, Z. *et al.* Solution-processable 2D semiconductors for high-performance large-area electronics. *Nature* **562**, 254–258 (2018).
14. Shao, Y. *et al.* 3D crumpled ultrathin 1T MoS₂ for inkjet printing of Mg-ion asymmetric micro-supercapacitors. *ACS Nano* **14**, 7308–7318 (2020).
15. Wang, T. *et al.* 3D printing-based cellular microelectrodes for high-performance asymmetric quasi-solid-state micro-pseudocapacitors. *J. Mater. Chem. A* **8**, 1749–1756 (2020).
16. Sollami Delekta, S., Laurila, M.-M., Mäntyselä, M. & Li, J. Drying-mediated self-assembly of graphene for inkjet printing of high-rate micro-supercapacitors. *Nano-Micro Lett.* **12**, 40 (2020).
17. Li, J. *et al.* Scalable fabrication and integration of graphene microsupercapacitors through full inkjet printing. *ACS Nano* **11**, 8249–8256 (2017).
18. Lin, Y., Gao, Y. & Fan, Z. Printable fabrication of nanocoral-structured electrodes for high-performance flexible and planar supercapacitor with artistic design. *Adv. Mater.* **29**, 1–8 (2017).
19. Giannakou, P., Tas, M. O., Le Borgne, B. & Shkunov, M. Water-transferred, inkjet-printed supercapacitors toward conformal and embedded energy storage. *ACS Appl. Mater. Interfaces* **12**, 8456–8465 (2020).
20. Choi, K. H., Yoo, J. T., Lee, C. K. & Lee, S. Y. All-inkjet-printed, solid-state flexible supercapacitors on paper. *Energy Environ. Sci.* **9**, 2812–2821 (2016).
21. Cheng, M., Deivanayagam, R. & Shahbazian-Yassar, R. 3D printing of electrochemical energy storage devices: A review of printing techniques and electrode/electrolyte architectures. *Batter. Supercaps* **3**, 130–146 (2020).
22. Egorov, V. *et al.* Evolution of 3D printing methods and materials for electrochemical energy storage. *Adv. Mater.* **32**, 1–27 (2020).
23. Zhang, F. *et al.* 3D printing technologies for electrochemical energy storage. *Nano Energy* **40**, 418–431 (2017).
24. Castellanos-Gomez, A. *et al.* Laser-thinning of MoS₂: On demand generation of a single-layer semiconductor. *Nano Lett.* **12**, 3187–3192 (2012).
25. Alexaki, K., Kostopoulou, A., Sygletou, M., Kenanakis, G. & Stratakis, E. Unveiling the structure of MoS₂ nanocrystals produced upon laser fragmentation of MoS₂ platelets. *ACS Omega* **3**, 16728–16734 (2018).
26. Hu, L., Shan, X., Wu, Y., Zhao, J. & Lu, X. Laser thinning and patterning of MoS₂ with layer-by-layer precision. *Sci. Rep.* **7**, 1–9 (2017).
27. Zhou, X. *et al.* Urchin-like MoS₂ prepared via a molten salt assisted method for efficient hydrogen evolution. *Chem. Commun.* **54**, 12714–12717 (2018).
28. Wang, D., Yu, C., Ma, J., Liu, W. & Shen, Z. Densification and crack suppression in selective laser melting of pure molybdenum. *Mater. Des.* **129**, 44–52 (2017).
29. Eda, G. *et al.* Photoluminescence from chemically exfoliated MoS₂. *Nano Lett.* **11**, 5111–5116 (2011).
30. Wang, D. *et al.* Phase engineering of a multiphase 1T/2H MoS₂ catalyst for highly efficient hydrogen evolution. *J. Mater. Chem. A* **5**, 2681–2688 (2017).
31. Lin, Y. C., Dumcenco, D. O., Huang, Y. S. & Suenaga, K. Atomic mechanism of the semiconducting-to-metallic phase transition in single-layered MoS₂. *Nat. Nanotechnol.* **9**, 391–396 (2014).
32. Zhu, C. *et al.* 3D printed functional nanomaterials for electrochemical energy storage. *Nano Today* **15**, 107–120 (2017).
33. Körner, C., Attar, E. & Heinel, P. Mesoscopic simulation of selective beam melting processes. *J. Mater. Process. Technol.* **211**, 978–987 (2011).
34. Yuan, W., Chen, H., Cheng, T. & Wei, Q. Effects of laser scanning speeds on different states of the molten pool during selective laser melting: Simulation and experiment. *Mater. Des.* **189**, 108542 (2020).
35. Leitz, K. H. *et al.* Multi-physical simulation of selective laser melting. *Met. Powder Rep.* **72**, 331–338 (2017).
36. Kazemi, S. H., Hosseinzadeh, B., Kazemi, H., Kiani, M. A. & Hajati, S. Facile synthesis of mixed metal-organic frameworks: Electrode materials for supercapacitors with excellent areal capacitance and operational stability. *ACS Appl. Mater. Interfaces* **10**, 23063–23073 (2018).
37. Bahmani, F. *et al.* CuMnO₂-reduced graphene oxide nanocomposite as a free-standing electrode for high-performance supercapacitors. *Chem. Eng. J.* **375**, 121966 (2019).
38. Li, Y. *et al.* Hierarchical MoS₂ hollow architectures with abundant Mo vacancies for efficient sodium storage. *ACS Nano* **13**, 5533–5540 (2019).
39. Zhang, C. *et al.* Additive-free MXene inks and direct printing of micro-supercapacitors. *Nat. Commun.* **10**, 1–9 (2019).
40. Li, L. *et al.* High-performance solid-state supercapacitors and microsupercapacitors derived from printable graphene inks. *Adv. Energy Mater.* **6**, 1600909 (2016).

Acknowledgements

Dr. Lauri Kollo, Prof. Maarja Grossberg, and Dr. Olga Volobujeva, are acknowledged for their research support and technical discussion. Dr. Xuying Wang is acknowledged for providing electrodes and tools. Prof. Prashanth KondaGokuldoss is acknowledged for sharing his initial opinions and providing powder feedstock. Dr. Pei Wang is appreciated for providing pure Mo powder. The research was funded by the European Regional Development Fund [ASTRA6-6], the Estonian Education and Youth Board and the Estonian Government [contract number: 5.10-6.1/21/23-4 and 5.10-6.1/21/327-2].

Author contributions

N.A.: conceptualization; SLM processing, experiments, and characterizations by SEM, XRD, Raman spectroscopy, and all electrochemical characterization; funding acquisition; investigation; writing original draft, reviewing, editing, and validation of data. S.H.K.: advisory of electrochemical characterizations; formal analysis, review, editing, and validation of data. I.O.: supervision, providing resources, instrumentation, and analytical tools, formal analysis, reviewing, editing, and validation of data.

Funding

Open access funding provided by Royal Institute of Technology.

Competing interests

The authors declare no competing interests.

Additional information

Supplementary Information The online version contains supplementary material available at <https://doi.org/10.1038/s41598-022-08921-7>.

Correspondence and requests for materials should be addressed to I.O.

Reprints and permissions information is available at www.nature.com/reprints.

Publisher's note Springer Nature remains neutral with regard to jurisdictional claims in published maps and institutional affiliations.



Open Access This article is licensed under a Creative Commons Attribution 4.0 International License, which permits use, sharing, adaptation, distribution and reproduction in any medium or format, as long as you give appropriate credit to the original author(s) and the source, provide a link to the Creative Commons licence, and indicate if changes were made. The images or other third party material in this article are included in the article's Creative Commons licence, unless indicated otherwise in a credit line to the material. If material is not included in the article's Creative Commons licence and your intended use is not permitted by statutory regulation or exceeds the permitted use, you will need to obtain permission directly from the copyright holder. To view a copy of this licence, visit <http://creativecommons.org/licenses/by/4.0/>.

© The Author(s) 2022

Curriculum vitae

Personal data

Name: Navid Alinejadian
Date of birth: 17.04.1984
Place of birth: Iran
Citizenship: Iranian

Contact data

E-mail: navid.alinejaidan@taltech.ee
navidali@kth.se
n.alinejadian@outlook.com

Education

2018–2022 Tallinn University of Technology, Estonia – PhD
2013–2016 Sahand University of Technology, Iran – MSc
2005–2007 Islamic Azad University, Iran – BSc
2001–2004 Technical and vocational college of Tabriz, Iran – Associate’s degree

Language competence

English Advanced
Persian Fluent
Azeri Good

Professional employment

2017–2018 Green Nanoscale Technology Co. (Startup), Iran – CEO and Co-founder
2016–2018 Institute for Advanced Studies in Basic Sciences, Iran – Research assistant
2010–2012 Irankhodro Aluminium Casting company (IKACO), Iran – R&D and QC expert, and head of QC laboratories

Awards

2022 Dora Plus Scholarship for short-term Ph.D. Mobility | Archimedes Foundation [5.10-6.1/21/327-2] | Additive Manufacturing and Functional Materials, KTH Royal Institute of Technology, Sweden.
2021 Dora Plus Scholarship for long-term Ph.D. Mobility | Archimedes Foundation [5.10-6.1/21/23-4] | Additive Manufacturing and Functional Materials, KTH Royal Institute of Technology, Sweden.
2020 Kristjan Jaak Scholarship for Short Visiting Study | Archimedes Foundation | Additive Manufacturing, EIT RawMaterials and EMPA (European Powder Metallurgy Association), Germany.
2019 TalTech Doctoral School Scholarship | Tallinn University of Technology | Developing Successful Commercialization of Technologies, EIT RawMaterials/Riga Technological University, Latvia.
2018 Top Poster Award | Effect of improved geometric surface area and enhanced nanoscale surface roughness on the promotion of electroactivity on three-dimensional grown Ni/G nanocomposite. 7th International Conference on Nanostructures (ICNS7), Sharif University of Technology, Iran.
2010 IKACO Green Card Award | Development of codified instruction of refractory materials used in aluminum casting Industries. Iran Khodro Aluminum Casting Co (IKACO), Iran.
2001 The 1st rank Honor | The 1st rank in the field of technical drawing among 181 examinees at the 2nd stage of National Trial University Entrance Examination, Iran.

Elulookirjeldus

Isikuandmed

Nimi: Navid Alinejadian
Sünniaeg: 17.04.1984
Sünnikoht: Iraan
Kodakondsus: iraanlane

Kontaktandmed

E-post: navid.alinejaidan@taltech.ee
navidali@kth.se
n.alinejadian@outlook.com

Hariduskäik

2018–2022 Tallinn University of Technology, Estonia – PhD
2013–2016 Sahandi Tehnikaülikool, Iraan – MSc
2005–2007 Islami Azadi Ülikool, Iraan – BSc
2001–2004 Tabrizi tehnika- ja kutsekõrgkool, Iraan – Associate’s kraad

Keelteoskus

Inglise keel Kõrgtase
Pärsia keel Ladus
Aser keel Hea

Teenistuskäik

2017–2018 Green Nanoscale Technology (Startup), Iraan – tegevjuht ja kaasasutaja
2016–2018 Põhiteaduste Kõrgteaduste Instituut, Iraan – Teadusassistent
2010–2012 Irankhodro Aluminium Casting Company (IKACO), Iraan – uurimis- ja arendustegevuse ning kvaliteedikontrolli ekspert ning kvaliteedikontrolli laborite juht

Auhinnad

2022 Dora Plusi stipendium lühiajaliseks doktorikraadiks. Liikuvus | Sihtasutus Archimedes [5.10-6.1/21/327-2] | Lisandite tootmine ja funktsionaalsed materjalid, KTH Kuninglik Tehnoloogiainstituut, Rootsi.

2021 Dora Plusi stipendium pikaajalisele doktorikraadile. Liikuvus | Sihtasutus Archimedes [5.10-6.1/21/23-4] | Lisandite tootmine ja funktsionaalsed materjalid, KTH Kuninglik Tehnoloogiainstituut, Rootsi.

2020 Kristjan Jaagu stipendium lühikülalisõppeks | Sihtasutus Archimedes | Lisandite tootmine, EIT RawMaterials ja EMPA (European Powder Metallurgy Association), Saksamaa.

2019 TalTechi doktorikooli stipendium | Tallinna Tehnikaülikool | Developing Successful Commercialization of Technologies, EIT RawMaterials/Riga Technological University, Läti.

2018 aasta parima plakati auhind | Täiustatud geomeetrilise pinna ja nanomõõtmelise pinna kareduse mõju kolmemõõtmelise kasvatatud Ni/G nanokomposiidi elektroaktiivsuse soodustamisele. 7th International Conference on Nanostructures (ICNS7), Sharifi Tehnikaülikool, Iraan.

2010 aasta IKACO roheline kaardi auhind | Alumiiniumivalutööstuses kasutatavate tulekindlate materjalide kodifitseeritud juhendi väljatöötamine. Iran Khodro Aluminium Casting Co (IKACO), Iraan.

2001 1. järgu autasu| Iraani riikliku katseülikooli sisseastumiseksami 2. etapi 181 eksaminandi seas tehnilise joonestamise alal 1. koht.

ISSN 2585-6901 (PDF)
ISBN 978-9949-83-876-9 (PDF)